Marine Carbon Cycle Evolution in the Eastern Equatorial Pacific over the Last Deglaciation

Tesis doctoral presentada por María de la Fuente García para obtener el grado de Doctora por la Universidad de Las Palmas de Gran Canaria

Programa de Doctorado en Oceanografía

Directoras: Eva Calvo Costa e Isabel Cacho Lascorz

Universidad de las Palmas de Gran Canaria

Institut de Ciències del Mar (ICM-CSIC)

Universitat de Barcelona

Barcelona, julio de 2016

La doctoranda La directora La codirectora

Portada: CLIMAP Project Members (1981). Seasonal Reconstruction of the Earth's Surface at the Last Glacial Maximum. Geological Society of America, Map and Chart Series, 36, 18pp.

Contraportada: Geographic Map of the Circum-Pacific Region, The American Association of Petroleum Geologists, 1978

Composition by Luke Skinner

A todo lo que me hace sonreir..

CONTENTS

List of figures

Chapter 1

Chapter 2

Chapter 3

Chapter 4

Chapter 5

Chapter 6

Chapter 7

List of tables

ABSTRACT

Although the glacial-interglacial climate cycles of the late Pleistocene were very likely paced by changes in solar insolation, the full amplitude of these climate cycles was only achieved with the help of strong feedbacks within the Earth system, including variations in the atmospheric CO_2 concentration. It is thought that these CO_2 changes resulted primarily from perturbations of the marine carbon cycle. Thus, for example, an increase in the efficiency of the marine carbon pumps (more specifically the solubility pump and biological pumps) may have permitted the accumulation of larger amounts of CO_2 in the ocean interior, away from the atmosphere. The goal of this thesis is to investigate the existence of such a theoretical stock of CO_2 in the glacial ocean and to assess the mechanisms through which it may have arisen. To this end, I have analysed a combination of proxies in sediment core ODP1240 from the Eastern Equatorial Pacific (EEP) over the last deglaciation, all of which related to past changes in ocean interior carbon content. These proxies include: radiocarbon "ventilation ages" as a proxy for deep ocean turn-over time, benthic foraminiferal B/Ca ratios as a proxy for deep water $\Delta[CO_3^{2-}]_{\text{in situ-sat}}$ (and therefore $[CO_3^{2-}]$), $\delta^{13}C$ as a proxy for respired carbon content, and $\Delta\delta^{13}C_{(\text{epifaunal-infaunal})}$ as an additional estimate of water oxygenation. The results demonstrate that the deep- and shallow-subsurface EEP were much more poorly ventilated during the Last Glacial Maximum (LGM) relative to the Holocene epoch. This would suggest an increased residence time for carbon in the deep Pacific and an increase in the efficiency of the marine biological carbon pump via a decrease in its "leakiness", which could have been further enhanced by an increase in local export productivity during the last glacial period. The increase in deep ocean respired carbon levels that would be expected from these changes, is confirmed by deep-water $[CO_3^{2-}]$ reconstructions (derived here using the novel LA-ICPMS technique), as well as benthic $\delta^{13}C$ and oxygenation estimates. All together indicate a more respired CO_2 enriched and more oxygen-depleted deep EEP during the last glacial period. This greater accumulation of respired CO_2 in the glacial ocean would have been achieved at the expense of the surface ocean and atmosphere. However, the $\Delta[CO_3^{2-}]_{LGM\text{-}Holocene}$ reconstructed in this study location is relatively small compared to the changes estimated in radiocarbon ventilation for the same period, suggesting that a “counteracting” mechanism, such as carbonate dissolution at the seafloor, should have also played a role. This mechanism would have increased average ocean alkalinity, allowing even more atmospheric CO_2 to be “sequestered” by the ocean during the glaciation. An initial comparison with results from the South Pacific and Southern Oceans suggests that a promising avenue for future work might be to extend the approach adopted in this study to a larger number of sites from around the global ocean, with the aim of moving closer to a quantification of the glacial marine respired carbon stock and the proposed increase in average ocean alkalinity.

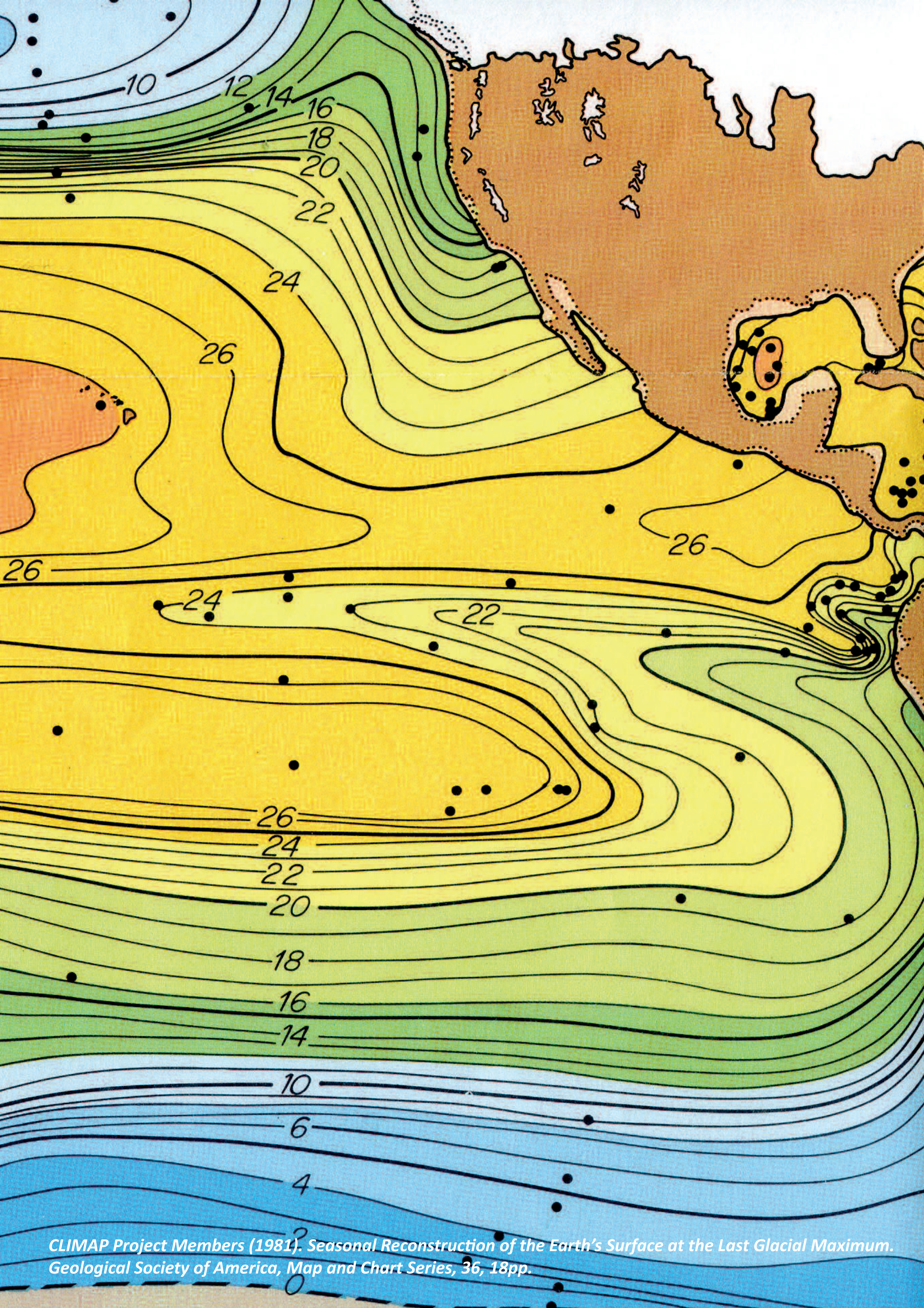

CLIMAP Project Members (1981). Seasonal Reconstruction of the Earth's Surface at the Last Glacial Maximum. Geological Society of America, Map and Chart Series, 36, 18pp.

CHAPTER 1

1. General introduction

1.1. Late Pleistocene Glacial/Interglacial cycles

1.1.1. Insolation pacing of global temperature change

The last 800 kyr are characterised by cold (glacial)-warm (interglacial) cycles of ~100 kyr duration, that ultimately seem to have been paced by insolation variations, the dominant external forcing of Earth's climate on timescales of 10^4-10^5 years (Hays et al., 1976). These insolation variations are produced by changes in the eccentricity, obliquity and precession, which modulate the amount of solar radiation that arrives at the top of the atmosphere across latitude and through the annual cycle (Milankovitch, 1941) (Fig. 1.1). Insolation varies with characteristic periodicities of ~100 kyr for the eccentricity of the Earth's orbit, 41 kyr for the obliquity or tilt of the Earth's spin axis and ~23 kyr for the precession of the equinoxes, which are clearly recorded in a host of proxy climate records of past climate change, including the marine stable oxygen-isotope record in particular (Hays et al., 1976; Shackleton, 2000). The striking similarity of the frequency structure of insolation and climate records demonstrates a clear link between the two, and is the basis for the hypothesis that insolation changes have paced past climate change. The original formulation of the "orbital theory of the ice ages" (Milankovitch, 1941) proposes that the intensity of peak summer insolation at 65°N (i.e. the primary latitude of ice sheet growth and decay during the Pleistocene) is crucial for pacing global climate change, via its impact on summer ice sheet melt. Therefore, the local-seasonal redistribution of solar radiation, rather than global average changes in solar energy input that is only affected by eccentricity and amounts to very little (e.g. <0.5 Wm^{-2}), has always been conceived of as the primary means of global climate forcing in this context.

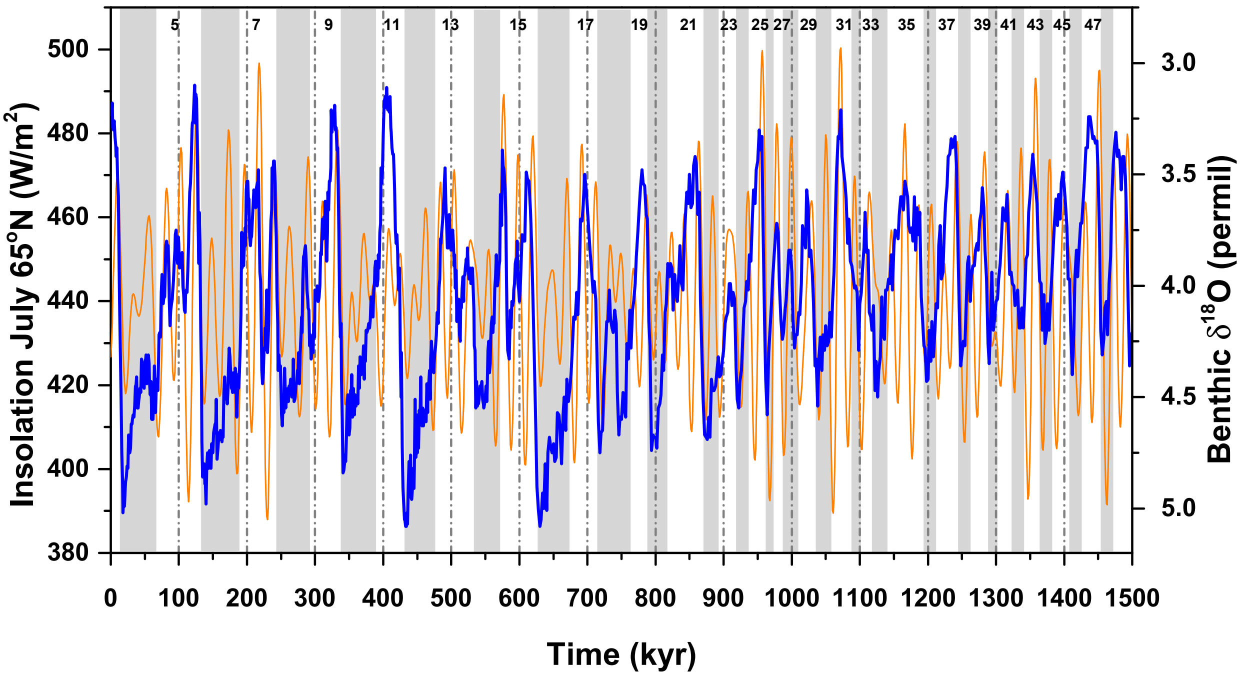

Figure 1.1. Insolation variations in July at 65°N (orange line; Berger and Loutre, 1991; Berger, 1999) and the LR04 global stack of benthic δ^{18}O records indicating changes in global climate over the last 1500 kyr (blue line; Lisiecki and Raymo, 2005). Odd numbers at the top of the panel indicate Marine Isotope Stage (MIS) for interglacial states, while vertical grey bands highlight glacial states.

Despite the very strong correspondence between astronomical/insolation periodicities and climatic variability, it has been observed that the magnitude of insolation changes (the presumed forcing) is not always related to the amplitude of glacial/interglacial transitions (G/IG, the presumed response), e.g. the so-called “Stage 7 and Stage 11 problems”, where a large/small insolation change produces a “counterintuitively” small/large climatic response, respectively (Paillard, 2001) (Fig. 1.1). Furthermore, while summer insolation variability at 65°N in particular is dominated by precession (~23 kyr), the global climate response over the last ~1 Ma has been dominated by a ~100 kyr period (resulting in the so-called “100kyr problem”), while earlier Pleistocene glacial cycles have been dominated by a 41 kyr cycle. Thus, a shift in a dominant periodicity in climate from 41 kyr to 100 kyr at ~1 Ma (referred to as the Mid-Pleistocene Transition, MPT) without any such change in insolation presents a further enigma, and points to a "non-linear" process linking insolation and climate change (Imbrie and Imbrie, 1980). Indeed, climatic archives show that G/IG cycles, apart from being clearly linked with changes in solar insolation, are also marked by changes in ice-sheet volume/sea level, land-cover, atmospheric dust loading and atmospheric CO_2 (Fig. 1.2), all of which affect global energy balance via changes in planetary albedo and emissivity.

In light of these shortcomings of the Milankovitch theory, the contemporary conception of glacial-interglacial climate change typically emphasizes that the *effects* of G/IG climate change are also largely the *drivers* of G/IG climate change. Another way of saying this is that while insolation may act as the pacemaker of G/

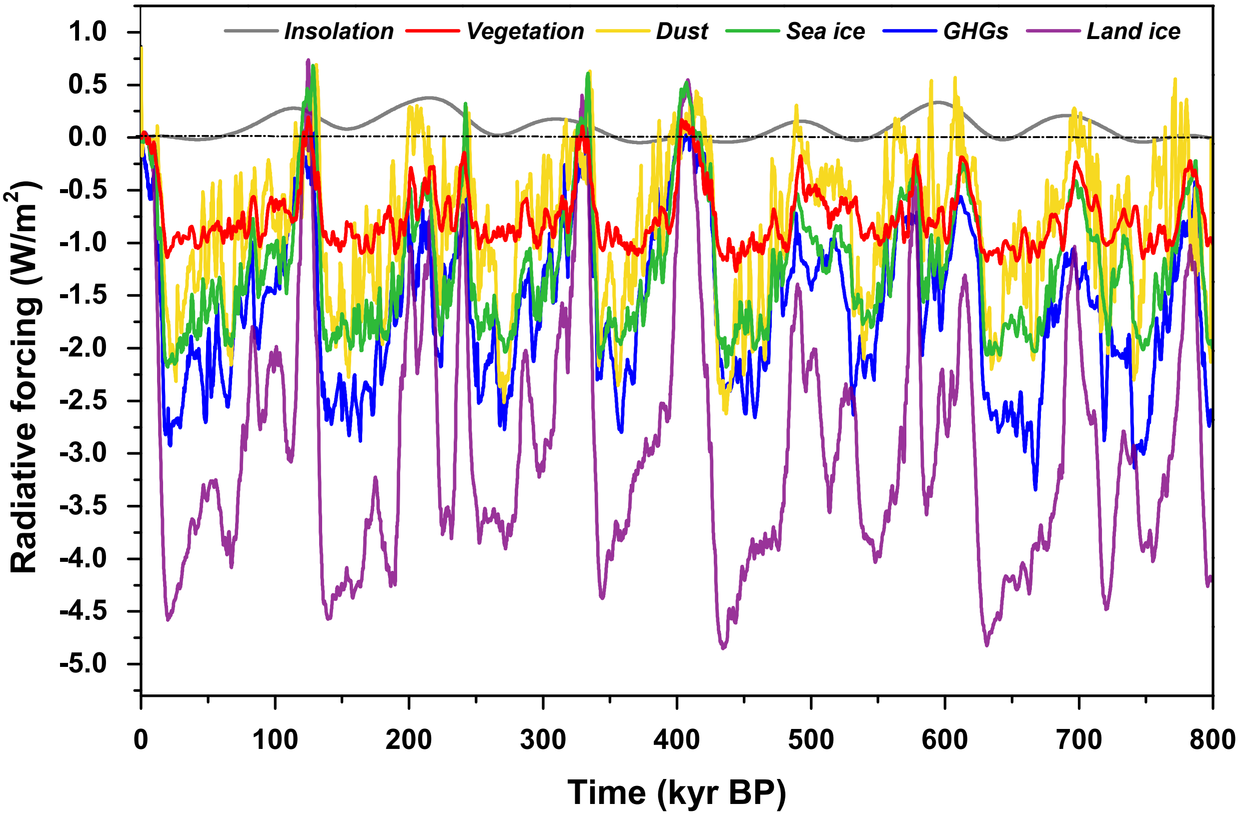

Figure 1.2. Individual radiative forcings from vegetation, atmospheric dust loading, sea ice, GHGs (including CO_2, CH_4 and N_2O) and land cryosphere (including ice-sheets and associated snow cover and sea level change) over the last 800 kyr. Horizontal dashed grey line notes 0 W/m^2 (adapted from Köhler et al., (2010)).

IG climate change, it is internal feedbacks in the Earth system acting in response to insolation change that are primarily responsible for pushing the Earth's climate between cold/glacial and warm/interglacial states (e.g. Köhler et al., 2010; Paillard, 2001).

From a dynamical system perspective, insolation is clearly pacing G/IG climate change via these feedbacks, and in a manner that must involve thresholds or "state dependence/conditionality" in the feedbacks (e.g. Paillard, 2001, 1998). In other words, a given magnitude and duration of insolation change will have different impacts depending on the state of the climate system that it acts upon. Furthermore, the mechanisms that underlie this non-linear insolation-climate linkage must operate by channeling impacts from very short timescales (e.g. diurnal, seasonal) to much longer timescales (e.g. 10-100 kyr) (e.g. Huybers, 2006). From a global energy balance perspective, insolation changes contribute essentially nothing to G/IG global temperature change, since global radiative forcing from eccentricity changes is very small compared to the ~12 Wm^{-2} needed to cause a typical ~4°C global average G/IG temperature change. Instead, these 12 Wm^{-2} are provided almost entirely by albedo and greenhouse gas feedbacks (e.g Köhler et al., 2010) (Fig. 1.2). When considering the energy balance feedbacks that contributed to G/IG global temperature change, these can be categorized as affecting either 1) planetary albedo or 2) atmospheric long-wave emissivity. In turn, land ice cover (i.e. ice volume) and atmospheric greenhouse gas concentrations (primarily carbon dioxide) emerge as the most important players in each of these categories. This is supported by numerical model studies, which suggest that G/IG cycles might be seen as arising from non-linear impacts of insolation on conditionally vulnerable ice-sheets, and amplified by atmospheric CO_2 change (e.g. Abe-Ouchi et al., 2013; Huybers, 2006; Paillard, 2001). The conditional vulnerability of ice sheets would arise due to a host of different instability mechanisms in large ice sheets, such as the saddle instability (Gregoire et al., 2012), isostatic adjustment instabilities (Abe-Ouchi et al., 2013), grounding-line instabilities (Schoof, 2007), and albedo feedback mechanisms (Ganopolski and Calov, 2011). While atmospheric CO_2 has been proposed as a key amplifier of insolation-albedo induced climate change, it very likely also helped to set the threshold at which insolation change is able to affect ice-sheets and climate while also responding to insolation itself (Ganopolski et al., 2016; Tzedakis et al., 2012). Atmospheric CO_2 change is therefore one of the most important internal feedbacks proposed to explain the amplitude (and perhaps also the timing) of G/IG cycles. Part of the key for understanding how insolation paces global climate change is to first understand G/IG atmospheric CO_2 change, and therefore the evolution of the global carbon cycle across G/IG transitions.

1.1.2. **CO_2 as a relevant internal feedback for G/IG cycles**

As noted above, changes in the atmospheric concentration of CO_2 (i.e. the atmospheric partial pressure of CO_2, or $p\mathrm{CO}_2$) due to variations in the exchange of this gas between different carbon reservoirs, have been hypothesised to act as a strong internal feedback amplifying G/IG cycles, and perhaps also determining what magnitude of insolation change was needed to trigger glacial inception and deglaciation. This is supported in part by the fact that CO_2 concentrations measured in air bubbles trapped in ice cores show a striking correlation with global climate change, with lower CO_2 during glacials and higher CO_2 during interglacials, within a range of ~80-100 ppm (Barnola et al., 1987; Petit et al., 1999; Siegenthaler et al., 2005) (Fig. 1.3). To explain such a change in atmospheric CO_2 between cold and warm periods is still a challenge in the palaeoclimatic community, but it is becoming clearer that these changes must have been due to a combination of several interrelated processes.

Independently of how much CO_2 helped to trigger G/IG cycles, the rapid increase of CO_2 in the atmosphere across a glacial termination compared to the slow and progressive drop over a glaciation, might suggest that a reservoir (or combination of reservoirs) would have behaved like a “box” that has been able to slowly accumulate an amount of CO_2 that would have somehow been “quickly” released back to the atmosphere after some time. This notion would suggest that a small imbalance in

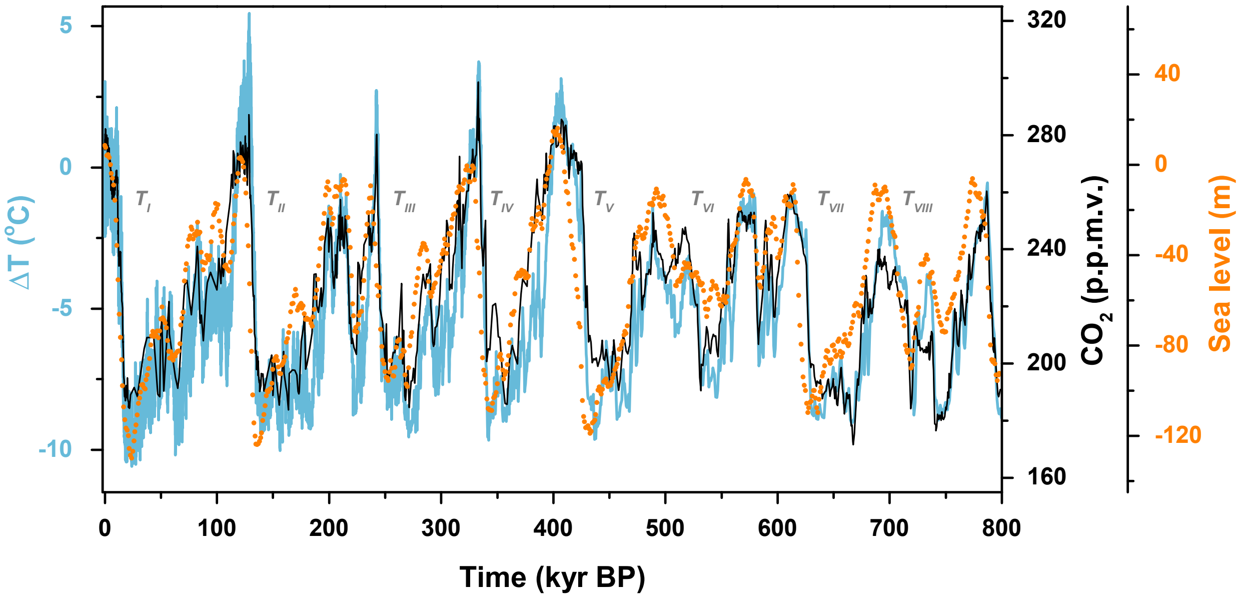

Figure 1.3. Climatic variability over the last 800 kyr, indicating coherent sawtooth cycles of air temperature (blue line; Jouzel et al., 2007), ice-volume (orange dots; Spratt and Lisiecki, 2016) and atmospheric CO_2 concentration (black line; (Lüthi et al., 2008 and references therein). The last eight glacial terminations are indicated by T_I-T_{VIII}.

carbon fluxes IN-OUT for a particular carbon reservoir during glacial inception gave way to a large imbalance of the flux OUT-IN for that reservoir during deglaciation. Thus, one of the most intriguing and pressing questions in palaeoclimatic sciences concerns where this CO_2 might have been "hiding" over a glacial period, how it was stored there, and how it was then released over a glacial termination.

In addition to the atmosphere, the global carbon cycle consists of the lithosphere, the terrestrial biosphere and the ocean. Although all of these may have played a role in G/IG atmospheric CO_2 change to some extent, on the one hand the exchange of CO_2 between the atmosphere and lithosphere is typically a very slow process, and therefore unlikely to account for G/IG atmospheric CO_2 changes, especially the rapid step changes (Sigman and Boyle, 2000). On the other hand, the terrestrial biosphere seems to have acted as a source of CO_2 to the atmosphere rather than a sink, increasing the atmospheric CO_2 content by ~18 ppm, since the generally cold and dry glacial conditions would have reduced plant production in specific important biosphere carbon uptake areas, as well as reduced the available land for the plants to growth due to the massive ice extension. This leaves us the ocean as the most likely candidate reservoir to have stored a significant amount of CO_2 over the late Pleistocene glacial periods (Broecker, 1982a).

This is indeed not very surprising as the modern ocean contains ~17 times more carbon than the terrestrial biosphere and ~60 times more than the atmosphere (Sarmiento and Gruber, 2004), which makes the ocean a major controller of atmospheric CO_2 at G/IG timescales. Furthermore, the marine carbon cycle is inherently linked to the global biogeochemical cycles and has a complicated seawater chemistry, which makes CO_2 special compared to other gases in the ocean.

Thus, several marine carbon cycle mechanisms have been invoked to explain the CO_2 changes in the atmosphere over G/IG cycles. However, before addressing these, the complex carbonate chemistry in seawater, as well as the current ocean carbon distribution and its controls need to be understood.

1.2. **Marine carbon cycle**

1.2.1. **Seawater carbonate chemistry**

The marine carbonate system is extremely important as it controls the pH (acidity) of the ocean where many pH-dependent reactions occur, with implications for biogeochemical cycling and the life of the ocean. CO_2 has a relatively complex chemistry in seawater, which makes this gas special compared to others with similar solubility (Sarmiento and Gruber, 2004). When CO_2 gas dissolves in seawater, it gets hydrated and several subsequent reactions occur:

$$CO_{2(aq)} + H_2O \xleftrightarrow[K_0]{} H_2CO_3 \xleftrightarrow[K_1]{} HCO_3^- + H^+ \xleftrightarrow[K_2]{} CO_3^{2-} + 2H^+ \quad (1)$$

where K_0, K_1 and K_2 are the equilibrium constants for each acid-base reaction, and depend on the temperature and salinity of seawater (Zeebe and Wolf-Gladrow, 2001). The concentration of all the inorganic carbon species in seawater is referred to as the dissolved inorganic carbon concentration or DIC, which is a very useful parameter as it is independent of temperature and pressure in the ocean interior, i.e. conservative in the absence of air-sea gas exchange. $CO_{2(aq)}$ and H_2CO_3 are usually combined together as CO_2* or H_2CO_3*, since they are hardly differentiable from each other, and are normally not taken into account because they represent a very small fraction of the total dissolved inorganic carbon in the pH range of seawater (~0.5%) compared to HCO_3^- (88.6%) and CO_3^{2-} (10.9%) (Fig. 1.4). Thus, the most common definition for DIC, if simplified, is:

$$DIC \approx [HCO_3^-] + [CO_3^{2-}] \quad (2)$$

Another very useful conservative parameter in the carbonate system is alkalinity (ALK). ALK is defined as the measure of the bases excess (proton acceptors) over acids (proton donors), i.e. the capability of water to neutralize acid, or in other words, the buffering capacity of the system. It is usually defined in terms of the "carbonate alkalinity" as:

$$ALK \approx [HCO_3^-] + 2[CO_3^{2-}] \quad (3)$$

Total ALK, as distinct from carbonate alkalinity, is also affected by seawater dissociation (OH^- + H^+), borate ($B(OH)_4^-$), and minor bases. However, these species contribute in such a small proportion to alkalinity that for simplicity, they are very often not considered (Fig. 1.4), and carbonate alkalinity serves as a viable approximation to total alkalinity.

As observed in reaction (1), the dissolution of CO_2 also produces protons (H^+), which are mostly buffered by the carbonate system (bicarbonate and carbonate anions), preventing drastic changes in seawater pH.

An alternative way to illustrate the stoichiometry of the thermodynamic equilibrium of CO_2 dissolving in seawater would be:

$$CO_2 + H_2O + CO_3^{2-} \leftrightarrow 2HCO_3^- \quad (4)$$

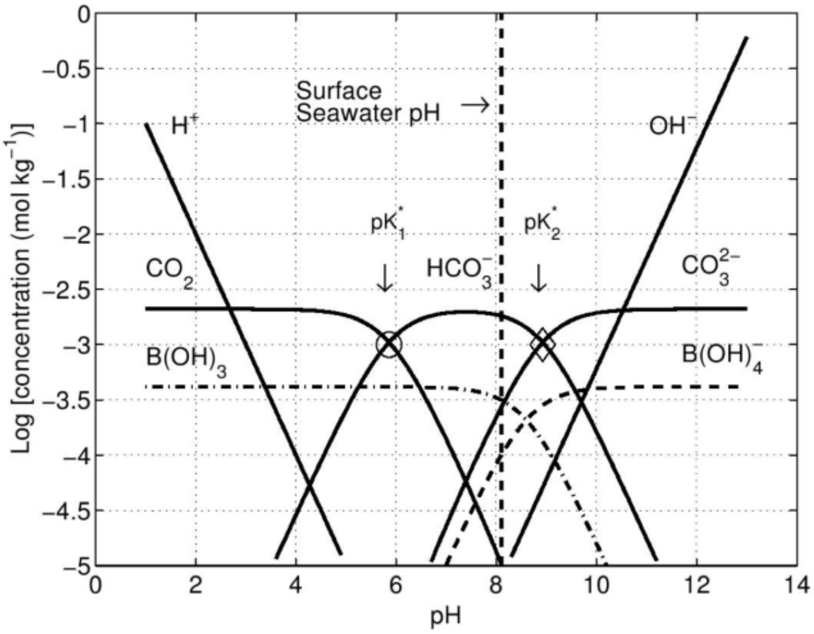

Figure 1.4. Graphical representation of the equilibrium relationships of the carbonate system, commonly referred to as a “Bjerrum plot”. The circle and the diamond correspond to the dissociation constants pK^*_1 ($=[H^+]\cdot[HCO_3^-]/[CO_2]$) and pK^*_2 ($=[H^+]\cdot[CO_3^{-2}]/[HCO_3^-]$), respectively. Surface seawater pH is shown by a vertical dashed line (Figure from Zeebe and Wolf-Gladrow, 2001).

Thus, when a molecule of CO_2 is dissolved in seawater, HCO_3^- and H^+ are rapidly formed. Protons are then partly neutralized by reaction with available CO_3^{2}, which further increases the concentration of HCO_3^- (reaction 4). Thus, on the one hand, CO_2 invasion causes DIC to increase (similarly, its removal decreases DIC), while on the other hand, none of these processes cause ALK to change, as the charge balance is maintained (reaction 4).

The amount of CO_2 that dissolves in seawater, i.e. the air-sea CO_2 exchange rate, depends on the partial pressure ($p\text{CO}_2$) in both reservoirs, which in turn depends primarily on surface ocean properties, since atmospheric CO_2 homogenizes relatively quickly. Seawater $p\text{CO}_2$ is thus set by salinity, temperature, DIC and ALK (Sarmiento and Gruber, 2004), as it can be seen in the following equation:

$$pCO_2 \approx \frac{K_2}{K_0 \cdot K_1} \frac{(2DIC - ALK)^2}{ALK - DIC} \tag{5}$$

The equilibrium constants, as mentioned previously, are controlled by the temperature and salinity of the seawater, which are strongly influenced by local atmospheric temperature, evaporation-precipitation balance and global ice-volume change. The temperature/salinity dependence of the dissociation constants causes CO_2 solubility to increase for colder and fresher water, such that lower temperature and salinity will lead to increased seawater $p$$CO_2$ for a given DIC and ALK, and vice versa. However, what process(es) control DIC and ALK, and therefore ultimately the seawater $p$$CO_2$ regardless of temperature and salinity? Understanding these other processes, and their link to climate-driven changes in CO_2 solubility and air-sea gas exchange is central to the study of the climate of the past and its relation with the carbon cycle, including in particular the G/IG atmospheric CO_2 changes observed in the late Pleistocene.

1.2.2. **Processes that set up sea surface *p*CO_2: "Carbon pumps"**

Modern vertical profiles of DIC and ALK across all oceans show a gradient between the surface and the ocean interior, as well as latitude/longitude differences in surface ocean DIC and ALK. These patterns suggest the existence of active processes in the carbonate system that maintain chemical gradients against the homogenizing influence of the ocean circulation (Sarmiento and Gruber, 2004). The processes that determine the vertical gradients in the oceans are often referred to as "marine carbon pumps" (based on the analogy of a pump that maintains a pressure gradient between two locations), which are commonly subdivided into the "solubility pump" and the "biological pump", where the latter is further subdivided into the "soft tissue-" and "carbonate-" pumps (Fig. 1.5) (Volk and Hoffert, 1985).

The so-called "solubility pump" has been partly addressed in the previous subsection, as it refers to the capacity of the ocean to hold CO_2 away from the atmosphere

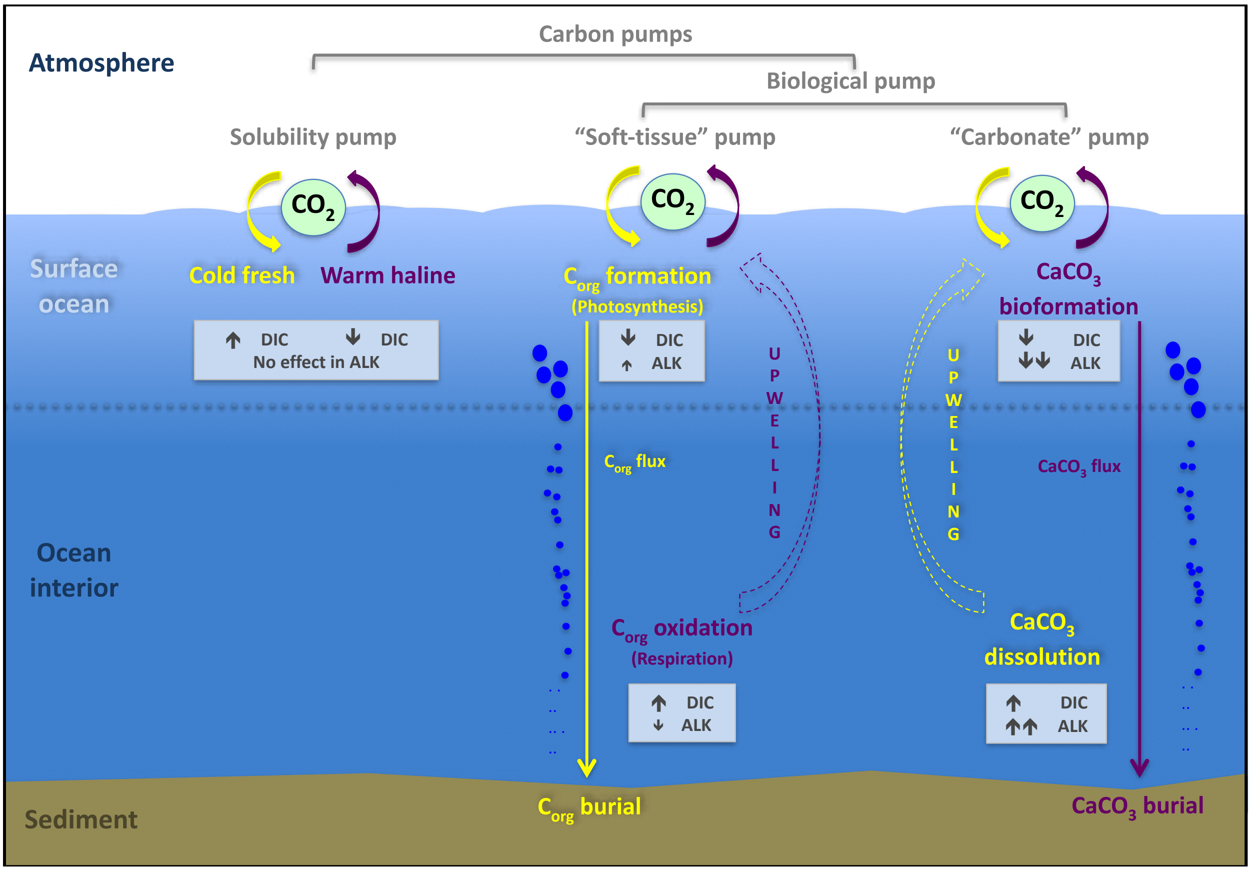

Figure 1.5. Schematic representation of the marine carbon pumps, including the solubility and biological pumps, where the latter is further subdivided into the soft-tissue and carbonate pumps. The arbitrary division between the surface and interior ocean is indicated by a horizontal dashed line. Yellow arrows and text indicate processes/mechanisms that tend to contribute to atmospheric CO_2 uptake, while purple arrows and text indicate processes/mechanisms that tend to contribute to CO_2 release. Grey boxes summarize the effect of such processes/mechanisms on DIC and ALK. Blue circles represent both organic (C_{org}) and calcium carbonate ($CaCO_3$) particles, whose size represents the rapidly diminishing degree of oxidation/dissolution with depth, as the particles sink (modified from Heinze et al., 1991).

as a function of temperature and salinity of seawater and in the absence of any processes that might otherwise create DIC/ALK gradients in the ocean. The solubility pump therefore depends on air-sea CO_2 exchange efficiency ((Wanninkhof, 1992) and CO_2 solubility. It could be argued that the term "solubility pump" is not entirely appropriate in this case, as these processes do not act as pumps that maintain chemical gradients, but rather the opposite; they just equilibrate the pCO_2 of seawater with that of the atmosphere as a function of seawater properties. Indeed, they are only responsible for the vertical gradients insofar as a certain amount of DIC can be directly advected into the deep ocean by the large scale overturning circulation (which occurs only in specific areas of the planet), with impacts on DIC but not on ALK. Because of this, the effects of the solubility pump are directly dependent on the ocean circulation. This notion has led some to use the term "physical pump", in order to more clearly emphasize the important role played by ocean physics, which would combine the effects of solubility with those of ocean transport. Thus, although solubility and air-sea exchange processes are very important for ocean-atmosphere carbon cycling, it is the ocean circulation and its interaction with the "soft-tissue" and the "carbonate" pumps that are responsible for most of the DIC and ALK gradients that are observed in the water column (Fig. 1.6).

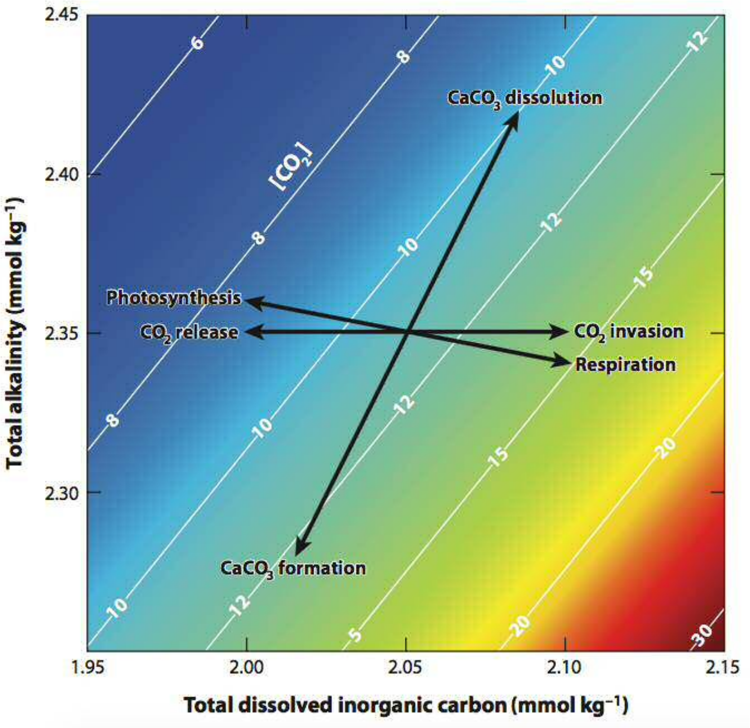

Figure 1.6. Graphical relationship between dissolved inorganic carbon (DIC) and total alkalinity (ALK) in the ocean at constant temperature (T = 15°C), salinity (S = 35) and pressure (P = 1 atm). The processes that modify carbonate chemistry parameters are displayed by black arrows. CO_2 concentration contours (in µmol/kg) are indicated by diagonal white lines and rainbow colours (Figure from Zeebe, 2012).

The “soft-tissue pump” maintains a chemical gradient in the water column by fixing CO_2 from the upper ocean through photosynthesis and releasing it back into the ocean interior through organic matter respiration (also called oxidation). More specifically, the photosynthetic organisms that live in the upper photic zone of the ocean use light, water, nutrients and CO_2 to grow, thus turning dissolved inorganic carbon (DIC) into particulate organic carbon (POC or organic matter), that is transferred through the marine food web in the upper layers. When the photosynthetic and non-photosynthetic organisms die, they sink so that POC is exported into the deep ocean where it is progressively degraded back into CO_2 and nutrients by microorganisms. A small percentage of this organic carbon remains captured in marine sediments, and is eventually returned to the ocean, for instance, via volcanism and more recently anthropogenic emissions. Photosynthesis therefore fixes CO_2 making the DIC decrease in the sea surface, while respiration produces a commensurate increase in DIC in the deep ocean by releasing this CO_2 into the ocean interior (Fig. 1.6). These processes also produce a slight change in ALK (in the opposite direction to DIC) as they consume/release protons in association with nutrients fixation/remineralization (charged species such as NO_3^-) (Fig. 1.6). Thus, photosynthesis (respiration) is analogous to CO_2 release to (invasion from) the atmosphere in the way that it decreases (increases) DIC, but photosynthesis (respiration) differs as it also affects ALK slightly.

The processes mentioned so far have primarily produced changes in DIC, with no change or relatively little in ALK. What therefore creates the significant vertical and lateral ALK gradients observed in the ocean? The main process responsible for these gradients is the other biological pump called the “carbonate pump”, which refers to the formation/dissolution of biogenic calcium carbonate ($CaCO_3$) in the surface/deep ocean, respectively. Calcifying organisms such as coccolithophores and foraminifera build their shells by removing CO_3^{2-} and Ca^{2+} from the surface (i.e. $CO_3^{2} + Ca^{2+} \leftrightarrow CaCO_3$), which are returned to the deep ocean when they die and sink. Thus, carbonate formation in the sea surface reduces both DIC and ALK, and vice versa in the deep ocean, affecting each in a ratio of 1:2 (DIC:ALK) (Fig. 1.6).

Having surveyed the processes that influence DIC and ALK distributions in the ocean, we can go back to what concerned us in the beginning, i.e. what can drive significant changes in seawater *p*CO_2? Looking at equation 5 and Figure 1.6, seawater *p*CO_2 would decrease with decreased DIC (from CO_2 release to the atmosphere and/or enhanced photosynthesis), as well as with increased ALK (from increased $CaCO_3$ dissolution), and vice versa (see Table 1.1 for a summary).

Table 1.1. Processes affecting DIC, ALK and *p*CO_2. Decreasing arrows are indicated in grey and increasing arrows in black. The size and number of arrows for DIC and ALK indicate the magnitude of change, as also shown in Figure 1.6.

	Solubility pump		**Biological pump**			
			Soft-tissue pump		**Carbonate pump**	
	Invasion CO_2	**Release CO_2**	**Production Organic C (Photosynt.)**	**Oxidation Organic C (Respirat.)**	**Formation $CaCO_3$**	**Dissolution $CaCO_3$**
DIC	↑	↓	↓	↑	↓	↑
ALK	-	-	↑	↓	↓↓	↑↑
***p*CO_2** (seawater)	↑	↓	↓	↑	↑	↓

This shows a counter-balance effect of the carbonate pump that exists within the biological pump, such that the impact on surface ocean *p*CO_2 will depend on the abundance of calcifying *vs* non-calcifying organisms in the upper layers of the ocean. Nevertheless, the biological pump will always tend to decrease the *p*CO_2 of the upper ocean, as the bulk of biological export productivity consists of organic carbon rather than carbonate (the latter being about a quarter of that of organic carbon flux; Li et al., 1969), with DIC:ALK being exported from the mixed layer on average at a ratio of ~0.2-0.3 (Kwon and Primeau, 2008). In the ocean interior, however, the balance of DIC and ALK supply at a given depth will depend more on the different remineralization profiles that apply to organic carbon and carbonate, which will cause the ratio of DIC:ALK delivery to the ocean interior to vary with water depth. A further influence will come from changes in the position of the carbonate compensation depth (CCD), which can be caused by changes in the ocean circulation and the soft-tissue pump and can result in the addition of carbonate ions to the deep ocean via the dissolution of previously deposited carbonate sediments.

Having reviewed the processes that control the current partitioning of CO_2 between the oceanic and atmospheric carbon reservoirs, the proposed mechanisms for explaining the atmospheric CO_2 drawdown over the last glacial period are in turn addressed below.

1.3. **Marine mechanisms proposed for the glacial atmospheric CO_2 decrease**

An atmospheric temperature drop during the glacial inception due to solar insolation variations and attendant radiative feedbacks would have cooled the sea surface, thus enhancing CO_2 solubility and causing an estimated drop of ~30 ppm in the atmospheric CO_2 content (Sigman and Boyle, 2000). However, reduced glacial temperatures would have also been accompanied by a saltier ocean on average, due to the accumulation of fresh water in the ice-sheets, which would have partially counter-balanced the temperature-driven enhanced solubility of CO_2, adding ~18 ppm to the atmosphere (Sarmiento and Gruber, 2004; Sigman and Boyle, 2000). Thus, glacial estimates taking into account lower temperature and higher salinity in the sea surface, along with the lower content of carbon in terrestrial vegetation mentioned previously, would end up producing a net CO_2 change close to 0 ppm (Sigman and Boyle, 2000).

However, it is worth noting that these calculations depend on assumptions regarding air-sea exchange efficiency and ocean circulation (as discussed above), whereas: 1) air-sea gas exchange may well have been modified in glacial periods by other physical processes such as sea-ice cover and ocean stratification; and 2) the precise impact of altered solubility of CO_2 in the glacial ocean will have depended on changes in the ocean circulation (Ito and Follows, 2013; Skinner, 2009), which remain uncertain. Nevertheless, it is clear that lower glacial atmospheric CO_2 cannot be accounted for easily by temperature, salinity and terrestrial biosphere changes alone.

In light of the above issues and given that the ocean seems to have been the key place to store a significant amount of CO_2 over glacial times, several marine carbon cycle mechanisms have been invoked to explain most of the atmospheric CO_2 drawdown observed over the last glacial period (e.g. Kohfeld and Ridgwell, 2009; Sigman and Boyle, 2000). They can be categorised broadly as deriving primarily from: 1) changes in CO_2 solubility and the rate or efficiency of air-sea gas exchange (i.e. the "solubility pump"; e.g. Volk and Hoffert, 1985); 2) changes in the efficiency of the "biological carbon pumps" (i.e. "soft-tissue" *vs* "carbonate" pumps; e.g. Volk and Hoffert, 1985); 3) changes in whole ocean carbonate chemistry (e.g. Archer, 1991; Broecker and Peng, 1989; Keir, 1995). The specific mechanisms included in these categories are many, but the most significant ones are listed below:

Category 1. a) Change in sea-ice cover at high southern latitudes (Stephens and Keeling, 2000); b) Change in the rate of ocean overturning due to an altered wind-field (Toggweiler, 1999); c) Change in ocean density-stratification due to brine formation in the Southern Ocean (Adkins et al., 2002; Roberts et al., 2016); d) buoyancy forcing in the Southern Ocean (Ferrari et al., 2014; Watson and Naveira Garabato, 2006); e) solubility effects (Sigman and Boyle, 2000); f) volumetric effects (Skinner, 2009).

Category 2. a) Increase in biological export productivity due to increased iron supply from dust (Calvo et al., 2004; Martínez-Garcia et al., 2014); b) increased Si-leakage from the Southern Ocean to lower latitudes (Brzezinski et al., 2002; Matsumoto et al., 2002); c) remineralization depth changes (Kwon et al., 2009; Matsumoto, 2007); d) whole ocean phosphate changes (Broecker, 1982b; Wallmann, 2010).

Category 3. a) Increase in the ocean's average alkalinity due to carbonate compensation/carbonate dissolution at the seafloor (Keir, 1995) and/or loss of biogenic carbonate and coral deposition in marine shelf areas (Berger, 1982; Opdyke and Walker, 1992); b) Increase primarily in the surface Southern Ocean's alkalinity due to changes in the AMOC (Broecker and Peng, 1989); c) rain ratio (Archer and Maier-Reimer, 1994).

How does the ocean produce the above changes to exert a control on atmospheric CO_2? Are physical mechanisms primarily responsible for controlling atmospheric CO_2, or is it marine biology that plays the dominant role, or perhaps changes in the whole ocean chemistry do? While the categories described above might be useful for organising our thinking about past marine carbon cycle change, it is important to emphasize that all these mechanisms need not have operated in isolation from each other. Furthermore, despite substantial differences between all of them, most would directly or indirectly involve changes in the efficiency of the biological pump (Volk and Hoffert, 1985).

Defining biological pump efficiency in terms of its ability to store CO_2 in the deep ocean away from the surface ocean and thus from the atmosphere, we find that such changes could be achieved by variations in the "leakiness" of the biological carbon pump (the soft tissue pump primarily, as opposed to the carbonate pump) or by changes in its "strength". Here, leakiness can be defined as the return flux of remineralised nutrients and carbon from the deep interior to the sea surface achieved as a result of the ocean's large scale overturning circulation and upwelling, and strength refers to export production rates. Thus, for example, the hypothetical mechanisms listed above in category 1) would refer primarily to changes in the leakiness of the soft tissue pump, while those in category 2) would imply changes in its strength. The mechanisms listed under category 3) could in principle arise as a positive feedback on soft-tissue pump efficiency (i.e. via respired carbon accumulation in the deep ocean driving carbonate ion decrease and carbonate dissolution), although they could also arise independently as a result of a reduction in carbonate deposition.

A more efficient biological carbon pump can occur as a result of either an increase in its strength or a reduction in its leakiness, with a direct impact on surface ocean

DIC and ALK and therefore atmospheric CO_2. However, if increased biological pump efficiency is achieved by a change in the ocean's large-scale overturning circulation, it would very likely co-occur with a change in the conditions of air-sea gas exchange and the solubility pump. Furthermore, regardless of how biological carbon pump efficiency is increased (and as long as the soft-tissue pump remains dominant), this would lead to more respired carbon storage in the deep ocean (thus sequestering CO_2 from the atmosphere), which could eventually reduce deep ocean carbonate ion concentrations enough to cause seafloor carbonate dissolution. The latter would eventually increase the whole ocean alkalinity budget and lead to further atmospheric CO_2 drawdown. This illustrates the point made above, that the various processes (physical, biological and sedimentary/geochemical) need not, or perhaps even could not, have operated in isolation from each other. Indeed, an increase in the biological carbon pump efficiency, due to a decrease in its leakiness (possibly in association with a reduction in air-sea CO_2 exchange rates) and/or an increase in its strength, leading to an increase in the ocean's average alkalinity as a consequence, represents a particularly effective way to cause an increase in deep-ocean carbon storage over the last glacial period, which would involve a combination of physical, biological and geochemical processes.

1.4. **Current understanding of G/IG marine carbon cycle change**

Theory points to CO_2 variability as the most important mechanism to amplify insolation-albedo driven G/IG climate changes, and the ocean as the key reservoir for storing and releasing atmospheric CO_2. Most of the mechanisms proposed have a base in modeling studies (both conceptual and complex numerical models), which are extremely useful for hypothesis development, but which need to be assessed against observations. We currently lack a complete explanation of the causes of G/IG atmospheric CO_2 variations, let alone a clear confirmation of the hypothesis that a significant amount of additional CO_2 was indeed stored in the ocean interior during the last glacial. Thus, in a practical way, evidence from real data must be sought. Are we able to find such evidence in the deep glacial ocean? What areas might be important to look at? What proxies might be essential to infer the state of the carbon cycle and the marine carbon inventory in the past? Are there novel potential successful techniques to explore that might help us to understand proxies better?

The Southern Ocean is thought to be a key place to look for such evidence, as it is currently the area where "old" water masses highly charged in respired CO_2 make their first contact with the atmosphere and where the bulk of the ocean interior undergoes air-sea exchange (Gebbie and Huybers, 2011; Primeau, 2005). However, other locations are equally important as monitoring locations, including the deep Pacific for example, which is relatively homogeneous and accounts for the bulk of the ocean volume, or the Eastern Equatorial Pacific which is directly connected to both the Southern Ocean and the North Pacific via the transport and upwelling of waters derived from these high latitude regions.

There are some specific tracers for carbon cycle reconstructions that are extremely useful when combined together. Radiocarbon activities from the bottom of the ocean compared to the coeval radiocarbon in the atmosphere over time is one of these, as it gives us an idea of the ventilation state of the ocean, whereby higher radiocarbon differences between the two reservoirs indicate longer carbon residence times in the ocean interior and therefore a greater potential for respired CO_2 accumulation via the biological carbon pump (see next chapters for further explanation). If some carbonate system parameters such as $[CO_3^{2-}]$ or pH can also be inferred, as well as approximations of the amount of carbon respiration in the deep ocean through variations in O_2 content or stable carbon isotopes ($\delta^{13}C$), then relative, or even quatitative changes in ocean interior respired carbon storage could in principle be constrained.

Using such techniques, evidence for a larger deep ocean CO_2 inventory during the last glaciation has been advanced for the Atlantic sector of the Southern Ocean, for example based on radiocarbon evidence of reduced ventilation across the water column (Burke and Robinson, 2012; Skinner et al., 2010), as well as lower O_2 and $[CO_3^{2-}]$ indicating increased respired CO_2 accumulation at the bottom of the ocean (Gottschalk et al., 2016, 2015). Similar evidence has also been advanced for the Pacific Ocean, indicating reduced radiocarbon ventilation in some areas (e.g. Galbraith et al., 2007; Skinner et al., 2015), as well as lower O_2 (e.g. Bradtmiller et al., 2010) and lower $[CO_3^{2-}]$ content (e.g. Allen et al., 2015; Yu and Elderfield, 2007). However, similar proxy reconstructions from other areas of the Pacific do not always agree (e.g. Broecker et al., 2008; De Pol-Holz et al., 2010; Lund et al., 2011). These discrepancies need to be addressed in order to properly understand marine carbon cycling in the largest of the world ocean basins. One simple explanation is that the apparent mismatches could stem from the different techniques that are applied, and how they are applied in each case. For example, glacial radiocarbon ventilation ages can be underestimated when using benthic-planktonic foraminifer radiocarbon age offsets (B-P) as an approximation for benthic-atmospheric radiocarbon age offsets (B-Atm) over time, as they do not take into account variations in the planktonic-atmosphere radiocarbon offset (reservoir age) (further details in next chapters). Another example is the technique applied for the inference of past seawater $[CO_3^{2-}]$. This is increasingly being estimated through B/Ca ratios in the calcite shell of benthic foraminifera, after an empirical relationship was established between the relative saturation state $\Delta[CO_3^{2-}]$ and B/Ca ratios (Yu and Elderfield, 2007). These analyses are normally made by bulk solution, which does not provide insights into B incorporation in foraminifer shells, and therefore may miss information about how the proxy might or might not work ultimately. Other techniques such as laser-ablation inductively-coupled-plasma mass spectrometry (LA-ICPMS) may allow this to be overcome, although this method is relatively novel in its application to B/Ca and other trace element analyses. With further development, the LA-ICPMS technique should permit observations of B (and other trace element) distributions in foraminifer shells, which will be useful to better understand the processes underlying the B/Ca proxy and how biases in measurements might impact on the interpretation of results.

Within the Pacific Ocean, the deep Eastern Equatorial Pacific (EEP) has not been really explored from all these perspectives. This area is relevant, not only for its deep connection with the Southern Ocean via Lower Circumpolar Deep Water (LCDW) and Pacific Deep Water (PDW), but also due to its link through "intermediate" water masses (Antarctic Intermediate Water, AAIW, Sub-Antarctic Mode Water, SAMW, Sub-Antarctic Water, SAW) that arrive to the thermocline of the EEP. This is the area where this thesis is focused on.

1.5. **Thesis objectives and Outline**

The main objective of this thesis is to infer the state of the deep EEP and its role in global carbon cycle evolution across the last glacial-interglacial transition based on the application of some of the carbon cycle tracers described above, such as radiocarbon (^{14}C), [CO_3^{2-}] and $\delta^{13}C$. Furthermore, LA-ICPMS has been applied for the trace element measurements (particularly B/Ca) in foraminiferal calcite in order to investigate B incorporation and for comparison with solution analysis.

More specifically, the objectives of this thesis are:

- To infer the past marine carbon cycle evolution in the shallow and deep Eastern Equatorial Pacific, using new radiocarbon, stable isotope and carbonate system reconstructions.
- To set up the laser ablation technique (LA-ICPMS) for B/Ca studies in foraminifera.
- To test the validity of B/Ca as a novel proxy for $\Delta[CO_3^{2-}]$, when analysed via LA-ICPMS.
- To interpret emerging new radiocarbon, stable isotope and carbonate ion reconstructions in the context of other available paleo-data from the Pacific and Southern Oceans, in order to arrive at an integrated view of carbon cycle

changes in the world's largest ocean basin.

- To provide new insights into the ocean's role in the carbon cycle and global past climate change by assessing the likely magnitude and causes of marine carbon inventory changes since the last glacial period.

The structure and content of the following chapters will be:

Chapter 2 presents the material and methods used to develop this thesis.

Chapter 3 describes the new age model(s) estimates by taking into account changes in the surface reservoir ages across the deglaciation.

Chapter 4 presents new estimates of deep- and shallow ocean radiocarbon ventilation over the last 30 kyr in the EEP, which are compared with other available ventilation records from the Southern and Pacific Oceans.

Chapter 5 describes the analysis of trace elements (mainly B/Ca) performed by LA-ICPMS. It is divided in two subchapters for simplicity: 5.1 shows the analytical set up of LA-ICPMS for B/Ca measurements in foraminifer's calcite shell, while 5.2 displays the profiles obtained in two foraminifer species and compares results with solution-ICPMS analyses over the same samples.

Chapter 6 shows B/Ca results by LA-ICPMS and $\delta^{13}C$ measurements in benthic foraminifera, and places them in context with other records from the Pacific Ocean.

Chapter 7 presents an integration of the results and the general conclusions of this thesis, including a perspective on future work.

A synopsis of how a given chapter is related to the previous ones is presented at the beginning of each chapter.

CHAPTER 2

2. Materials and methods: the palaeoceanographic toolbox

2.1. Study location: ODP Site 1240

2.1.1. Sediment core and site description

A sedimentary sequence from ODP (Ocean Drilling Program, Leg 202) Site 1240 (hereafter referred as sediment core ODP1240 for simplicity) was collected by an Advanced Piston Core on board of the *JOIDES Resolution* research vessel in 2002. This core site is located at the northern flank of the Carnegie Ridge (0°01.31'N, 86°27.76'W) in the southwestern margin of the Panama Basin at 2,921 m water depth (Mix et al., 2003), in the core of the Eastern Equatorial Pacific region (EEP) (Fig. 2.1). Specifically, ODP1240 is placed in a small basaltic crust pit with abyssal hills topography typical from expansive areas like the Cocos-Nazca region, which was formed 3 millions years ago (Hey et al., 1977). ODP1240 sedimentary sequence was divided in three subunits (1A, 1B, and 1C) according to their dominant sedimentological characteristics (Mix et al., 2003). This thesis is focused on the first ~400 cm of the subunit 1B covering the period between 0 and 30 kyr.

The equatorial nutrient-rich upwelling in the EEP caused by the trade winds (easterly winds, specially stronger during boreal summers) and its associated high primary productivity is situated above core ODP1240, which turns this region into a "sediment trap". Thus, this area is characterised by fossil-rich content and high accumulation rates (>10-15 cm/kyr; Mix et al., 2003; Pena et al., 2008b), which allows high temporal resolution measurements minimizing possible biases due, for instance, to bioturbation, and therefore making core ODP1240 ideal for accurate palaeoclimatic reconstructions.

2.1.2. Local modern hydrography and climatology at the Eastern Equatorial Pacific

The Panama Basin presents two main inflow passages for the deepest waters; one along the Ecuador Trench and another one across the broad central saddle of the Carnegie Ridge (sill depths ~2,900 m and ~2,300 m, respectively) (Laird, 1971; Lonsdale and Malfait, 1974). Thus, sediment core ODP1240 is currently bathed by a mixture of Upper Circumpolar Deep Water (UCDW) and Pacific Deep Water (PDW; also called Common Water (Montgomery, 1958)) as both occupy approximately the same density and depth range in the Pacific (Talley et al., 2011) (Fig. 2.1). Both UCDW and PDW are characterized by low oxygen (especially the UCDW), high nutrients and high ^{14}C age although their origins are different. PDW is formed internally in the North Pacific through very slow vertical mixing of bottom and intermediate waters, while UCDW represents a mixture of PDW and Indian Deep Water (IDW) that upwells just below the surface in the Antarctic Circumpolar Current (ACC) (Talley et al., 2011).

The shallow sub-surface circulation over the core location is governed by the Equatorial Undercurrent (EUC) between 50-300 m water depth flowing eastward along the tropics (Lukas, 1986; Toggweiler et al., 1991; Tsuchiya et al., 1989). The EUC is partially fed by intermediate water masses (Antarctic Intermediate Water (AAIW) and Subantarctic Mode Water (SAMW)) originated from upwelled Circumpolar Deep Water (CDW) in the Southern Ocean (Kessler, 2006), that are subsequently subducted by winter convection across the Antarctic Polar Front (APF) and Subantartic Front (SAF), respectively, spreading its signature into the Pacific interior. The EUC is also partially fed by Subantarctic Water (SAAW) which is a central water mass originating in the Subantartic zone that subducts at the Subtropical Front (STF; around 30°S) with its core flowing at 150-200 m water depth within the Subtropical gyre (Llanillo et al., 2013; Tsuchiya and Talley, 1998).

The surface circulation in this area is a complex system of jets flowing east- and

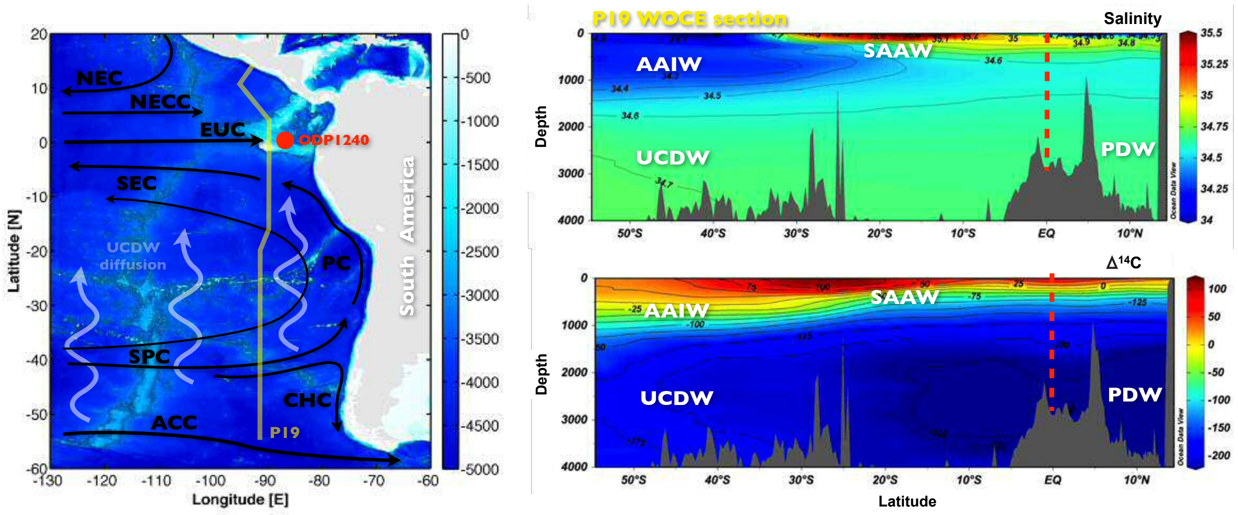

Figure 2.1. EEP hydrography. In the left panel, a map of the area displaying the bathymetry (blue scale), the location of the sediment core ODP1240 (red dot), the WOCE P19 transect (yellow meridional line), and a scheme of the upper (black arrows) and deep (white arrows) ocean circulation of the area: North Equatorial Current (NEC), North Equatorial Countercurrent (NECC), Equatorial Undercurrent (EUC), South Equatorial Current (SEC), Peru Current (PC), South Pacific Current (SPC), Cape Horn Current (CHC), Antarctic Circumpolar Current (ACC) and the northward diffusion of the Upper Circumpolar Deep Water mass (UCDW). In the right panel, two vertical sections of the WOCE P19 transect showing salinity and $\Delta^{14}C$. Water masses are indicated: Antarctic Intermediate Water (AAIW), UCDW, SubAntarctic Water (SAAW) and Pacific Deep Water (PDW). The red vertical dashed line indicates ODP1240 location.

westward. ODP1240 is situated south of the equatorial front in the equatorial divergence zone (Mix et al., 2003), where warm and low-salinity water masses confront with the cold saline waters from the so-called “Cold Tongue”. The latter is the result of convergence of the cold upwelled waters in this area and the South Equatorial Current (SEC) flowing westward between 4°N and 20°S. The ITCZ is also located in this region a bit north of the equator mainly due to the American geometry continent, but fluctuates over time depending on ocean-atmosphere interactions (Philander et al., 1996), like for instance ENSO (El Niño-Southern Oscillation system), and thus making the latitude surface salinity to change as the ITCZ position controls the amount of precipitation.

2.1.3. **Fossil foraminifera analysed in ODP1240**

The elemental composition of the foraminifer's calcite shell has been widely used as a proxy for past environmental conditions of seawater. These organisms build their shell depending on the hydrographic, geochemical and climatic conditions, which can be inferred by the analysis of different elements relative to calcium, or by the isotopic composition of their tests for instance. The two foraminifer species used to develop this thesis are the benthic species *Cibicides wuellerstorfi* and the planktonic species *Neogloboquadrina dutertrei*.

C. wuellerstorfi (Schwager, 1866) is an epibenthic foraminifer species that usually lives attached to structures on the seafloor (Lutze and Thiel, 1989) and has a robust calcareous shell with conspicuous hooked sutures (Fig. 2.2a). It has a trochospiral form being different between sides; the dorsal side is rather flat while the ventral side is conical, with perforations and a bilamellar radial wall (Galloway, 1933). It has

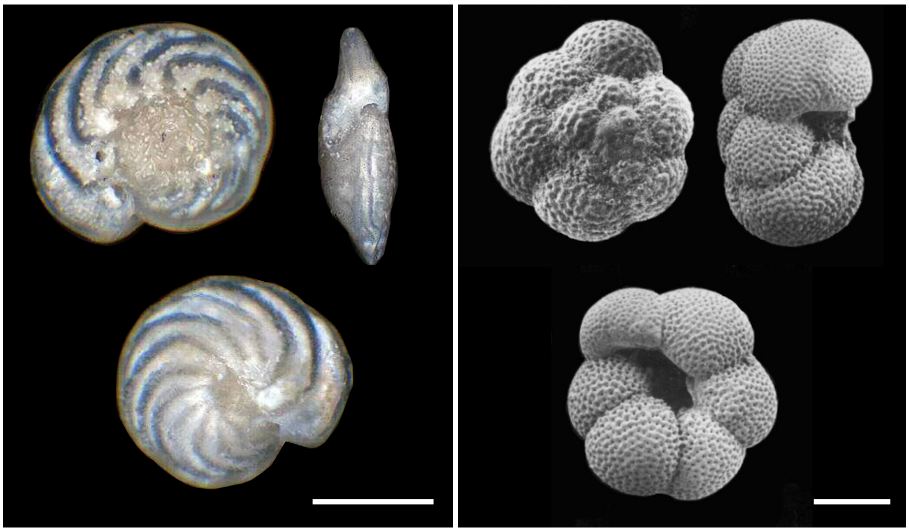

Figure 2.2. Images of the foraminifer species used in this thesis. The left panel shows the benthic foraminifer *Cibicides wuellerstorfi* (Schwager, 1866), Source: www.foraminifera.eu, Author: Robert W. Jones. The right panel shows the planktonic foraminifera *Neogloboquadrina dutertrei* (d'Orbigny, 1839), Source: www.marinespecies.org, Author: Bruce Hayward. The white horizontal line at the bottom left of each panel represents ~100 µm length.

been widely used in paleoceanographic studies as its habitat at the sediment-water interface makes it an ideal recorder of bottom water properties.

N. dutertrei (d'Orbigny, 1839) is a planktonic foraminifer species with a variable number of globular chambers that grow in a spiral form (Parker, 1962) (Fig. 2.2b). Its habitat is mainly restricted to tropical areas, with temperatures above 21-22°C, although it may also be found in some subtropical areas, and with no apparent specific range of salinity (Hilbrecht, 1997). It is common at the deep chlorophyll maximum (Fairbanks et al., 1982), as well as in upwelling zones in warm surface waters, and its diet is based on phyto- and zooplankton prey (Hemleben et al., 1989).

2.2. **Proxies and Methodologies**

2.2.1. **Radiocarbon (^{14}C)**

2.2.1.1. **The tracer**

Radiocarbon (^{14}C) is a natural radioactive isotope that is produced in the stratosphere by the interaction of cosmic rays with nitrogen (^{14}N) (Lal and Peters, 1967). As any other carbon isotope, ^{14}C atoms get oxidised forming molecules of CO_2, which spread to all carbon reservoirs including the ocean. Radiocarbon is a very useful and widespread tool for chronometric dating and as a carbon cycle tracer, since it is a radioactive isotope and decays over time with a half-life of 5,730 yr (Godwin, 1962) (although a "conventional" half-life of 5,568 yr (Libby, 1955) is used for reporting radiocarbon ages).

The ^{14}C budget in the atmosphere is not constant over time due to variations in its production rate, which in turn are due to changes in the solar and earth's magnetic fields (which shield the earth from cosmic radiation) and changes in solar intensity (Kovaltsov et al., 2012), as well as due to variations in the exchange of carbon between different reservoirs with different characteristic radiocarbon activities. Indeed, using records of other cosmogenic isotope production that do not participate in the carbon cycle like ^{10}Be and ^{36}Cl (Hughen et al., 2006; Muscheler et al., 2005), it has been shown that the observed atmospheric radiocarbon activity changes over the last ~40 ka cannot be explained by production rate changes alone, suggesting that carbon cycle changes also contributed to past atmospheric radiocarbon variability.

To assess the occurrence of such carbon cycle changes, reconstructions of the marine radiocarbon inventory are essential, as the ocean is the biggest reservoir of carbon and radiocarbon, so that small variations in its degree of carbon exchange with the atmosphere should produce significant (and opposite) changes in the atmospheric radiocarbon activity over time. Radiocarbon goes into the ocean through atmospheric CO_2 dissolution in the surface of the ocean depending on the partial pressure difference of this gas between the atmosphere and ocean, which in turn depends on physical and chemical seawater properties (see Chapter 1 for further details). Once in seawater, the carbon atoms that are part of the new chemical species formed when CO_2 is dissolved in seawater are transported by ocean circulation, while radiocarbon decays. Thus, in general terms, radiocarbon can be used as a tracer of the “age” of any parcel of water in the ocean. It is important to note however, that any given radiocarbon age estimate in a water parcel will be the result of the mixing of different water masses, each one contributing with its own radiocarbon signal depending on its specific transport time (the amount of time taken to arrive to that specific parcel), as well as with its correspondent atmospheric radiocarbon activity and air-sea gas exchange rate at the moment each water parcel sank into the ocean interior.

Despite this complexity, radiocarbon measurements provide very useful information about the amount of time, on average, that a parcel of water (or more accurately the carbon in that water) has been out of contact with the atmosphere. In order to take account of the fact that the timescale for air-sea radiocarbon equilibration is different (i.e. ~100x longer) than that for e.g. oxygen, the radiocarbon activity of a water parcel is commonly referred to in terms of “radiocarbon ventilation”. There are several metrics to estimate the radiocarbon ventilation of a specific water parcel, which in addition can be applied over time allowing the evolution of such ventilation to be inferred. One of the most straightforward and available metrics to measure radiocarbon ventilation, that is applied in this thesis, is the radiocarbon offset between coeval planktonic and benthic foraminifera (B-P). When measured along a marine sediment core, this metric can provide an estimate of the changing deep- versus surface ocean radiocarbon ventilation gradient over time (Fig. 2.3). In the same way, the radiocarbon offset between planktonic foraminifera and the atmosphere (often referred to as the surface ocean ”reservoir age”) offers information about the degree of equilibration between the marine and

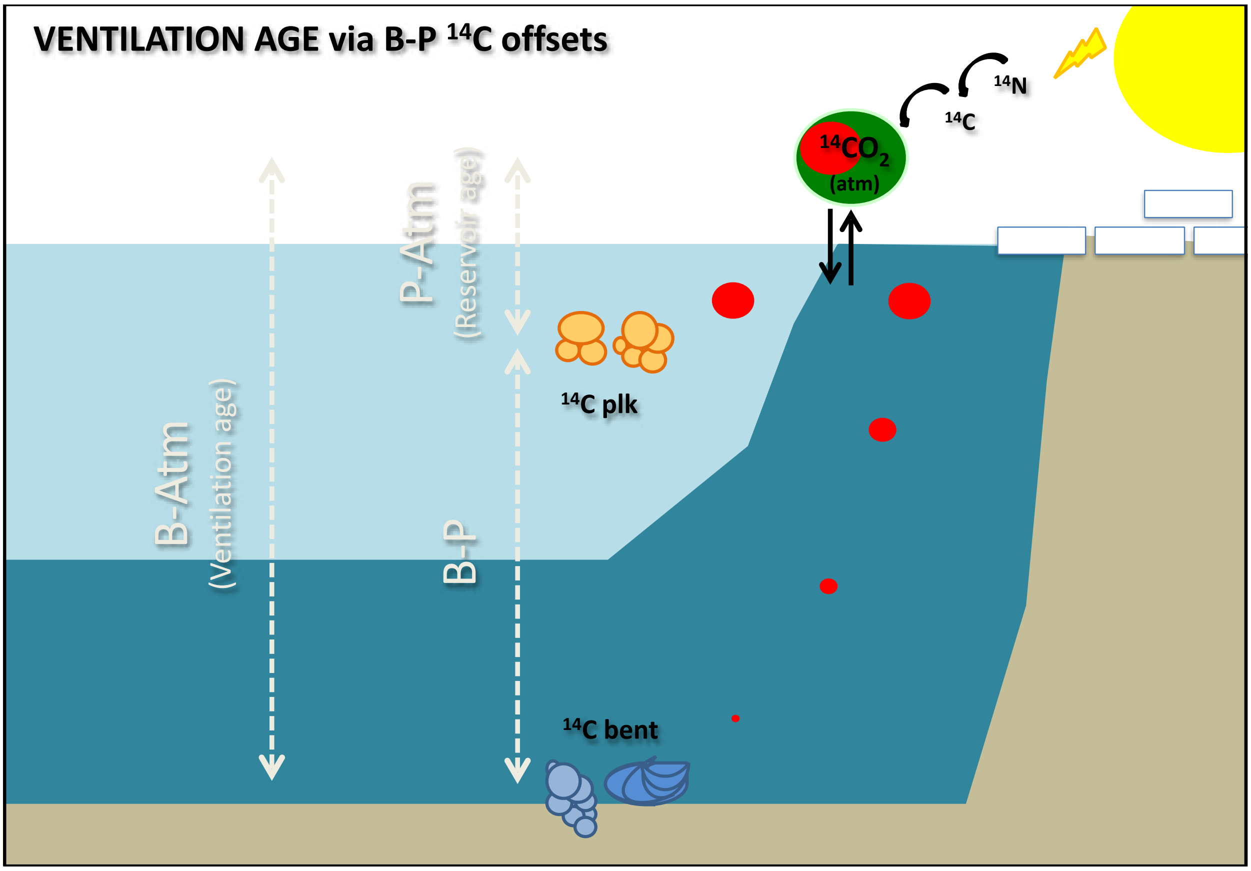

Figure 2.3. Simple schematic representation of the atmosphere-ocean radiocarbon (^{14}C) cycle and the utility of radiocarbon as a tracer for ventilation age estimates via benthic-planktonic foraminifera (B-P) and benthic-atmospheric (B-Atm) radiocarbon offsets. Radiocarbon atoms, which are produced in the atmosphere by cosmic ray impacts on ^{14}N atoms, incorporate into CO$_2$ molecules (green circle), which may enter into the surface ocean where they will gradually decay back to N atoms as they are advected into the ocean interior, away from exchange with the at-

mosphere. The size of the red circles represents the level of radiocarbon activity (the smaller, the little activity, i.e. less radiocarbon, and vice versa). Vertical white arrows show the metrics applied in this thesis to estimate ventilation ages (B-Atm) based, in a first step, on the radiocarbon offset between benthic and planktonic foraminifera (B-P), and secondly, on the radiocarbon offset between planktonic foraminifera and the atmosphere, the so-called “Reservoir age”. Note that radiocarbon activity at the shallow sub-surface is already lower than in the atmosphere (represented by different red circle size), which is why reservoir age estimates are required for accurate ventilation ages, as well as accurate age models.

atmospheric reservoirs. However, reservoir ages are not always easy to constrain, as they need independent calendar age control to be accurately estimated, which are often not available or are difficult to obtain depending on the region for instance (see Chapter 3 for further details). This is the reason why modern regional values are commonly applied over time, under the implicit assumption that local air-sea equilibration and sub-surface carbon entrainment have not changed over time. In any case, by combining these two radiocarbon offsets it is possible to infer deep ocean ventilation changes relative to the atmosphere (i.e. benthic-atmosphere radiocarbon offset, B-Atm) across the last 40-50 kyr, the upper dating limit of this technique (Fig. 2.3). All three of these metrics can help to shed light on the glacial-interglacial carbon cycle and ocean circulation changes, as well as their role in past climate dynamics.

2.2.1.2. **The technique: From the foraminiferal calcite shell to the Accelerator Mass Spectrometer**

In order to be able to measure the radiocarbon content of foraminifer shells, the carbon from the carbonate shell has to be concentrated in graphite form, which can readily be ionized in an (ion counting) accelerator mass spectrometer (AMS).

Samples from this thesis were graphitised in the radiocarbon preparation facility set up at the Godwin Laboratory for Palaeoclimate Research at the University of

Cambridge, UK for the analysis of small calcite samples (Fig. 2.4) (Freeman et al., 2016). The first step consists of dissolving the calcite shells in phosphoric acid and thereby releasing the carbon content as CO_2. The CO_2 is then introduced into a vacuum line, removing any water by contact with an ethanol bath at -60°C. Once into the vacuum line, the samples are sized and frozen down using liquid nitrogen into a reactor containing pre-conditioned iron powder and water-absorbing magnesium perchlorate. Pure hydrogen is then introduced into the reactor and heated to 550-650°C for up to 7 hours, causing the CO_2 to reduce to graphite, which grows in filaments on the iron catalyst, while water that is produced as a reaction by-product is absorbed by the magnesium perchlorate (Santos et al., 2004). The graphite/iron mixture produced is then pressed into stainless steel cathodes backed by aluminium wires, which are loaded into wheels for subsequent AMS analysis. Sample unknowns are typically graphitised in parallel with a set of oxalic acid (OXII) primary standards, a set of secondary standards (e.g. IAEA standards) and a set of "radiocarbon blanks" for assessing background levels. Samples and standards of various sizes are used in order to correct for size-dependent modern and dead carbon contamination (Santos et al., 2007).

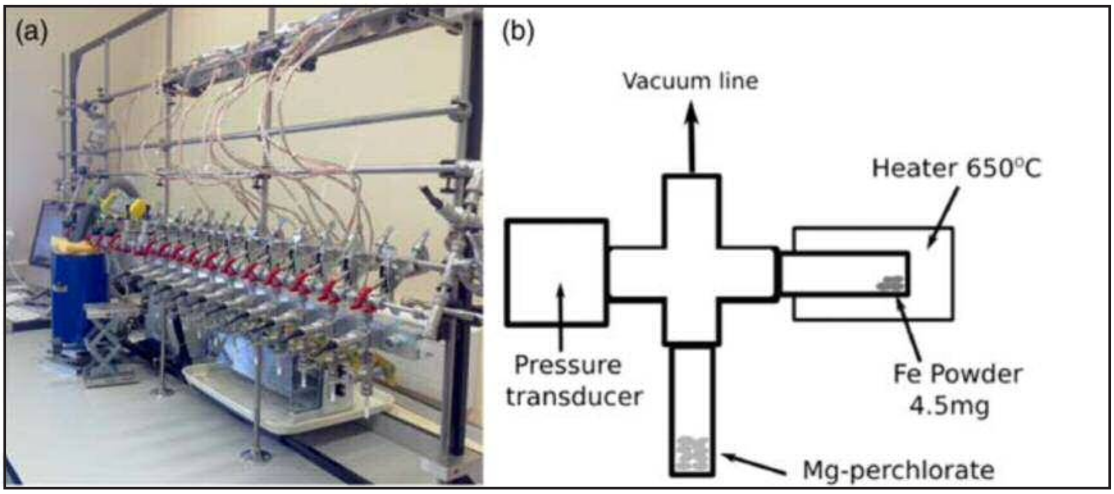

Figure 2.4. a) The radiocarbon preparation facility at the Godwin Radiocarbon Laboratory (University of Cambridge), showing the reactors, the vacuum line, the heaters and the tubes that contain the Mg-perchlorate and the Fe powder where the CO_2 reacts. b) Schematic diagram of the reactor setup. (Image and description from Freeman et al., 2016).

The samples were then sent for analysis by accelerator mass spectrometry (AMS) at the Chrono Centre, Queen's University Belfast, UK. In this centre, radiocarbon ages are calculated using the on-line $\delta^{13}C$ value measured in the AMS, following Stuiver and Polach (1977), which permits to monitor any fractionation that may occur in the accelerator. Thus, the $^{14}C/^{12}C$ and $^{13}C/^{12}C$ ratios were measured on a NEC 0.5 MV AMS and afterwards, the $^{14}C/^{12}C$ sample was background corrected and normalised to the OXII standard (Reimer et al., 2004).

In this thesis, this technique has been applied to coexisting planktonic (*N. dutertrei*) and mixed benthic foraminifera from ODP1240, both in order to derive new age models for the core by taking into account plausible reservoir ages (described in Chapter 3), and to estimate benthic-planktonic and benthic-atmosphere radiocarbon age-offsets as indicators of past ocean ventilation changes (described in Chapter 4).

2.2.2. **B/Ca ratio**

2.2.2.1. **The tracer**

The boron to calcium ratio (B/Ca) in foraminiferal calcite has been theoretically and experimentally proposed as a proxy for the carbonate system. The theory of the B/Ca is rooted in the dissolved boron species in seawater and their relative concentrations and isotopic composition dependence on pH (Hemming and Hanson, 1992) (Fig. 2.5).

Thus, a theoretical relationship between B/Ca and the carbonate system might be summarised as follows:

1) Boron is mainly found in seawater in two dissolved molecular species, boric acid ($B(OH)_3$) and borate ion ($B(OH)_4^-$), which depend on seawater pH and whose stoichiometric equilibrium constant (K_B) is close to seawater pH (i.e. $pK_B = 8.6$) (Fig. 2.5).

2) Assuming that only the charged species $B(OH)_4^-$ is incorporated into biogenic

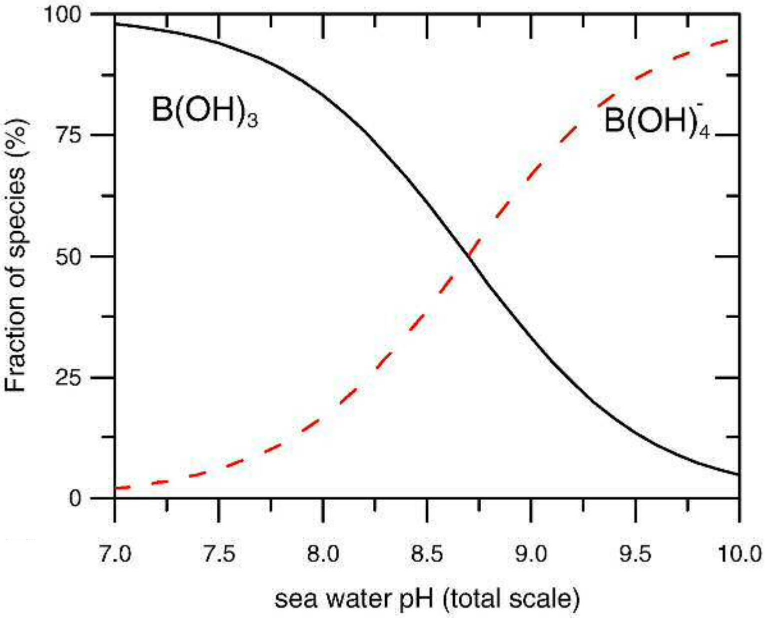

Figure 2.5. Proportions of dissolved boron species $B(OH)_3$ and $B(OH)_4^-$ changing with seawater pH. The curves are calculated with typical deep ocean conditions: T =2 °C, S = 35, water depth = 3500 m using $[B]_{total}$ =416 µmol/kg, $\delta^{11}B_{seawater}$ = 39.5‰, and α = 1.0272 (Figure from Yu et al., 2010b).

calcite, following the consistency found between modern isotopic marine carbonate values and the isotopic composition of $B(OH)_4^-$ in seawater (Hemming and Hanson, 1992), the next equation can be derived:

$$CaCO_3 + B(OH)_4^- \leftrightarrow CaHBO_3 + HCO_3^- + H_2O \tag{1}$$

3) Thus, if the seawater pH increases, the amount of boron available for incorporation into calcite as $B(OH)_4^-$ increases, thus increasing B/Ca ratios in marine carbonate material.

4) Therefore, as seawater pH is controlled by the partial pressure of CO_2 (pCO_2) in seawater, which in turn is determined by alkalinity and dissolved inorganic carbon ratios (ALK/DIC), B/Ca ratios seem to be a potential tool to reconstruct the past carbonate system in the ocean.

Although the theoretical assumption of $B(OH)_4^-$ as the primary species controlling boron incorporation into biogenic calcium carbonate minerals is compelling, it has not yet been resolved (Klochko et al. 2009). However, B/Ca ratios in benthic foraminifera have been empirically demonstrated to relate to deep water carbonate saturation state with respect to calcite $\Delta[CO_3^{2-}]$ (Fig. 2.6), allowing carbonate ion concentration $[CO_3^{2-}]$ to be inferred when temperature and salinity over time are known or else are assumed to have been invariant as a first approximation (Raitzsch et al., 2011; Yu and Elderfield, 2007; Yu et al., 2013).

Further information on the current literature of this proxy within different species is described in Chapter 5.

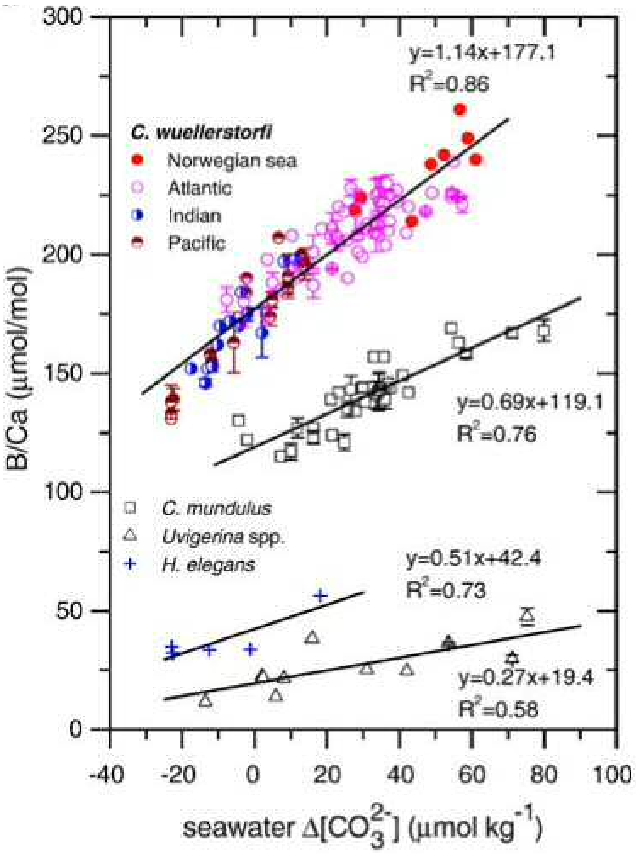

Figure 2.6. B/Ca-bottom water $\Delta[CO_3^{2-}]$ correlation estimated by Yu and Elderfield (2007) in four benthic species using Holocene sediments from the global ocean (solid lines representing linear fits for each species). The calibration equations and the correlation obtained are shown in the graphic.

2.2.2.2. **The technique: Trace elements performed by LA-ICPMS**

Laser-ablation inductively-coupled-plasma mass spectrometry (LA-ICPMS) is a micro-analytical technique that allows high spatial resolution analyses of the elemental and isotopic composition of solid material. Significant advances have been made over the past 20 years, especially on reducing laser wavelength and improving the geometry of the laser-ablation cell. The LA-ICPMS technique provides high-resolution depth profiling offering several advantages compared to other techniques. It allows, for instance, accurate and precise measurement of a wide range of trace elements to be achieved at very high spatial resolution, or the use of little material, or even allows laborious cleaning procedures to be avoided, which saves both time and loss of sample information. All these features make this technique highly suitable to investigate trace element incorporation in foraminifer species, which can be used to infer past climate conditions (e.g. Creech et al., 2010; Eggins et al., 2004; Evans et al., 2013; Raitzsch et al., 2011; Sadekov et al., 2009).

In this thesis, samples for trace element analysis have been run using the LA-ICPMS system set up at the Royal Holloway University of London (RHUL), UK, which consists on a RESOlution M-50 prototype 193 nm ArF laser ablation system coupled to an Agilent 7500ce ICPMS (Müller et al., 2009) (Fig. 2.7a). The foraminifer specimens are stuck on a double-sided adhesive tape (Fig. 2.7d,e) that is then placed into the two-volume laser-ablation cell available at RHUL (Fig. 2.7b,c). Ablation is performed under a helium (He) atmosphere (Eggins et al., 1998), which minimises the loss of aerosol and improves the transference of the sample to the ICPMS. An optional additional di-atomic gas, either nitrogen (N_2) or hydrogen (H_2), is also available in order to improve element sensitivity. The ablated material is conduced to the torch of the ICPMS by argon (Ar) gas through a smoothing manifold called a “squid”, which consists of ten tubes of different length. The ions generated at the torch are separated by their mass-to-charge ratio. Standards with well-known element concentrations are analysed regularly between foraminifer samples in order to convert

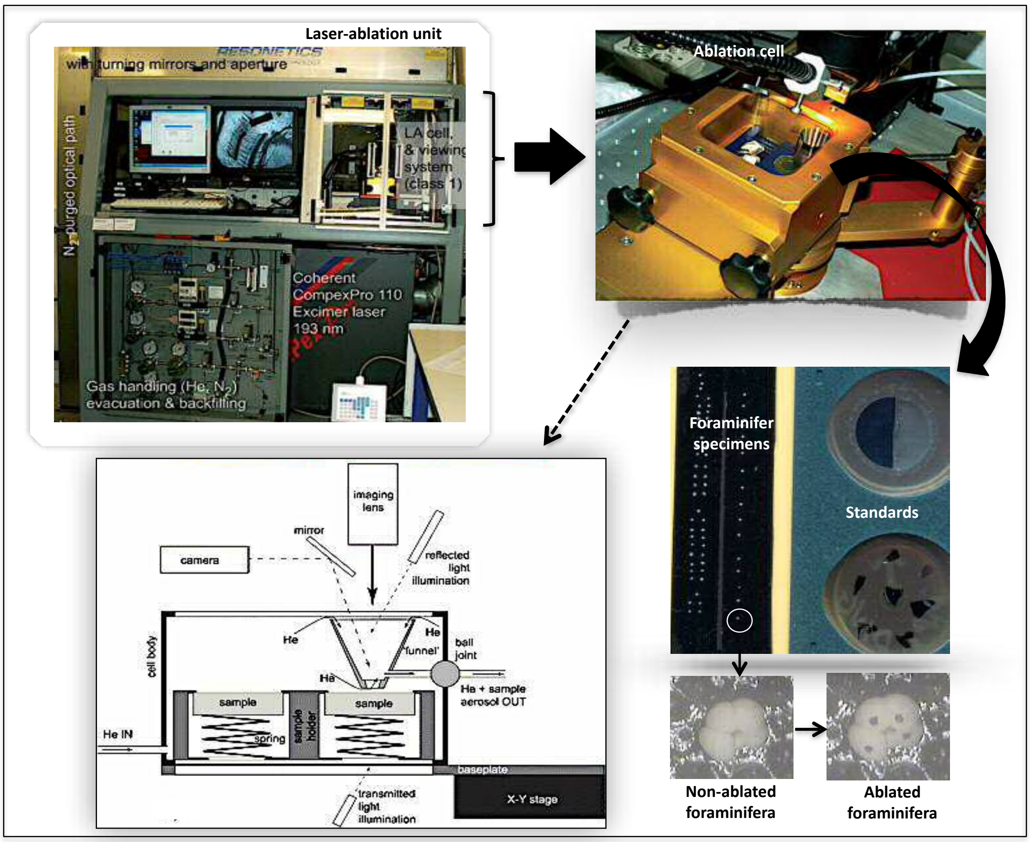

Figure 2.7. Laser-ablation system at Royal Holloway University of London, UK. Upper left panel: the laser-ablation unit (ICPMS not visible). Upper right panel: the Laurin two-volume laser-ablation cell with sample holder and funnel-shaped inner cell. Bottom panel: Details of the two-volume laser-ablation cell. On the left, schematic cross section of the Laurin two-volume laser-ablation cell (not to scale). Helium (He) enters the cell body at its bottom and flows through the funnel, where the He flow entrains the aerosol that condensed out from the laser-induced plasma. Funnel-shaped upper cell and tilted reflected light illumination overall improve the off-axis viewing system. Sample aerosol and He leave the LA cell for the ICPMS via an exit tube connected to the cell body via a ball joint. Ar and N_2 (optional) are admixed downstream, in front of the “squid” signal smoothing device (Adapted from Müller et al., 2009). On the right, standards and foraminifer samples mounted on double-sided tape, as well as detailed planktonic foraminifera before and after ablation.

the counts per second measured at the ICPMS into ppm or mmol/mol.

In this thesis, this technique has been applied to foraminifera in order to analyze the trace element composition of their calcite shells, focusing special attention on B/Ca ratios as a carbon cycle tracer proxy. Specifically, it has been applied in samples from:

- Downcore ODP1240, in both *C. wuellerstorfi* and *N. dutertrei* species (described in Chapters 5 and 6).
- Core-tops from the Atlantic Ocean in *C. wuellerstorfi* (described in Chapter 5).

2.2.3. **Stable carbon isotopes ($\delta^{13}C$)**

2.2.3.1. **The tracer**

The stable carbon isotopic composition of foraminifer shells is used as a tracer for organic matter fixation/oxidation variations in seawater. When the photosynthetic organisms produce their organic matter, the lighter carbon isotope (^{12}C) is preferentially taken up. Thus, the higher the productivity, the more enriched in the heavier carbon isotope (^{13}C) the seawater DIC (Dissolved Inorganic Carbon) would be, and therefore $^{13}C/^{12}C$ ($\delta^{13}C$) of DIC is usually high in surface water. On the contrary, when the organisms die and the organic matter is oxidised/respired, the lighter isotope is released to the surrounding/ambient seawater, decreasing $\delta^{13}C$ of DIC across the water column. These two processes typically occur at very different depths in the ocean water column, which allows us to track changes in both surface productivity and residence of the water masses over time, when $\delta^{13}C$ is measured in either planktonic or benthic foraminifer shells downcore.

2.2.3.2. **The technique: $\delta^{13}C$ by isotope-ratio (IR) mass spectrometry**

The $\delta^{13}C$ content in benthic foraminifera from ODP1240 core was analysed at University of Cambridge. For Thermo MAT253 stable isotope measurements, foraminifera were transferred into sample vials, crushed and then dried in an oven at

50°C. The vials were loaded into the carousel and analysed using a Thermo Kiel device attached to a Thermo MAT253 Mass Spectrometer in dual inlet mode. The preparation system operates automatically analysing samples in sequence. 100% orthophosphoric acid was dropped onto the evacuated vial and reacts with the calcium carbonate sample. The evolved carbon dioxide is cryogenically dried and then admitted to the dual inlet mass spectrometer for isotopic analysis by comparison with a reference gas. Each run of 30 samples was accompanied by 10 reference carbonates and 2 control samples. The results are reported with reference to the international standard VPDB and the precision is better than ± 0.06 ‰ for $^{12}C/^{13}C$ and ± 0.08 ‰ for $^{16}O/^{18}O$.

In this thesis, this technique has been applied in the benthic foraminifer species *C. wuellerstorfi* from ODP1240 core, in order to investigate how remineralisation rates might have changed over the past 25 kyr (Chapter 6).

CHAPTER 3

3. New age models for ODP1240 through reservoir age estimates

Synopsis

In this chapter, variable surface reservoir ages for ODP1240 have been assessed for the last 30 kyr and used to revise the previous age model for this core, which applied constant regional reservoir age corrections.

3.1. Introduction

Accurate age models for marine records are often difficult to constrain. The most common approach to obtain a chronology for the last 40-50 kyr is by radiocarbon dating in planktonic foraminifera, usually using species that live in the ocean's mixed layer or photic zone, and therefore should record the atmospheric radiocarbon activity. However, this approach suffers from two drawbacks: 1) even the mixed layer or photic zone will be somewhat out of equilibrium with respect to the atmosphere, resulting in the so-called "reservoir age effect" that must be corrected for when calibrating radiocarbon dates to calendar ages using an atmospheric radiocarbon calibration curve; and 2) this "reservoir age effect" can vary over time, not only due to radiocarbon activity changes in the atmosphere, but also due to variable mixing with deeper sub-surface waters with a different isotopic signal (generally more depleted ^{14}C), particularly in upwelling areas. Thus, in order to constrain accurate age models in marine sediment cores using radiocarbon, reservoir ages and their temporal variability must be estimated. However, this requires independent calendar age controls at different depths of the sediment core, and due to the difficulty of obtaining these, reservoir ages are not commonly estimated, instead the modern regional reservoir age is taken as a constant value.

One of the most useful and accurate ways to constrain the temporal variability of the reservoir ages in sediment cores is via tephrochronology, permitting marine radiocarbon ages to be compared with correlative atmospheric radiocarbon ages that have been established for well-identified tephra (Siani et al., 2013, 2001; Sikes et al., 2000; Skinner et al., 2015). Unfortunately, the oceanic regions where tephra layers can be found are quite restricted. An alternative method for reservoir age estimation is by chronostratigraphic alignment (Skinner et al., 2010). This method consists on providing calendar ages to the sediment core in study by matching its major climatic changes (through stratigraphic tie-points selection either by hand (e.g. Shackleton et al., 2000) or by dynamic programming (Lisiecki and Lisiecki, 2002), with proxies/records from well-dated archives, like ice core or speleothem records. These derived calendar ages have an atmospheric radiocarbon activity (or “age”) associated that can then be subtracted from the planktonic radiocarbon dates at each core depth, thus providing the so-called reservoir age (Soulet et al., 2016). The limitation of this methodology relies on the scarce availability of well-resolved records that can be correlated with well-constrained archives, as well as the assumption of event synchronicity, and the subjectivity involved in the alignment process itself.

It is interesting to note that the implementation of either the tephrochronology or the chronostratigraphic alignment methods already provide accurate age models that intrinsically constrain reservoir age variability. Thus, if achieving an age model is the goal and these methods are available, neither planktonic radiocarbon dates nor reservoir age estimates might be in principle necessary. However, radiocarbon age controls from planktonic foraminifera that can be corrected for reservoir age changes, can add detailed constraints to the age models. Furthermore, as addressed in the next Chapter 4, reservoir age estimates are useful in themselves as they provide information on shallow ocean circulation and air-sea carbon exchange rates, both of which are relevant to mechanisms of climate change.

The previous age model for core ODP1240 performed by Pena et al., (2008b) was based on 17 calibrated radiocarbon dates of *N. dutertrei*, corrected for a constant global-regional surface reservoir (R+ΔR) of ∼472 yr, as is often assumed. In this thesis, core ODP1240 chronology for the last 25 kyr has been rebuilt since, after assessing the variability of shallow sub-surface reservoir ages using independent chronostratigraphic constraints, the results indicate that shallow sub-surface reservoir ages varied significantly over the last 25 kyr. New age-models that take account of this variability have therefore been produced here, using the Bayesian depth-age modeling program Bchron (Parnell et al., 2008) and the IntCal09 radiocarbon calibration curve (Reimer et al., 2009).

3.2. **Material and methods**

19 radiocarbon dates on *N. dutertrei* (a thermocline-dwelling planktonic foraminifer species, thriving at 100-150 m depth (Fairbanks et al., 1982)) from core ODP1240 were graphitised (See Chapter 2 for further detail on this process) at the Godwin Laboratory for Palaeoclimate Research of the University of Cambridge (UK) (Table A1 in Appendix). *N. dutertrei* was picked from the >212 µm fraction (4-6 mg carbonate per sample) and, in order to avoid sample loss, a minimal cleaning approach was carried out: removal of particles, fibres, small carbonate clasts or other detritus with a fine hair brush followed by repeated rinses in deionized water. Cleaned foraminifera were placed into clean glass vials, rinsed with methanol, dried and evacuated prior to graphitisation. The calcite was hydrolysed in 0.5 ml of phosphoric acid and then reduced to graphite using a standard hydrogen and iron catalyst method (Vogel et al., 1984). Primary and secondary standards were graphitised in parallel with samples. NIST OXII was used as a primary reference standard (for normalisation) and IAEA-C7 and -C8 were used as secondary standards (for quality control). When samples were < 3 mg carbonate, size-matched aliquots of radiocarbon-dead Iceland Spar calcite were graphitized for small sample background (modern contamination) correction (Santos et al., 2007). The radiocarbon analyses were carried out at The

^{14}CHRONO Centre of the Queen’s University of Belfast (UK) using a National Electrostatic Corporation (NEC) compact model 0.5MV Accelerator Mass Spectrometer (AMS), with online $\delta^{13}C$ measurement.

3.3. **Results and discussion**

3.3.1. **Reservoir age assessment**

An assessment of shallow sub-surface reservoir age variability at the location of ODP1240 has been performed by chronostratigraphic alignment between the $\delta^{18}O_{ice}$ and the [Ca^{2+}] records from three Greenland ice cores (NGRIP, GRIP and GISP2 (Rasmussen et al., 2008)) placed on the recent GICC05 time scale (Svensson et al., 2006) and two independent records from ODP1240: a) Sea Surface Temperature (SST) based on the index (Calvo et al., unpublished) and b) $\delta^{18}O_{sw}$ obtained from the planktonic foraminifer *Globigerinoides ruber* (Pena et al., 2008b) (Fig. 3.1).

The proposed alignments are based on a host of previous studies, including previous palaeoclimate reconstructions/interpretations and numerical model studies all of which support the underlying premise of the stratigraphic alignments presented here (Dubois et al., 2014; Kienast et al., 2006; Leduc et al., 2007). The outcome of this previous work is that anomalies in sea surface temperatures recorded by alkenones and surface salinities reflected in surface water $\delta^{18}O$ reconstructions at ODP1240 location should coincide in time with North Atlantic/Greenland temperature anomalies. Thus, on one hand, the basis to select the index calls on the millennial-scale link between cold events in the North Atlantic and the Tropical Pacific SST (Kienast et al., 2006). On the other hand, the basis to select $\delta^{18}O_{sw}$ for this correlation calls on the apparent relationship between changes in Greenland temperatures and surface water salinity in the EEP through shifts in the mean latitude of the Intertropical Convergence Zone (ITCZ) (Leduc et al., 2007). There is therefore a set of well tested physical mechanisms underlying this correspondence that relate to changes in cross-equatorial temperature gradients and their impact on easterly

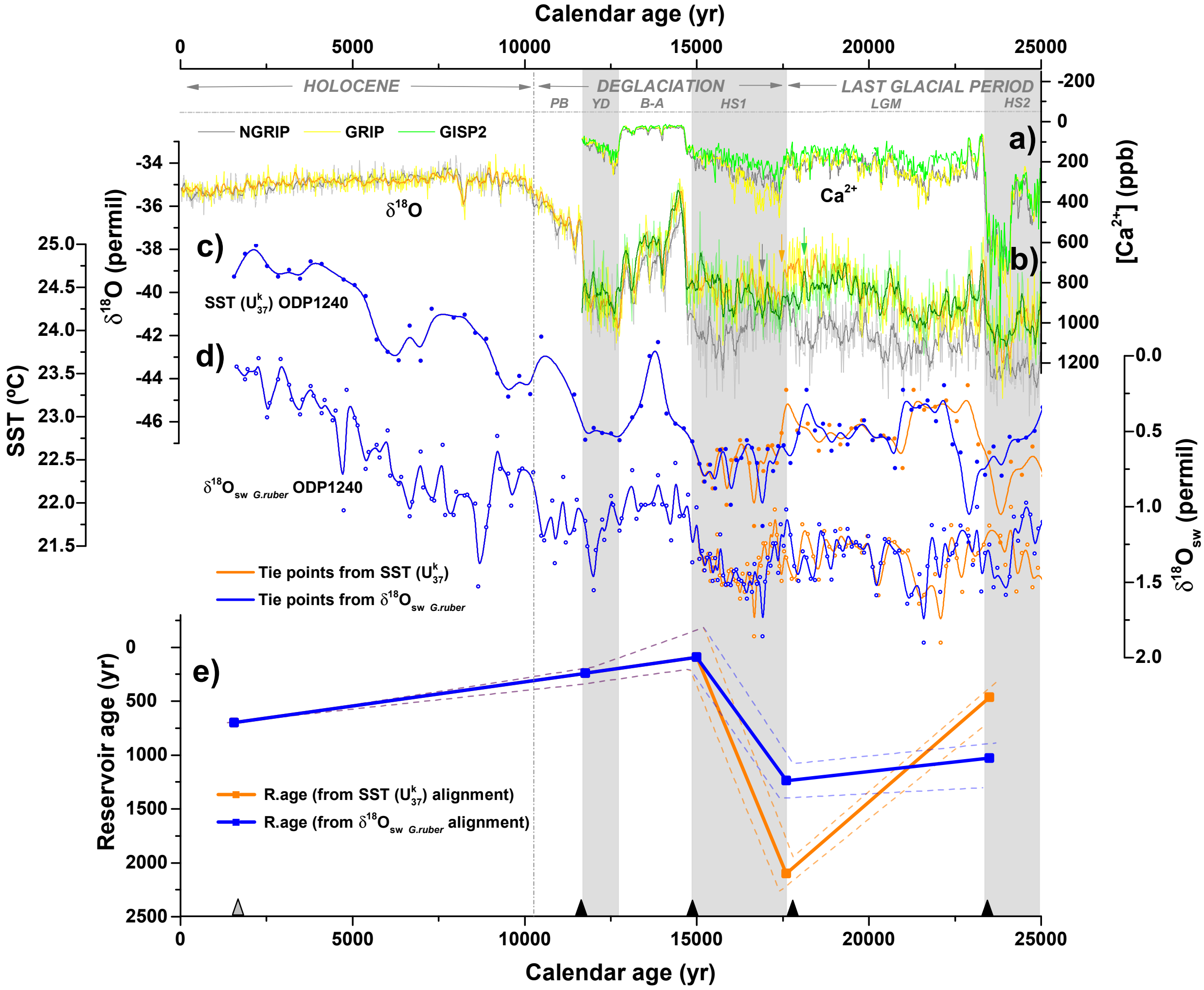

Figure 3.1. Surface reservoir age assessment for sediment core ODP1240 through the alignment between two independent ODP1240 records and three Greenland ice cores over the last 25 kyr. a) [Ca^{2+}] and b) $\delta^{18}O$ records from Greenland ice cores (Rasmussen et al., 2008): NGRIP (grey), GRIP (yellow) and GISP2 (green). Small vertical arrows above Greenland $\delta^{18}O$ records indicate the apparent HS1 onset for each ice core. (c) SSTs from the index and (d) $\delta^{18}O_{sw\ (G.ruber)}$ (Pena et al., 2008b) records from ODP1240 core. In blue, the alignment based on the SST tie-points and in orange, based on the $\delta^{18}O_{sw\ (G.ruber)}$ tie points. (e) Estimated reservoir age scenarios for ODP1240 core using the two alignments: Thick central lines represent the best reservoir age estimate and stippled indicate their upper and lower reservoir age limits (by taking an alignment uncertainty of ±200 yr) (in orange, based on the SST correlation and in blue, based on the $\delta^{18}O_{sw\ (G.ruber)}$ correlation). Selected tie-points are indicated at the bottom by black triangles. An additional core-top date (from Pena et al., 2008b), corrected and calibrated is also shown (grey triangle). Light grey bands highlight the main cold stadials of the last 25 kyr as defined in Greenland records.

winds, equatorial upwelling and moisture transport across the Isthmus of Panama.

For this alignment, four stratigraphic tie-points from the ice-core records were selected coinciding with major climatic changes at the Heinrich Stadial 2 (HS2) end, the Heinrich Stadial 1 (HS1) onset, the HS1/Bølling-Allerød (BA) transition and the Younger Dryas (YD) end (Fig. 3.1; Table A2 in the Appendix). The HS1 onset was designated only through the change in the [Ca^{2+}] record at 17.6 kyr since precipitation $\delta^{18}O$ records from the various Greenland ice-cores present differences between 19-16 kyr due to different site locations (Fig. 3.1a,b). An additional age constraint for the ODP1240 core-top was derived based on a single calibrated radiocarbon date (from Pena et al., 2008b), corrected for the modern shallow sub-surface reservoir age in the area (this is ~700 yr; see Material and Methods from Chapter 4 for further details).

On the basis of the above chronologies, two sets of reservoir age estimates were generated (i.e. one from each ODP1240 record used for stratigraphic alignment) (Fig. 3.1e; Table A2 in the Appendix). These differ due to slight mismatches between the patterns of SST and $\delta^{18}O_{sw}$ variability before 17 kyr (Fig. 3.1c,d). Reservoir ages were calculated as the difference between the interpolated ODP1240 planktonic ^{14}C for each tie-point (Skinner et al., 2010) and the atmospheric ^{14}C-age (IntCal09 curve (Reimer et al., 2009)) at the calendar age of each tie-point (note that the more recent IntCal13 radiocarbon calibration curve (Reimer et al., 2013) has not been used in order to avoid possible problems of inconsistency when comparing with previously published radiocarbon studies that are referenced to IntCal09; only minor differences would arise if IntCal13 curve was used instead). This approach provides reservoir age estimates only at the four proposed calendar age tie-points. An alternative approach of interpolating calendar ages (and on this basis $^{14}C_{atm}$) for all the planktonic radiocarbon dates in ODP1240 would yield spurious reservoir ages where no direct calendar age constraints exist (as would occur in the Holocene for example, where no tie-points were designated).

As observed in Figure 3.1e, despite small quantitative differences between the two sets of reservoir ages estimates generated from SST and $\delta^{18}O_{sw}$ alignments, they both show a broadly similar pattern of variability across the last deglaciation indicating large changes in the shallow sub-surface ocean ventilation over this time interval. Furthermore, these reservoir ages begin to decline coincident with the beginning of the deglaciation (HS1 onset), continuing to drop across HS1 until minimum reservoir ages are reached around the HS1/B-A transition. Quantitatively, they show glacial shallow sub-surface reservoir ages of ~970 and ~1,105 yr respectively, that is ~405 and ~540 yr older than during the Holocene (when reservoir ages are ~565 yr on average, including the modern value of ~735 yr). These results allow the pre-existing radiocarbon based age model for ODP1240 to be refined for the last 25 kyr.

3.3.2. **Age models**

Four age models were thus derived using the Bayesian age-depth modelling program Bchron (Parnell et al., 2008) and the IntCal09 radiocarbon calibration curve (Reimer et al., 2009) (Fig. 3.2; Table A3 in the Appendix): 1) two of them by calibrating 17 *N. dutertrei* radiocarbon dates corrected for the two sets of reservoir age estimates (Fig. 3.2a); and 2) two more using only the stratigraphic tie-points (Fig. 3.2b). The purpose of this was to check the consistency of the age models when ignoring the radiocarbon age constraints between stratigraphic tie points, as well as the radiocarbon age reversals that are automatically rejected by Bchron as outliers in the first two age models.

Notably, all of these four chronologies are in good agreement, indicating a good degree of consistency between the various chronostratigraphic constraints that have been adopted, within their respective uncertainty ranges. Only across the Holocene, where no stratigraphic tie-points were selected, do large differences between the radiocarbon- and stratigraphic age models emerge, reflecting significant changes in sedimentation rate that cannot be captured by the stratigraphic alignment performed in this thesis over this interval.

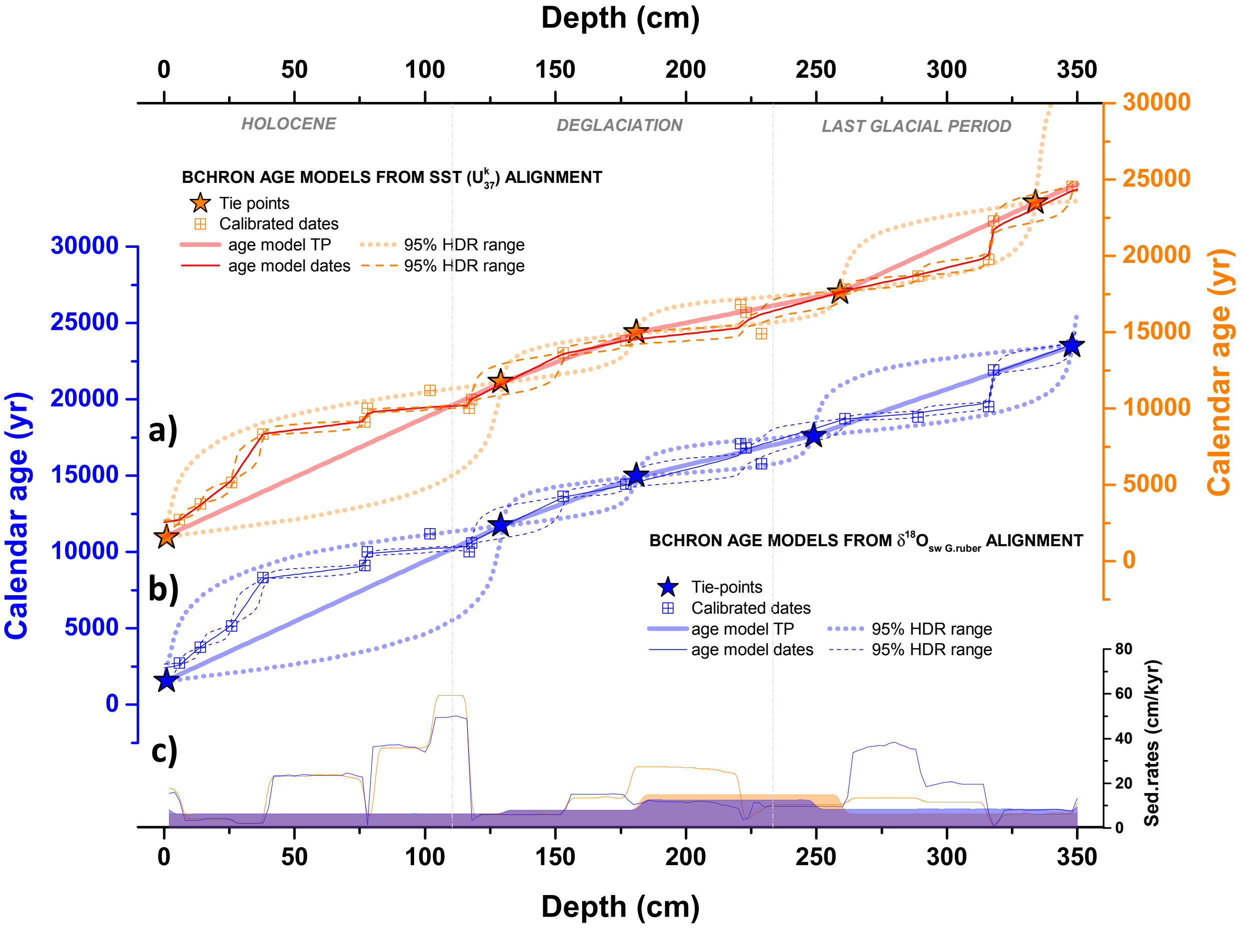

Figure 3.2. Age models for core ODP1240. Four possible Bchron age models and their uncertainties (95% HDR range) for core ODP1240 derived from; a) two from the δ^{18}O $_{\text{(Greenland ice cores)}}$ – SST $_{\text{(ODP1240)}}$ records alignment (orange curves) and b) two from the δ^{18}O $_{\text{(Greenland ice cores)}}$ – δ^{18}O$_{sw\ (G.ruber)}$ $_{\text{(ODP1240)}}$ records alignment (blue curve). Thick solid lines and stars represent the age models derived only from the tie-points (the error is 200 yr). Thin solid lines and squares denote age models using the planktonic radiocarbon measurements corrected for the correspondent interpolated reservoir age obtained from the alignments. c) Sedimentation rates obtained from the four age models; Shaded areas correspond to sedimentation rates using only the tie-points and solid lines using the radiocarbon dates. As for a) and b), orange colors refer to the SST alignment, and blue colours refer to the δ^{18}O$_{sw\ (G.ruber)}$ alignment.

Finally, circumstantial support for the age-models is also provided by the fact that deglacial minima in the *N. dutertrei* δ^{13}C record from ODP1240 (Pena et al., 2008b) correspond with similar *G. bulloides* δ^{13}C minima from the sub-Antarctic Atlantic (Skinner et al., 2014) and peak upwelling intensities indicated by the opal flux record observed in the Southern Ocean (Anderson et al., 2009) (Fig. 3.3). The two minima also broadly coincide with periods of CO_2 rise and with minima in the atmospheric $\delta^{13}CO_2$ record (Schmitt et al., 2012) (Fig. 3.3).

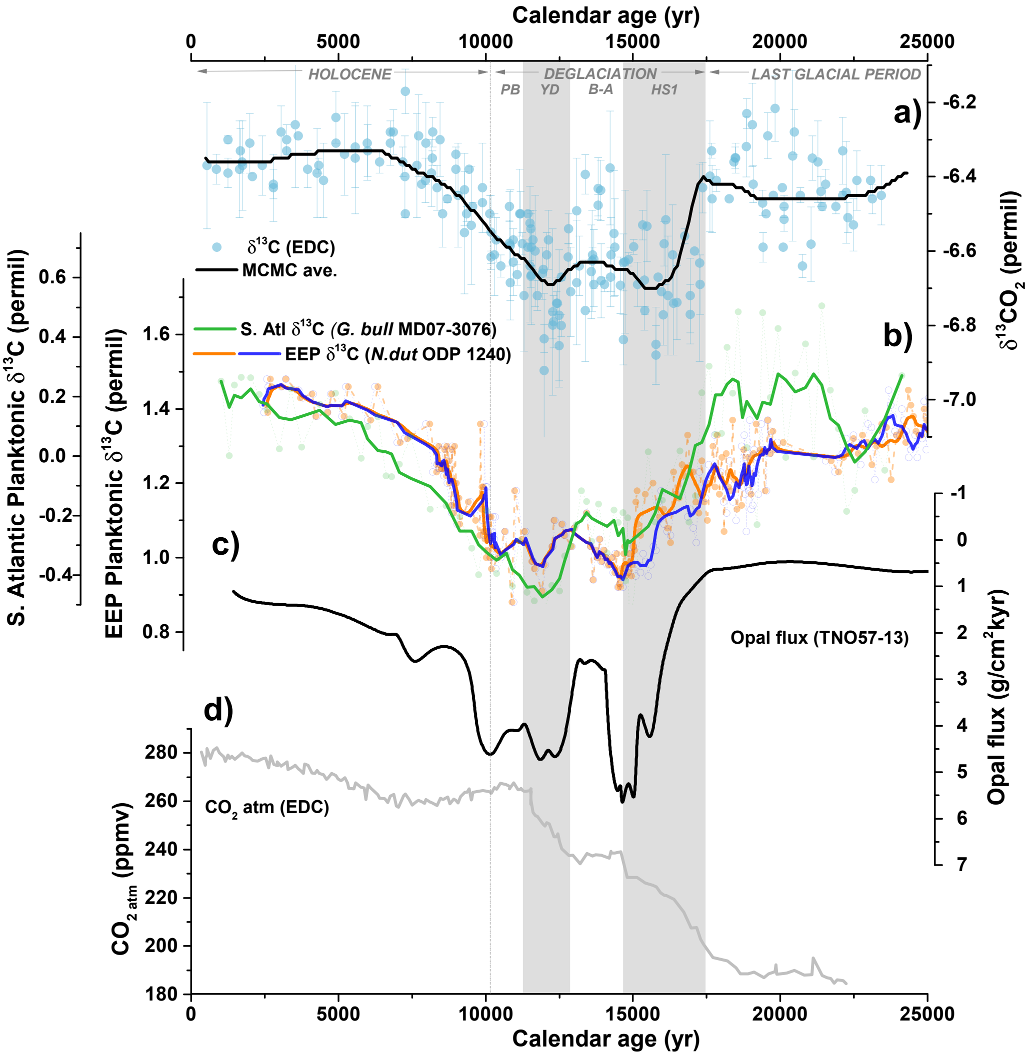

Figure 3.3. Comparison of marine and atmospheric $\delta^{13}C$ records. a) Atmospheric $\delta^{13}CO_2$ record compilation (Schmitt et al., 2012). b) *N. dutertrei* $\delta^{13}C$ record from ODP1240 (Pena et al., 2008b) placed on the revised age models of this study (orange/blue dashed lines with solid/hollow dots from SST/$\delta^{18}O$sw alignments, respectively) and *G. bulloides* $\delta^{13}C$ record from MD07-3076 (Skinner et al., 2014) from the sub-Antarctic Atlantic (green dashed line). Solid thick lines indicate the 5-point running averages. c) TN057-13 opal flux record in a reverse scale (Anderson et al., 2009). d) Atmospheric CO_2 concentrations from EPICA Dome C (EDC) ice core (for the deglacial period (Monnin et al., 2001); for the Holocene period (Flückiger et al., 2002)), placed on the age scale of Lemieux-Dudon et al. (2010).

This general agreement is what one would expect based on the canonical view that all these records reflect the release of "isotopically light" carbon from the deep ocean to the atmosphere via the Southern Ocean and the EEP (e.g. Spero and Lea, 2002). However, it is worth mentioning that when looking at the records in detail, the marine $\delta^{13}C$ records are apparently in closer agreement with each other, as well as the opal flux record (Anderson et al., 2009), than they are with the atmosphere. In particular, the marine records agree in showing the first occurrence of minimum $\delta^{13}C$ values relatively late in the Heinrich Stadial 1.

3.4. **Conclusions**

Based on the chronostratigraphic alignment between two proxies from ODP1240 core and Greenland ice-cores, variable reservoir ages were obtained for the last 25 kyr, with LGM-Holocene differences of ~405 and ~540 yr depending on the alignment.

This has implications in both the age model construction and the climatic features occurred. On light of this, several age models have been estimated in this thesis taking into account the variable reservoir ages. They have been validated by the comparison with both the age models obtained from the "pure" chronostratigraphic alignment performed here and the synchronicity obtained between proxies from other marine and atmospheric records that should be related to ODP1240 core.

The new age models estimated in this chapter, specifically the one estimated from the SST alignment, will be applied from now on in this thesis. The climatic causes and implications of the reservoir age variability across the last deglaciation will be addressed in Chapter 4.

CHAPTER 4

4. Shallow sub-surface and deep radiocarbon ventilation in the EEP and its context in the whole south Pacific and Southern oceans

Synopsis

In this chapter, the ventilation of the shallow sub-surface and deep EEP is estimated in order to provide new insights on the behaviour of the ocean over the last glacial/interglacial period and on its potential relationship with the observed atmospheric CO_2 changes across these periods. The new age models developed in the previous Chapter 3 are applied here.

4.1. Introduction

The Pacific accounts for ~50 % of the total ocean volume, such that changes in its average chemistry may exert a significant influence on that of the global average ocean and therefore that of the atmosphere and the Earth's climate. Indeed, it has long been proposed that a reduction in the ocean's average rate of overturn (Toggweiler, 1999) and/or ocean-atmosphere CO_2 exchange (Stephens and Keeling, 2000) may have been the single most important contributor to reduced atmospheric CO_2 during past glacial periods, and that this would be confirmed by the identification of a significant increase in the average extent of radiocarbon depletion (i.e. the ocean-atmosphere radiocarbon disequilibrium or radiocarbon "ventilation age") in the Pacific Ocean during the last glacial period (Broecker et al., 1990). Despite a surge of marine radiocarbon studies focusing on this issue in recent years, and despite circumstantial support for this hypothesis from atmospheric radiocarbon concentration- and production reconstructions (Broecker and Barker, 2007; Hughen et al., 2004; Muscheler et al., 2004), the glacial radiocarbon inventory of the Pacific Ocean and its evolution across the last deglaciation remain poorly constrained. Thus, radiocarbon ventilation reconstructions from throughout the mid-depth (~500-1500 m) and deep (>1500 m) Pacific are in apparent conflict, with some indicating very little or no change in radiocarbon ventilation between the Last Glacial Maximum (LGM) and the pre-industrial period (Broecker et al., 2008, 2007, 2004a, 2004b, 1990, 1988; De Pol-Holz et al., 2010; Okazaki et al., 2012), some indicating transient anomalies of varying magnitude and sense (Ahagon et al., 2003; Lund et al., 2011; Marchitto et al., 2007; Stott et al., 2009), and with others showing quite significant changes, expressed as a net change between the LGM and the pre-industrial (Sarnthein et al., 2013; Shackleton et al., 1988; Sikes et al., 2000; Skinner et al., 2015) or as a positive anomaly in the deglaciation (Galbraith et al., 2007; Ikehara et al., 2011; Max et al., 2014; Siani et al., 2013) (Table 4.1). Although much of the apparent conflict between the various Pacific radiocarbon ventilation records may reflect small-scale aspects of the glacial circulation as compared to the present (resulting in highly localised signals or errors in water-mass attribution), it could also reflect to a large extent the different methods and assumptions that are adopted in the various studies. Perhaps the most important methodological consideration is whether or not independent calendar age control, and therefore surface reservoir age reconstructions are available. It is notable that most of the existing

Table 4.1. Summary of radiocarbon ventilation records from the Pacific Ocean over the last deglaciation grouped by water depth (>/< 1500 m) and area. *0) Little or no change in radiocarbon ventilation between the Last Glacial Maximum (LGM) and the pre-industrial period; 0+) Transient anomalies of varying magnitude and sense; 1) Quite significant changes, expressed as a net change between the LGM and the pre-industrial period; 1+) Quite significant changes, expressed as a net change between the LGM and the pre-industrial period but with a positive anomaly in the deglaciation. EEP: Eastern Equatorial Pacific; WEP: Western Equatorial Pacific; CEP: Central Equatorial Pacific; SEP: South East Pacific; SWP: South West Pacific; NEP: North East Pacific; NWP: North West Pacific. B-P: benthic-planktonic radiocarbon offset method; Proj.age: projection age method from Adkins and Boyle, (1997).

Area	Coordinates		Core Name	Water Depth (m)	Study	Method to calculate deep ventilation age	Reservoir age variability assessment?	* Type of deep ventilation reconstructions
Sediment cores <1,500 m water depth								
EEP	0.5°S	82.1°W	VM19-27	1,370	(Broecker et al., 2004b)	B-P	NO (constant R.age)	0
	1°13'S	89°41'W	MV21-30	617	(Stott et al., 2009)	B-P	NO (constant R.age)	0+
SEP	36°13'S	73°40'W	SO161-SL22	1,000	(De Pol-Holz et al., 2010)	B-P	NO (constant R.age)	0
NEP	23.5°N	111.6°W	MV99-MC19/GC31/PC08	705	(Marchitto et al., 2007)	Proj.age	NO	0+
NWP	41°07.1'N	142°24.2'E	MR01-K03 PC4/PC5	1,366	(Ahagon et al., 2003)	Proj.age	NO	0+
	52°N-56°N	144°E-169°E	Several cores from Bearing Sea and Okhotsk Sea	630-1,765	(Max et al., 2014)	B-P	NO (constant R.age)	1+
	34°N	137°E	Several cores from off the Tokai area	1,076-1,356	(Ikehara et al., 2011)	B-P	YES (TEPHRAS)	1+
Sediment cores >1,500 m water depth								
EEP	3°37.2'S	83°58'W	TR163-31B	3,210	(Shackleton et al., 1988)	B-P	NO (constant R.age)	1
	1.5°S	85.8°W	RC11-238	2,570	(Broecker et al., 2004b)	B-P	NO (constant R.age)	0
	5.5°S	106.8°W	VM21-40	3,180	(Broecker et al., 2004b)	B-P	NO (constant R.age)	0
	0°01.31'N	86°27.76'W	ODP1240	2,921	This thesis	B-P	YES (chronostratigraphy)	1+
SEP	46°S	75°W	MD07-3088	1,536	(Siani et al., 2013)	B-P	YES (TEPHRAS, partially)	1+
SWP	40°22.935'S	177°59.68'E	MD97-2121	2,314	(Skinner et al., 2015)	B-P	YES (TEPHRAS)	1
	36°S-45°S	177°E-179°E	Several cores from Bay of plenty and Chatman Rise	1,300-2,700	(Sikes et al., 2000)	B-P	YES (TEPHRAS)	1
NEP	54.37°N	148.45°W	ODP 887	3,648	(Galbraith et al., 2007)	B-P	NO	1+
	42.1°N	125.8°W	W8709A-13PC	2,710	(Lund et al., 2011)	Proj.age	Partially, only after 15 kyr	0+
NWP	18°54'N	115°46'E	Sonne 50-37KL	2,695	(Broecker et al., 1990)	B-P	NO (constant R.age)	0
	36°04'N	141°49'E	MD01-2420	2,101	(Okazaki et al., 2012)	Proj.age	NO	0
	51°27'N	167°73'E	MD01-2416	2,317	(Sarnthein et al., 2013)	B-P	YES (^{14}C Plateau tuning)	1
	20°07'N	117°23'E	GIK 17940	1,727	(Sarnthein et al., 2013)	B-P	YES (^{14}C Plateau tuning)	1
	7°12'N	112°5'E	V35-5	1,953	(Broecker et al., 1988)	B-P	NO (constant R.age)	0
WEP	6°N	126°E	MD98-2181	2,100	(Broecker et al., 2004a)	B-P	NO (constant R.age)	0
	1°S	146°E	MD98-2138	1,900	(Broecker et al., 2004a)	B-P	NO (constant R.age)	0
	1.1°N	130°E	MD01-2386	2,820	(Broecker et al., 2008, 2007)	B-P	NO (constant R.age)	0
CEP	10°17'S	111°20'W	TT154-10	3,225	(Broecker et al., 1988)	B-P	NO (constant R.age)	0

radiocarbon ventilation records from the Pacific are based on the commonly used method of calculating benthic-planktonic radiocarbon age offsets (B-P) (Table 4.1), which ignores the possible impact of variable surface reservoir ages on the inferred radiocarbon disequilibrium of deep waters relative to the atmosphere (i.e. the benthic-atmosphere radiocarbon age offset, B-Atm). Furthermore, it is also notable that studies adopting this method or the ^{14}C projection-age method (Adkins and Boyle, 1997), and assuming invariant surface reservoir ages, tend not to find evidence of poorly ventilated glacial mid/deep Pacific ocean waters (Broecker et al., 2008, 2007, 2004a, 2004b, 1990, 1988; De Pol-Holz et al., 2010; Okazaki et al., 2012) (Table 4.1). However, numerical model experiments have suggested that surface reservoir age should in principle have varied since the last glacial period (Butzin et al., 2012), and this has been confirmed via a range of techniques applied, not only in the Pacific Ocean (Lund et al., 2011; Sarnthein et al., 2013; Siani et al., 2013; Skinner et al., 2015), but also in the Southern Atlantic Ocean (Skinner et al., 2010) and other basins (Bard et al., 1994; Siani et al., 2001). Notably, Siani et al. (2013) suggested that data from a previous study at a nearby location (core SO161-SL22; De Pol-Holz et al., 2010) would indeed show significant changes in ventilation ages over the glacial period if their surface reservoir ages were taken into account. These observations serve to underline the importance of assessing the variability of the surface reservoir ages, especially when using the B-P offset approach to calculate radiocarbon ventilation ages.

Today, the Southern Ocean is the main region where water from the ocean interior makes its first contact with the surface, and where surface water first enters the ocean interior (Primeau, 2005). It is also the main source of deep- and abyssal water exported to the rest of the global ocean (Orsi et al., 1999), and it therefore plays a key role in the water mass budget and the ventilation (i.e. the mixing of surface water properties into the ocean interior) of the Pacific Ocean (Talley et al., 2011). It is for this reason that the Southern Ocean has been proposed as the main area for the release of “old” carbon-rich deep water from the ocean interior at the close of the last glacial, possibly due to increased upwelling and/or air-sea gas exchange as a result of altered winds (Anderson et al., 2009) and/or sea-ice/shallow sub-surface density stratification (Skinner et al., 2014, 2010). A connection between the high- and low latitude Pacific is provided through upwelled shallow sub-surface/intermediate waters from the Southern Ocean (See Material and methods for further details) in the Eastern Equatorial Pacific (EEP) via the Equatorial Undercurrent (EUC), identified for both the modern- (Lukas, 1986; Toggweiler et al., 1991; Tsuchiya et al., 1989) and the glacial circulation (Anderson et al., 2009; Calvo et al., 2011; Pena et al., 2013, 2008b; Spero and Lea, 2002). This far-field dynamical connection would imply that changes occurring in the Southern Ocean should exert an influence on the hydrography of the thermocline in low latitude areas like the EEP. The EEP thus provides an excellent study location for assessing past changes in Pacific radiocarbon ventilation, in particular where these are believed to originate in the Southern Ocean.

Here it is presented deep- and shallow sub-surface (i.e. deep-thermocline) radiocarbon ventilation age reconstructions for the EEP, from sediment core ODP Site 1240 located in the Panama Basin (0°01.31’N, 86°27.76’W; 2,921 m water depth). This core site is currently bathed by Upper Circumpolar Deep Water (UCDW) and/or Pacific Deep Water (PDW), with southern sourced shallow sub-surface/intermediate waters contributing to the EEP thermocline via the EUC. Deep water radiocarbon ventilation ages are estimated from B-P age offsets (B: mixed benthic foraminifera; P: *N. dutertrei*, a deep thermocline-dwelling planktonic foraminifer, 100-150 m water depth (Fairbanks et al., 1982)), plus a variable shallow sub-surface reservoir age (yielding B-Atm age offsets), which are derived on the basis of chronostratigraphic alignment to Greenland ice core records (see Chapter 3). Notably, the revised chronology that it is derived in this thesis for this core implies a significant increase in both deep water and shallow sub-surface radiocarbon reservoir/ventilation ages during the last glacial period in the EEP, consistent with a significant change in the radiocarbon concentration of waters exported from the Southern Ocean to the rest of the global ocean during the last glacial period.

4.2. Material and methods

4.2.1. Radiocarbon dates

19 radiocarbon dates on *N. dutertrei* (which have been described in the previous Chapter 3 when assessing the variability of the surface reservoir age) and 17 samples of mixed benthic foraminifera were performed from core ODP1240 (i.e. 17 paired B-P radiocarbon dates). Mixed benthic foraminifera were picked from the >150 µm fraction (1-6 mg carbonate per sample; adjacent sediment samples were combined when the amount of carbonate was less than 1 mg). The samples were cleaned, analysed and measured according to the description made for *N. dutertrei* in Chapter 3.

4.2.2. Radiocarbon calculations in modern water column

The modern radiocarbon values for ODP1240 core site were obtained from section P19 of the World Ocean Circulation Experiment (WOCE) (Tsuchiya and Talley, 1998), very close to this core site. Using the “Δ14C natural” and applying the equation of Stuiver and Polach (1977) ($t=-8033\ln(1+(\Delta^{14}C/1000))$), the current shallow sub-surface and deep ventilation ages are calculated in this site. Thus, the ventilation ages would summarise as: modern shallow sub-surface ventilation age (Reservoir age) at ~150 m water depth is ~735 radiocarbon years; modern deep ventilation age (B-Atm) at ~3,000 m water depth is ~1,985 radiocarbon years; modern B-P radiocarbon offset between 150 m and 3,000 m water depth is ~1,250 radiocarbon years.

4.3. Results

4.3.2. B-P offsets and reservoir ages

17 paired planktonic and benthic radiocarbon measurements and the offset

between them (B-P) are shown in Figure 4.1a and b respectively, and summarised in Table A1 in the Appendix. Of the data shown in Figure 4.1a and 1b, three B-P pairs (depth intervals 26, 223 and 289; see Fig. 4.1b in grey) were flagged up as potential outliers in the present study, on the basis that: these three pairs yield B-P offsets

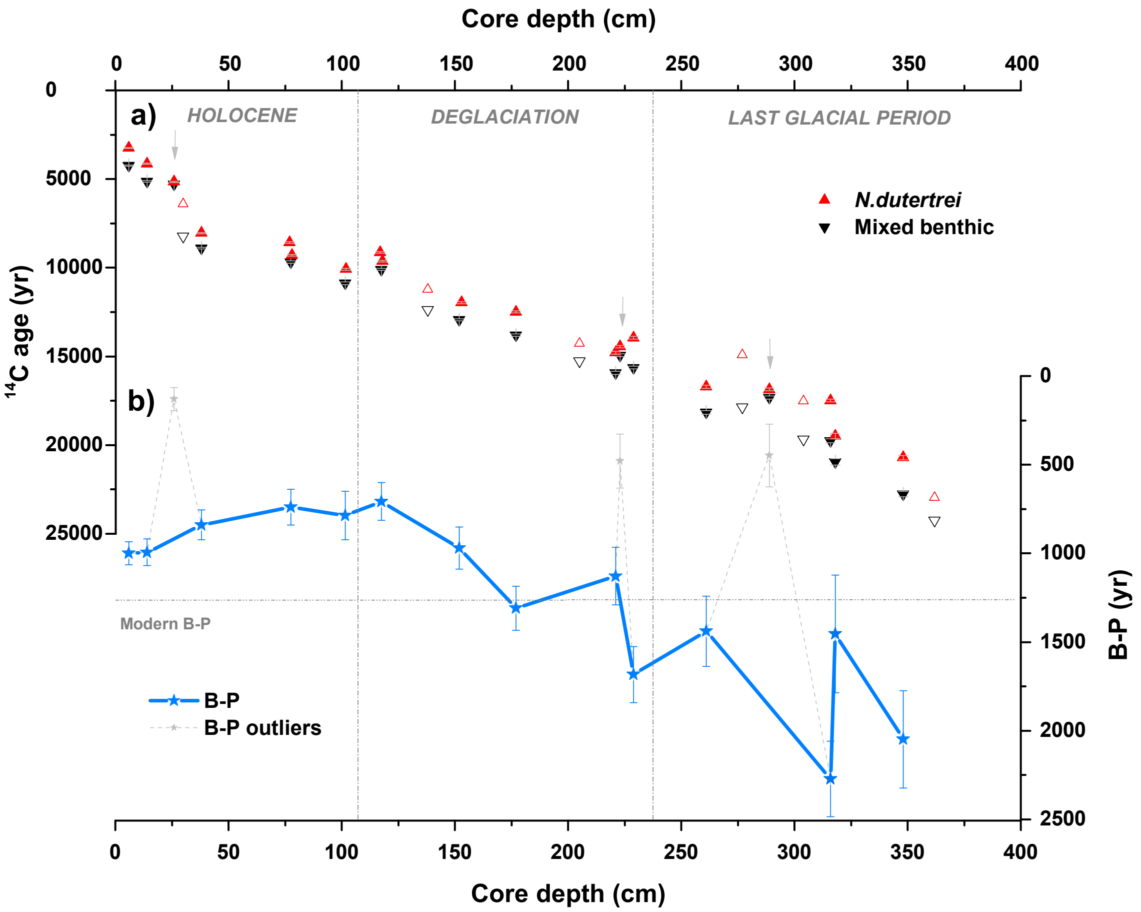

Figure 4.1. Summary of planktonic and benthic radiocarbon dates and their offsets from core ODP1240. a) Radiocarbon dates from *N. dutertrei* (red triangles) and mixed benthic foraminifera (black triangles) (all dates were δ^{13}C-normalised, without reservoir age correction and uncalibrated to calendar years), with associated 1σ-uncertainties. The discarded B-P offsets are indicated by a grey vertical arrow. Note that planktonic dates from intervals 77/78 and 117/118 were averaged for B-P calculation in order to be able to compare with the coeval benthic radiocarbon dates which were combined due the low carbonate abundance of each interval (see Material and methods and Table 1 in the Appendix). b) Benthic-Planktonic radiocarbon offset (B-P) (thick light blue line and stars) plus the discarded B-P offsets (stapled light grey line) (error bars represent combined 1σ error in ^{14}C dates). Modern B-P offset is shown by a dashed horizontal line and relevant climatic periods are separated by dashed vertical lines.

that fall anomalously far away from the three-point running mean of the dataset and; the benthic ages converge on their planktonic counterparts far more rapidly than could be expected due to real changes in deep ocean circulation/ventilation. However, these tentative flyers are shown in Figure 4.1a and 1b in order to note that it is possible (if not presently demonstrable) that other studies in the region might in future provide support for their veracity.

The 14 retained radiocarbon B-P pairs (Fig. 4.1b) indicate a change of ~870 yr between the last part of the last glacial period (average B-P ~1,805 yr) and the Holocene (average B-P ~935 yr, including the modern B-P offset of ~1,250 yr; see Material and methods). Across the deglaciation, decreasing B-P offsets indicate enhanced deep ocean ventilation, that peaks in the early Holocene and then drops again to modern values across this period. These results thus provide clear evidence for a drop in deep equatorial Pacific radiocarbon ventilation ages since the Last Glacial Maximum.

As described in Chapter 3, two reservoir ages were estimated and were used to both perform the age models and to estimate deep ocean ventilation ages (Fig. 4.2b, figures in Chapter 3 and Table A2 and A3 in the Appendix). The two sets of reservoir age estimates show a broadly similar pattern of variability across the last deglaciation, indicating large changes in the shallow sub-surface ocean ventilation over this time interval (Fig. 4.2b). Quantitatively, small differences are found between both SST and $\delta^{18}O_{sw}$ alignments, yielding glacial shallow sub-surface reservoir ages of ~970 and ~1,105 yr respectively, that is ~405 and ~540 yr older than during the Holocene (when reservoir ages are ~565 yr on average, including the modern value of ~735 yr). As shown in Fig. 4.2b, shallow sub-surface reservoir ages begin to decline coincident with the beginning of the deglaciation (HS1 onset), continuing to drop across HS1 until minimum reservoir ages (i.e. maximum ventilation) are reached around the HS1/B-A transition.

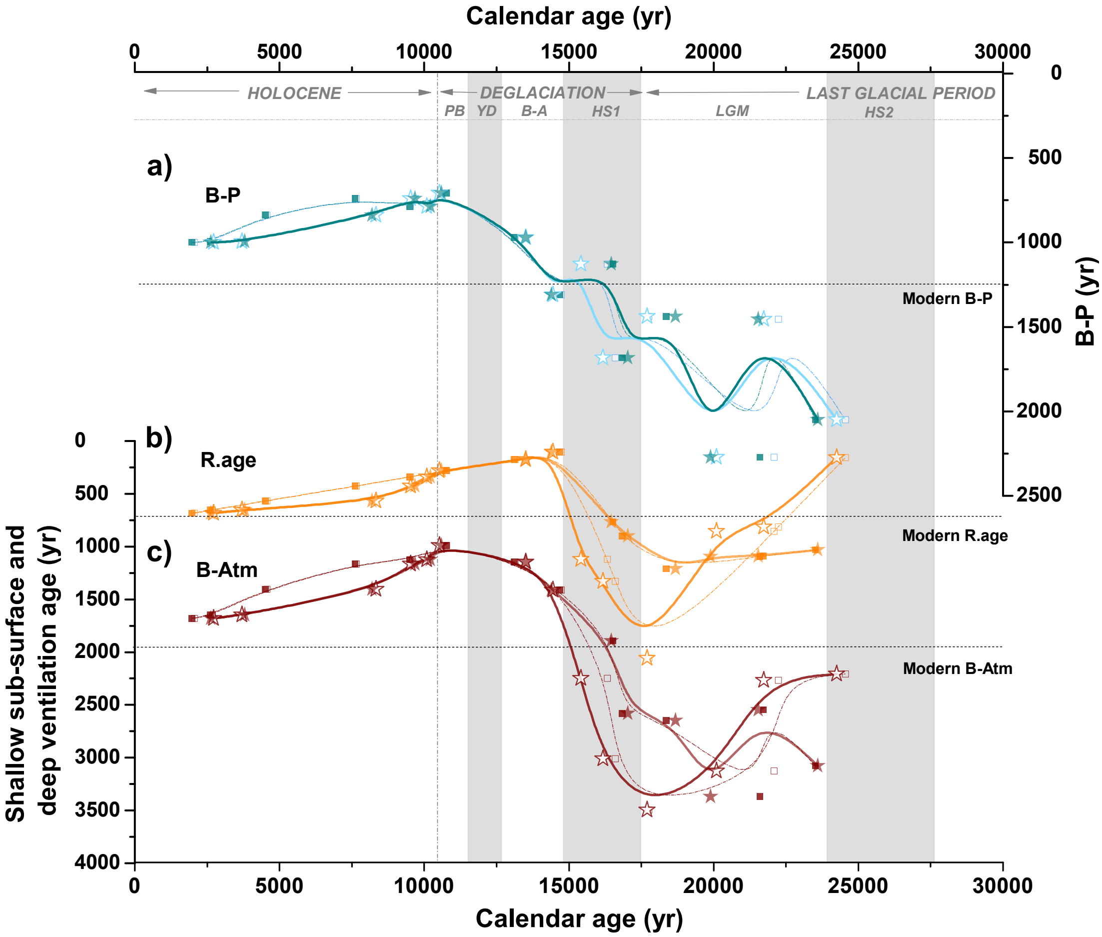

Figure 4.2. Ventilation scenarios for core ODP1240 over the past 25 kyr using the four estimated age models from Chapter 3 (b-spline smoothed). a) B-P offset; b) Shallow sub-surface reservoir age; c) Ventilation age (B-Atm offset). Thick solid lines with stars denote age models using the planktonic radiocarbon measurements corrected for the correspondent interpolated reservoir age obtained from the alignments, and thin stapled lines with squares represent the age model derived only from the tie-points, (hollow/solid in all cases corresponds to UK37’ /$\delta^{18}O_{sw}$ *(G.ruber)* alignments, respectively). Modern offsets are shown by dashed horizontal lines. Light grey bands highlight the coldest periods of the last 25 kyr and delimit relevant climatic periods. Note the different Y-axis scale in a-c.

4.3.2. **Ventilation ages**

Using the observed radiocarbon offsets between benthic-planktonic (B-P; Fig. 4.1b and 4.2a) and between planktonic-atmosphere (i.e. reservoir ages; Fig. 4.2b), the offset between benthic-atmosphere (i.e. deep-ocean ventilation; calculated as B-Atm = B-P + R.age; Fig. 4.2c) can be estimated. Thus, Fig. 4.2 displays the ventilation history at the location of ODP1240, taking into account all four possible age models and their associated reservoir age implications.

As observed in the shallow sub-surface reservoir age reconstructions, the deep-ocean ventilation (Fig. 4.2c) also exhibits different amplitude and slightly different trends since the LGM depending on the various alignments (SST or $\delta^{18}O_{sw}$), but still broadly similar patterns of variability. Quantitatively, the averages from both SST and $\delta^{18}O_{sw}$ alignments indicate B-Atm values of ~2,775 and ~2,910 yr, respectively, during the last part of the glacial period, which would correspond to a ~1,275 and ~1,410 yr older deep glacial ocean than during the Holocene (on average ~1,500 yr including the modern B-Atm value of ~1,985 yr at 3,000 m water depth; see Material and methods). Enhanced ventilation of the deep eastern Pacific is thus observed from the start of HS1, with peak ventilation (minimum B-Atm) being reached at the end of the deglaciation, in the early Holocene (Fig. 4.2c).

4.4. **Discussion**

The ventilation reconstructions from ODP1240 indicate a glacial-interglacial B-P change of ~870 yr that, taking into account the shallow sub-surface (deep-thermocline) reservoir age change of ~405/540 yr (from both SST and $\delta^{18}O_{sw}$ alignments, respectively), imply a glacial-interglacial B-Atm change of ~1,275/1,410 yr (Fig. 4.2; Table A3 in the Appendix). Taken together, these results indicate that both deep- and shallow sub-surface reservoir ages (Fig. 4.2b,c) were significantly increased at the LGM and that both evolved in a similar manner over the last 25 kyr, albeit with a larger change in the deep ventilation ages (as indicated by the change in B-P across the deglaciation; Fig. 4.2a). A poorly ventilated glacial shallow sub-surface and deep EEP is thus demonstrated by the reservoir age reconstructions and by both the B-P offsets and the B-Atm offsets, with implications for the glacial ocean's total radiocarbon inventory and its role in glacial-interglacial CO_2 change (Broecker and Barker, 2007).

The changes in B-P offsets between the LGM and modern observed in ODP1240 clearly reflect a discernable trend in deep equatorial Pacific ventilation across the last deglaciation that is consistent with other B-P records from the northern- and southern high latitude Pacific Ocean (SWP (Sikes et al., 2000; Skinner et al., 2015); SEP (Siani et al., 2013); NEP (Galbraith et al., 2007)) (Fig. 4.3). All of these studies indicate slightly higher B-P age offsets during the last glacial period (~200-600 yr) and, although they are not extremely large, they should not be downplayed. Indeed, it has been argued that the full 190 ‰ drop in atmospheric $\Delta^{14}C$ since the LGM (ignoring changes in radiocarbon production) could in principle be explained

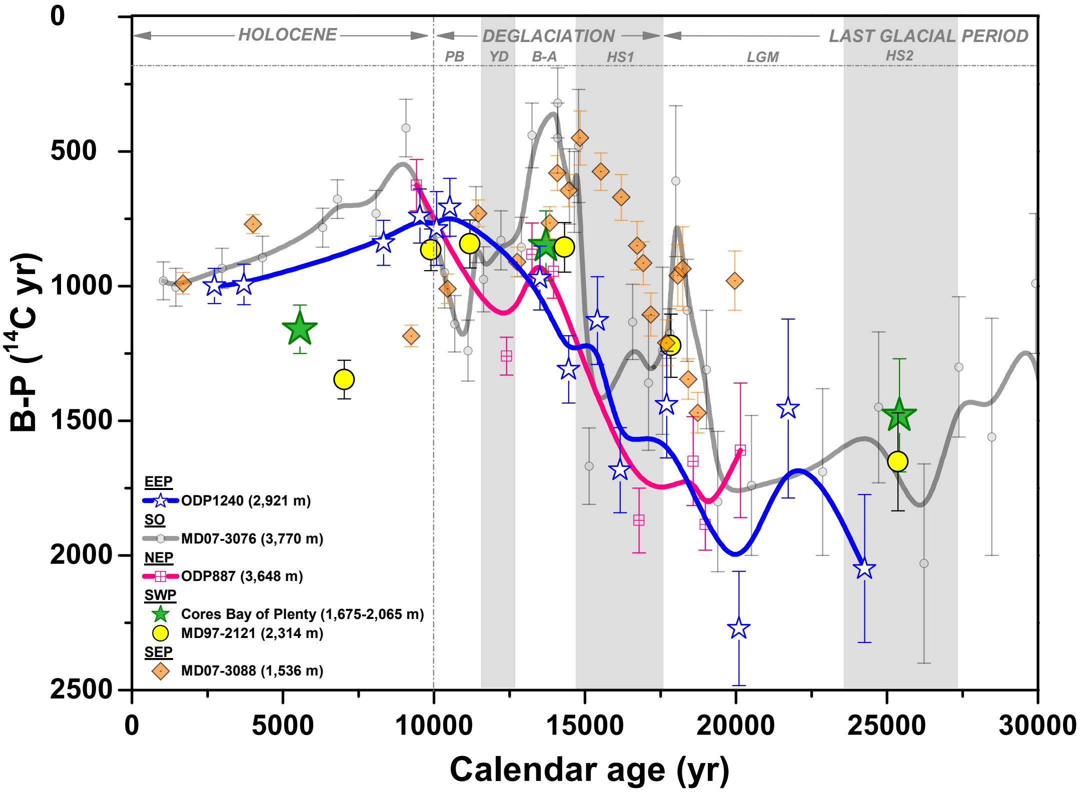

Figure 4.3. B-P radiocarbon offsets from several locations in the Pacific and Southern Oceans over the last 25 kyr (B-spline smoothed): ODP1240 (2,921 m; blue hollow stars from SST alignment; this study); Bay of Plenty (1,675-2,065 m; green stars; Sikes et al., 2000); MD97-2121 (2,314 m; yellow dots; Skinner et al., 2015); MD07-3088 (1,536 m; orange diamonds; Siani et al., 2013); MD07-3076 (3,770 m; grey dots; Skinner et al., 2010); ODP887 (3,648 m; pink squares; Galbraith et al., 2007). Light grey bands highlight the coldest periods of the last 25 kyr and delimit relevant climatic periods.

by rather small changes in the mean ventilation age of the whole upper ocean (e.g. ~100 yr over 60 % of the ocean) if these were combined with a slightly larger change in the mean ventilation of the deepest ocean (e.g. ~3,000 yr on average, over 35 % of the ocean) (Skinner et al., 2010).

Although B-P offsets in ODP1240 are clearly observed to decrease across the last deglaciation (Fig. 4.1b and 4.2a), a larger drop in B-Atm offsets is inferred on the basis of the shallow sub-surface reservoir age reconstructions estimated in this thesis. In a first instance, the regional coherence of these shallow sub-surface reservoir age reconstructions is explored via a comparison of planktonic stable isotope records from the studied core and core TR163-31B (Shackleton et al., 1988) (located in the same area and also with *N. dutertrei* radiocarbon dates), performed by placing each core on its own conventional ^{14}C age scale (Fig. 4.4). For this purpose the

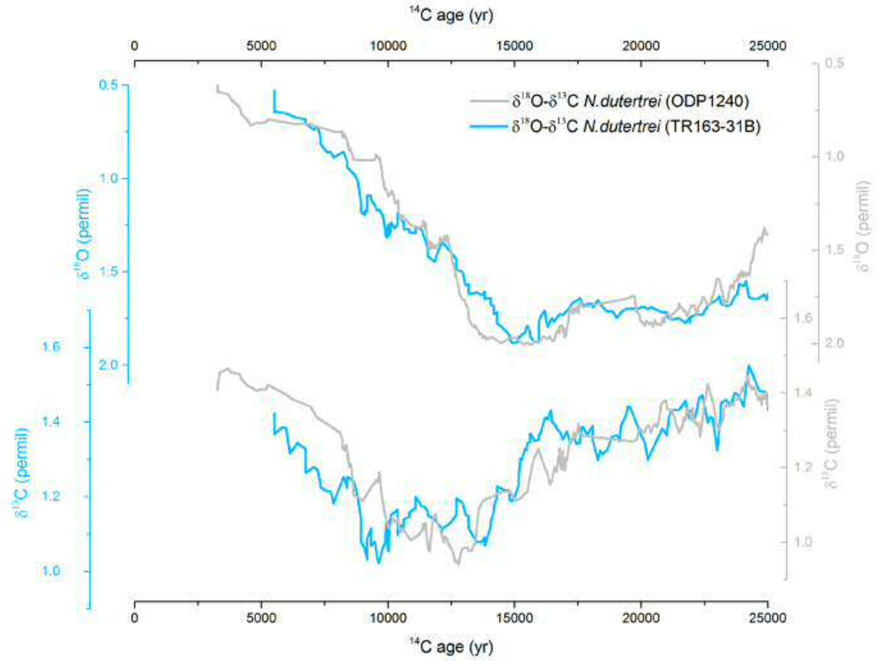

Figure 4.4. Comparison of stable isotopes (from *N. dutertrei*) between cores ODP1240 (grey lines) and TR163-31B (blue lines; Shackleton et al., 1988), each one placed on its own radiocarbon age scale, showing broad coherence of signals and therefore of reservoir age histories. Upper panel displays δ^{18}O records and lower panel δ^{13}C records.

radiocarbon data from Shackleton et al. (1988) has been used. The fact that the isotope stratigraphies and radiocarbon data from the two cores are consistent (Fig. 4.4) indicates that both locations have experienced broadly similar reservoir age changes. On this basis, a "regional radiocarbon calibration" can be used to transfer calendar ages (and therefore reservoir ages) from ODP1240 to TR163-31B. This in turn allows B-Atm offsets to be derived for core TR163-31B, using the few available benthic radiocarbon dates from Shackleton et al. (1988), as described below.

While the comparison described above demonstrates that similar reservoir age changes were experienced at the locations of ODP1240 and TR163-31B, it does not provide an independent confirmation of the reservoir ages derived for ODP1240. However, direct support for the observation made in this thesis of significantly enhanced glacial shallow sub-surface reservoir ages is provided by the few studies in the South Pacific Ocean that have also sought to constrain reservoir age variability using paleoceanographic observations (Fig. 4.5c), as well as direct support for a deglacial change in deep equatorial Pacific ventilation (Figure 4.6d). Both comparisons are discussed below.

As shown in Figure 4.5, the radiocarbon ventilation rate of both the thermocline and the deep EEP are observed to increase broadly in time with the onset of deglaciation, the rise in atmospheric CO_2 (Monnin et al., 2001) and the drop in atmospheric ^{14}C (Hughen et al., 2004; Reimer et al., 2013) (Fig. 4.5a,b). These results would thus support the hypothesised role of reduced ocean-atmosphere CO_2 exchange rates in sequestering carbon in the glacial ocean interior, and the release of this carbon to the atmosphere across the last termination. The demonstration of reduced radiocarbon ventilation rates in both the deep and shallow sub-surface Pacific Ocean is crucial in this respect, as this basin accounts for ~50 % of the ocean's total volume. Thus, small ventilation or carbon sequestration effects in the Pacific can have a particularly large impact on global ocean chemistry, as well as that of the atmosphere.

Going back to the reservoir age support from other Pacific records, in the southwest

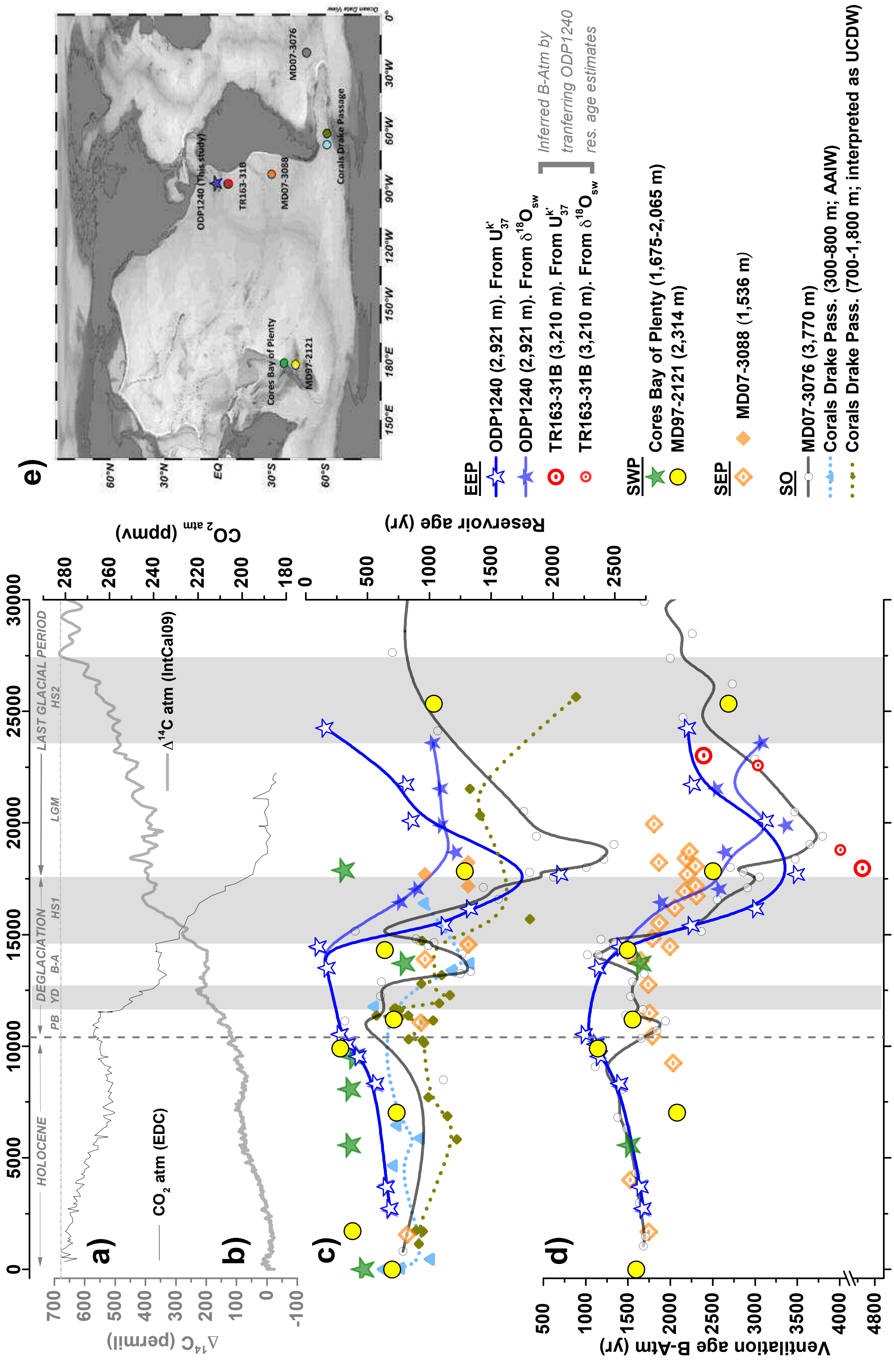
Calendar age (yr)
HOLOCENE
DEGLACIATION
LAST GLACIAL PERIOD
PB
YD
B-A
HS1
LGM
HS2
a)
b)
c)
d)
e)
CO2 atm (EDC)
Δ14C atm (IntCal09)
CO2 atm (ppmv)
Δ14C (permil)
Reservoir age (yr)
Ventilation age B-Atm (yr)
ODP1240 (This study)
TR163-31B
MD07-3088
MD07-3076
Corals Drake Passage
Cores Bay of Plenty
MD97-2121
EEP
ODP1240 (2,921 m). From U37k'
ODP1240 (2,921 m). From δ18Osw
TR163-31B (3,210 m). From U37k'
TR163-31B (3,210 m). From δ18Osw
Inferred B-Atm by tranferring ODP1240 res. age estimates
SWP
Cores Bay of Plenty (1,675-2,065 m)
MD97-2121 (2,314 m)
SEP
MD07-3088 (1,536 m)
SO
MD07-3076 (3,770 m)
Corals Drake Pass. (300-800 m; AAIW)
Corals Drake Pass. (700-1,800 m; interpreted as UCDW)
60°N
30°N
EQ
30°S
60°S
150°E
180°E
150°W
120°W
90°W
60°W
30°W
0°
Ocean Data View

Figure 4.5. Comparison of reservoir- and ventilation age reconstructions from the South Pacific and Southern Ocean over the last deglaciation grouped according to their likely water-mass affiliations. a) Atmospheric CO_2 concentrations from EPICA Dome C (EDC) ice core (for the deglacial period (Monnin et al., 2001); for the Holocene period (Flückiger et al., 2002), placed on the age scale of Lemieux-Dudon et al. (2010). b) Atmospheric radiocarbon activity ($\Delta^{14}C$) changes (IntCal09 calibration curve; Reimer et al., 2009). c) Surface/shallow sub-surface reservoir age records and d) deep-water ventilation reconstructions from several locations in the Pacific and Southern Oceans over the last 25kyr (B-spline smoothed): ODP1240 (2,921 m; *N. dutertrei*; dark blue hollow/solid stars from SST/$\delta^{18}O_{sw}$ alignments, respectively; this study); TR163-31B (3,210 m; *N. dutertrei*; red hollow big/small circles from SST/$\delta^{18}O_{sw}$ alignments in ODP1240, respectively; Shackleton et al., 1988); Bay of Plenty (1,675-2,065 m; *Globorotalia inflata*; green stars; Sikes et al., 2000)); MD97-2121 (2,314 m; *G. inflata*; yellow dots; Skinner et al., 2015); MD07-3088 (1,536 m; *Globigerina bulloides*; light orange diamonds from Carel et al. (2011) and Haberle and Lumley (1998)); dark orange diamonds from Siani et al. (2013)); MD07-3076 (3,770 m; *G. bulloides* and *G. inflata*; dark grey dots; Skinner et al., 2010); Corals from the Drake Passage (300-800 m “shallow corals”; small light blue triangles and 700 - 1,800 m “deep corals” small dark green dots; Burke and Robinson, 2012). Note that the age models used for ODP1240 are those obtained using the calibrated radiocarbon dates and not the tie-points. Note the Y-axis breaks in plot d. e) Locations of marine records showed in c) and d).

Pacific (SWP) a pioneering study in the Bay of Plenty, using ^{14}C-dated tephra, found a considerable increase in shallow sub-surface reservoir ages during the last glacial period (Sikes et al., 2000) that, with the recently updated age for the Kawakawa tephra (Vandergoes et al., 2013), increases the inferred glacial reservoir ages to ~3,200 yr. The latter is an extreme value for a shallow sub-surface radiocarbon reservoir age in the modern context and, although it may yet be proven correct, in this thesis, the Bay of Plenty data in Figure 4.5 it is tentatively reported excluding the glacial point. Indeed, a recent study in the same area (SWP) in core MD97-2121, also using the revised age of the Kawakawa tephra and radiocarbon dates on the same deep dwelling planktonic species (*Globigerina inflata*), found a ~337 yr increase in shallow sub-surface reservoir ages, from 700 to ~1,037 yr, during the last glacial period (Skinner et al., 2015). The latter values compare well with other reservoir age estimates from core MD07-3088 in the southeast Pacific (SEP), also based on tephrostratigraphy and marine radiocarbon dates in *G. bulloides*, which indicate ~500 yr older reservoir ages over the latest part of the deglaciation, as compared to modern (Carel et al., 2011; Haberle and Lumley, 1998). These reservoir age estimates have been extended beyond the range of available ^{14}C-dated tephra by assuming an inverse relationship between B-P offsets and planktonic versus benthic foraminiferal $\Delta\delta^{13}C$ from the same core, suggesting that increased surface reservoir ages also prevailed during the earlier part of the deglaciation (Siani et al., 2013).

The coherence of these various surface reservoir age estimates (Siani et al., 2013; Sikes et al., 2000; Skinner et al., 2015; this study) from different regions and water column depths may be explained by the transport pathways that link them together in the modern ocean circulation, as noted by a large number of studies (Kessler, 2006; Toggweiler et al., 1991; Tsuchiya et al., 1989). Under the premise that the glacial circulation pathways were not wildly different from the modern (i.e. a broadly similar pattern of buoyancy and wind forcing), a numerical model simulation (Skinner et al., 2015) can be used to show a direct dynamical connection between all these areas and depths (Fig. 4.6). This illustrates that an increase in the shallow sub-surface reservoir age across the Southern Ocean (e.g. as proposed by Skinner et al., 2010) should also be conveyed to the shallow sub-surface of the EEP and SWP via the dominant transport pathways in the ocean interior (Fig. 4.6), as is also indicated for the surface SEP, where *G. bulloides* (dated by Siani et al., 2013) currently thrives.

In agreement with this proposition, ODP1240 shallow sub-surface reservoir ages also generally exhibit trends and values that are consistent with reconstructions from the Southern Ocean, including the records based on chronostratigraphically dated planktonic foraminifera from core MD07-3076 from the sub-Antarctic Atlantic (Skinner et al., 2010) and Drake Passage corals from water depths of 300-800 m and 700-1,800 m (hereafter referred to as “shallow corals” and “deep corals”, respectively) (Burke and Robinson, 2012) (Fig. 4.5c). The planktonic foraminifera from core MD07-3076 would have lived north of the Sub-Antarctic Front (SAF) where

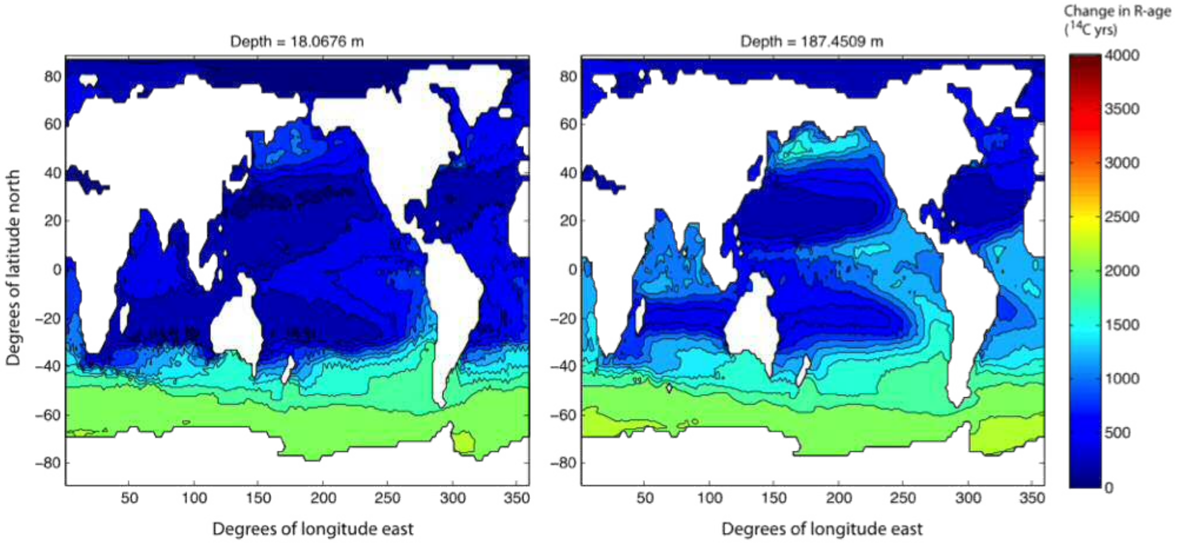

Figure 4.6. Numerical model simulation of marine radiocarbon ages (relative to the atmosphere), as reported by Skinner et al. (2015), showing ages for 18 m (left) and 187 m (right) water depth. The simulation adopts the model framework of DeVries (2014) and assumes the modern circulation, albeit with >1,000 yr surface reservoir ages arbitrarily imposed in the Southern Ocean. The simulation thus demonstrates how an increase in Southern Ocean surface reservoir ages would be transmitted to other regions of the global ocean, including the EEP in particular, simply due to the dominant transport pathways of the ocean circulation. Coherent surface reservoir age changes in the Southern Pacific, Southern Atlantic and EEP could conceivably be explained in this way.

some intermediate waters are subducted and the "shallow corals" from the Drake Passage have been interpreted to provide a record of Antarctic Intermediate Water (AAIW) ventilation ages. Interestingly, the "deep corals", although initially proposed to reflect the radiocarbon ventilation age of UCDW, are rather similar to the rest of the shallow sub-surface/intermediate water candidate reconstructions (Fig. 4.5c). This could suggest that, at least over the glacial/deglacial period, the deep Drake Passage corals might have been substantially influenced by SO-intermediate waters, instead of UCDW as previously proposed (Burke and Robinson, 2012). Such an interpretation would also help to reconcile the large differences between glacial ventilation ages observed in the deep Drake Passage corals (Burke and Robinson, 2012) versus the deep sub-Antarctic Atlantic (Skinner et al., 2010), which would reflect a large radiocarbon ventilation age gradient between AAIW and LCDW, rather than between UCDW and LCDW.

This consistency between shallow sub-surface reservoir ages in the EEP and the Atlantic- and Pacific sectors of the Southern Ocean would support the idea of the proposed link between these two regions through shallow sub-surface/intermediate waters transported by the EUC to the base of the EEP thermocline; an idea that has been advanced previously based on other records (Anderson et al., 2009; Calvo et al., 2011; Pena et al., 2008b; Spero and Lea, 2002). It is therefore proposed here that the variability seen in *N. dutertrei* from ODP1240 is primarily related to the changing Southern Ocean end-member signature that is being “upwelled” in (or at least transported to) the base of the EEP thermocline (where *N. dutertrei* lives), rather than to, for example, shifts in *N. dutertrei’s* habitat toward the Southern Ocean end-member, e.g. due to “more upwelling”. Nevertheless, it is underlined that this interpretation is not inconsistent with evidence for variable upwelling in the EEP, or indeed for changes in the contribution of southern sourced water in the EUC (Pena et al., 2013). Such changes would only exacerbate the impacts that have been inferred by making *N. dutertrei* experience sub-surface waters that are more similar to an “older/younger” Southern Ocean origin, even if the latter effect was the largest, as it is proposed here on the basis of the regional comparisons and associations shown in Figure 4.5 and the numerical model “thought experiment” illustrated in Figure 4.6.

Regardless of their dynamical associations, or indeed their causes, increased glacial surface/shallow sub-surface reservoir ages have been reconstructed across the South Pacific and Southern Ocean using a range of different approaches, including U-series dating of corals (Burke and Robinson, 2012), tephrochronology (Siani et al., 2013; Sikes et al., 2000; Skinner et al., 2015) and chronostratigraphic alignments (Skinner et al., 2010; this study), as well as radiocarbon “plateau tuning” records in the North Pacific (Sarnthein et al., 2013). Collectively, these observations challenge the common assumption of invariant reservoir ages, in particular at high latitudes but also in tropical upwelling areas, as it is emphasised here.

In addition to this general agreement of surface/shallow sub-surface reservoir age reconstructions, a broad similarity between deep ventilation age variability across the Equatorial and South Pacific as well as across the Southern Ocean is also apparent (Fig. 4.6d). Thus, B-Atm estimates from core ODP1240 indicate a significant glacial/interglacial change in radiocarbon ventilation, as also observed in the nearby core TR163-31B when the “regional radiocarbon calibration” implied by the chronology estimated here for ODP1240 is applied to the few available benthic radiocarbon dates from this core (Shackleton et al., 1988) (Fig 4.5d). Similarly, deep water ventilation changes observed in the SWP (Sikes et al., 2000; Skinner et al., 2015) and the SEP (Siani et al., 2013) all show a broadly similar deglacial trend compared to the EEP, as well as comparable B-Atm values. This coherence is highly significant, as it would confirm that a large volume of the ocean interior was indeed very poorly ventilated during the last glacial period; a proposition that has so far been supported by a paucity of data.

The modern deep South- and Equatorial Pacific is currently influenced by UCDW and/or PDW, which occupy similar density and depth ranges and are characterised by low oxygen, high nutrients and high ^{14}C age (Talley et al., 2011). A hydrographic/dynamical connection between the various ventilation age reconstructions compared in Fig. 4.5d is therefore entirely plausible; however it could be seen to conflict with the previous attribution of an AAIW association for core MD07-3088 from the SEP (Siani et al., 2013). Alternatively, the radiocarbon ventilation record from 1,536 m in the SEP (Siani et al., 2013) may in fact reflect the influence of deeper and older water masses such as PDW/UCDW, instead of AAIW as previously proposed (Siani et al., 2013). This speculation is supported by the fact that the SEP core MD07-3088 is currently located just at the boundary between AAIW and PDW. In any event, the deep-water radiocarbon ventilation ages from ODP1240 (this study), and other cores from the deep Eastern Equatorial- and South Pacific are all in good agreement with deep radiocarbon ventilation ages from core MD07-3076 from the sub-Antarctic Atlantic (Skinner et al., 2010) (Fig. 4.5d), which is consistent with a Southern Ocean source of deep waters to the deep Pacific.

4.5. **Conclusions**

In this chapter it is argued that even relatively small changes in B-P radiocarbon ventilation ages are relevant to the question of deglacial radiocarbon and carbon cycling, especially where these are observed over a large ocean volume like the Pacific. Furthermore, due to the possibility (indeed the likelihood) of significant changes in shallow sub-surface reservoir ages since the last glacial period, relatively small deglacial changes in B-P offsets may not necessarily rule out the occurrence of much larger changes in ocean interior radiocarbon ventilation, even in the low latitudes, as it is demonstrated here for the EEP. Indeed, the results presented in this thesis underline the crucial importance of constraining surface reservoir ages (or radiocarbon-independent calendar ages). Furthermore, these findings are found to be consistent with other surface- and deep water ventilation age reconstructions from the southern Pacific and Atlantic. This may reflect glacial circulation patterns that were not very different from modern, albeit with altered surface boundary conditions (air-sea exchange efficiency) in the Southern Ocean in particular, which it is identified here as the main source region for poorly ventilated deep glacial waters in the shallow sub-surface and deep EEP. These results have implications for the ocean's role in glacial-interglacial carbon cycling, demonstrating an increase in the Pacific Ocean's mean carbon residence time, which very likely would have contributed to lower atmospheric CO_2 during the last glacial period. Furthermore, it would appear that this change in the ventilation state of the glacial Pacific may have stemmed in large part from less effective ocean-atmosphere CO_2 exchange in the Southern Ocean in particular.

CHAPTER 5

5. B/Ca foraminifer analyses by LA-ICPMS

- **Subchapter 5.1: LA-ICPMS set up for B/Ca analysis**
- **Subchapter 5.2: Application of the LA-ICPMS method to down-core and core-top B/Ca analyses**

Synopsis

As mentioned in the previous Chapter 4, carbonate system proxies would offer valuable information to complement the ventilation inferences obtained from radiocarbon in the EEP over the last 30 kyr. In order to achieve this, B/Ca ratios from benthic foraminifer calcite shells, as a proxy for $\Delta[CO_3^{2-}]$ (and therefore $[CO_3^{2-}]$), are investigated here. The primary focus of this chapter is on the novel application of the LA-ICPMS technique in this field, and its comparison to the more commonly encountered solution-ICPMS method. This chapter is subdivided into two subchapters: Subchapter 5.1, which investigates the accuracy of the laser ablation analytical technique and assesses the best LA-ICPMS set up for the analysis of B/Ca ratios in foraminifera; and Subchapter 5.2, which discusses laser-ablation profiles obtained from the benthic foraminifer species C. wuellerstorfi and compare them with the values obtained on the same samples analysed by the solution-ICPMS technique. Subchapter 5.2 also shows core-top ”proxy calibration” analyses in C. wuellerstorfi and preliminary information on B/Ca distribution in the planktonic foraminifera N. dutertrei.

5.1. **Subchapter 5.1: LA-ICPMS set up for B/Ca analysis**

5.1.1. **Introduction**

Laser-ablation inductively-coupled-plasma mass spectrometry (LA-ICPMS) is a micro-analytical technique applied to many disciplines that permits the analysis of samples in a solid state at very high spatial resolution. Over the last decade, this technique has become more and more prevalent in the study of the trace element composition of foraminifer shells for paleoenvironmental reconstructions (Eggins et al., 2003; Hathorne et al., 2003; Pena et al., 2005; Raitzsch et al., 2011; Sadekov et al., 2009). The LA-ICPMS technique provides high-resolution depth profiling, offering accurate and precise measurements of a wide range of elements at very high spatial resolution, avoiding laborious cleaning procedures, and using only a few foraminifer specimens per sample (which depending on the species can be very valuable). The most noticeable advantage, however, is probably that this technique allows element distributions to be scrutinized on a single specimen through the calcite test ablation, thus providing information about biomineralization processes via their influence on trace element variability within a foraminiferal test (Anand and Elderfield, 2005; Eggins et al., 2004, 2003; Hathorne et al., 2003; Sadekov et al., 2008, 2005). It is important to constrain such intra-test composition variability in order to properly understand the relationship between the bulk chemistry of the test and the supposed environmental controls, which might be masked by significant “vital effects”, with implications for the accuracy of paleoenvironmental reconstructions.

However, a “handicap” that is usually found when using LA-ICPMS to analyse carbonate material stems from the need to match the sample material with the material used for analytical calibration, i. e. the standards (e.g. Hathorne et al., 2008). Ideally, calcite standards should be used in the context of foraminifer calcite analyses, but the chemical homogeneity of the available standard material remains poorly constrained (Hathorne et al., 2013). For this reason, glass standards are commonly used instead and, although in some cases they have been described to present matrix effect issues as well as isotopic fractionation, this problem seems to have been fixed by using laser systems with wavelengths of 193 nm (Hathorne et al., 2008; Jochum et al., 2012, 2007). In any event, the accuracy of the glass standards should be assessed for any analytical set-up by calibrating well-known material with these standards.

Among the elemental ratios in benthic foraminiferal calcite, the boron to calcium ratio (B/Ca) has been proposed to relate to the carbonate system, and more specifically the degree of carbonate ion unsaturation ($\Delta[CO_3^{2-}]$) (Yu and Elderfield, 2007). Foraminifer B/Ca ratios are therefore a potential tool for reconstructing past ocean carbonate unsaturation changes. However, B is found in very low concentrations in foraminifer shells and is a ubiquitous element, presenting challenges with respect to maintaining a sufficiently low instrumental B background and therefore maintaining good reproducibility of foraminifer analyses.

In this subchapter, the optimal conditions for foraminifer B/Ca measurements are set up by testing how different parameters (such as the type of tubing used to transfer the ablated material from the LA system to the ICPMS) may cause the instrumental B background to vary. Then, the accuracy of LA-ICPMS B/Ca measurements is assessed using glass standard materials. Finally, how such instrumental B background variations might have repercussions for paleoceanographic interpretations is assessed by analysing *N. dutertrei* specimens from ODP1240 (as this species is highly abundant in this core), by both LA-ICPMS and solution-ICPMS techniques in the same specimens.

5.1.2. **Material and methods**

5.1.2.1. **LA-ICPMS set up through standard material**

The RESOlution M-50 prototype 193 nm ArF laser ablation system coupled to an Agilent 7500ce ICPMS available at Royal Holloway University of London, UK (Müller et al., 2009) (see Figures in Chapter 2) has been used for B/Ca analysis in foraminifera. This analytical set-up (193 nm of wave length) minimises the possibility of element fractionation in trace elements like Boron (Hathorne et al., 2008; Jochum et al., 2007).

All the ablations were done at 2 Hz pulse rate, at a fluence of 4.4 J/cm^2 and were analysed for trace element abundances relative to Ca (^{11}B, ^{24}Mg, ^{25}Mg, ^{27}Al, ^{43}Ca, ^{55}Mn, ^{88}Sr, ^{89}Y, ^{138}Ba and ^{238}U), although with a primary focus on B/Ca ratios. The analyses were carried out under a Helium atmosphere and Argon was used as a carrier gas. An additional di-atomic gas was also applied to enhance the sensitivity (nitrogen or hydrogen) and, with the purpose of checking which of these two gases produced better sensitivity for the elements of interest, some tests were made. The system at Royal Holloway has a manifold coupled called “squid” that smooths laser pulses and is especially important for repetition rates lower than 10 Hz, as it is the case for foraminifer analysis (Eggins et al., 1998; Evans and Müller, 2013; Müller et al., 2009). All the instrumental operating conditions and the acquisition time for each isotope are summarised in Table 5.1.

National Institute of Standards and Technology (NIST) SRM 610 and 612 glasses were used as external standards for calibration using the concentration data from Jochum et al. (2011). In order to assess the standard accuracy and be able to select

Table 5.1. Instrumental operation conditions used in this study.

Laser parameters	
N_2/H_2 gas flow	6 ml/min
Fluence	4.4 J/cm^2
Repetition rate	2 Hz
Laser spot size	74-96 µm
ICPMS parameters	
Analysed isotopes (m/z) and acquisition time (s)	^{11}B (0.05), ^{24}Mg (0.03), ^{25}Mg (0.03), ^{27}Al (0.01), ^{43}Ca (0.02), ^{55}Mn (0.01), ^{88}Sr (0.005), ^{89}Y (0.01), ^{138}Ba (0.005) and ^{238}U (0.01)
RF power	~ 1,270 W
Carrier gas flow	0.45 l/min

the more appropriate NIST standard for the foraminiferal analyses, MPI-DING komatiite glasses GOR128 and GOR132 (Jochum et al., 2006) were also measured. Thus, GOR reference materials were treated as unknowns and calibrated with NISTs standards by using all possible combinations between unknowns-standards-spot sizes (e.g. GOR128-NIST612-96μm, GOR128-NIST610-74 μm, and so on).

Two types of tubing were used during different sessions in order to test its influence on boron instrumental backgrounds: the common Nylon tubing, which produced high B background conditions and signal/noise ratios between 4-15, and Nylon6 free of sulphur tubing (Nylon6 free-S), which achieved low B background conditions and ratios up to 100.

5.1.2.2. **Test-analyses in foraminifer calcite**

5.1.2.2.1. **Analysis by LA-ICPMS**

In order to test if the different background conditions might quantitatively affect B/Ca results in foraminifer calcite, 8-10 *N. dutertrei* specimens from nine ODP1240 samples were picked from fraction size 315-355 μm. Three samples (intervals 33, 89 and 223) were analysed under high background conditions (i.e. using common Nylon tubing), and six more samples (intervals 9, 45, 89, 129, 203 and 283) under low background conditions (i.e. using Nylon6 free-S tubing). All specimens were measured under the instrumental conditions described above and with a spot size of 74 μm, as this was considered a good balance for the depth profiling analysis in this species.

Before ablation, the individuals were rinsed in milliQ water (with no ultrasonication step as the specimens were too delicate) and secured on double-sided adhesive tape mounted onto glass slides (see Chapter 2). Samples were ablated for a maximum of 120 s with delays of 30 s between measurements, while NIST610/612 were ablated after ~ 6-8 samples for a duration of 120 s with delays of 40 s between measurements. Data reduction was carried out by using an Excel template, where shell surface enrichments were avoided, and the remaining data were "despiked" (to remove anomalous flyers), standardised with NIST glasses, checked for machine drift, and normalised to Ca. Further details about laser data reduction performed in this thesis can be found in the next subchapter 5.2.

5.1.2.2.2. **Analysis by Solution-ICPMS**

The specimens from most of the samples analysed by LA-ICPMS were removed from the double-sided tape after laser ablation, cleaned and analysed by solution-ICPMS. A quick test to check if the double-sided tape might bring any contamination to the solution-ICPMS measurements was performed by picking new individuals from the same sample vials (the same amount of individuals per sample), cleaned and analysed in parallel with the previously laser-ablated material. The cleaning procedure for solution-ICPMS analysis, carried out at the University of Barcelona (Spain), consisted of crushing all foraminifer tests between two clean glass slides, transferred to acid leached 0.5 ml Eppendorf vials and rinsed with MilliQ water and methanol in order to remove clays and other detrital material. The samples were then cleaned applying the "Oxidative" cleaning protocol (Barker et al., 2003) with a final weak acid leaching. The reductive step was not applied, as it has been shown to produce negligible effect on benthic B/Ca measurements (Yu and Elderfield, 2007; Yu et al., 2007a). Cleaned samples were dissolved in 0.1 M HNO_3 and centrifuged before analysis at the Godwin Laboratory for Palaeoclimate Research at the University of Cambridge (UK). The solution-ICPMS analyses were performed by both ICP-OES (Varian® VISTA) and ICP-MS (Thermo® Element XR). ICP-OES was used for calcium determination. In order to minimize instrumental memory effects and boron background contamination, ICP-MS was used to determine B/Ca at 10 ppm [Ca] in a matrix of nitric and hydrofluoric acid (0.1 M HNO_3 and 0.3 M HF) (Misra et al., 2014). The trace elements ^{7}Li, ^{25}Mg, ^{27}Al, ^{55}Mn, ^{87}Sr, ^{111}Cd, ^{137}Ba and ^{238}U were measured at Low Resolution (LR), ^{23}Na, ^{47}Ti, ^{55}Mn, ^{56}Fe, ^{66}Zn at Medium Resolution (MR) and ^{11}B and ^{43}Ca at both resolutions.

5.1.3. Results and discussion

5.1.3.1. Standard accuracy through LA-ICPMS

Accuracy was assessed over the course of 15 months (in 3 periods of time) by calibrating 18 analyses of the MPI-DING glasses GOR132 and GOR128 (taken as unknowns) to both NIST610 and NIST612 (through all possible combinations) measured under the same ablation conditions and using the reported values from Jochum et al. (2011) for NIST standard glasses. Two extra variables were also introduced in order to find the better accuracy for the elements of interest, as well as the most suitable standard for each element: 1) the use of two different additional di-atomic gases (N_2 and H_2), and 2) the use of two types of tubing. Thus, accuracy was estimated with Nylon tubing and N_2 (period 1), Nylon6 free-S tubing and N_2 (period 2) and Nylon6 free-S tubing and H_2 (period 3) (Fig. 5.1). The results are given as a percentage offset between the reported value from Jochum et al. (2006) for MPI-DING glasses and the mean value measured here (such as in Evans et al. (2013), i. e. the lower percentage the better accuracy.

As shown in Figure 5.1, a striking trade-off between the heaviest isotopes ^{138}Ba and ^{238}U *versus* the other elements is observed when using the Nylon6 free-S tubing (yellow and green bars). B accuracy highly improves when the new tubing Nylon6 free-S is used and under H_2 conditions. For Mn and Mg the largest change seems to depend on the type of NIST standard used. The use of H_2 clearly improves Mn accuracy. For Al, H_2 makes the accuracy slightly worse and for Mg, the result depends on the NIST used. Sr and Y accuracy is quite high in all cases.

It is therefore remarkable how the B accuracy improves when the new tubing is used, and how Mn accuracy is enhanced when the additional di-atomic gas H_2 is used (B accuracy is slightly enhanced in this case too). With the exception of Ba and U that accuracy gets worse, the rest of the elements hardly experience significant changes with the use of either the different tubing or gas. The reason why Nylon6

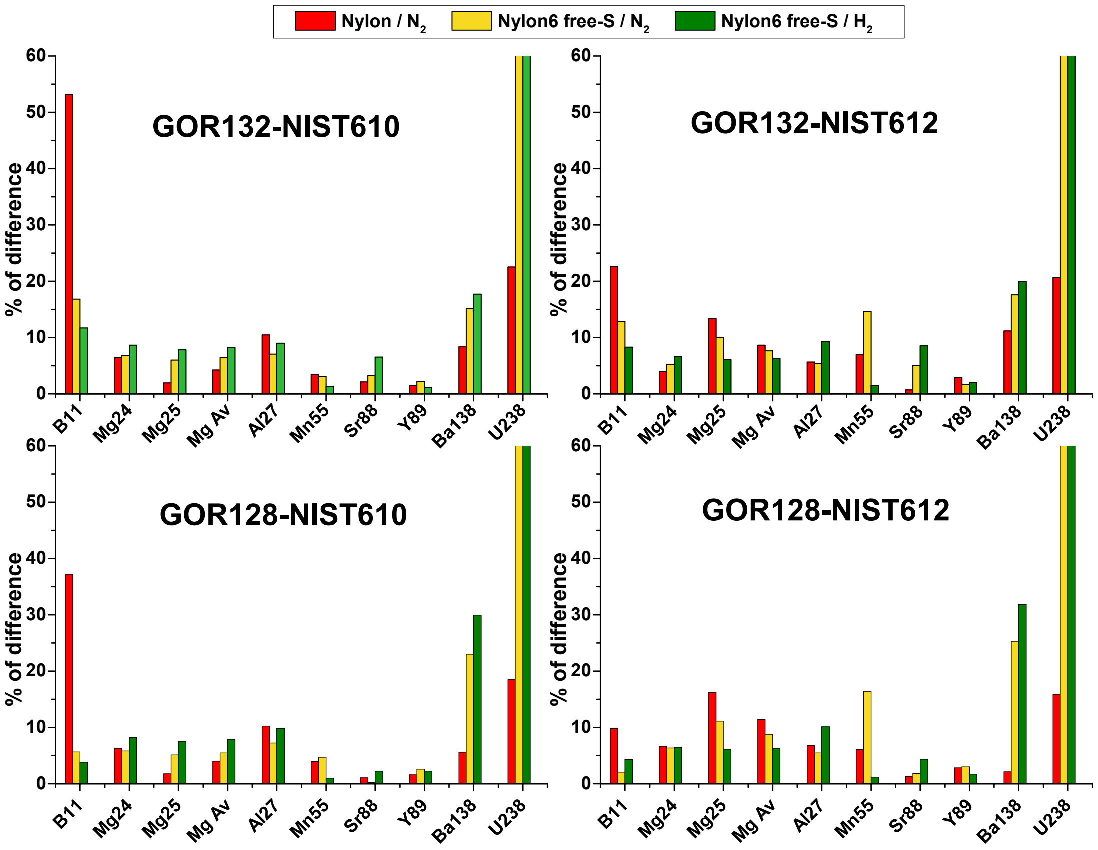

Figure 5.1. Standard accuracy assessment through MPI-DING komatiite glasses GOR128 and GOR132 standards (Jochum et al., 2006) used as unknowns and calibrated with NISTs standards glasses. All possible combinations between unknowns and standards, as well as the use of two type of tubings (common Nylon and Nylon6 free-S) and two type of gases (N_2 and H_2), are shown.

free-S tubing improves B accuracy seems to be related to the fact that lower S background also decreases the background of other volatile elements like B (Evans et al., unpublished). Why U and Ba accuracy increases so badly with the use of Nylon6 free-S tubing is for now not constraint. Mn accuracy improves when using H_2 instead of N_2 as the additional di-atomic gas because: 1) H_2 suppresses the high instrumental Mn background, thus obtaining better signal to noise ratios, and 2) the ^{55}Mn isotope suffers from ^{40}Ar^{15}N interference (Evans et al., 2015). These results demonstrate the suitability of glass standards in calcite analysis when using a 193 nm laser device, as the accuracy for most of element/Ca ratios is better than 5% (also reported by Evans et al., 2015). The recommended standards for each element and corresponding accuracy are shown in Table 5.2.

Table 5.2. Laser spot analysis data accuracy (mean deviation from reported values ±2SD) for 74-96 µm spot sizes (n=18). NIST standard concentration data taken from Jochum et al. (2011).

Element/Ca	Accuracy ± 2SD (%)	MPI-DING glass	Recommended calibration standard
B/Ca	3.8 ± 3.1	GOR128-G	NIST612
Mg/Ca	6.3 ± 9.2	GOR128-G	NIST610
Al/Ca	9.0 ± 3.9	GOR132-G	NIST612
Mn/Ca	1.0 ± 1.2	GOR132-G	NIST610
Sr/Ca	2.2 ± 1.0	GOR132-G	NIST612
Y/Ca	1.1 ± 3.2	GOR128-G	NIST610
Ba/Ca	17.7 ± 6.7	GOR128-G	NIST612
U/Ca	70.3 ± 19.6	GOR128-G	NIST612

5.1.3.2. **The importance of boron instrumental background conditions**

Three *N. dutertrei* samples (intervals 33, 89 and 223) from ODP1240 were measured using the common Nylon tubing, which produced high B instrumental background conditions, and six samples (intervals 9, 45, 89, 129, 203 and 283) were analysed using Nylon6 free-S tubing, which produced low B instrumental background conditions. Figure 5.2a shows how this different B background translates into apparent anomalous B/Ca ratios, as the values significantly deviate from the measurements done when the B background was much lower by using Nylon6 free-S tubing. These differences cannot be apparently explained by changes in the hydrographic or climatic conditions experienced by the foraminifera. On the one hand, *N. dutertrei* specimens from interval 89 mcd (green circle in Fig. 5.2a) that were measured under both background conditions, show very different values in each case, consistent with the type of tubing used in each case. On the other hand, when comparing all the laser results performed here with solution-ICPMS analysis made on the same specimens once they were removed from the double-sided tape after ablation, the same issue is revealed (Fig. 5.2a). As observed in this figure, these techniques do not necessarily produce quantitative comparable results (which will be discussed in the next subchapter 5.2). However, they give us an idea of the element/Ca variation between intervals within each technique, which clearly confirms that the intervals measured under high B laser instrumental background conditions are anomalous.

A solution-ICPMS cross-plot between the samples removed from the double-sided tape after ablation and the same amount of specimens per sample picked again from

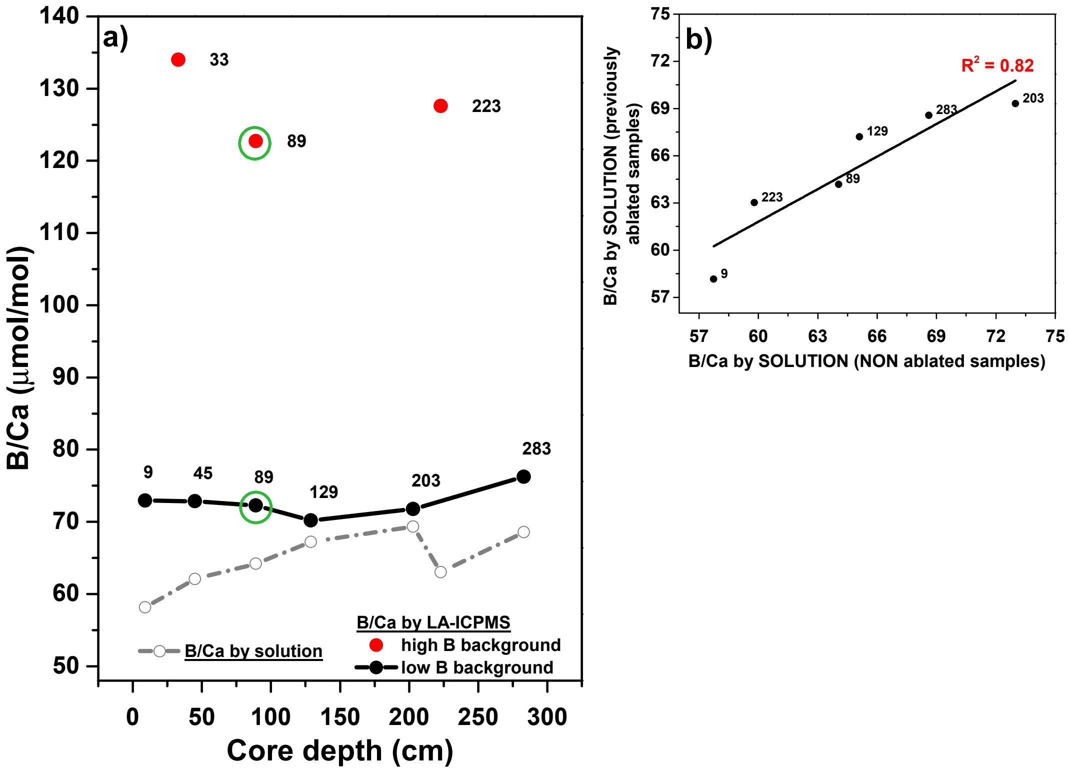

Figure 5.2. a) B/Ca data analysed by LA-ICPMS and solution-ICPMS in *N. dutertrei* from ODP1240. Intervals measured by LA-ICPMS using the common Nylon tubing (red dots) and using the Nylon6 free-S tubing (black line-dots), which produced high and low instrumental B background, respectively. Solution-ICPMS measurements performed in the same individuals of each sample are displayed at the bottom of the panel (grey dashed line-hollow circles). Same specimens from depth interval 89 (green circle) were measured under both laser instrumental background conditions. b) Solution-ICPMS B/Ca cross-plot between samples removed from the double-sided tape and new specimens picked again from the vial.

the vial (all of them cleaned and analysed by solution-ICPMS in parallel), reveal an excellent correlation ($R^2 = 0.82$) (Fig. 5.2b). This suggests that no major effect results from removing the specimens from the double-sided tape, and therefore, that the comparison made here between LA- and solution-ICPMS techniques is feasible.

This example demonstrates that, due to the very low B concentrations in foraminifera, B analysis in this context requires strict contamination controls (Rae et al., 2011), including the maintenance of very low ICPMS boron background levels.

5.1.4. **Conclusions**

The results presented in this subchapter support overall the suitability of the 193 nm laser and NIST glasses for B/Ca measurements (Hathorne et al., 2008; Jochum et al., 2012, 2007).

The use of different tubing and gases shows that B accuracy highly improves when the new tubing Nylon6 free-s is used, and Mn accuracy is largely enhanced when the additional di-atomic gas H_2 is applied. The rest of the elements hardly experience significant changes, with the exception of Ba and U whose accuracy largely decrease with the new tubing, indicating that not all these elements can be targeted within a single study.

In a practical application to real calcite samples, B/Ca measurements performed under high B background by the use of common Nylon tubing fall far away from the results obtained using Nylon6 free-S tubing, which are supported by solution-ICPMS analysis of the same specimens. No effect from the double-sided tape is observed in solution analysis, which encourages the use of this practice to measure several proxies over the same individuals.

In conclusion, the use of Nylon6 free-S tubing and H_2 gas, as well as the calibration with the NIST612 standard are recommended for B/Ca analysis by LA-ICPMS and therefore, they are applied from now on in this thesis.

5.2. Subchapter 5.2: Application of the LA-ICPMS method to down-core and core-top B/Ca analyses

5.2.1. Introduction

The theory of the B/Ca as a proxy for [CO_3^{2-}] is rooted in the dissolved boron species in seawater and their relative concentrations and isotopic composition dependence on pH (Hemming and Hanson, 1992), as explained in Chapter 2. As seawater pH is a function of alkalinity (ALK) and dissolved inorganic carbon (DIC) and is also closely related to seawater pCO$_2$ and [CO_3^{2-}], B/Ca reconstruction seems to be a potential tool to reconstruct the past carbonate system in the ocean (see Chapter 2 for further details).

Thus, over the past few years, B/Ca ratios in benthic foraminifera have been widely analysed and empirically proved to relate with deep water carbonate saturation state with respect to calcite (Δ[CO_3^{2-}]), allowing carbonate ion concentration [CO_3^{2-}] to be inferred (Allen et al., 2015; Rae et al., 2011; Raitzsch et al., 2011; Yu and Elderfield, 2007; Yu et al., 2013). The benthic epifaunal species *C. wuellerstorfi* has been analysed and used in B/Ca-Δ[CO_3^{2-}] calibration analysis, fundamentally by solution-ICPMS (Allen et al., 2015; Brown et al., 2011; Rae et al., 2011; Yu and Elderfield, 2007; Yu et al., 2013), but also by LA-ICPMS (Raitzsch et al., 2011). The calibration equations produced from both techniques (Raitzsch et al., 2011; Yu and Elderfield, 2007) seem to be in good agreement. However, these linear regressions indeed permit a large range of B/Ca values (~30 µmol/mol) for a given Δ[CO_3^{2-}], thus allowing possible B/Ca differences between techniques to be masked.

This might suggest that a more careful investigation of B/Ca values obtained from both techniques is required to assess the reliability and comparability of [CO_3^{2-}] inferences based on each method. It would also suggest that more “calibration” analyses are needed on core-tops, sediment traps and/or culture experiments, especially via LA-ICPMS.

Despite promising and consistent results for B/Ca in benthic foraminifera as a proxy for [CO_3^{2-}], planktonic B/Ca results have proven more difficult to establish as a proxy. Most of the B/Ca studies in planktonic foraminifera have consisted of culture experiments varying both physical and chemical seawater conditions, resulting in conflicting results between species and ambiguity regarding the hydrographic variable that B/Ca in planktonic foraminifera might represent (Allen and Honisch, 2012; Allen et al., 2012, 2011; Yu et al., 2007b). However, little has been done to look at the B/Ca distribution within the planktonic foraminifer shell, despite the fact that this might help to reveal some reasons of the conflicting results.

This subchapter focuses on the incorporation of B along the foraminifer calcite shell (i.e. chamber by chamber, across the foraminifer's lifetime), investigated by LA-ICPMS in the benthic species *C. wuellerstorfi* from sediment core ODP1240 located in the Eastern Equatorial Pacific (EEP). These samples cover the last glacial/ interglacial transition (results that will be palaeoceanographically interpreted and discussed in the next Chapter 6) and are further analysed by solution-ICPMS technique so the consistency between techniques can be compared. Core-top *C. wuellerstorfi* samples from various locations in the Atlantic Ocean are also analysed by LA-ICPMS with the purpose of adding more data points to the existing calibrations. Finally, preliminary information from the B/Ca distribution in a planktonic foraminifer species, *N. dutertrei* is also presented. This species has been poorly studied so far from a B/Ca perspective (Dai et al., 2016; Foster, 2008), and is investigated here by using the six ODP1240 samples analysed by both techniques (laser- and solution-ICPMS) and discussed in subchapter 5.1.

5.2.2. **Material and methods**

5.2.2.1. **LA-ICPMS analyses: Material, analytical technique and data reduction**

Between three and six *C. wuellerstorfi* specimens from each of the 15 downcore samples selected from sediment core ODP1240 and two to nine specimens from nine core-top samples (Table 5.3) were picked from the >212 μm size fraction and drilled with a 96 μm spot size. For *N. dutertrei,* as described in subchapter 5.1, 8-10 specimens from six ODP1240 samples were picked from the 315-355 μm size fraction and drilled with a 74 μm spot size. Samples were ablated for a maximum of 200 s and 120 s for *C. wuellerstorfi* and *N. dutertrei*, respectively, with delays of 30 s between measurements in both cases, and applying the analytical setup described in subchapter 5.1 (using H_2 as additional di-atomic gas and Nylon6 free-S tubing).

Table 5.3. Core-top sample information. A location map can be seen in Figure 5.8 below.

Region and Cruise	Site/Station	Latitude	Longitude	Depth (m)
Artic				
HERMIONE-ARTIC	stC	77˚14.90' N	09˚30.98' E	2,011
	stE	76˚22.67' N	14˚35.72' E	615
North Atlantic				
CATARINA-PALEOACID	KTA-CG-01	52˚06.38' N	42˚51.67' W	4,147
	KTA-BC-02	54˚34.96' N	39˚07.53' W	3,002
	KTA-BC-03	45˚26.39' N	34˚33.14' W	4,014
	KTA-BC-05	46˚11.16' N	18˚18.83' W	3,938
Iberian Margin				
JC089	JC089-03-SHAK-03-3B	37˚42.54' N	10˚29.56' W	3,731
	JC089-11-SHAK-11-9B	37˚51.51' N	09˚20.14' W	618
South West Atlantic				
GEOTRACES	st10	29˚ S	35˚ W	3,879

that elevated Al could indicate contamination by aluminosilicates (clays), as has been done in previous studies of Mg/Ca in planktonic foraminifera, although with a lower contamination threshold, as planktonic species are usually less susceptible to Al incorporation (Bolton et al., 2011; Boyle, 1983; Marr et al., 2011).

Once the data reduction has been done for the whole data set, a last step to screen

Several steps to reduce the data by removing any contaminant phase were applied after using an Excel template to “despike”, standardise with NIST glasses and normalise data to Ca. Thus, the first step of the data reduction process, and an advantage when using laser ablation, is to eliminate the surface enrichments of the shells. Apparently, this contamination is either adhered onto the outer part or goes into the pores once the specimens are dead (Reichart et al., 2003), or it could also be an original part of the shell as has been observed in samples from sediment traps that were never deposited or incorporated into the sediments (Hathorne et al., 2009). Regardless of their origins, these surface enrichments are a potential factor to bias measurements away from those representative of pure foraminiferal calcite, and therefore to bias paleoenvironmental inferences if they are included in the final averages.

A second step of data reduction is to select the segment of the profile suitable for integration. In this thesis two approaches have been applied: 1) selecting the part of the profile with constant calcium (hereafter referred as “flat calcite” approach) and, 2) selecting also the part of the ablation that presents a progressive element intensity decrease, as long as it does not correspond to the ablation of another material rather than foraminifer shell, such as the tape or the glass slide indicated by very noisy element signals (hereafter referred as “whole ablation” approach). The decrease in element intensity along the ablation is a typical feature in laser ablation analysis since the material extraction becomes harder as ablation depth increases, and it is commonly excluded from integration (retaining only the part of the ablation that present “flat calcite”), as it might potentially produce isotopic fractionation and/or might alter the element/Ca ratios by triggering a variation in the volatility of the different elements. However, as solution-ICPMS analyses are made by using whole specimens, long ablations have been performed in this thesis so that different profile integrations can be further compared between techniques.

The next step of this process consists of discarding the profile segment from each analysis with Al/Ca ratios higher than 500 µmol/mol, even when this restriction might imply disregarding a whole profile. This criterion is based on the premise for potential contaminant phases that might exclusively bias B/Ca estimates would consist of removing all chambers with B/Ca that are higher than the interval average plus 2SD, defined as outliers (Evans and Müller, 2013). This is on the premise that outliers may occur as a result of effects additional to or independent of aluminosilicate contamination specifically.

The final suitable profile segments selected for integration are then averaged by chamber, then by specimen and finally by sediment interval for subsequent palaeoreconstructions, which are discussed in Chapter 6.

5.2.2.2. **Solution-ICPMS analyses**

The *C. wuellerstorfi* individuals from 12 of the 15 ODP1240 samples analysed by LA-ICPMS at RHUL were removed from the double-sided tape, cleaned by using the "oxidative" approach at the University of Barcelona, and analysed by solution at the University of Cambridge, as described in Subchapter 5.1 for *N. dutertrei*. The *N. dutertrei* samples used in subchapter 5.1 are also screened here.

5.2.3. **Results and discussion**

5.2.3.1. **Downcore B/Ca measurements in *C. wuellerstorfi***

C. wuellerstorfi chambers are typically narrow and contain low B concentration. This fact initially invited the use of a 96 μm spot size for ablation, which covered parts of the shell rather than single chambers. The nomenclature adopted for each ablation in every specimen is the commonly used in these type of studies, which is related to the direction of shell growth and goes from the foraminifer's youngest chamber (*f*, from the "final" chamber that was built) towards the foraminifer's oldest chamber (*f-X*, where the larger the X, the older the chamber). Thus, two to three depth profiles were performed per shell in this species: one on the oldest part (*f-2*), one on the middle (*f-1*) and one on the youngest part (*f*) of each individual. They will be referred to as “chambers” in this species from now on, as they are not real chambers (Fig. 5.3a).

5.2.3.1.1. **Element laser profiles and intra-/inter-“chambers” variability**

Figure 5.3b displays representative examples of the trace element depth profiles across three “chambers” of two *C. wuellerstorfi* specimens from ODP1240, where different thickness between chambers is observed (the older the chamber, the thicker the wall and vice versa) due to the bilamellar type of growth of this species, where a new layer of material is secreted over all existing chambers when a new chamber is formed (Saraswati and Srinivasan, 2015). Surface enrichments are present in all samples and are especially visible for ^{27}Al, ^{55}Mn and ^{238}U and less pronounced for ^{24}Mg and ^{25}Mg (Creech et al., 2010; Eggins et al., 2003; Pena et al., 2005; Reichart et al., 2003; Sadekov et al., 2008). However, ^{11}B surface enrichments are hardly perceptible, as also reported by Hathorne et al. (2009) for several planktonic foraminifera. They are not observed for ^{88}Sr either. In any event, they were always removed before data integration.

The remaining element signals across the shell generally present regular profiles, with the exception of Al (and other elements like Mg or U that follow Al trends in some cases) that, depending on the specimens, may present internal variations. B signal, although generally relatively flat, and therefore suggesting that is not affected by other trace element’s incorporation, seem to consistently present a “bump” across the profile, specifically in the oldest “chamber”, which is also the thickest one, and therefore represent the whole period of life of each specimen.

The progressive element intensity decrease typical from laser ablation analysis is observed in this study. The two data reduction approaches applied in this thesis, “flat calcite” and “whole ablation”, correspond to the integration of around 3-10 µm and 16-32 µm, respectively, as the ablation depth per second is ~0.16 µm

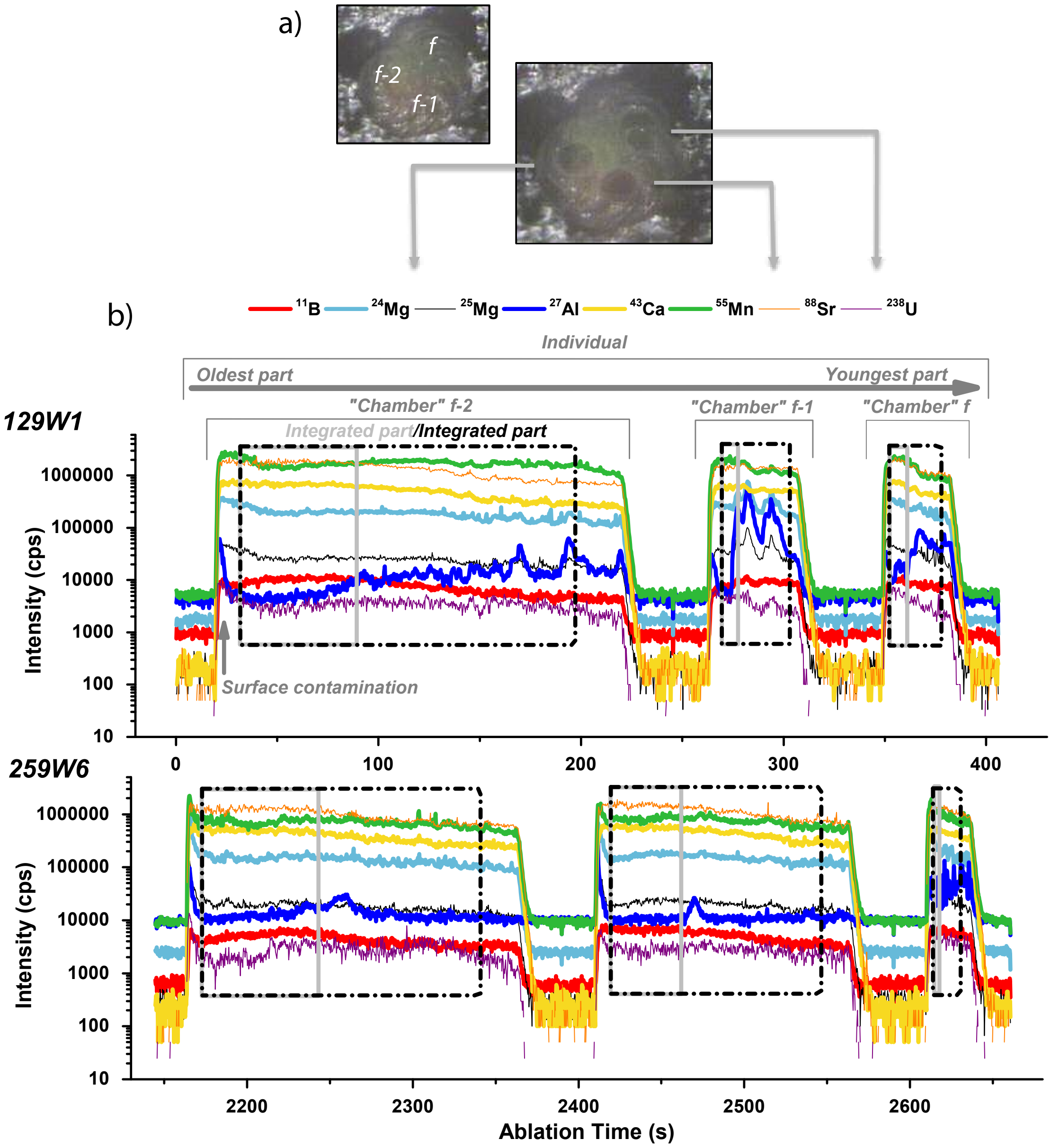

Figure 5.3. Illustration of laser ablation approach in *C. wuellerstorfi*. a) *C. wuellerstorfi* specimen before and after ablation displaying the nomenclature used in this thesis. b) Trace element profiles across the foraminifer shell of two *C. wuellerstorfi* individuals (129W1 and 259W6), displaying three "chambers" per specimen. The two approaches applied in this thesis for selecting the segment to integrate are shown by black ("whole ablation") and grey lines ("flat calcite"), both removing the surface enrichments.

(Fig. 5.3b). In Figure 5.4, the resultant integrated segments of B related to Ca from "chambers" displayed in Figure 5.3 can be seen for both approaches. Intra-chamber

B/Ca variability of any "chamber" is between 12-13% for both approaches, representing much lower variability than previous reported LA-ICPMS measurements in this species (Raitzsch et al., 2011: ~40% of intra-chamber variability). The "bump" observed in B profiles in the thickest "chambers" in Figure 5.3 is translated into a cyclical B/Ca rise and drop in the case of the "whole ablation" approach and only the first rise (or part of it) in the case of the "flat calcite" approach, where a shorter part of the profile is selected (Fig. 5.4). If the consistently observed cyclical B/Ca rise and drop in the oldest-thickest "chamber" reflects composition changes associated with bilamellar growth of the *Cibicides* genus on either side of an equatorial plane (towards dorsal and ventral faces; Saraswati and Srinivasan, 2015), then a long ablation at this spot might cover not only one "chamber", but also some other "primary chambers" underneath. If this is correct, this would reflect an interesting decreasing pattern in B incorporation as the chamber is built (in both

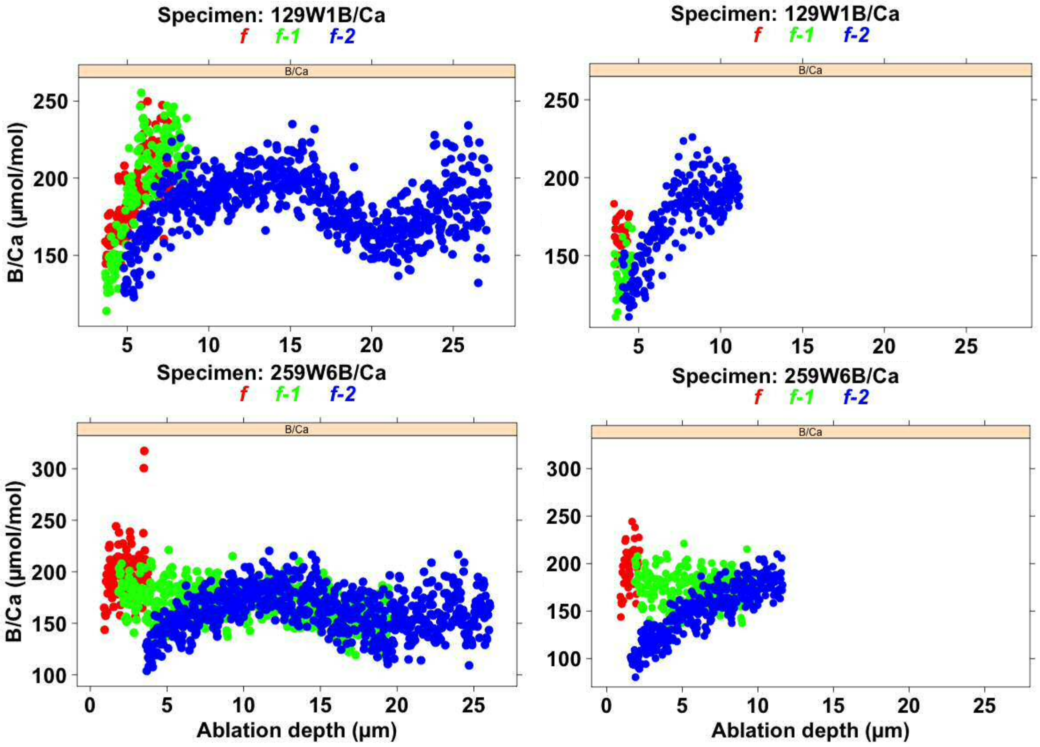

Figure 5.4. LA-ICPMS B/Ca profiles for selected segments of two *C. wuellerstorfi* specimens' "chambers". a) and c) "Whole profile" approach. b) and d) "Flat calcite" approach. Colours represent the different "chambers" of one specimen, from the oldest (*f-2*) to the youngest (*f*).

dorsal and ventral directions), that might be due to changes in the microenvironmental conditions, but more likely due to ontogenetic processes. Elucidating these is beyond the scope of this study. However, as B/Ca has been empirically proved to relate to $\Delta[CO_3^{2-}]$, what it is interesting here is how this feature might modify the final average values between approaches, as only part of the dorsal face is usually integrated when taking the “flat calcite” approach.

Besides the intra-“chamber” variability, the B/Ca composition between different “chambers” (or inter-chambers) also present some differences, with a gradient from low to high B concentrations (in average) as you move from the oldest part of the shell (*f-2*) to the youngest part (*f*) (Fig. 5.5a). Note that this way of showing the “chambers” trend is not ideal, as it includes individuals from different sediment depth and therefore “chambers” variability and potential climatic/hydrographic signals might conflated (e.g. higher B/Ca from “chambers” *f-2* in the Holocene period might be coincident with lower B/Ca from “chambers” *f* during the glacial). However, the few “chambers” analysed in each specimen does not allow for a more representative inter-chamber comparison within intervals. Despite of this, Figure 5.5 gives us an idea of the inter-“chamber” trends in this species, which is actually supported by an unpublished study focused on inter-(real) chamber comparison (Kerr et al., unpublished) that shows the same variability range and trend, from lower to higher B/Ca ratios along the chambers formation.

When looking at other trace elements, a similar trend between “chambers” is also found in Al/Ca ratios, which also display higher values from *f-2* towards *f* (Fig. 5.5b), while Mg/Ca and Mn/Ca ratios hardly differ between “chambers” (Fig. 5.5c and d, respectively). B/Ca does not correlate with Mg/Ca or Mn/Ca, and despite the fact that B/Ca presents a similar pattern to Al/Ca along the foraminifer shell, it does not exhibit a significant correlation across the shell walls nor between “chambers” ($R^2 = 0.1$) (also pointed out by Rae et al. (2011) and Yu and Elderfield (2007) in bulk analysis).

This indicates that, in principle, the reason for an apparent B/Ca gradient between

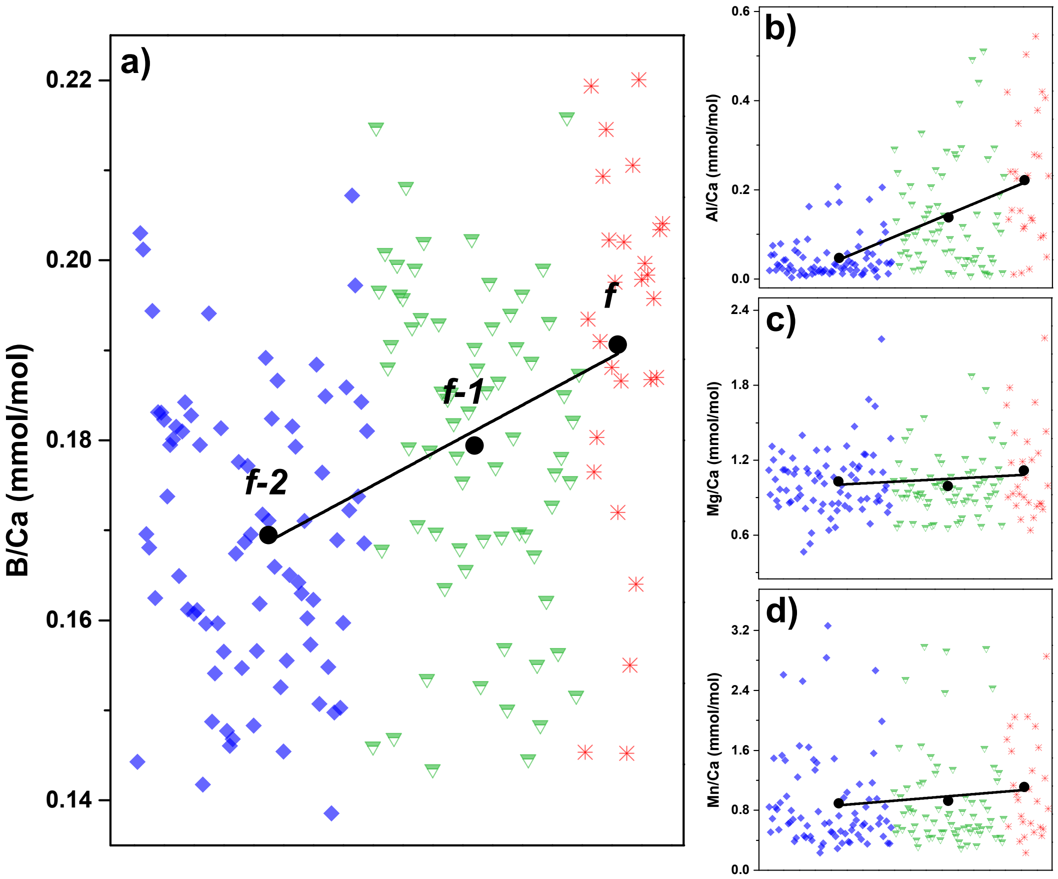

Figure 5.5. Element/Ca per "chamber" for all *C. wuellerstorfi* measured in this thesis. a) B/Ca, b) Al/Ca, c) Mg/Ca, d) Mn/Ca. Colours represent the different "chambers", from the oldest (*f-2*) to the youngest (*f*). Black dots represent the average element/Ca ratios for each type of "chamber". Black line indicates the trend in element/Ca ratios through shell growth.

"chambers" might be attributed to "natural" changes, either micro-environmental or ontogenetic and that B/Ca ratios are not biased by diagenetic coatings or silicate contamination in this species. However, it should be pointed out that the youngest "chamber" (*f*) typically contains very high Al and often B, indicating a higher susceptibility of this youngest "chamber" to authigenic coatings or metal adsorption. This is important since the rejection of many of these last "chambers" for further integration due to either a higher than 500 µmol/mol of Al/Ca content or a higher 2SD B/Ca bias will affect the B/Ca final average.

A slight significant correlation is consistently found between Mg/Ca and Mn/Ca (R^2 = 0.3). This has been pointed out before in this EEP area, as a result of the existence of Mn-Mg-rich phases in the foraminifera shell, that prevents the reconstruction of accurate temperature records using the Mg/Ca-palaeothermometer, unless the reductive cleaning method is applied (Pena et al., 2008a, 2005).

5.2.3.1.2. **Comparison between laser and solution analyses**

A comparison between laser- and solution-ICPMS B/Ca analyses is shown in Figure 5.6. The results between approaches and techniques are quantitatively different, with higher B/Ca values obtained by solution and lower values by the LA-ICPMS "flat calcite" approach. Between the two LA-ICPMS approaches applied in this thesis, the "whole ablation" approach better represents the common solution analysis, both in shape and magnitude. In terms of magnitude this might be expected, as a greater part of the shell is included in the total average. Importantly, this would suggest that isotope fractionation and/or differences in element volatilities in deep laser ablations is not an issue when using LA-ICPMS for B/Ca studies. In terms of shape, with the exception of a few intervals, an intriguing constant offset is observed between solution- and laser "whole ablation" approach measurements (Fig. 5.6).

What are the reasons for such a consistent offset between techniques? Firstly, it seems it cannot be attributed to the rejection of outliers, as the resulting curve is, in both approaches, nearly identical to that given by the curve including them, as only some "chambers" lie beyond the 2SD range of its respective interval in both approaches. An obvious and simple reason for the offset observed might be the type of standard used as, apparently, the use of NIST standards instead of calcite in LA-ICPMS analysis usually gives results less consistent with solution-ICPMS measurements (Hathorne et al., 2003). However, another possible reason for this consistent offset (as this study points out) is the removal of many of the final "chambers" during the data reduction of LA-ICPMS analyses, or at least part of them, due to the high Al content (which is usually coincident with higher B/Ca

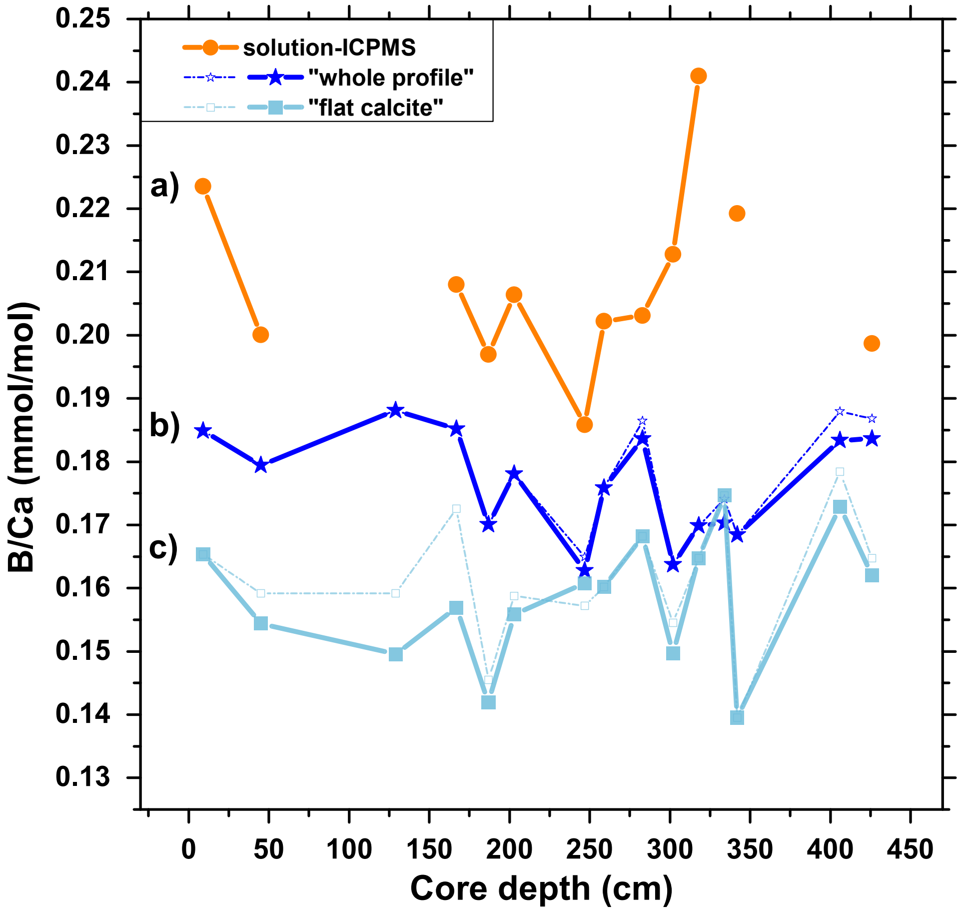

Figure 5.6. B/Ca comparison between the two data reduction LA-ICPMS approaches and solution analysis of the same *C. wuellerstorfi* samples downcore. a) Solution-ICPMS. b) “Whole ablation” approach. c) “Flat calcite” approach. Dashed and thick solid lines in b) and c) indicate data with and without outliers, respectively. Note that not all the intervals measured by LA-ICPMS were also measured by solution.

ratios). These final “chambers” are thinner than the rest, but also represent a large area of the shell, and solution-ICPMS analysis includes them all in the final average. This fact, therefore, might increase the final values obtained by solution creating the offset observed between both techniques. In other words, solution-ICPMS measurements would consistently include high-B/Ca final “chamber” calcite (which would have to be offset by a constant amount relative to the rest of the tests), while LA-ICPMS measurements would omit these. In support of this idea, interestingly, the largest discrepancies between solution and LA-ICPMS “whole ablation” approach measurements are precisely the ones with higher Al/Ca ratios in solution, with the exception of one value that has no apparent explanation (Fig. 5.7). Indeed, the B/Ca value from 9 cm obtained by solution would be rejected as it contains extremely high Al/Ca. However, the other two intervals would be around the "Al/Ca rejection limit" depending on the analyser, as it is often 500 µmol/mol. With such a rejection limit, these intervals might be retained, resulting in large differences in the interpreted B/Ca data. Considering the LA-ICPMS results, values higher than 200 µmol/mol Al/Ca should be discarded in solution analysis as this could largely bias the final results (Fig. 5.7). A high correlation (R^2 = ~0.7) between techniques is found when the "anomalous" solution values are not taken into account.

Several questions arise from these analyses. If laser "whole ablation" approach measurements present a consistent offset from solution measurements due to the rejection of final "chambers" with high Al content, would this mean that, 1) solution measurements are overestimating the proxy by including "contamination", or 2) the Al contamination threshold for LA-ICPMS should be higher than 500 µmol/mol, or 3) if the offset is constant, is a method-specific calibration for LA-ICPMS measurements needed to achieve quantitatively comparable [CO_3^{2-}] estimates from both techniques? Other questions regarding why the "flat calcite" approach also exhibits an offset from solution measurements, albeit less constant than for the "whole ablation" approach, would be: are these data even "cleaner" and therefore more correct; and if so, such that only the outer portion of the wall is needed for the B/Ca proxy, why would this be? All these questions cannot be addressed in this study, but they raise interesting issues to take into account when applying both solution- and LA-ICPMS techniques to paleoceanographic studies.

When looking at other elements, Mg/Ca measurements are consistent between techniques (albeit with a corresponding offset), and seem to exhibit no association with other elements (Fig. 5.7). Notably, a good relationship between Mn and U, both of which are often associated with diagenetic incorporation, is observed using both techniques, Mn/Ca ratios in particular. Despite the offsets found between techniques in almost all elements, which demand careful attention if absolute

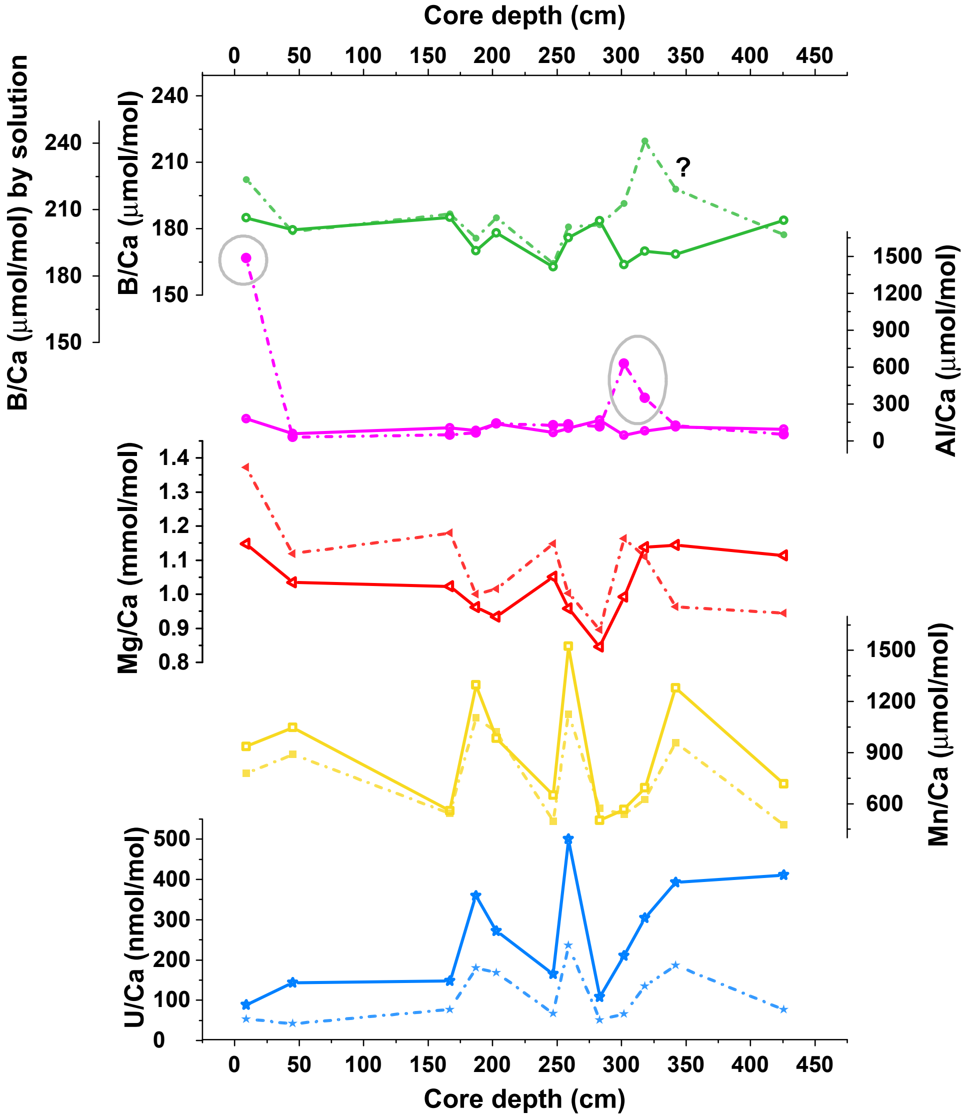

Figure 5.7. Comparison of element/Ca ratios between LA-ICPMS "whole ablation" (solid lines) and solution-ICPMS (dashed lines) in *C. wuellerstorfi*. Grey circles indicate intervals where B/Ca measurements disagree between techniques, which correspond to high Al/Ca values in solution. The question mark (?) indicates the only sample with a mismatch between laser and solution analysis that cannot be explained by contamination of solution analyses. Note the displacement of the y-axis in the upper panel.

values need to be compared (e.g. when applying calibrations; see next section), these results indicate a good qualitative consistency between techniques and thus provide confidence in LA-ICPMS trace element analysis in foraminifer shells.

5.2.3.2. ***C. wuellerstorfi* B/Ca core-top results**

Nine Atlantic core-top samples of *C. wuellerstorfi* were analysed for B/Ca by LA-ICPMS (Fig. 5.8). In light of the down-core B/Ca results, the "whole profile" approach was selected and outliers > 2SD from the mean were removed, for maximum consistency with solution analyses. Core-tops above the first 2,000 m water depth show higher B/Ca ratios than those between 3,000-3,500 m. B/Ca ratios moderately increase back between 4,000-4,500 m. These results are consistent with the $[CO_3^{2-}]$ distribution along the Atlantic Ocean (Key et al., 2004).

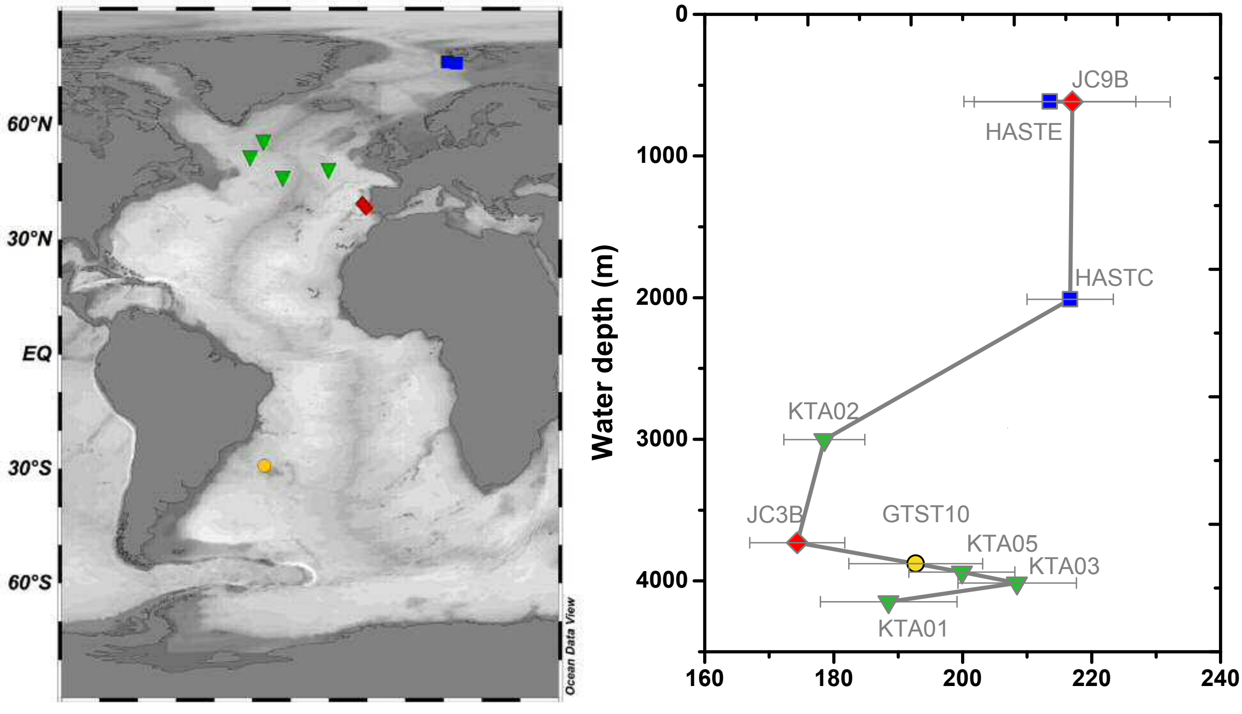

Figure 5.8. *C. wuellerstorfi* core-top B/Ca (±2SE) *vs* water depth (right panel) from several locations in the Atlantic Ocean (left panel) analysed in this thesis.

Modern carbonate ion saturation state ($\Delta[CO_3^{2-}]$) was estimated as the difference between modern in situ $[CO_3^{2-}]$ and the modern $[CO_3^{2-}]$ saturation ($[CO_3^{2-}] - [CO_3^{2-}]_{sat}$), where $[CO_3^{2-}]_{sat}$ is equivalent to modern $[CO_3^{2-}]$ divided by the modern saturation state for calcite ($[CO_3^{2-}]/\Omega_{calcite}$). $\Omega_{calcite}$ is $[Ca^{2+}] \bullet [CO_3^{2-}]/K_{sp}$, where K_{sp} is the solubility constant of calcite at a given temperature and pressure and $[Ca^{2+}]$ is often suppressed as it is usually considered constant in seawater at these timescales (Zeebe and Wolf-Gladrow, 2001). Thus, the general equation is the following:

$$\Delta[CO_3^{2-}] = [CO_3^{2-}] - ([CO_3^{2-}]/\Omega_{calcite}) \qquad (1)$$

Estimates of $\Delta[CO_3^{2-}]$ were obtained using the CO2SYS software package (Lewis et al., 1998; Pierrot et al., 2006) and either data from the corresponding cruises when available, or else data from nearby Global Ocean Data Analysis Project (GLODAP) sites (Key et al., 2004); in both cases by deriving values for $[CO_3^{2-}]$ and $\Omega_{calcite}$ (Table 5.4).

Table 5.4. Seawater chemistry data for the B/Ca-$\Delta[CO_3^{2-}]$ core-top calibration. CO_3^{2-} and Ω_C have been estimated by using CO2SYS (Lewis et al., 1998; Pierrot et al., 2006) with seawater data from: * GLODAPv2 (HA-stC: 58GS20090528 transect; station 290; 1,970 m; HA-stE: 77DN20020420 transect; station 9; 640 m); **CATARINA cruise data; *** BD3 cruise data (1989); ****GLODAP data (WOCE A17 transect data; station 23075B in A17; 3,935 m).

Core name (in this study)	Water depth (m)	AVE B/Ca (µmol/mol)	SD B/Ca (µmol/mol)	SE	Aprox depth m	$[CO_3^{2-}]$ (µmol/kg)	Ω_C	$[CO_3^{2-}]_{sat}$ (Ω_C)	$\Delta[CO_3^{2-}]$ (Ω_C)
Artic									
HA-stC *	2,011	216.7	34.8	6.7		98.1	1.54	64	34
HA-stE *	615	213.5	46.2	13.3		116.1	2.43	48	68
N Atlantic									
KTA-01 **	4,147	188.5	39.7	10.6		97.7	1.04	94	4
KTA-02 **	3,002	178.5	24.4	6.3		102.9	1.35	76	27
KTA-03 **	4,014	208.5	31.9	9.2		100.8	1.07	94	7
KTA-05 **	3,938	199.9	31.8	8.2		104	1.13	92	12
Iberian Margin									
JC-3B ***	3,731	174.3	28.6	7.4		64.4	0.75	86	-22
JC-9B ***	618	217.0	58.9	15.2		90.3	1.91	47	43
SW Pacific									
GT-st10 ****	3,879	192.7	27.4	10.4	3,935	96.3	1.04	93	4

C. wuellerstorfi B/Ca results from the core-tops are compared to their corresponding $\Delta[CO_3^{2-}]$ values, as well as to other available core-top data that currently exist (e.g. Brown et al., 2011; Rae et al., 2011; Raitzsch et al., 2011; Yu and Elderfield, 2007; Yu et al., 2013) (Fig. 5.9).

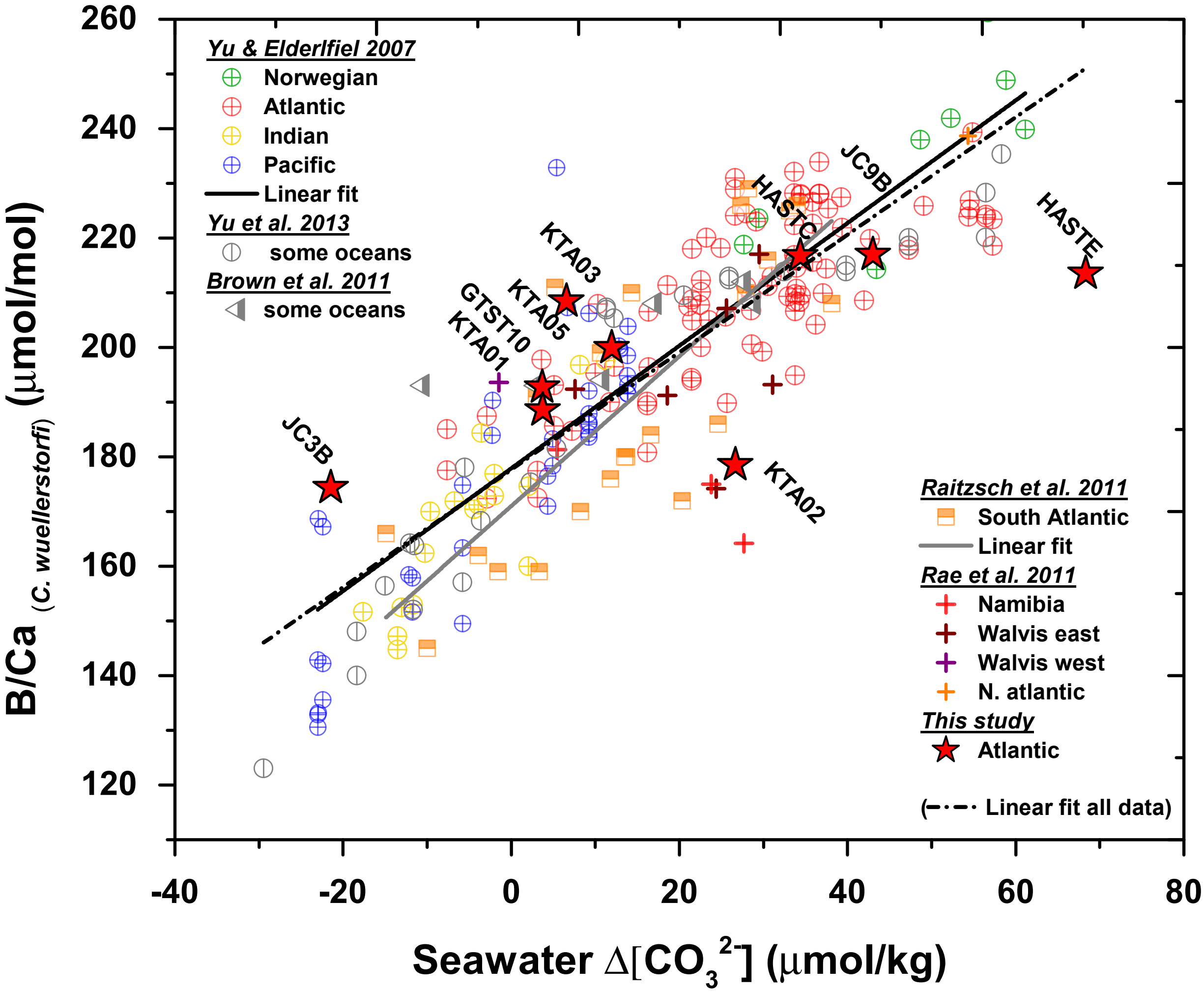

Figure 5.9. Bottom water $\Delta[CO_3^{2-}]$ *vs* B/Ca ratios in *C. wuellerstorfi* from core-top samples across the oceans (Brown et al., 2011; Rae et al., 2011; Raitzsch et al., 2011; Yu and Elderfield, 2007; Yu et al., 2013), including the core-tops from the Atlantic Ocean analysed in this thesis (red stars). Black solid line represents the linear fit from Yu and Elderfield (2007) by solution-ICPMS, while grey solid line represents the linear fit from Raitzsch et al. (2011) by LA-ICPMS. Black dashed line represent the linear fit from all the records together including the core-tops analysed in this thesis.

As observed in Figure 5.9, the new core-top measurements fit well within the two existing linear regressions, and indeed produce an indistinguishable new calibration equation when taking all the core-top data together (~230 core top samples including this study).

B/Ca (<u>μmol/mol)</u> = 1.14 x $\Delta[CO_3^{2-}]$ (<u>μmol/kg)</u> + 177.1 (Yu and Elderfield, 2007)

B/Ca (<u>μmol/mol)</u> = 1.37 x $\Delta[CO_3^{2-}]$ (<u>μmol/kg)</u> + 170.9 (Raitzsch et al., 2011)

B/Ca (<u>μmol/mol) </u>= 1.07 x $\Delta[CO_3^{2-}]$ (<u>μmol/kg)</u> + 177.7 (including this study)

This provides support for B/Ca as a proxy for $\Delta[CO_3^{2-}]$ and for LA-ICPMS as a suitable technique for this type of analysis. However, as the variability range of this correlation is large (~30 µmol/mol); do the new laser ablation core-top values fall into the right spot? In order to be able to properly answer this question, many additional core-tops analysed by both solution- and LA-ICPMS techniques should be done. In any case, Yu and Elderfield (2007)'s calibration seems to be, for now, the most suitable calibration equation to infer past $[CO_3^{2-}]$ through B/Ca analysis also by LA-ICPMS, as it contains more than 100 core-top samples, has been applied in most of the studies, and the new data fit in quite well.

5.2.3.3. B/Ca *N. dutertrei* profiles

N. dutertrei shells are usually composed of five globular chambers that are relatively fragile and contain low B concentration. A spot size of 74 μm was considered as a good compromise to achieve high B signal/background ratios covering the central part of each chamber without destroying the test when ablating. Thus, when possible, five depth profiles were performed per shell (one per chamber), with the commonly used nomenclature adopted for each ablation from the foraminifer's oldest chamber (*f-4*) to the foraminifer's youngest chamber (*f*) (Fig. 5.10a). In this case, only the "whole ablation" approach was applied, so that potential changes in B incorporation could be fully observed.

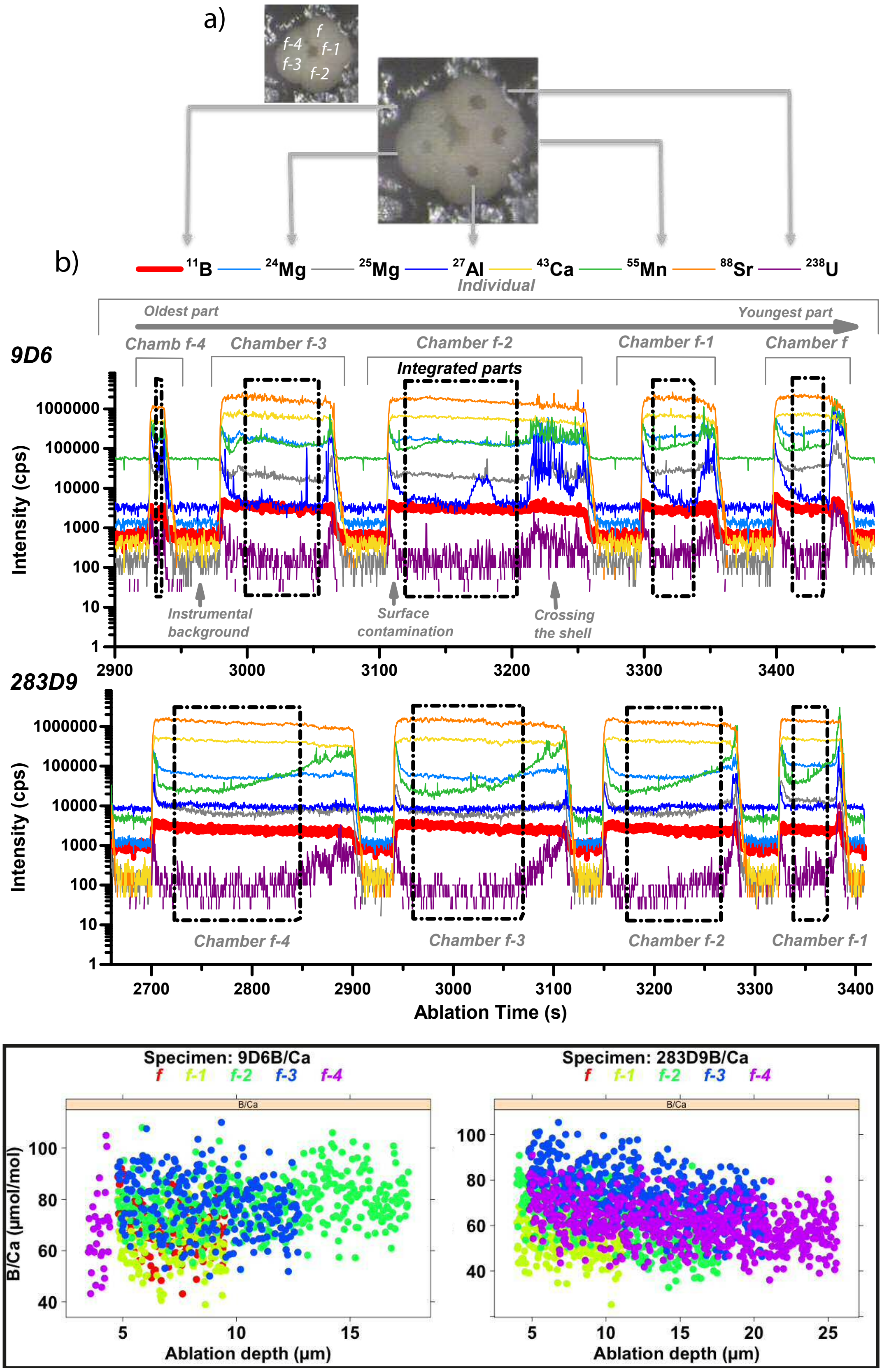
a)
f
f-4
f-1
f-3
f-2
b)
^{11}B
^{24}Mg
^{25}Mg
^{27}Al
^{43}Ca
^{55}Mn
^{88}Sr
^{238}U
Individual
Oldest part
Youngest part
9D6
Chamb f-4
Chamber f-3
Chamber f-2
Chamber f-1
Chamber f
Integrated parts
Intensity (cps)
1000000
100000
10000
1000
100
10
1
Instrumental background
Surface contamination
Crossing the shell
2900
3000
3100
3200
3300
3400
283D9
Chamber f-4
Chamber f-3
Chamber f-2
Chamber f-1
2700
2800
2900
3000
3100
3200
3300
3400
Ablation Time (s)
Specimen: 9D6B/Ca
f f-1 f-2 f-3 f-4
B/Ca
B/Ca (µmol/mol)
100
80
60
40
5
10
15
Ablation depth (µm)
Specimen: 283D9B/Ca
f f-1 f-2 f-3 f-4
B/Ca
100
80
60
40
5
10
15
20
25
Ablation depth (µm)

Figure 5.10. Illustration of laser ablation approach in *N. dutertrei.* a) *N. dutertrei* specimen before and after ablation displaying the nomenclature used in this thesis. b) Trace element profiles across the foraminifer shell of two *N. dutertrei* individuals (9D6 and 283D9), with 4-5 chambers per specimen. c) *N. dutertrei* B/Ca selected segments of the two specimens' chambers. Colours represent the different chambers of one specimen, from the oldest (*f-4*) to the youngest (*f*).

Two representative examples of the trace element depth profiles across each chamber of two *N. dutertrei* specimens from ODP1240 core are shown in Figure 5.10b. Wall thickness varies consistently and significantly between chambers (also reported by Eggins et al., 2003), with the central chambers *f-2* and *f-3* presenting the thickest walls and therefore the longest profiles. Chamber *f-4* (the oldest one) is usually hidden and very small (although when visible it is also thick), and chamber *f* (the youngest one) is often very thin and fragile. For these reasons, *f-4* and *f* chambers were not always ablated.

As for *C. wuellerstorfi*, surface enrichments are visible for all elements (with the exception of ^{11}B and ^{88}Sr, indicating again that these are not major constituents of surface contaminant phases), and were always removed before data integration. The B signal is very uniform in all chambers indicating that, apparently, B incorporation does not change over chamber growth and that it is not affected by other trace elements' incorporation. Al presents an irregular profile with internal variability, as it was also observed for *C. wuellerstorfi.*

The B/Ca shape for all chambers from the resulting integrated parts of the two *N. dutertrei* specimens seems to be either pretty flat or with a discrete slope from the inner to the outer part (Fig. 5.10c). B/Ca variability within a single profile (in a given chamber) is between 21-26 %, being not very different between chambers. As for *C. wuellerstorfi*, B/Ca ratios are different between chambers, but following a different pattern. Thus, chamber-specific patterns show that, on average, the central chambers *f-2* and *f-3* chambers tend to present higher B/Ca as compared to the youngest chamber *f* and the oldest *f-4*, which tend to have the lowest (Fig. 5.11). Lower B/Ca in the oldest chamber has also been reported in *Globorotalia sacculifer* (Allen et al., 2012).

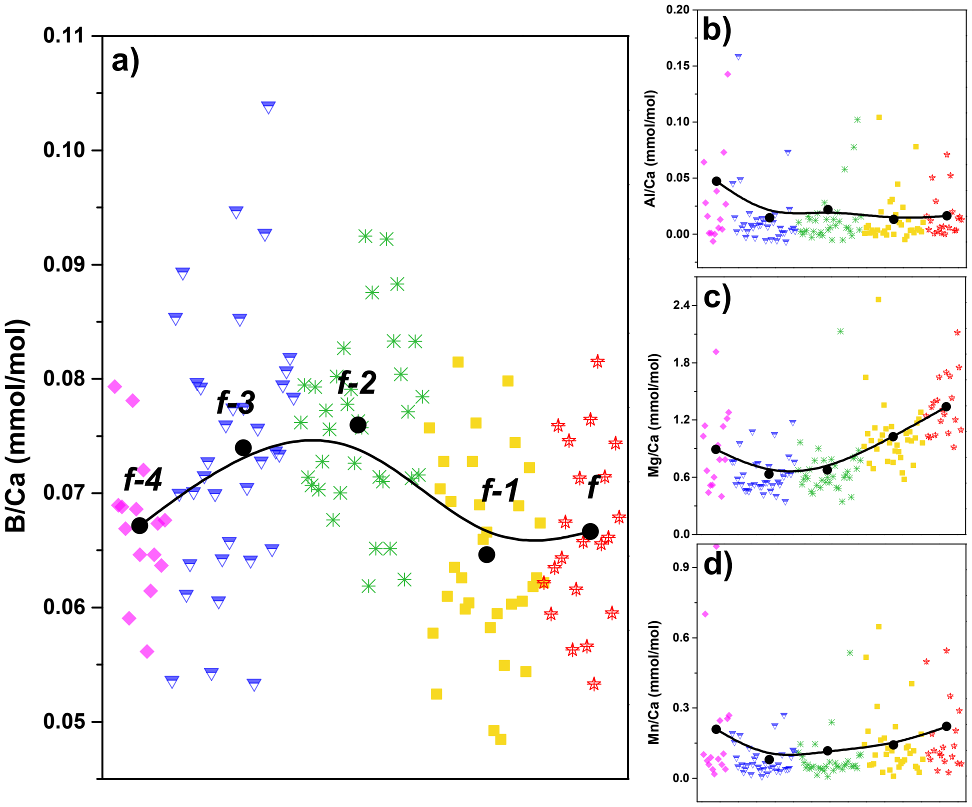

Figure 5.11. Element/Ca per chamber for all *N. dutertrei* measured in this thesis. a) B/Ca. b) Al/Ca. c) Mg/Ca. d) Mn/Ca. Colours represent the different chambers, from the oldest (*f-4*) to the youngest (*f*). Black dots represent the average element/Ca ratios for each chamber. Black line indicates the apparent trend in element composition through shell growth.

Other chamber-specific elemental ratios, such as Mg/Ca, seem to behave in the opposite manner, i.e. the chambers with higher Mg/Ca contain the lowest B/Ca and vice versa. This might suggest that either the variable/variables controlling B incorporation is/are related to ontogenetic processes rather than microenvironmental changes, as temperature and carbonate system parameters are usually positively related, or that B/Ca in *N. dutertrei* is not a consistent proxy for the carbonate system. Al/Ca and Mn/Ca from different chambers do not follow any consistent pattern, though the youngest chamber *f* typically presents very high values in some intervals, indicating the higher susceptibility of these chambers to authigenic coatings or metal adsorption.

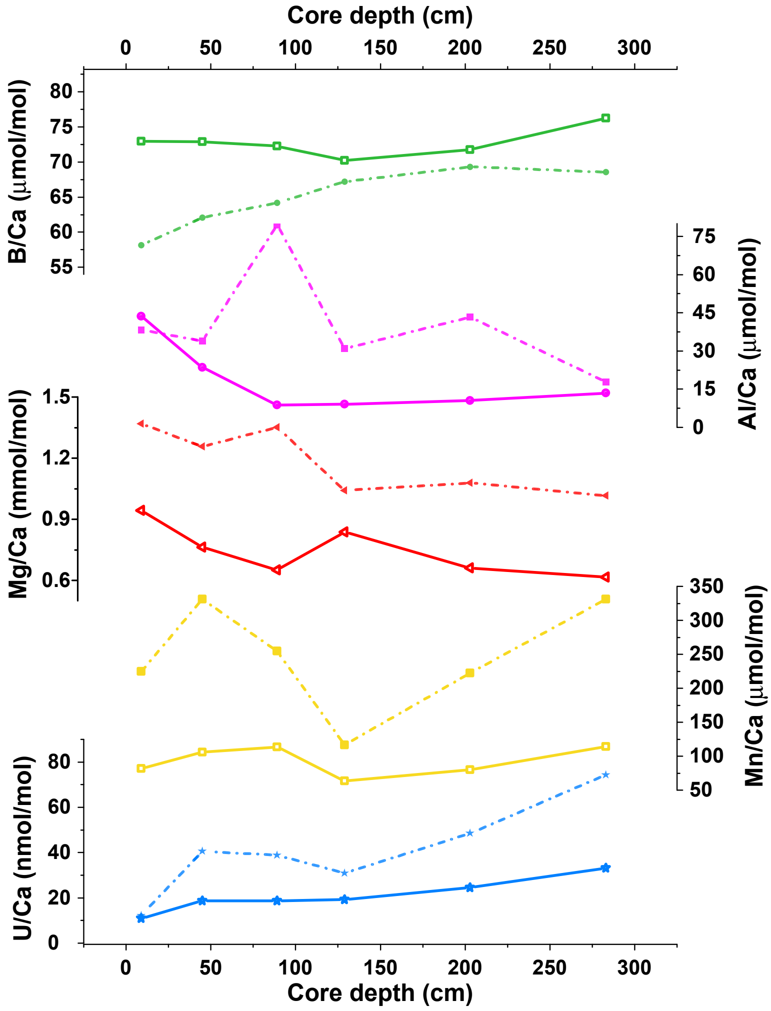

Figure 5.12. Comparison of element/Ca ratios between LA-ICPMS (solid lines) and solution-ICPMS (dashed lines) in *N. dutertrei*.

A poorer relationship between laser and solution measurements on the same *N. dutertrei* specimens compared to *C. wuellerstorfi* is observed for all elements (Fig. 5.12). The reason of this disagreement is not well constrained, but it might be related to the wall structure of this species, as the fact of being less dense and flat, as well as more porous and ornamented, usually yield worse laser ablation profiles than in benthic foraminifera. Other possible reasons for the observed laser versus solution- discrepancy in *N. dutertrei* may be possible, but are as yet unknown.

5.2.4. **Conclusions**

The B signal across the “chambers” of *C. wuellerstorfi* is generally quite uniform, with no surface enrichments, and no correlation with Al. Mg correlates with Mn, indicating the importance of the reductive cleaning application for further Mg/Ca analysis in this area (Pena et al., 2008a, 2005). Wall thickness and B/Ca ratios in *C. wuellerstorfi* seem to be related with the bilamellar growth of this species, going from lower B/Ca in the thicker-oldest part (*f-2*) to lower values in the thinner-youngest part (*f*). When comparing B/Ca final averages between the two LA-ICPMS approaches and the solution analyses performed on the same samples, longer ablations yield results that are more consistent with solution-ICPMS analyses, presenting similar variations but with a constant offset. It is suggested that, apart from the potential influence of using a non-calcite standard, this consistent lower offset in “whole profile” approach versus solution analyses might be due to the different rejection thresholds applied in both techniques to avoid Al contamination, which are typically higher in solution-ICPMS. This study has shown that final “chambers” *f* usually contain higher Al/Ca than the rest of the shell, as well as higher B/Ca, which are rejected during the data reduction of LA-ICPMS analyses. This calls for a revision of the Al/Ca rejection threshold in solution analysis, which the results from this study suggest should be lower. Although longer ablations seem to be more consistent with solution measurements, further assessment of which ablation selection method is optimal, and indeed how calibrations are affected by these choices, is probably warranted, as the “flat calcite” approach decreases the analysis time by 3 times, thus increasing analysis efficiency and significantly reducing analysis costs. In order to achieve a low and constant error and to be statistically representative of the time interval being analysed for B/Ca ratios, especially in the context of benthic foraminifera, a minimum of 5-6 individuals should be analysed, as often 1 or 2 individuals per sample cause significant biases from the average in many cases.

Core-top *C. wuellerstorfi* B/Ca ratios by LA-ICPMS are in good agreement with corresponding modern seawater $\Delta[CO_3^{2-}]$ values. Furthermore, although offsets between

LA-ICPMS and solution analyses may exist, calibrations made using core-top solution- and LA-ICPMS analyses are indistinguishable, suggesting that data using both approaches might be combined. However, a new calibration for LA-ICPMS B/Ca analysis may be needed in the future in order to quantitatively compare results between techniques accurately.

Regarding *N. dutertrei* analysis, no surface enrichments or correlation with Al are found and B signal across the shell is typically quite flat. Mn is not as high as in *C. wuellerstorfi*. Wall thickness also varies depending on the chamber, but going from thicker in the central chambers (*f-3* and *f-2*) to thinner in the youngest (*f*) and oldest (*f-4*) chambers. B/Ca also seems to relate to this distribution, but curiously in the opposite way than *C. wuellerstorfi*, i. e. *N. dutertrei* shows lower B/Ca values in the thinnest chambers. When the samples are analysed by solution-ICPMS, the similarities presented between techniques are not as striking as in the case of *C. wuellerstorfi*, which might be related to the wall structure of this planktonic species for example, which is not as "homogeneous" as in benthic foraminifera. This preliminary study at the B/Ca distribution in *N. dutertrei*, while yielding typical values obtained for this species by solution (Dai et al., 2016; Foster, 2008), might suggest that it is not a viable carbonate system proxy (or at least not for $\Delta[CO_3^{2-}]$; Dai et al., 2016). However, culture experiments should be performed in this species in order to understand what oceanographic/climatic variable, if any, B/Ca might be related to.

As a take home message, this study shows the suitability and advantages of LA-ICPMS technique for B/Ca analysis in *C. wuellerstorfi*. Importantly, it permits the rejection of chambers or even entire specimens with anomalous values that might quantitatively bias the final averages for palaeoceanographic interpretation. This may be especially important for analyses of very small samples.

CHAPTER 6

6. The evolution of deep ocean chemistry in the Eastern Equatorial Pacific over the last deglaciation

Synopsis

In this chapter, the B/Ca results from C. wuellerstorfi analysed by LA-ICPMS and described in Chapter 5 are interpreted. They are supported by new $\delta^{13}C$ measurements and discussed in the context of the radiocarbon ventilation records addressed in Chapter 4 (using the age model described in Chapter 3). The new results are also complemented with other existing records from core ODP1240 and with B/Ca records from other locations in the Pacific Ocean.

6.1. Introduction

Several marine carbon cycle mechanisms have been invoked to explain, at least, a major part of the atmospheric CO_2 drawdown observed over the last glacial period (e.g. Kohfeld and Ridgwell, 2009; Sigman et al., 2010). These mechanisms can be categorised broadly as deriving primarily from: 1) changes in the rate or efficiency of air-sea gas exchange (i.e. the "solubility pump"; e.g. Volk and Hoffert, 1985); 2) changes in whole ocean carbonate chemistry (e.g. due to carbonate compensation/dissolution; e.g. Archer and Maier-Reimer, 1994; Broecker and Peng, 1989; Keir, 1995); or 3) changes in the efficiency of the "biological carbon pumps" (i.e. "soft-tissue" *vs* "carbonate" pumps; e.g. Volk and Hoffert, 1985; see Chapter 1 for further details). While these categories might be useful for organising our thinking about past marine carbon cycle changes, it is important to emphasize that they need not have operated in isolation from each other. Indeed, a more efficient biological carbon pump can occur as a result of either an increase in its strength (i.e. average export production rates; e.g. Martínez-Garcia et al., 2014), or a reduction in its leakiness (i.e. the return flux of remineralised nutrients and carbon from the deep interior to the surface ocean; e.g. (Stephens and Keeling, 2000; Toggweiler, 1999). If the latter is achieved by a change in the ocean's large-scale overturning circulation, it would very likely co-occur with a change in the conditions of air-sea gas exchange and the solubility pump. Furthermore, regardless of how biological carbon pump efficiency is increased, and as long as the soft-tissue *vs* carbonate pump remains dominant, this would lead to more respired carbon storage in the deep ocean (thus sequestering CO_2 from the atmosphere), which could eventually reduce deep ocean carbonate ion concentrations enough to cause seafloor carbonate dissolution (a mechanism also referred to as "respiratory calcite dissolution", (Archer and Maier-Reimer, 1994; Archer, 1996, 1991). The latter would eventually increase the whole ocean alkalinity budget and lead to further atmospheric CO_2 drawdown. Therefore, changes in the efficiency of the biological carbon pump due to variations in its leakiness and/or its strength, through their association with ocean circulation and air-sea exchange effects and their potential impact on whole ocean carbonate chemistry, represents a particularly effective way to cause changes in deep-ocean carbon storage over the last glacial period.

As discussed in Chapter 4, the EEP has been shown to be less ventilated over the last part of the last glacial period, getting better ventilated at the onset of the Heinrich Stadial 1 (de la Fuente et al., 2015). This would indirectly support the idea of a more efficient biological pump during the last glacial, due to a longer residence time for carbon in the deep ocean, thus reducing the leakiness of the biological pump. As a consequence, this would have stored more carbon in the form of dissolved inorganic carbon (DIC) in the deep ocean, on the condition that the average rate of carbon export to the deep ocean did not decrease significantly. If this had been the case, an increase in respired DIC should be indirectly inferred from changes in other parameters from the deep EEP carbonate system during the last glaciation, such as the DIC $\delta^{13}C$ and $[CO_3^{2-}]$, both of which are dependent on respired CO_2 variations in the deep ocean (see discussion below and Chapter 1 for more details).

Seawater $\delta^{13}C$ estimates can be derived from foraminiferal $\delta^{13}C$ measurements, which are easy to perform as long as the right species is available in sufficient abundance. However, $[CO_3^{2-}]$ estimates have been shown to be more challenging to obtain. Over the past few years, B/Ca ratios in *C. wuellerstorfi* calcite shells have been experimentally proved to correlate with deep water carbonate saturation state ($\Delta[CO_3^{2-}]_{\text{in situ-sat}}$) in the modern ocean, based on a simple linear correlation from global core-top measurements (Yu and Elderfield, 2007), thus providing a proxy for past deep-water $[CO_3^{2-}]$ changes where saturation $[CO_3^{2-}]$ can be assumed to have remained relatively constant. As explained in Chapters 2 and 5, the theoretical basis for such a relationship relies on the seawater pH dependency in the proportion of the two boron molecular species, boric acid, $B(OH)_3$, and borate ion, $B(OH)_4^-$, and the suggestion that only $B(OH)_4^-$ is incorporated into biogenic calcite material (Hemming and Hanson, 1992), although this aspect is still not clear (Klochko et al., 2009; Uchikawa et al., 2015). Thus, changes in pH, which is a function of alkalinity (ALK) and DIC, and are therefore closely related to seawater pCO_2 and $[CO_3^{2-}]$ (note that $[CO_3^{2-}] \sim$ ALK minus DIC), should produce changes in the proportion of $B(OH)_4^-$ and $B(OH)_3$, and thus affect the B/Ca ratios in foraminifer calcite shells. This novel proxy has been applied to several cores from the North Atlantic and the Pacific oceans showing, e.g. small $[CO_3^{2-}]$ changes in the Pacific and larger decreases in the deep Atlantic at the LGM vs the Holocene, in accordance with estimates of sedimentary calcium carbonate preservation (e.g. Allen et al., 2015; Yu et al., 2010a).

In this thesis chapter, estimates of $[CO_3^{2-}]_{\text{B/Ca-based}}$ and $\delta^{13}C$ have been analysed in the benthic species *C. wuellerstorfi* from core ODP1240, in order to investigate if the carbon content of deep waters was indeed greater during the LGM, as suggested by the radiocarbon ventilation ages from this area. B/Ca measurements were carried out by the more challenging LA-ICPMS technique, as described in Chapter 5.

6.2. **Materials and methods**

6.2.1. **B/Ca analysis by LA-ICPMS and [CO_3^{2-}] estimates**

The epibenthic foraminifer *C. wuellerstorfi* was picked from 15 samples from the first 3 meters of sediment core ODP1240 covering the last 30 kyr. Each sample was composed by ~6 specimens that were rinsed in miliQ water and secured on a double-sided tape on a slide for LA-ICPMS analysis. Between 2-3 ablations were made per shell, covering the full span of chambers in each individual, using the RESOlution M-50 prototype 193nm ArF laser ablation system coupled to an Agilent 7500ce ICPMS available at the Royal Holloway University of London (Müller et al., 2009) (see Chapter 2 and 5 for further details). Data from chambers in which measured B/Ca was higher than the individual foraminifer average plus 2SD were removed and not included in further palaeoclimatic interpretations.

C. wuellerstorfi B/Ca ratios have been experimentally shown to linearly relate to $\Delta[CO_3^{2-}]_{\text{in situ-sat}}$ through equation 1 (Yu and Elderfield, 2007), thereby allowing [CO_3^{2-}] to be estimated from equation 2, albeit with some caution.

$$B/Ca\ (\mu mol/mol) = 1.14 * \Delta[CO_3^{2-}]_{\text{in situ-sat}}\ (\mu mol/kg) + 177.1 \qquad (1)$$

$$[CO_3^{2-}] = \Delta[CO_3^{2-}]_{\text{in situ-sat}} + [CO_3^{2-}]_{\text{sat}} \qquad (2)$$

Typically, seawater $[CO_3^{2-}]_{\text{sat}}$ is assumed to remain constant and is estimated from modern water column $[CO_3^{2-}]/\Omega_{\text{calcite}}$ data and assuming constant [Ca^{2+}] in seawater since past values are difficult to constrain due to the influence of pressure, bottom water temperature and salinity (Yu and Elderfield, 2007). A study from the South Western Pacific has pointed to negligible effects in $[CO_3^{2-}]_{\text{sat}}$ when applying glacial deep temperature, salinity and pressure from that area (Allen et al., 2015). Although this finding is encouraging, it is important to be aware that the assumption of the $[CO_3^{2-}]_{sat}$ constancy over time must not be applicable to all areas, and that is therefore only viable as a working hypothesis. Thus, in this thesis, to estimate a hypothesised invariable $[CO_3^{2-}]_{sat}$ over time, $[CO_3^{2-}]$ and $\Omega_{calcite}$ have been inferred from instrumental measurements of ALK and DIC available in the GLODAP dataset (WOCE P19C transect; Tsuchiya and Talley, 1998). For these estimations, the CO2SYS software package (Lewis et al., 1998; Pierrot et al., 2006) and the equilibrium constants from Dickson and Millero (1987) and Mehrbach et al. (1973) were used. The obtained modern values at a depth of 2,888 m were 67.7 μmol/kg for $[CO_3^{2-}]$ and 0.9 for $\Omega_{calcite}$, leading to a $[CO_3^{2-}]_{sat}$ of 75.2 μmol/kg (station: 18373; LAT: 0.004 N; LONG: 85.84 W).

Thus, the general equation to estimate $[CO_3^{2-}]$ through B/Ca ratios measured in the calcite shell of *C. wuellerstorfi* would be:

$$[CO_3^{2-}] = ((B/Ca - 177.1)/1.14) + ([CO_3^{2-}]_{(mod)}/\Omega_{calcite\ (mod)}) \qquad (3)$$

As shown in Chapter 5, since the initial calibration of Yu and Elderfield (2007) was published, several studies have provided additional core-top measurements (including this study). However, given that the resulting calibration equation when including all the available core-top measurements hardly differs from the original, and that most studies have used the Yu and Elderfield (2007)'s equation, this calibration is also adopted here for downcore $\Delta[CO_3^{2-}]_{insitu\text{-}sat}$ estimates in ODP1240.

6.2.2. δ^{13}C measurements

The δ^{13}C content was analysed in 46 downcore samples from ODP1240 core, covering the last 25 kyr and exclusively composed by *C. wuellerstorfi*, using a Thermo Kiel device attached to a Thermo MAT253 Mass Spectrometer in dual inlet mode at the University of Cambridge. The sample size was around 100 μg each with the exception of a few samples of 20 μg, which is the detection limit of this machine. A few additional measurements obtained previously at the University of Barcelona (Povea et al., unpublished) are also shown as they present high consistency with the $\delta^{13}C$ record obtained in this thesis and span further back in time than 25 kyr. Details on the methods used in each laboratory are described in Chapter 2.

6.3. Results and discussion

B/Ca ratios from *C. wuellerstorfi* in ODP1240 core are ~12 μmol/mol lower over the last glacial period, with an average of ~172 ± 9 μmol/mol (±2SE), than across the Holocene, which exhibits values of ~184 ± 21 μmol/mol (±2SE) (Fig. 6.1). When converted into $[CO_3^{2-}]$ the difference between glacial (~71 μmol/kg) and interglacial (~81 μmol/kg) is ~10 μmol/kg. $\delta^{13}C$ in ODP1240 also presents a reduction during the LGM compared to the Holocene of ~0.4 ‰ (Fig. 6.1).

6.3.1. A comparison of ocean ventilation and carbonate system changes in the EEP

A poorly ventilated deep EEP over the last part of the last glacial period compared to the present has been shown by the radiocarbon offsets between benthic foraminifera and atmospheric records (B-Atm) (Chapter 4; de la Fuente et al., 2015). This study also revealed how this area of the Pacific started being better ventilated at the onset of the deglaciation, demonstrating a consistency with other ventilation records from the Pacific (Siani et al., 2013; Sikes et al., 2000; Skinner et al., 2015) and the Southern Ocean (Burke and Robinson, 2012; Skinner et al., 2010), all of which varied in time with atmospheric changes in both ^{14}C and CO_2. Thus, when CO_2 rose and $\Delta^{14}C$ dropped in the atmosphere at the deglaciation onset, all these deep records exhibit enhanced ventilation (Fig. 6.2a-c, and for the rest of the Pacific

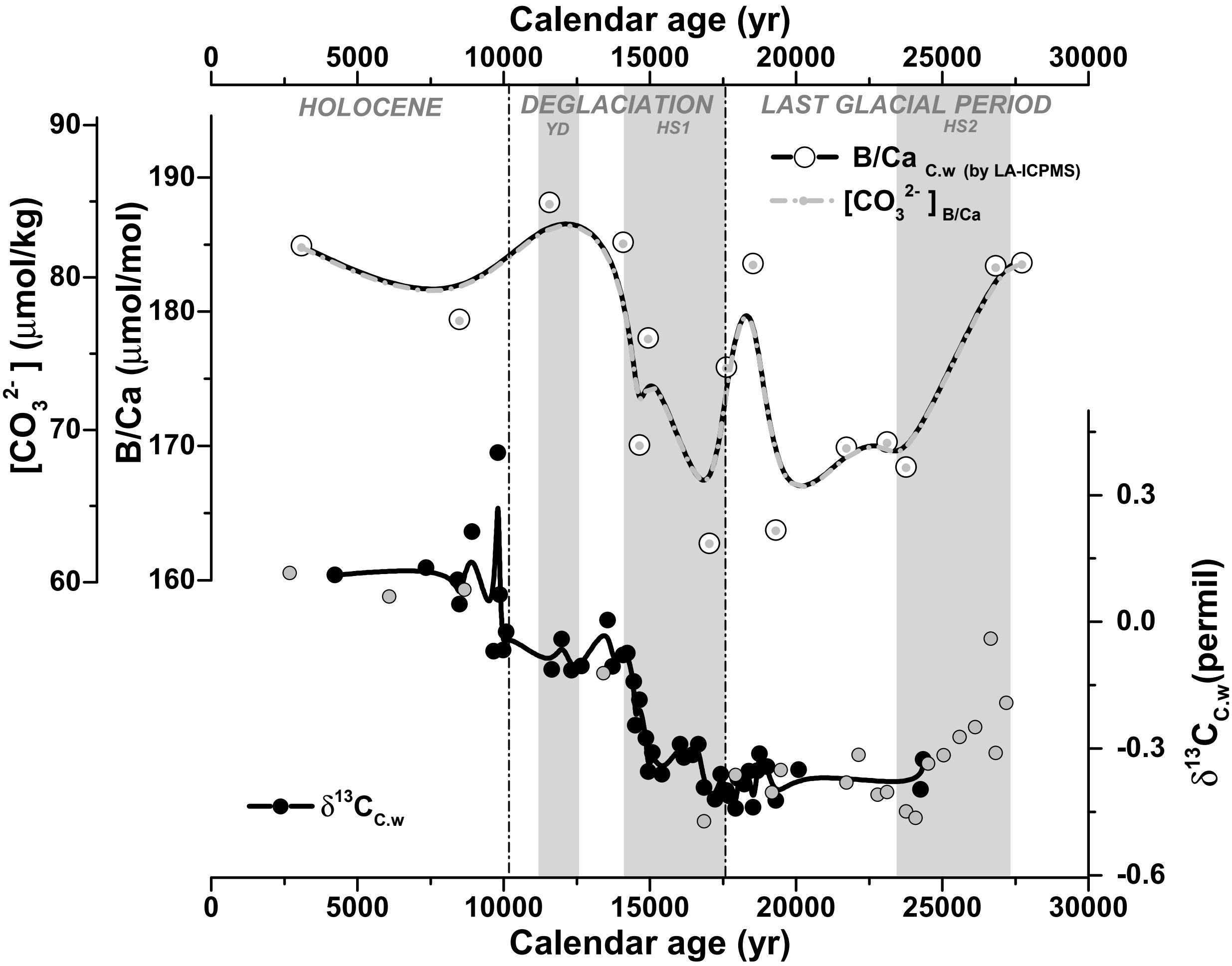

Figure 6.1. Deep carbon records from *C. wuellerstorfi* in ODP1240 over the last 30 kyr. The upper panel displays B/Ca ratios measured by LA-ICPMS (solid black line) and, overlapping, $[CO_3^{2-}]$-B/Ca based (dashed grey line). $[CO_3^{2-}]$ was estimated by using the calibration equation from Yu and Elderfield (2007) and modern $[CO_3^{2-}]$ and $\Omega_{Calcite}$ values (67.6 µmol/kg and 0.9, respectively) from the GLODAP dataset (WOCE P19 transect). The lower panel displays benthic $\delta^{13}C$ from this thesis (black line and dots) and from Povea et al., unpublished (grey dots). All lines are B-spline smoothed. Vertical dashed lines delimit relevant climatic periods, and light grey vertical bands highlight the coldest periods of the last 30 kyr.

records see Chapter 4 or de la Fuente et al., 2015). There are at least two implications of this finding: 1) that the deep ocean, including the EEP, might have had a higher concentration of CO_2 during the glaciation as compared to the late Holocene, specifically due to a higher respired carbon inventory; and 2) that the deglacial evolution of deep ocean ventilation is directly and causally linked to the deglacial increase in atmospheric CO_2.

When looking at benthic radiocarbon data from marine cores, it is important to be aware that these data tell us about the average residence time of DIC in the deep water at the study location. This residence time may vary as a result of changes in the mean transit times of the various water masses that contribute to the deep water present locally, as well as changes in the initial radiocarbon activity of these contributing water masses in their source region(s) (Devries and Primeau, 2011; Skinner and Shackleton, 2004). It is also possible, although relatively unlikely, that radiocarbon measurements might be affected by hydrothermal/volcanic or hydrocarbon seep sources of radiocarbon-depleted CO_2 that exist in few regions of the ocean (Lund et al., 2011 and references therein). However, in the absence of such ocean interior carbon sources, radiocarbon will behave as a semi-conservative tracer that is not significantly affected by biological or chemical reactions within the ocean, and that tracks the mean time-scale for carbon exchange with the atmosphere. Radiocarbon ventilation estimates therefore allow us to isolate the contribution of ocean ventilation changes to those in the efficiency of the biological pump.

This said, the fact that the radiocarbon ventilation record of ODP1240 during the last late glacial period indicates higher residence time of the prevailing water mass in this area, would have likely implied an increase in the amount of organic matter remineralisation/oxidation in the ocean interior, i.e. more carbon respired by micro-organisms per unit volume due to more time for this respired carbon to accumulate. If this happened, the most noticeable consequences might be, on the one hand, a decrease in seawater $\delta^{13}C$ due to enhanced lighter carbon isotope (^{12}C) release, and on the other hand, a greater CO_2 accumulation in seawater as a product of respiration. Such an increase in seawater $[CO_2]$ would have altered the carbonate system equilibrium (reaction 4), leading to a drop in $[CO_3^{2-}]$ in order to buffer the change in seawater pH (reaction 5) (Sarmiento and Gruber, 2004; Williams and Follows, 2011; Zeebe and Wolf-Gladrow, 2001).

$$CO_{2(aq)} + H_2O \underset{K_0}{\longleftrightarrow} H_2CO_3 \underset{K_1}{\longleftrightarrow} HCO_3^- + H^+ \underset{K_2}{\longleftrightarrow} CO_3^{2-} + 2H^+ \tag{4}$$

$$CO_2 + H_2O + CO_3^{2-} \leftrightarrow 2HCO_3^- \tag{5}$$

The [CO_3^{2-}] and $\delta^{13}C$ results presented here from the same core ODP1240 are in good agreement with the suggestion of a longer residence time of the deep water driving a more efficient biological carbon pump (Fig. 6.2). Lower $\delta^{13}C$ during the late glacial would reflect higher respired DIC levels during this period, which would in turn be indicated by a decrease in [CO_3^{2-}] levels. By extension, in response to enhanced deep ocean ventilation across the last deglaciation, the amount of remineralised organic carbon would have decreased (signalled by higher $\delta^{13}C$) accompanied by a lower dissolved CO_2 concentration (signalled by higher [CO_3^{2-}]).

Another consequence of the hypothetical increase in respired carbon due to a longer residence time of deep water during the LGM would have been a drop in [O_2], as the microorganisms consume O_2 during the respiration process in order to break down the organic matter. Following reformulations of the traditional Redfield ratios of remineralised organic matter (Redfield, 1963), the release of 106 CO_2 molecules consumes 150 molecules of O_2 (Anderson, 1995). However, it should be noted that other processes such a reduced air-sea gas exchange, could also contribute to lower dissolved oxygen concentrations, in some instances without contributing to similarly enhanced dissolved CO_2 levels due to the longer equilibration time for CO_2 as compared to other soluble gases (Stephens and Keeling, 2000). Measurements of authigenic uranium (aU) in core ME0005-24JC (recovered from nominally the same location as Site 1240; Kienast et al., 2007) support this idea, presenting higher aU (i.e. lower O_2) during the glacial compared to the Holocene (Bradtmiller et al., 2010; Kienast et al., 2007) (Fig. 6.2f, black line). This oxygenation proxy is based on the redox chemistry of U in seawater, and makes reference to the precipitated U in the sediments as the O_2 is consumed, shifting from the soluble form U(VI) in oxygenated

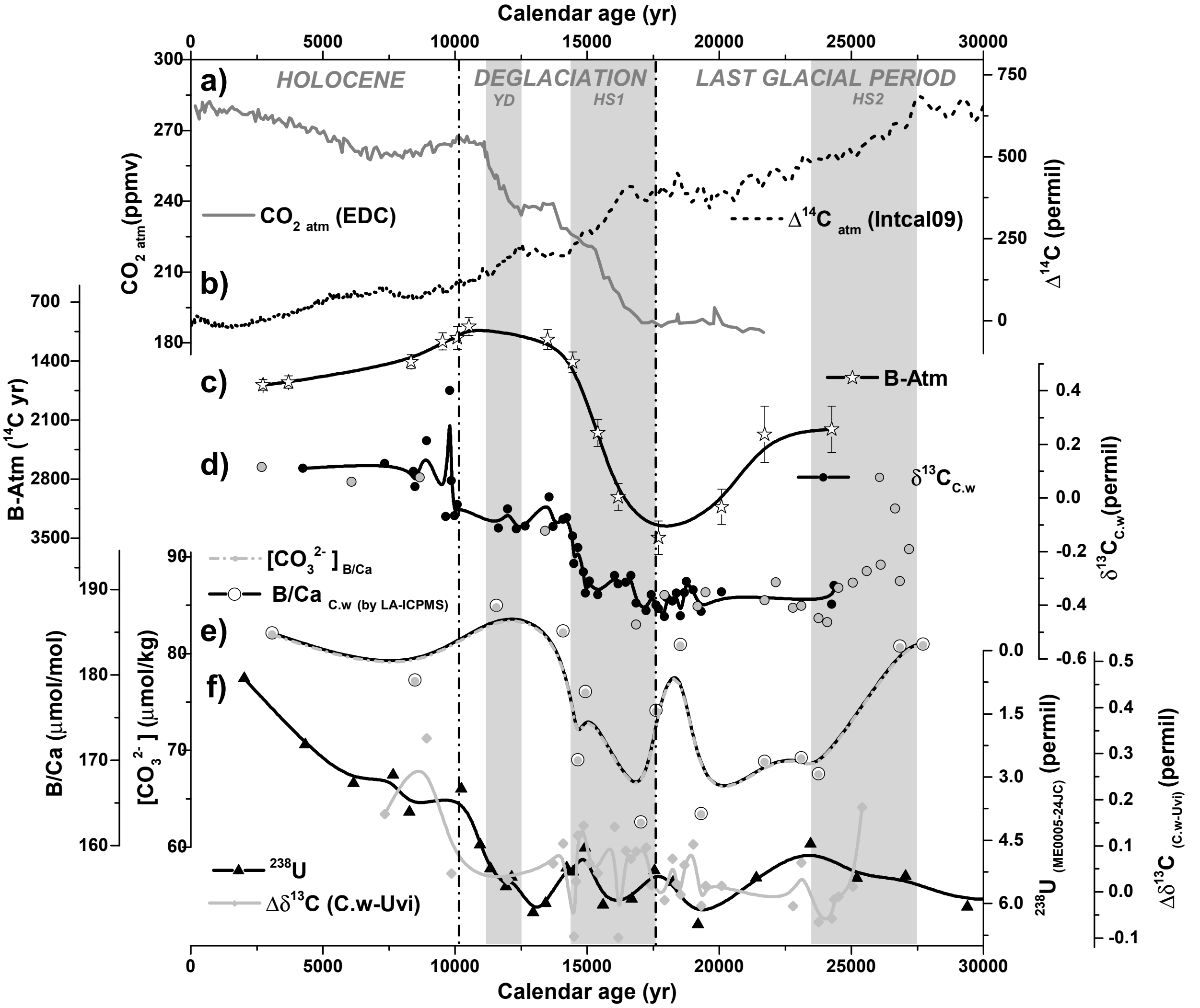

Figure 6.2. Comparison of deep ocean records from ODP1240 with records of atmospheric CO_2 and radiocarbon activity over the last 30 kyr. a) Atmospheric CO_2 concentrations from EPICA Dome C (EDC) ice core (for the deglacial period (Monnin et al., 2001); for the Holocene period (Flückiger et al., 2002)), placed on the age scale of Lemieux-Dudon et al. (2010). b) Atmospheric radiocarbon activity ($\Delta^{14}C$) changes (IntCal09 calibration curve; (Reimer et al., 2009). c) Deep-water ventilation reconstruction (B-Atm, from SST alignment; de la Fuente et al., 2015). d) $\delta^{13}C$ from *C. wuellerstorfi*. e) B/Ca and $[CO_3^{2-}]_{(B/Ca\text{-}based)}$. f) Oxygenation proxies: ^{238}U from ME0005-24JC (same location as Site 1240; Bradtmiller et al., 2010; Kienast et al., 2007; black line/triangles), and $\Delta\delta^{13}C$ between epibenthic and infaunal foraminifera species (*C. wuellerstorfi* (this study) and *Uvigerina sp*. (Povea et al., unpublished); grey line/dots). All lines are B-spline smoothed. Vertical dashed lines delimit relevant climatic periods, and light grey vertical bands highlight the coldest periods of the last 30 kyr.

waters to the insoluble species U(IV) as the medium depletes in oxygen (Cochran et al., 1986; Langmuir, 1978; Morford and Emerson, 1999). In support of the aU measurements, $\Delta\delta^{13}C$ estimates between epibenthic and infaunal foraminifera species (Hoogakker et al., 2014; McCorkle and Emerson, 1988), *C. wuellerstorfi* and *Uvigerina* from core ODP1240, show a similar trend (Fig. 6.2f, grey line). The $\Delta\delta^{13}C$ between the sediment/water interface and the sedimentary anoxic boundary should vary with the oxygen concentration of bottom waters. Thus, a smaller $\Delta\delta^{13}C$ at the LGM would indicate less oxygen penetration into the sediments (where *Uvigerina* lives), thus driving less organic carbon respiration below the seawater-sediment interface and therefore less negative infaunal (*Uvigerina*) $\delta^{13}C$ as compared to the seawater-sediment interface (where *C. wuellerstorfi* lives). It should be noted that quantitative calculations of changes in $[O_2]$ based on the $\Delta\delta^{13}C$ results presented here (e.g. using the calibration of Hoogakker et al., 2014) might actually yield slightly biased results, as the infaunal species used in this thesis is *Uvigerina,* which is not an obligate zero-oxygen species such as *Globobulimina affinis*. The reason for this choice of species is the scarcity of *G. affinis* found in ODP1240. Nevertheless, the qualitative relative oxygenation changes indicated by $\Delta\delta^{13}C$ seem robust, and are supported by the good agreement with the aU results (Fig. 6.2f).

Thus, all the records presented here, i.e. $[CO_3^{2-}]$, $\delta^{13}C$ and oxygenation proxies, are in good agreement with the deep radiocarbon ventilation in the EEP, and lend support to the hypothesis of a higher efficiency of the biological pump due to changes in its leakiness. Despite such remarkable agreement, it is interesting to note that both oxygenation proxies, aU and $\Delta\delta^{13}C$, do not change synchronously with the rest of the proxies at the beginning of the deglaciation, but later at the termination. A plausible explanation for this apparent mismatch might rely on a decoupling of pore-water and deep water chemistry, for example due to a productivity pulse between ~17-14 kyr (as seen by Calvo et al., 2011) that would have depleted O_2 in the pore-fluids of the sediment (which the oxygenation proxies would record), even after the radiocarbon ventilation and carbonate saturation of the ambient deep-water started to increase. Nevertheless, taken together, all the records presented here point to the deep EEP as a plausible contributor to the decreased atmospheric CO_2 during the LGM, by storing more respired carbon at the expense of the surface ocean and atmospheric carbon inventories. Other possible contributions to the apparent increase in the respired carbon content of the deep EEP are further investigated below.

6.3.2. **Export productivity in the EEP**

The higher residence time of the water masses above core ODP1240 over the LGM indicated by the decrease in radiocarbon ventilation (considering that radiocarbon is not especially sensitive to changes in the soft-tissue or carbonate pumps as mentioned above), along with the quantitative and qualitative consistency of this record with ventilation records from the Southern Ocean and the South Pacific (de la Fuente et al., 2015), suggest that changes in the efficiency of the biological pump due to changes in ocean circulation affected a large volume of the ocean and thus played an important role in the glacial/interglacial atmospheric CO_2 variations.

However, several studies in core ODP1240 have pointed out an increase in the strength of the biological pump (i.e. export productivity rates) in this area as a mechanism contributing to the glacial atmospheric CO_2 drawdown (Calvo et al., 2011; Pichevin et al., 2009; Robinson et al., 2009). The glacial changes observed in deep $[CO_3^{2-}]$, $\delta^{13}C$ and oxygenation records from ODP1240 described in the previous subsection of this chapter might indeed be compatible with an increase in surface productivity over the LGM, with the consequent higher export to the bottom of the ocean and therefore an increase in the efficiency of the biological pump. Thus, a larger flux of organic matter to the deep ocean in this area might have contributed to the observed drop in $[CO_3^{2-}]$ and $\delta^{13}C$ described in this chapter as a consequence of higher remineralisation rates that would have also increased the release of respired CO_2 to deep water and the consumption of dissolved O_2. These processes would be independent of, or in addition to, contributions from changes in ocean ventilation constrained using radiocarbon measurements.

Focusing on the LGM changes, these studies advocate for an increase in surface productivity, with a consequent higher export to the deep ocean, caused by the documented increase in dust-borne iron delivery to the iron-limited low-latitude Pacific Ocean at the last glacial period (McGee et al., 2007). A first inspection of the opal % in ODP1240 as a proxy for silica-fixing organisms abundance (such as diatoms) was however contradictory, as it presented lower values over the LGM, opposite to the proposed increase in surface productivity in the EEP (Fig. 6.3d). However, the also lower opal δ^{30}Si during the glacial (as a proxy for the relative utilization of the silica) was interpreted as an indication of a decline in the Si:C uptake ratio due to an iron-replete glacial ocean. This interpretation would thus be compatible with the assumption of higher productivity over this period (Pichevin et al., 2009) (Fig. 6.3d). In the same way, nitrogen isotopes (δ^{15}N) from bulk sediments in ODP1240 core show lower values over the LGM compared to the Holocene. Lower sedimentary δ^{15}N values could be interpreted as indicative of lower nutrient consumption, but this would be inconsistent with both the absence of iron-silicon limitation (Pichevin et al., 2009) and the observed higher C_{org} fluxes (Robinson et al., 2009) (Fig. 6.3b,c). However, the correction of the nitrogen isotope signal for denitrification effects occurring closer to the Central American margin (using the sedimentary δ^{15}N signal from core ODP1242, situated in this denitrification region), reverses the glacial/interglacial trend and indicates the highest δ^{15}N in ODP1240 during the LGM. This would suggest highest local nutrient consumption at that period, which would be consistent with higher surface productivity over the LGM (Robinson et al., 2009) (Fig. 6.3c).

An increase in organic carbon (C_{org}) accumulation rates in the EEP over the LGM has been documented in core ODP1240 (Pichevin et al., 2009) (Fig 6.3b), as well as in the nearby core P6 (Pedersen, 1983). At the same time, higher abundances of organic biomarkers (alkenones and brassicasterol) are shown in this core during the LGM, as compared to the present (Calvo et al., 2011) (Fig. 6.3e). Both the higher C_{org} accumulation and phytoplankton abundances might have been the result of an increase in surface productivity, consistent with the isotopic evidence described

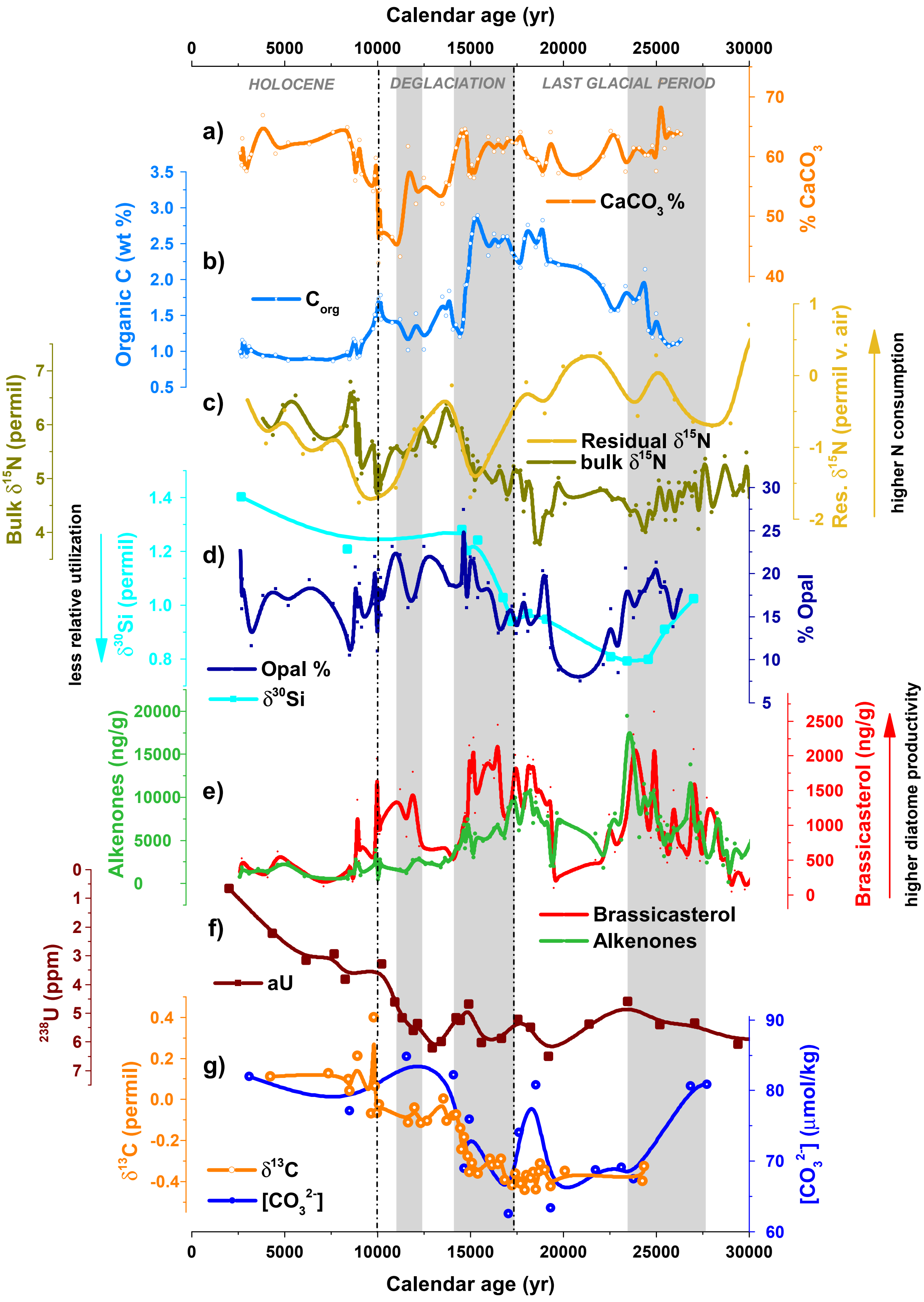
Calendar age (yr)
0
5000
10000
15000
20000
25000
30000
HOLOCENE
DEGLACIATION
LAST GLACIAL PERIOD
a)
$CaCO_3$ %
% $CaCO_3$
70
60
50
40
b)
C_{org}
Organic C (wt %)
3.5
3.0
2.5
2.0
1.5
1.0
0.5
c)
Residual $\delta^{15}N$
bulk $\delta^{15}N$
Bulk $\delta^{15}N$ (permil)
7
6
5
4
Res. $\delta^{15}N$ (permil v. air)
1
0
-1
-2
higher N consumption
less relative utilization
d)
Opal %
$\delta^{30}Si$
$\delta^{30}Si$ (permil)
1.4
1.2
1.0
0.8
% Opal
30
25
20
15
10
5
e)
Alkenones (ng/g)
20000
15000
10000
5000
0
Brassicasterol (ng/g)
2500
2000
1500
1000
500
0
higher diatome productivity
Brassicasterol
Alkenones
f)
aU
^{238}U (ppm)
0
1
2
3
4
5
6
7
g)
$\delta^{13}C$
$[CO_3^{2-}]$
$\delta^{13}C$ (permil)
0.4
0.2
0.0
-0.2
-0.4
$[CO_3^{2-}]$ (µmol/kg)
90
80
70
60
Calendar age (yr)

Figure 6.3. ODP1240 records reflecting both surface and deep ocean changes over the last 30 kyr. a) % $CaCO_3$ (orange line) (Pichevin et al., 2009); b) % C_{org} (blue line) (Pichevin et al., 2009); c) bulk (green line) and residual $\delta^{15}N$ (orange line) (Robinson et al., 2009); d) $\delta^{30}Si$ (light blue line), % opal (dark blue line) (Pichevin et al., 2009); e) Concentration of brassicasterol (red line) and alkenones (green line) (Calvo et al., 2011); f) authigenic uranium (^{238}U) (brown line) (Bradtmiller et al., 2010; Kienast et al., 2007); g) $[CO_3^{2-}]_{(B/Ca\text{-}based)}$ by LA-ICPMS (blue line) and $\delta^{13}C$ (orange line), from *C. wuellerstorfi* (this thesis). All lines are B-spline smoothed. Vertical dashed lines delimit relevant climatic periods. Light grey vertical bands highlight the coldest periods of the last 30 kyr.

above. Thus, these proxies suggest that an increase in surface productivity over the LGM might have taken place in the EEP area, which would have contributed to increase the efficiency of the biological pump and the atmospheric CO_2 drawdown. However, the exact magnitude of this contribution remains unclear.

Indeed, the question arises: was the observed increase in the biological pump efficiency in the glacial EEP mainly due to changes in ocean circulation, or changes in the carbon export productivity in this area; how much did the proposed increase in organic carbon export productivity affect carbon storage in the deep ocean? Arguably this question cannot be fully resolved without accurate quantitative estimates of export productivity- and deep ocean apparent oxygen utilization changes. At present it is clear at least that ocean ventilation changes made some contribution, though only qualitative conclusions, such as those drawn above, are possible.

6.3.3. Carbonate dissolution as a complementary mechanism for $[CO_3^{2-}]$ EEP changes

A decrease in deep ocean ventilation along with an increase in carbon export productivity in the EEP at the LGM are therefore proposed as the mechanisms responsible for the decrease in both deep $[CO_3^{2-}]$ and $\delta^{13}C$ observed in this area. The action of any of these mechanisms (alone or together) might be expected to achieve a relatively large [CO_3^{2-}] glacial-Holocene difference. However, the results from this thesis indicate only a small [CO_3^{2-}] change between these two periods (~12 µmol/kg), suggesting that a "counteracting" mechanism, such as seafloor respiratory calcite dissolution, might have also played a role. When carbonate dissolves in seawater, both [CO_3^{2-}] and ALK increase (Broecker and Peng, 1989; Zeebe and Wolf-Gladrow, 2001).

If this was the case, a decrease in the $CaCO_3$ concentration might be initially expected. However, $CaCO_3$ % indicates no changes between 25-15 kyr. This might suggest that any $CaCO_3$ dissolution that occurred in the deep EEP at the LGM would have been masked, for instance, by higher carbonate export productivity rates, which in turn would be consistent with higher abundance of alkenones, Fig. 6.3e. Furthermore, the contribution of any such $CaCO_3$ dissolution to increased average ocean [CO_3^{2-}], would have also been masked to some extent by opposing changes in deep ocean carbonate ion concentrations driven by organic carbon respiration.

Thus, $CaCO_3$ seafloor dissolution in the deep Pacific, as recorded in core ODP1240, not only might have "buffered" glacial [CO_3^{2-}] changes without affecting $\delta^{13}C$ in the EEP, but also might have played a role in the atmospheric CO_2 drawdown during the LGM by contributing to increased average ocean alkalinity via [CO_3^{2-}] supply to the ocean (Keir, 1995; Sigman and Boyle, 2000). This would have further reinforced the effects of higher biological pump efficiency achieved by the circulation and surface productivity changes proposed above.

6.3.4. **$\Delta[CO_3^{2-}]_{(Hol-LGM)}$ derived from B/Ca across the Pacific Ocean**

Although B/Ca ratios in benthic foraminifera is a relatively novel proxy for deep water [CO_3^{2-}], it has been used already a number of times in marine sediment samples from the Pacific Ocean over the last years (Allen et al., 2015; Doss and Marchitto, 2013; Elmore et al., 2015; Yu et al., 2010a). In Figure 6.4, a compilation of averaged [CO_3^{2-}] from these studies is presented where, LGM averages (open squares) across the equatorial-south Pacific Ocean are generally consistent with each other. These records indicate a LGM variation between sites of only ~5 µmol/kg, with the exception of the deepest core in the central Pacific (PC61; 4,300 m), which displays a larger LGM value (Fig. 6.4). In fact, this deep core also presents an almost identical [CO_3^{2-}] for the Holocene, which might point to a constant higher degree of $CaCO_3$ dissolution in this central deep area. In contrast, Holocene-modern

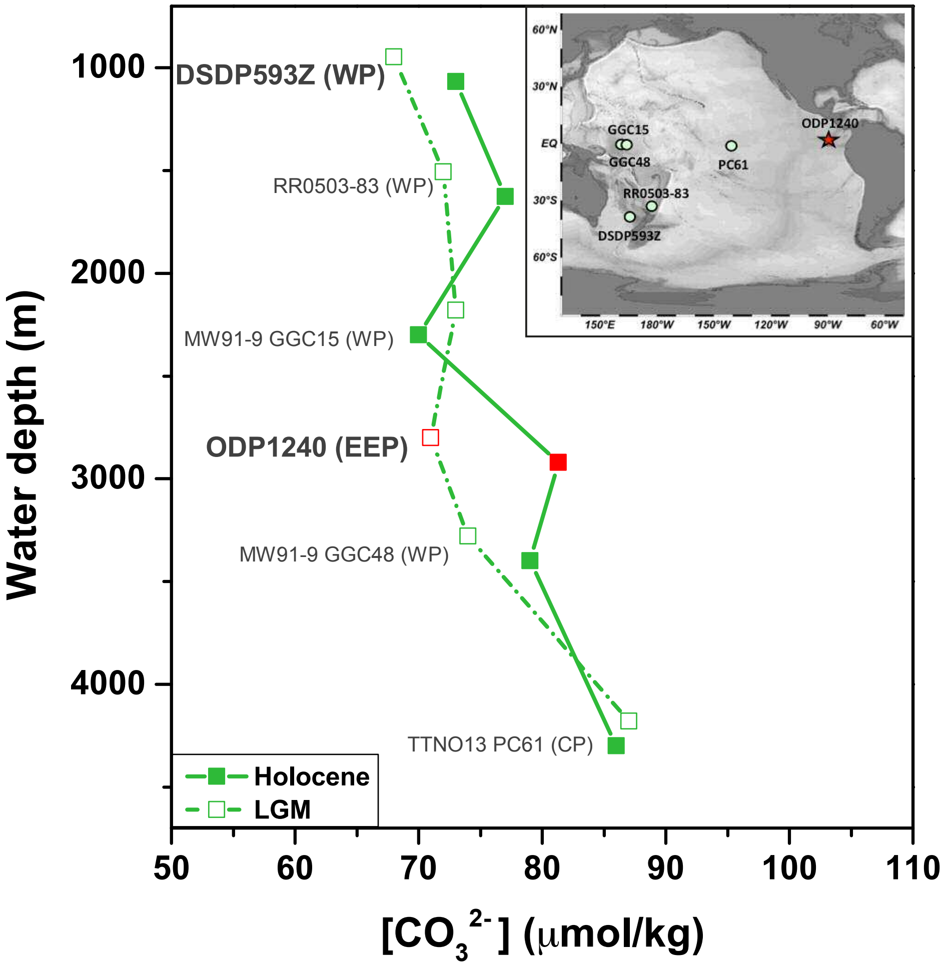

Figure 6.4. Deep [CO_3^{2-}] records from several Pacific Ocean sediment cores, showing relatively small changes in carbonate saturation between the Holocene and LGM in the Pacific: DSDP593Z (Elmore et al., 2015), RR0503-83 (Allen et al., 2015), GGC15 and GGC48 (Yu et al., 2010a), PC61 (Yu et al., 2013) and ODP1240 (this thesis, highlighted in red). LGM data points are marked by a dashed line/open squares and Holocene by a solid line/filled squares. Modified and updated from Allen et al. (2015) and Yu et al. (2013). Note that the 120 m sea level difference between the Holocene and the LGM was taken into account. Map location at the top right of the figure.

$[CO_3^{2-}]$ averages (filled squares in Fig. 6.4) from all the other cores indicate higher variation between sites, which might suggest a more "homogeneous" glacial deep equatorial-south Pacific Ocean.

Regarding glacial-Holocene/modern $[CO_3^{2-}]$ differences, these studies overall suggest little $[CO_3^{2-}]$ change in the deep Pacific between the two periods (Fig. 6.4). This "unexpected" small variation has been attributed to the large buffering capacity of carbonate sediments in the Pacific Ocean (Allen et al., 2015; Yu et al., 2013, 2010a). $[CO_3^{2-}]$ changes between the LGM and the Holocene at ODP1240 site agree well with this hypothesis. Core GGC15 at the South West Pacific SWP (2,300 m) is the only one displaying, in average, lower $[CO_3^{2-}]$ at the Holocene compared to the LGM. The authors have speculated that this core site might have been influenced by glacial NPDW/southern-sourced differences in the mixing ratio (Yu et al., 2010a) as well as by carbonate compensation effects.

The $\Delta[CO_3^{2-}]_{(Hol\text{-}LGM)}$ changes observed in Figure 6.4 are smaller than the changes observed in the Atlantic and Southern Oceans (Gottschalk et al., 2015; Yu et al., 2014, 2013). This is expected, precisely because of the current shallower calcite compensation depth (CCD) in the Pacific due to the greater carbonate dissolution in the modern Pacific Ocean as compared to the Atlantic.

6.4. **Conclusions**

In this chapter, a possible increase in the biological pump efficiency over the LGM has been investigated as a mechanism for the atmospheric CO_2 drawdown over that period. Radiocarbon ventilation is not affected by any biochemical change and indirectly supports higher biological pump efficiency through a decrease in its leakiness over the LGM. In the same way, productivity proxies from this area also suggest an increased efficiency by an increase in the strength of the biological pump. Both $[CO_3^{2-}]$ and $\delta^{13}C$ changes observed in this thesis, along with published oxygenation proxies, support these observations by presenting lower values in the

EEP at the LGM compared to the Holocene. However, the decrease in [CO_3^{2-}] in this area is relatively small, suggesting that these mechanisms were not the only ones operating or indeed contributing to the drop in the glacial atmospheric CO_2. This has also been observed in other Pacific [CO_3^{2-}] records and has been suggested to be a consequence of larger carbonate dissolution over the LGM in this basin. Thus, respiratory calcite dissolution not only might explain the relatively small change in deep ocean [CO_3^{2-}] despite a larger $\delta^{13}C$ difference between the glacial and Holocene periods, but also would have likely and directly contributed to the glacial atmospheric CO_2 decrease by increasing the ocean average ALK and therefore decreasing the surface ocean pCO_2, thus allowing the surface ocean to take up more CO_2. In conclusion, the deep EEP, and probably much of the wider deep Pacific, very likely sequestered a significant amount of atmospheric CO_2 during the LGM, specifically due to a more efficient biological carbon pump caused by both lower ventilation rates and enhanced export productivity, but also due to an increase in average ocean alkalinity by greater carbonate dissolution.

CHAPTER 7

7. Integration of results and conclusions

7.1. Glacial period

Two of the most hotly pursued topics in palaeoclimate research are the precise mechanisms that cause global climate to alternate between glacial and interglacial states. It is widely accepted that changes in insolation must have paced the transitions between these climatic states (Hays et al., 1976). However, it is also quite clear that this external forcing would have triggered a chain of events (i.e. feedbacks) that ultimately might have brought the Earth system to thresholds beyond which global climate transitions were irrevocable, regardless of subsequent reversals in insolation forcing (e.g. Abe-Ouchi et al., 2013; Ganopolski et al., 2016; Paillard and Parrenin, 2004). This non-linearity might also account for the variable amplitude of glacial-interglacial cycles, as well as the different rapidity of climatic transitions into *vs* out of glacial climate states.

Glacial-interglacial variations in the concentration of atmospheric CO_2 seem to have provided an important feedback in both glacial inceptions and glacial terminations: they were a consequence of the initial processes that triggered climatic transitions, but were also an essential amplifier to achieve the full amplitude of the observed climate cycles. Thus, as a key player in the global carbon cycle, and one of the most plausible contributors to glacial-interglacial atmospheric CO_2 changes, the ocean has become a central focus of palaeoclimate research that seeks to explain the glacial cycles of the late Pleistocene.

This thesis has mainly addressed the study of the marine carbon cycle over the last glacial period (more specifically the latest part of the last glacial period), including the search of a hypothetical “excess” CO_2 pool stored in the ocean interior (away from the atmosphere), as well as the potential mechanisms that would have allowed such an “excess” CO_2 pool to accumulate during the last glacial period. The results show that reduced ocean ventilation in the deep Eastern Equatorial Pacific (EEP) would have played a role in increasing the efficiency of the biological pump by “retaining” water masses in the ocean interior for longer during the glaciation, and thus allowing larger amounts of respired carbon to accumulate in the deep ocean. Furthermore, the new generated data also support that, as a consequence of this deep ocean accumulation of respired carbon, the ocean’s average alkalinity might have increased on the time-scale of global ocean mixing due to enhanced carbonate dissolution, a secondary process that would have also contributed to increase the glacial uptake of atmospheric CO_2.

These emerging results are compelling but they are from just one location in the ocean, and therefore need to be regarded in a global context. As noted in Chapter 4, coherent radiocarbon ventilation changes are indeed seen in the glacial ocean, in regions that today are linked by the modern transport pathways, e.g. from the Southern Ocean (SO) to the EEP (de la Fuente et al., 2015; Skinner et al., 2015, 2010). Complementary records of past deep-ocean carbon cycling, via biological carbon pump efficiency changes and/or carbonate dissolution (i.e. $[CO_3^{2-}]$, $\delta^{13}C$ and oxygenation proxies) are also available from two locations on the dominant transport pathway from the SO to the EEP (Fig. 7.1). This permits a wider integration and interpretation of the results obtained in core ODP1240 over the last 30 kyr with data from the deep South Pacific and Southern Oceans, which together account for the vast majority of the global deep ocean volume.

As observed in Figure 7.1, oxygenation proxies, either aU or U/Mn from foraminiferal coatings (see Gottschalk et al., 2016 for further information on the basis of the latter proxy), $\delta^{13}C$, and $[CO_3^{2-}]$ reconstructions from sediment cores from the SO, the south western Pacific (SWP) and the EEP show a consistent correlation with changes in deep ocean radiocarbon ventilation (Fig. 7.1). Thus, data from across the Southern-Pacific Ocean indicate a widespread change in ocean circulation at

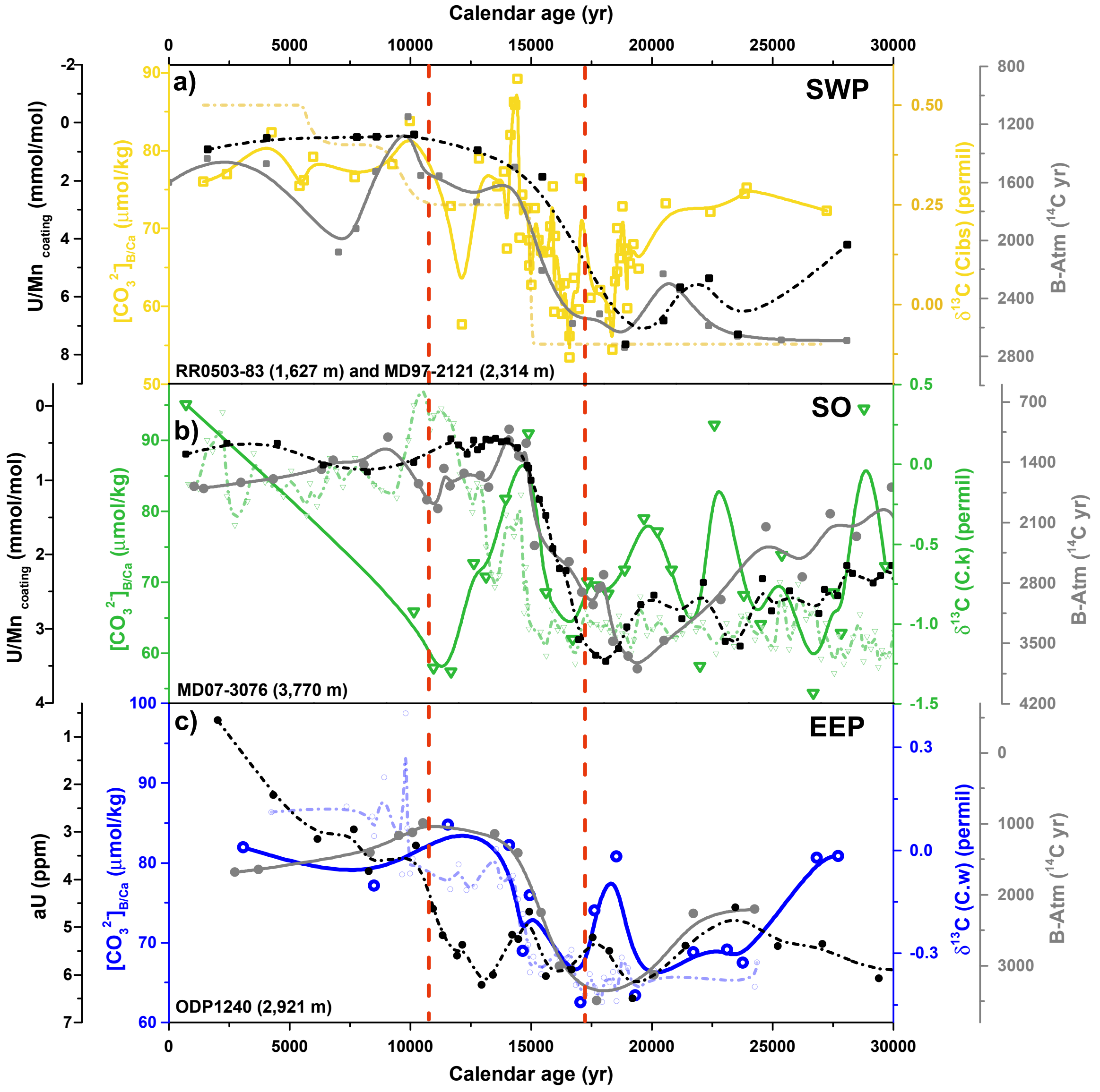

Figure 7.1. Compilation of several carbon cycle proxies from three Pacific-Southern Oceans cores over the last 30 kyr. a) Two cores from the SWP: MD97-2121 (2,314 m; B-Atm offsets; (Skinner et al., 2015) and U/Mn$_{\text{coating}}$ (from *Globorotalia truncatulinoides*; Skinner et al., in preparation)), and RR050383 (1,627 m; $[CO_3^{2-}]_{B/Ca}$ and δ^{13}C (Allen et al., 2015); the latter being only roughly estimated here, as data are not published in Allen et al., 2015). b) From the SO: MD07-3076 (3,770 m; B-Atm offsets (Skinner et al., 2010), $[CO_3^{2-}]$B/Ca (Gottschalk et al., 2015), U/Mn$_{\text{coating}}$ (from averaged *Uvigerina* and *Globigerina bulloides*) (Gottschalk et al., 2016), and δ^{13}C (Waelbroeck et al., 2011)). c) From the EEP: ODP1240 (2,921 m; B-Atm offsets, $[CO_3^{2-}]_{B/Ca}$ and δ^{13}C (this thesis), authigenic uranium (aU) from ME0005-27JC (Bradtmiller et al., 2010). B-Atm radiocarbon offsets (grey solid lines); $[CO_3^{2-}]_{B/Ca}$ (coloured solid lines); δ^{13}C (coloured dashed lines); and oxygenation proxies (black dashed lines). Vertical red dashed lines separate glacial-deglacial-Holocene periods, from right to left.

the LGM, where the deep ocean water masses remained for a longer time without any contact with the atmosphere, thus promoting an increase in the biological pump efficiency that is reflected in lower [CO_3^{2-}], $\delta^{13}C$ and [O_2].

The evolution of deep ocean hydrography over the last deglaciation is less clear in these reconstructions, due to discrepancies between some of these proxies over certain climatic periods. For instance, based on radiocarbon ventilation, [CO_3^{2-}] in the SWP before LGM seems to be much higher than expected This feature is not observed in the other two regions, EEP and SO, perhaps indicating that carbonate dissolution had progressed further at that moment in this area of the Pacific, though the reasons for this remain unclear (Fig. 7.1a). In contrast, a minimum in [CO_3^{2-}] in the SO at the onset of the Holocene is not accompanied by a correlative change in the other proxies from this core, or indeed from the other cores from the SWP and EEP (Fig. 7.1b). However, the low resolution of measurements in this core means that this anomaly may represent an artefact, without any clear explanation. Therefore, despite the broad coherence of radiocarbon, [CO_3^{2-}], $\delta^{13}C$ and oxygenation records across the deep Pacific and Southern Oceans, further replication of the trends seen in these regions, and the generation of new records from elsewhere in the global ocean is needed to fully resolve global deglacial carbon cycle changes.

In any case, it is becoming clearer that the glacial deep ocean played an essential role in storing carbon, primarily by a decrease in the turn-over rate of the deep ocean's carbon inventory (e.g. as shown here), but possibly also by an increase in the surface productivity through upper ocean micronutrient fertilization (e.g. Hain et al., 2010). Focusing on the reduced glacial deep ocean turn-over rate, which is the mechanism most emphasised by the results of this thesis: what physical processes would have produced such a reduction in the leakiness of the marine biological carbon pump? One theory, proposed by Adkins (2013), is that the system goes from interglacial to glacial states by achieving a more density-stratified deep ocean that would thus be more efficient in retaining respired carbon. His idea is different from the one proposed by e.g. Toggweiler (1999), which instead suggested a reduction in wind-driven overturning, in that it is based on the influence of NADW cooling on the AABW properties, which would become saltier and thus enhance the density stratification of the water column. This would make it harder for winds and vertical mixing processes for example to drive deep ocean overturning, rather than reducing the amount of energy available to do so, as proposed by Toggweiler (1999). Further alternative mechanisms are also possible for reducing the average ocean turn-over rate, for example by altering the buoyancy forcing at the surface of the Southern Ocean through temperature changes (Watson and Naveira Garabato, 2006), or summer sea-ice margin and brine formation changes (Ferrari et al., 2014), which would reduce the rate of mixing across the ocean water column. Furthermore, as pointed out in a recent numerical modelling study (Ferrari et al., 2014), many of these processes (winds, sea ice, water mass distributions and buoyancy, etc) are likely to be dynamically linked and therefore co-occur. On the other hand, certain processes for altering the marine carbon cycle might also exhibit a different dominant timing and order of occurrence (Brovkin et al., 2012). For example, starting with pure physical processes at the glacial inception such as higher CO_2 solubility due to lower surface temperature, as well as a slower deep ocean turn-over rate (including a possible "standing volume" effect; Skinner, 2009), that little by little allowed the biological pump to become more efficient during the second half of the glaciation, and in turn altered the ocean's carbonate chemistry by increasing the whole ocean alkalinity.

7.2. **Glacial termination**

Whatever the mechanisms for getting into a glacial state and for sequestering more carbon in the deep ocean (e.g. via a more efficient biological carbon pump), the deglacial process must consist of "undoing" their effects. Despite the fact that the main focus of this thesis has been on the potential marine mechanisms that might have increased the efficiency of the biological pump over glacial periods in the EEP, as well as any attendant feedbacks arising from these, all the new results presented here and the existing data from the Pacific and Southern Oceans shown in Fig. 7.1, also demonstrate that the inferred excess of respired carbon was gradually released from the deep ocean to another carbon reservoir (presumably the atmosphere) across the deglaciation (Fig. 7.1), and broadly in time with atmospheric CO_2 rise.

Again, in light of the observations that point to an active role of the marine carbon cycle in deglacial CO_2 rise, the question arises: what mechanisms would have triggered the CO_2 release? Three main ensembles of mechanisms for the deglacial increase in atmospheric CO_2 have been put forward (Sigman et al., 2010): 1) a reduction in export productivity driven by a drop in iron fertilization in the Southern Ocean (Jaccard et al., 2013; Martínez-Garcia et al., 2014); 2) increased upwelling in the Southern Ocean due to a southward shift of the Westerlies associated with global warming and with millennial-scale climate impacts originating in the North Atlantic (Anderson et al., 2009; Denton et al., 2010; Toggweiler, 2009; Toggweiler et al., 2006); and 3) the retreat of Antarctic sea-ice due to global warming and/or regional Antarctic warming linked to millennial-scale climate impacts (e.g. Skinner et al., 2013), which would have prevented wind-driven overturning and/or air-sea gas exchange over the glaciation (Ferrari et al., 2014; Stephens and Keeling, 2000). Clearly, all of these mechanisms could operate in unison or in sequence, and the problem once again is determining the extent to which each may have played a role and at what times.

7.3. **Conclusions and outlook**

This thesis has addressed the role of the ocean in glacial-interglacial atmospheric CO_2 and climate change by using geochemical analyses on marine sediments from the EEP to derive four key findings:

- First, radiocarbon ventilation ages determined by combining B-P offsets with past surface reservoir age estimates, demonstrate that the deep EEP was more poorly ventilated at the LGM compared to the Holocene, which would have directly contributed to a less “leaky”, and therefore more efficient, biological pump during the glacial period.

- Second, the LA-ICPMS technique is a viable and particularly informative approach for the analysis of B/Ca ratios in benthic foraminifera, which serve as a proxy for deep water $\Delta[CO_3^{2-}]$ and may therefore inform on past changes in the deep respired carbon inventory.

- Third, LA-ICPMS B/Ca measurements, in conjunction with other carbon cycle proxies such as $\delta^{13}C$ and $\Delta\delta^{13}C$, suggest that deep water $[CO_3^{2-}]$, $\delta^{13}C$ and oxygenation were lower at the LGM compared to the present, confirming an increase in respired carbon storage in the deep EEP during the last glacial.

- Fourth, the observed relationships between $[CO_3^{2-}]$, $\delta^{13}C$ and radiocarbon in the deep EEP, and in similar records from the Pacific and Southern Ocean, are interpreted as the occurrence of carbonate dissolution in the deep ocean (derived from the increased biological pump efficiency and respired CO_2 accumulation), which would have further contributed to marine CO_2 uptake during the last glacial period via an increase in average ocean alkalinity.

Overall, these results contribute to our understanding of G/IG CO_2 changes by demonstrating the contribution of the ocean circulation to enhanced carbon sequestration at the LGM, both via direct impacts of the soft tissue pump and indirectly via $CaCO_3$ dissolution (alkalinity) effects. The results presented here also raise new questions, and emphasise how the "biogeochemical fingerprint" approach applied in this thesis by combining reconstructions of ^{14}C, $\delta^{13}C$, $[CO_3^{2-}]$ and oxygenation, might provide a complementary effort to constrain changes in the biological pump at the LGM, thus providing a template for future studies.

A wider application of the multiproxy approach followed in this thesis at higher temporal resolution in key areas of the ocean, and also in conjunction with biogeochemical numerical models, has the potential to better quantify the magnitude of the carbon inventory changes across reservoirs and thus, their impacts on atmospheric CO_2 over the late Pleistocene.

APPENDIX

Tables

Table A1. **Compiled radiocarbon data from core ODP1240.** Benthic (mixed) and planktonic (*N. dutertrei*) radiocarbon dates (δ^{13}C-normalised, without reservoir age correction and uncalibrated to calendar years), and B-P offsets from core ODP1240. *These dates represent the average of two consecutive intervals (77/78 and 117/118) in order to be able to compare with the benthic dates, where two consecutive intervals were combined due the low carbonate abundance of each interval. **These intervals are not exactly the same for planktonic and benthic foraminifera, but immediately consecutive. ***The B-P radiocarbon errors represent the addition of planktonic and benthic 1σ radiocarbon errors. Note that the discarded B-P offset intervals are marked in italics and highlighted in grey.

Benthic dates summary				Planktonic dates summary				B-P		
Depth cm	^{14}C age (benthic) ^{14}C yr	±1σ ^{14}C yr	Species	Depth cm	^{14}C age (planktonic) ^{14}C yr	±1σ ^{14}C yr	Species	Depth cm	B-P ^{14}C yr	±1σ *** ^{14}C yr
6	4,242	38	mixed benthics	6	3,243	27	*N.dutertrei*	6	999	65
14	5,130	48	mixed benthics	14	4,136	27	*N.dutertrei*	14	994	75
26	5,285	33	mixed benthics	26	5,154	32	*N.dutertrei*	*26*	*131*	*65*
38	8,885	47	mixed benthics	38	8,046	37	*N.dutertrei*	38	839	84
				77	8,583	45	*N.dutertrei*			
				78	9,292	43	*N.dutertrei*			
77.5	9,677	57	mixed benthics	77.5	*8,938	44	*N.dutertrei*	77.5	740	101
**101.5	10,875	76	mixed benthics	**102	10,089	61	*N.dutertrei*	101.5	786	137
				117	9,145	44	*N.dutertrei*			
				118	9,631	46	*N.dutertrei*			
117.5	10,095	62	mixed benthics	117.5	*9,388	45	*N.dutertrei*	117.5	707	107
**152	12,934	64	mixed benthics	**153	11,964	55	*N.dutertrei*	152	970	119
177	13,801	67	mixed benthics	177	12,492	58	*N.dutertrei*	177	1,309	125
221	15,922	86	mixed benthics	221	14,794	77	*N.dutertrei*	221	1,128	163
223	14,933	83	mixed benthics	223	14,454	70	*N.dutertrei*	*223*	*479*	*153*
229	15,630	79	mixed benthics	229	13,947	79	*N.dutertrei*	229	1,683	158
261	18,152	107	mixed benthics	261	16,713	91	*N.dutertrei*	261	1,439	198
289	17,307	91	mixed benthics	289	16,859	86	*N.dutertrei*	*289*	*448*	*177*
316	19,756	118	mixed benthics	316	17,485	94	*N.dutertrei*	316	2,272	212
318	20,946	178	mixed benthics	318	19,492	154	*N.dutertrei*	318	1,454	332
348	22,753	159	mixed benthics	348	20,705	116	*N.dutertrei*	348	2,049	275

Table A2. Reservoir age estimates for ODP1240. Selected tie-points from the alignment between $U^{K'}_{37}/\delta^{18}O_{sw\ (G.\ ruber)}$ and $\delta^{18}O_{(Greenland\ ice\text{-}cores)}$ and estimated shallow sub-surface reservoir ages (from the calendar ages obtained from the tie-points (BEST ESTIMATE) and with an error of ±200 yr (UPPER AND LOWER ESTIMATE)). *^{14}C date (Pena et al., 2008b) corrected for modern reservoir age = 700 yr and calibrated, using the IntCal09 calibration curve (Reimer et al., 2009), by Bchron (Parnell et al., 2008). ** The interpolated planktonic ^{14}C from ODP1240 dates is the same for all reservoir ages estimates (BEST, LOWER AND UPPER) since the core depths do not vary. All planktonic dates were used for the planktonic ^{14}C interpolation since they did not present any apparent anomaly. ***Modern shallow sub-surface reservoir age at 150 m water depth at ODP1240 site.

TIE-POINTS SUMMARY				^{14}C PLANKTONIC**	RESERVOIR AGE ESTIMATES								
					BEST ESTIMATE			LOWER ESTIMATE			UPPER ESTIMATE		
Tie-points ODP1240 (depth) cm	Tie-points ICE CORES (cal. age) yr	Event	Source	Interp. from ODP 1240 planktonic dates yr	Cal. Age from ICE CORES yr	^{14}C atm Interp. from IntCal09 yr	R. Age yr	Cal. Age (-200 yr) yr	^{14}C atm Interp. from IntCal09 yr	R. age yr	Cal. Age (+200 yr) yr	^{14}C atm Interp. from IntCal09 yr	R. age yr
1	1,560	ODP1240 core-top ^{14}C date *		-	-	-	735***	-	-	735***	-	-	735***
129	11,760	YD end	SST/$\delta^{18}O_{sw}$	10,364	11,760	10,124	240	11,560	10,017	347	11,960	10,177	187
181	15,000	HS1-BA transition	SST/$\delta^{18}O_{sw}$	12,701	15,000	12,609	92	14,800	12,499	202	15,200	12,883	-182
249	17,600	HS1 onset	$\delta^{18}O_{sw}$	15,676	17,600	14,440	1,236	17,400	14,275	1,401	17,800	14,596	1,080
259	"	"	SST	16,540	"	"	2,100	"	"	2,265	"	"	1,944
334	23,500	HS2 end	SST	20,139	23,500	19,675	464	23,300	19,401	738	23,700	19,817	322
348	"	"	$\delta^{18}O_{sw}$	20,705	"	"	1,030	"	"	1,304	"	"	888

Table A3. Summary of the radiocarbon dates selected for the estimations of B-P, reservoir ages (R.age) and deep ventilation ages (B-Atm) from the two alignments and the four estimated age models. Note that the discarded intervals in Table A1 are not represented in this table. However, all planktonic dates were used for the planktonic ^{14}C interpolation and for the age models since they did not present any apparent anomaly. (SST) and ($\delta^{18}O_{sw}$) represent data estimated from the SST and $\delta^{18}O_{sw}$ alignments, respectively. * These radiocarbon errors represent the addition of planktonic and benthic 1σ radiocarbon errors.

SUMMARY OF ODP1240 DATES						B-P, R.ages and B-Atm ESTIMATES							AGE MODELS			
Depth ODP1240	^{14}C age	±1σ	Depth ODP1240	^{14}C age	±1σ	B-P		R. ages		B-Atm			From stratigraphic tie-points		From plk^{14}C corr. for the 2 R.age sets	
								(SST)	($\delta^{18}O_{sw}$)	(SST)	($\delta^{18}O_{sw}$)		(SST)	($\delta^{18}O_{sw}$)	(SST)	($\delta^{18}O_{sw}$)
	Mixed benthics			Planktonic (*N.dutertrei*)		B-P	±1σ	R.age	R.age	B-Atm	B-Atm	±1σ*	Cal. age	Cal. age	Cal. age	Cal. age
cm	^{14}C yr	^{14}C yr	cm	^{14}C yr	^{14}C yr	^{14}C yr	^{14}C yr	yr	yr	yr	yr		yr	yr	yr	yr
6	4,242	38	6	3,243	27	999	65	682	682	1,681	1,681	65	2,061	1,976	2,729	2,621
14	5,130	48	14	4,136	27	994	75	653	653	1,647	1,647	75	2,687	2,616	3,705	3,793
38	8,885	47	38	8,046	37	839	84	567	567	1,406	1,406	84	4,563	4,502	8,337	8,201
77.5	9,677	57	77.5	8,938	44	740	101	425	425	1,165	1,165	101	7,651	7,619	9,534	9,688
101.5	10,875	76	102	10,089	61	786	137	339	339	1,125	1,125	137	9,525	9,512	10,085	10,215
117.5	10,095	62	117.5	9,388	45	707	107	282	282	989	989	107	10,776	10,774	10,532	10,590
152	12,934	64	153	11,964	55	970	119	175	175	1,145	1,145	119	13,140	13,118	13,504	13,511
177	13,801	67	177	12,492	58	1,309	125	104	104	1,413	1,413	125	14,728	14,674	14,455	14,395
221	15,922	86	221	14,794	77	1,128	163	1,122	765	2,250	1,893	163	16,325	16,521	15,410	16,465
229	15,630	79	229	13,947	79	1,683	158	1,328	899	3,011	2,582	158	16,594	16,840	16,171	17,042
261	18,152	107	261	16,713	91	1,439	198	2,056	1,211	3,495	2,650	198	17,759	18,355	17,710	18,690
316	19,756	118	316	17,485	94	2,272	212	856	1,096	3,128	3,368	212	22,085	21,598	20,096	19,890
318	20,946	178	318	19,492	154	1,454	332	813	1,092	2,267	2,546	332	22,243	21,715	21,727	21,538
348	22,753	159	348	20,705	116	2,049	275	158	1,030	2,207	3,078	275	24,550	23,520	24,257	23,594

RESUMEN EN CASTELLANO

Resumen

A pesar de que los ciclos climáticos glaciales-interglaciales del Pleistoceno tardío fueron muy probablemente modulados por cambios en la radiación solar, la amplitud completa de estos ciclos solamente se logró con la ayuda de retroalimentaciones dentro del sistema terrestre, incluyendo variaciones en la concentración de CO_2 atmosférico. Se piensa que estos cambios de CO_2 se debieron principalmente a perturbaciones del ciclo del carbono marino. Así, por ejemplo, un aumento en la eficiencia de las bombas marinas de carbono (en concreto, la bomba de solubilidad y la bomba biológica) podrían haber permitido la acumulación de grandes cantidades de CO_2 en el interior del océano, lejos de la atmósfera. El objetivo de esta tesis es investigar la existencia de una acumulación de CO_2 en el océano glacial y evaluar los mecanismos mediante los cuales esto podría haber ocurrido. Con este fin, se han analizado y combinado una serie de trazadores relacionados con cambios en el contenido de carbono en el interior del océano en el testigo ODP1240 situado en el océano Pacífico Este Ecuatorial (EEP) durante la última deglaciación. Estos registros incluyen: la "ventilación oceánica de radiocarbono" como un trazador del tiempo de residencia de las aguas en el interior del océano, la relación B/Ca en foraminíferos bentónicos como trazador de $\Delta[CO_3^{2-}]_{\text{in situ-sat}}$ en aguas profundas (y por lo tanto $[CO_3^{2-}]$), $\delta^{13}C$ como trazador del contenido de carbono respirado, y $\Delta\delta^{13}C_{(\text{epifaunal-infaunal})}$ como estimación del grado de oxigenación de las agua de fondo.

Los resultados demuestran que las aguas profundas y sub-superficiales del EEP estuvieron peor ventiladas durante el último máximo glacial (LGM) con respecto a la época del Holoceno. Esto sugiere un aumento en el tiempo de residencia del carbono en el interior del Pacífico que habría permitido una mayor eficiencia de la bomba de carbono biológica marina, la cuál se podría haber visto incrementada además por un aumento en la productividad exportada local durante el LGM. El aumento en los niveles de carbono respirado en el océano profundo que cabría esperar con estos cambios, se confirma con la reconstrucción de $[CO_3^{2-}]$ (aquí derivada usando la novedosa técnica de LA-ICP-MS), así como con las estimaciones de $\delta^{13}C$ y oxigenación. En conjunto, estos resultados indican que las aguas profundas del EEP estuvieron más enriquecidas en CO_2 respirado y más empobrecidas en oxígeno durante el último período glacial. Esta mayor acumulación de CO_2 respirado en el océano glacial se habría conseguido a expensas de la superficie del océano y la atmósfera. Sin embargo, el $\Delta[CO_3^{2-}]_{LGM\text{-}Holoceno}$ reconstruido en esta ubicación es relativamente pequeño en comparación con los cambios estimados en la ventilación de radiocarbono para el mismo período, lo que sugiere la participación de un mecanismo amortiguador de estos cambios, como podría ser la disolución del carbonato cálcico en el fondo marino. Este mecanismo habría incrementado la alcalinidad media del océano, permitiendo al océano secuestrar aún más CO_2 de la atmósfera durante la glaciación.

1. Introducción

Marco general: Radiación solar y CO_2 en los ciclos Glacial-Interglacial del Pleistoceno tardío

Los últimos 800.000 años se caracterizan por una sucesión de ciclos fríos (glaciales) y ciclos cálidos (interglaciares) de ~100.000 años de duración, que parecen haber sido modulados, en última instancia, por variaciones en la insolación, ya que es el forzamiento externo que domina el clima de la Tierra en escalas de tiempo de 10^4-10^5 miles de años (Hays et al. 1976). Estas variaciones en la insolación se producen por cambios en la excentricidad, oblicuidad y la precesión, que modulan la cantidad de radiación solar que llega a la parte superior de la atmósfera en latitud y a través del ciclo anual (Milankovitch 1941), con periodicidades características de ~100.000 años para la excentricidad de la órbita de la Tierra, ~41.000 para la oblicuidad o inclinación del eje de rotación de la Tierra y ~23.000 para la precesión de los equinoccios, las cuales son claramente visibles en gran cantidad de registros climáticos del pasado (Hays et al. 1976; Shackleton 2000). La sorprendente similitud entre la frecuencia de insolación y de los registros climáticos demuestra una clara relación entre los dos, y es la base de la hipótesis de que cambios en la insolación han modulado los cambios climáticos del pasado, principalmente mediante la intensidad de la radiación solar a 65ºN, crucial para la estimulación del cambio climático global a través de su impacto en el derretimiento de la capa de hielo en verano.

A pesar de la fuerte correspondencia entre la periodicidad astronómica y la variabilidad climática, se ha observado que la magnitud de los cambios en la insolación (el presunto forzamiento) no está siempre relacionado con la amplitud de las transiciones glacial/interglacial (G/IG, la presunta respuesta) (Paillard, 2001), lo que apunta a un proceso "no lineal " que vincula insolación y cambio climático (Imbrie & Imbrie 1980). De hecho, los archivos climáticos muestran que los ciclos G/IG, aparte de concordar en general con cambios en la radiación solar, están marcados por cambios en el volumen de hielo/nivel del mar, cobertura vegetal, polvo atmosférico y CO_2 atmosférico, todos ellos afectando el balance global de energía a través de cambios en el albedo del planeta y en las emisiones. Por tanto, mientras que la insolación actuaría como el "marcapasos" del cambio climático G/IG, parece que son las retroalimentaciones internas del sistema terrestre, en respuesta al cambio de insolación, las responsables de "empujar" el clima de la Tierra entre períodos glaciales e interglaciales (Paillard 2001; Köhler et al. 2010).

El volumen de hielo y las concentraciones de gases de efecto invernadero atmosférica (principalmente CO_2) emergen como los "ingredientes" más importantes de cada una de estas categorías. Modelos numéricos apoyan esta teoría sugiriendo que los ciclos G/IG se podrían ver como el resultado de los efectos no lineales de la insolación en la capa de hielo, y se amplificarían por el cambio de CO_2 atmosférico (e.j. Abe-Ouchi et al. 2013; Huybers 2006; Paillard 2001). De esta manera, el cambio en la concentración de CO_2 atmosférico debido a variaciones en el intercambio de este gas entre los diferentes reservorios de carbono, se ha propuesto como uno de los retroalimentadores internos más importantes para explicar la amplitud, y quizás también la duración de los ciclos G/IG.

Esto es sugerido, en parte, por el hecho de que las concentraciones de CO_2 medidas en las burbujas de aire atrapadas en los testigos de hielo muestran una correlación sorprendente con el cambio climático global, con concentraciones de CO_2 más bajas durante períodos glaciales y más altas durante períodos interglaciares, con una diferencia de ~ 80-100 ppm (Barnola et al. 1987; Petit et al. 1999; Siegenthaler et al. 2005) (Fig 1).

Explicar este cambio de CO_2 en la atmósfera entre períodos fríos y cálidos sigue siendo un reto en la comunidad paleoclimática, pero cada vez está más claro que estos cambios deben haber venido de la combinación de varios procesos interrelacionados, lo que sugiere que algún reservorio (o combinación de reservorios) se habrían comportado como una «caja» capaz de acumular lentamente una cantidad

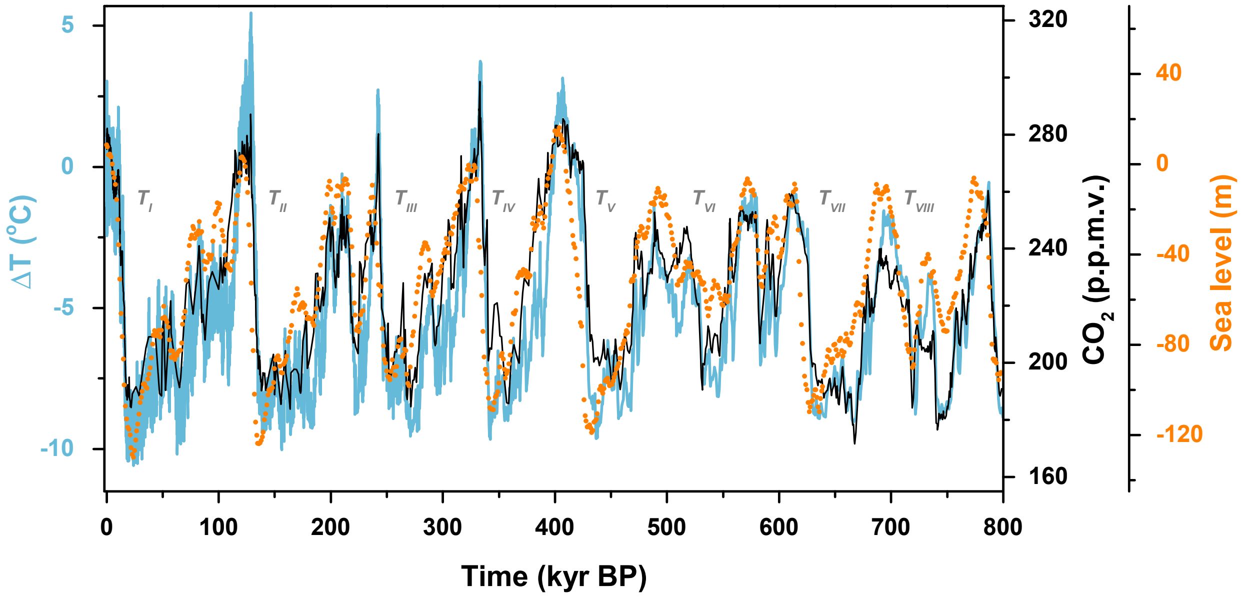

Figura 1. Variabilidad climática en los últimos 800.000 años, indicando la coherencia entre los ciclos de temperatura del aire (línea azul; Jouzel et al. 2007), volumen de hielo (puntos naranjas; Spratt & Lisiecki 2016) y CO_2 atmosférico (línea negra; Lüthi et al. 2008). Las últimas ocho terminaciones glaciales se indican mediante T_I-T_{VIII}.

de CO_2 liberándolo "rápido" de nuevo a la atmósfera después de algún tiempo. Por lo tanto, una de las preguntas más intrigantes y apremiantes en las investigaciones paleoclimáticas es dónde se podría haber "ocultado" este CO_2 durante un período glacial, cómo se habría almacenado allí, y cómo se habría liberado posteriormente a la atmósfera durante el cese glacial.

Además de la atmósfera, el ciclo global del carbono involucra a la litosfera, la biosfera terrestre y al océano. Aunque todos estos reservorios, en cierta medida, podrían haber jugado un papel en las variaciones atmosféricas de CO_2 durante los ciclos G/IG, por un lado, el intercambio de CO_2 entre la atmósfera y la litosfera es normalmente un proceso muy lento, y por lo tanto poco probable en escalas de tiempo G/IG (Sigman & Boyle 2000). Por otro lado, la biosfera terrestre parece haber actuado como una fuente de CO_2 a la atmósfera en lugar de un sumidero, aumentando así el contenido de CO_2 en la atmósfera en ~18 ppm, ya que las condiciones glaciares generalmente frías y secas habrían reducido la producción de plantas en áreas importantes de captación de carbono. Esto nos deja el océano como el candidato más plausible que podría haber almacenado una cantidad significativa de CO_2 durante los períodos glaciales del Pleistoceno (Broecker 1982). De hecho, esto no es muy sorprendente, ya que el océano actual contiene ~17 veces más carbono que la biosfera terrestre y ~60 veces más que la atmósfera (Sarmiento & Gruber 2004), lo que hace del océano un controlador fundamental de la concentración de CO_2 atmosférico en escalas de tiempo G/IG. Por otra parte, el ciclo del carbono marino está intrínsecamente ligado a los ciclos biogeoquímicos globales y tiene una química marina complicada, lo que hace al CO_2 especial en comparación con otros gases en el océano (Sarmiento & Gruber 2004).

Química del cabonato y su ciclo en el mar

El sistema del carbonato marino es extremadamente importante, ya que controla el pH (acidez) del océano, donde se producen muchas reacciones dependientes del pH, con implicaciones para los ciclos biogeoquímicos y la vida del océano. Cuando el CO_2 se disuelve en agua de mar, se hidrata y se producen varias reacciones:

$$CO_{2(aq)} + H_2O \underset{K_0}{\longleftrightarrow} H_2CO_3 \underset{K_1}{\longleftrightarrow} HCO_3^- + H^+ \underset{K_2}{\longleftrightarrow} CO_3^{2-} + 2H^+ \qquad (1)$$

donde K_0, K_1 y K_2 son las constantes de equilibrio de cada reacción ácido-base, y dependen de la temperatura y la salinidad del agua de mar (Zeebe & Wolf-Gladrow 2001). Existen dos parámetros en el sistema del carbonato muy útiles y ampliamente utilizados ya que son conservadores, es decir, son independientes de la temperatura y la presión en el interior del océano: la concentración de todas las especies de carbono inorgánicos en el agua de mar (DIC por sus siglas en inglés) (Ecuación 2); y la medida del exceso de bases (aceptores de protones) y ácidos (donantes de protones), o lo que es lo mismo la capacidad de amortiguación del sistema (alcalinidad, ALK por sus siglas en inglés) (Ecuación 3). Ambos parámetros se ven afectados por otras disociaciones que ocurren en el agua de mar, pero que a menudo y por simplicidad no se tienen en cuenta ya que contribuyen en pequeña proporción.

$$DIC \approx [HCO_3^-] + [CO_3^{2-}] \qquad (2)$$

$$ALK \approx [HCO_3^-] + 2[CO_3^{2-}] \qquad (3)$$

La invasión de CO_2, por tanto, provoca un aumento del DIC (de manera similar, su retirada disminuye el DIC), mientras que por otro lado, ninguno de estos procesos causan cambios en la ALK, ya que el equilibrio de cargas se mantiene. Esto se puede observar más claramente en la reacción (4) que ilustra de una forma alternativa la estequiometría del equilibrio termodinámico cuando el CO_2 se disuelve en agua marina:

$$CO_2 + H_2O + CO_3^{2-} \leftrightarrow 2HCO_3^- \qquad (4)$$

La cantidad de CO_2 que se disuelve en el agua de mar, es decir, el intercambio de CO_2 atmósfera-océano, depende de la presión parcial (*p*CO_2) en ambos reservorios, que a su vez depende principalmente de las propiedades superficiales del océano ya que el CO_2 atmosférico se homogeniza con relativa rapidez. Así pues, la *p*CO_2 del agua marina se establece mediante salinidad, temperatura, DIC y ALK (Sarmiento & Gruber 2004), como se puede ver en la siguiente ecuación:

$$pCO_2 \approx \frac{K_2}{K_0 \cdot K_1} \frac{(2DIC - ALK)^2}{ALK - DIC} \qquad (5)$$

Las constantes de equilibrio, como se mencionó anteriormente, están controladas por la temperatura y la salinidad del agua de mar, que están fuertemente influenciadas por la temperatura atmosférica local, el balance de evaporación-precipitación y el cambio global de volumen de hielo. La dependencia de la temperatura/salinidad de las constantes de disociación hace que la solubilidad del CO_2 aumente en agua fría y dulce, de tal manera que una temperatura y salinidad más bajas darán lugar a un aumento de la *p*CO_2 en el agua marina para un determinado DIC y

ALK, y viceversa. Ahora bien, ¿qué proceso(s) controlan DIC y ALK y por lo tanto, en última instancia, la $p\mathrm{CO}_2$ del agua de mar independientemente de la temperatura y la salinidad?

La comprensión de estos otros procesos y su relación con los cambios inducidos por el clima en la solubilidad del CO_2 y en el intercambio gaseoso atmósfera-océano, es fundamental para el estudio del clima del pasado y su relación con el ciclo del carbono.

Así pues, la existencia actual de gradientes verticales de DIC y ALK entre la superficie y el interior de todos los océano, sugiere la existencia de procesos activos en el sistema del carbonato responsables de mantener estos gradientes químicos en contra de la homogeneización que la circulación oceánica tiende a producir (Sarmiento & Gruber 2004). Estos procesos se refieren a menudo como “bombas de carbono marino” (basado en la analogía de una bomba que mantiene un gradiente de presión entre dos ubicaciones), que son comúnmente subdivididas en la “bomba de solubilidad” y la “bomba biológica”, cuando este último se subdivide a su vez en el “bomba de tejido blando” y “bomba de carbonato” (Fig. 2) (Volk & Hoffert 1985).

La denominada “bomba de solubilidad” se ha abordado, en parte, anteriormente, y depende por tanto de la eficiencia de intercambio de CO_2 atmósfera-océano (e.j. Wanninkhof 1992) y de la solubilidad del CO_2. Su función por tanto es equilibrar la $p\mathrm{CO}_2$ de agua de mar con la de la atmósfera en función de las propiedades del agua marina, en particular temperatura y salinidad, con impactos en el DIC, pero no en la ALK. Debido a esto, los efectos de la bomba de solubilidad son directamente depen-

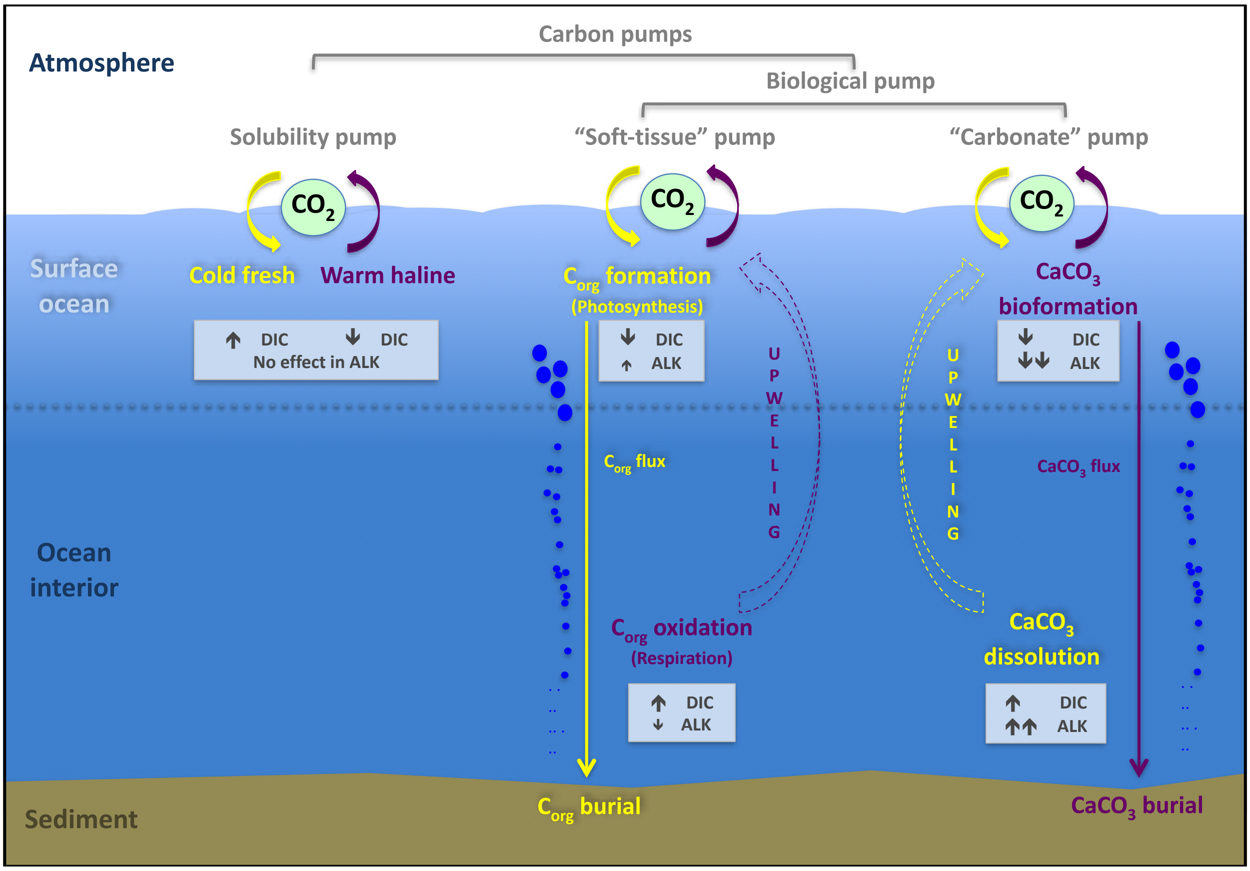

Figura 2. Representación esquemática de las bombas de carbono marinas, incluyendo la bombas de solubilidad y las biológicas. La división arbitraria entre el océano superficial e interior se indica mediante una línea horizontal. Las flechas y texto en color amarillo indican mecanismos que tienden a contribuir en la absorción de CO_2 atmosférico, mientras que las flechas y texto en color morado indican mecanismos que tienden a contribuir en la liberación de CO_2 a la atmósfera. Los recuadros grises resumen el efecto de tales mecanismos en el DIC y la ALK. Los círculos azules representan las partículas de carbono orgánico (C_{org}) y de carbonato cálcico ($CaCO_3$), cuyo tamaño representa el grado de disminución de la oxidación/disolución con la profundidad, a medida que las partículas se hunden (modificada de Heinze et al. 1991).

dientes de la circulación de los océanos. Esta idea ha llevado a algunos científicos a utilizar el termino de "bomba física", con el fin de resaltar más claramente el papel tan importante que desempeña la física del océano, que combinaría los efectos de la solubilidad de CO_2 con los del transporte oceánico. Por lo tanto, si bien los procesos de cambio de solubilidad y de intercambio atmósfera-océano son muy importantes en el ciclo de carbono, parece que la circulación de los océanos y su interacción con las bombas biológicas de carbono serían los mayores responsables de las variaciones en los gradientes de DIC y ALK observados en la columna de agua (Fig. 2).

La "bomba de tejido blando" mantiene un gradiente químico en la columna de agua mediante la fijación de CO_2 en la capa superior del océano a través de la fotosíntesis, el cual es posteriormente liberado en el interior del océano a través de la respiración (también llamada oxidación o degradación) de la materia orgánica llevada a cabo por microorganismos. Por lo tanto, la fotosíntesis fija CO_2 provocando una disminución del DIC en la superficie oceánica, mientras que la respiración produce un aumento proporcional del DIC en el interior del océano cuando el CO_2 es liberado (Fig. 2). Estos procesos también producen un ligero cambio en la ALK (en dirección opuesta a la del DIC), ya que consumen/liberan protones asociados a la fijación/remineralización de nutrientes (especies cargadas tales como NO_3^-) (Fig. 2). Por lo tanto, la fotosíntesis (respiración) es un proceso análogo a la liberación de CO_2 a la atmósfera (invasión) en tanto que disminuye (aumenta) el DIC, pero difieren en que la fotosíntesis (respiración) también afecta ligeramente a la ALK.

La «bomba de carbonato» se refiere a la formación/disolución del carbonato cálcico biogénico ($CaCO_3$) en la superficie/profundidad del océano, respectivamente, y es la que produce mayores cambios en la ALK del océano. Organismos como cocolitofóridos y foraminíferos construyen sus conchas con carbonato cálcico extrayendo así CO_3^{2-} y Ca^{2+} de la superficie (es decir, $CO_3^{2-} + Ca^{2+} \leftrightarrow CaCO_3$), que es devuelto al interior del océano cuando estos mueren y se hunden. Por lo tanto, la formación de $CaCO_3$ biogénico en la superficie marina reduce el DIC y la ALK, y viceversa en el océano profundo cuando se disuelve, en una proporción de 1: 2 (DIC: ALK) (Fig. 2).

Teniendo en cuenta todos los procesos descritos, se puede concluir que la pCO_2 de la superficie del océano disminuiría con la disminución de DIC (mediante la liberación de CO_2 a la atmósfera y/o un aumento de las tasas de fotosíntesis), y también podría disminuir con el aumento de la ALK (mediante un aumento en la disolución de $CaCO_3$), y viceversa. Esto muestra un efecto antagonista dentro de la bomba biológica, entre la bomba de carbonato y la bomba de tejido blando, de tal manera que el impacto sobre la pCO_2 de la superficie del océano dependerá de la abundancia de organismos calcificadores *versus* no-calcificadores en las capas superiores del océano. Sin embargo, la bomba biológica siempre tenderá a disminuir la pCO_2 de la capa superior del océano, ya que el grueso de la productividad biológica exportada consiste mayormente en carbono orgánico en lugar de carbonato. En el interior del océano, sin embargo, el balance de DIC y ALK a una determinada profundidad dependerá más de los diferentes perfiles de remineralización que se aplican al carbono orgánico y carbonato. Una influencia adicional provendrá de cambios en la posición de la Profundidad de Compensación del Carbonato (CCD, por sus siglas en inglés), que pueden ser causados por cambios en la circulación oceánica y en la bomba de tejido blando, pudiendo resultar en la adición de iones carbonato al océano profundo mediante la disolución de sedimentos de carbonato previamente depositados.

Ahora bien, cómo podría haber sido el funcionamiento de todos estos mecanismos en el pasado para haber producido una reducción del CO_2 atmosférico durante el último período glacial?

Mecanismos marinos propuestos para la disminución de CO_2 en la atmósfera glacial

Un descenso de la temperatura atmosférica durante el inicio de la glaciación debido a variaciones en la radiación solar y a retroalimentaciones internas habría enfriado la superficie del mar, aumentando así la solubilidad del CO_2 provocando una disminución en el contenido de CO_2 atmosférico de ~30 ppm (Sigman & Boyle 2000). Sin embargo, la reducción de las temperaturas durante el glacial, también habrían ido acompañada por un aumento, en promedio, de la salinidad del océano debido a la acumulación de agua dulce en las capas de hielo, contrarrestando así parcialmente el aumento en la solubilidad de CO_2 impulsada por la temperatura, añadiendo ~18 ppm a la atmósfera (Sigman & Boyle 2000; Sarmiento & Gruber 2004). Por tanto, teniendo en cuenta la bajada de temperaturas, el aumento de salinidad en la superficie del mar, y el menor contenido de carbono en la vegetación terrestre que se mencionó anteriormente, las estimaciones para períodos glaciales auguran un cambio neto de CO_2 alrededor de 0 ppm (Sigman & Boyle 2000). Esto apunta a que los cambios en el resto de bombas marinas de carbono habrían jugado también un papel importante en la disminución de CO_2 atmosférico durante el último glacial (Volk & Hoffert 1985; Sigman et al. 2010; Kohfeld & Ridgwell 2009).

En conjunto, los mecanismos marinos que podrían haber contribuido a las variaciones de CO_2 atmosférico durante las glaciaciones, se podrían clasificar en términos generales como derivados principalmente de:

1) variaciones en la tasa de solubilidad del CO_2 y/o en la eficiencia del intercambio gaseoso atmósfera-océano, específicamente por ejemplo, cambios en la banquisa de hielo en las latitudes altas del hemisferia sur (Stephens & Keeling 2000), o en la tasa de circulación oceánica debido a una alteración en los campos de viento (Toggweiler 1999), o en la densidad/estratificación del océano debido a la formación de salmuera en el Océano Austral (Adkins et al. 2002; Roberts et al. 2016);

2) variaciones en la eficiencia de las bombas biológicas de carbono debidos, por ejemplo, a cambios en la productividad biológica exportada por cambios en la llegada de hierro (Calvo et al. 2004; Martínez-García et al. 2014), o en la distribución de Si desde el Océano Austral hasta latitudes más bajas (Brzezinski et al. 2002; Matsumoto et al. 2002), o en la profundidad de remineralización (Matsumoto 2007; Kwon et al. 2009);

3) variaciones globales en la química del carbonato en el océano, como por ejemplo, en la alcalinidad media de los océanos debido a la compensación/disolución de carbonato en el fondo marino (Keir 1995) y/o en la pérdida de carbonato biogénico y deposición de coral en la plataforma marina (Berger 1982; Opdyke & Walker 1992).

Es importante destacar que las categorías descritas anteriormente son útiles para organizar nuestro pensamiento, pero que probablemente todos estos mecanismos hayan operado en conjunto. Por otra parte, a pesar de las diferencias sustanciales entre todos ellos, la mayoría implicaría, de forma directa o indirecta, cambios en la eficiencia de la bomba biológica (Volk & Hoffert 1985).

Si la eficiencia de la bomba biológica se define en términos de su capacidad para almacenar CO_2 en el interior del océano lejos de la superficie del océano y por lo tanto de la atmósfera, encontramos que estos cambios se podrían conseguir mediante variaciones en la “fuga” de la bomba biológica de carbono (la bomba de tejido blando principalmente), o por cambios en su “fuerza”. Aquí, fuga puede definirse como el flujo de retorno de nutrientes remineralizados y carbono del interior del océano a la superficie del mar como resultado de la circulación de retorno a gran escala y de las surgencias, y la fuerza se refiere a las tasas de productividad exportada. Así, por ejemplo, los mecanismos mencionados anteriormente en la categoría 1) harían referencia principalmente a cambios en la fuga de la bomba de tejido blando, mientras que los de la categoría 2) implicarían cambios en su “fuerza”. Los mecanismos que figuran en la categoría 3) podrían surgir, en principio, como respuesta positiva a la eficiencia de la bomba de tejido blando (es decir, la acumulación de carbono respirado en las profundidades del océano disminuiría la concentración de ión carbonato y la aumentaría la disolución de carbonato cálcico), aunque también podrían surgir independientemente como resultado de una reducción en la deposición de carbonato.

Así, un aumento en la eficiencia de la bomba biológica de carbono, debido a una disminución en su pérdida hacia la atmósfera y/o un aumento de la productividad exportada, lo que llevaría a un aumento en la alcalinidad media del océano como consecuencia (y posiblemente en asociación con una reducción en la tasa de intercambio de CO_2 entre la atmósfera y el océano), representa una forma particularmente efectiva de aumentar el almacenamiento de carbono en el océano profundo durante el último período glacial, lo que implicaría una combinación de procesos físicos, biológicos y geoquímicos.

Actualmente carecemos de una explicación completa de las causas de las variaciones de CO_2 atmosférico entre períodos G/IG, y mucho menos de una confirmación clara de que una cantidad significativa de CO_2 estuvo almacena en el interior del océano durante el último glacial. La mayoría de los mecanismos propuestos se basan en estudios con modelos numéricos, los cuales son de gran utilidad para desarrollar hipótesis, pero que han de ser validados mediante evidencias con datos reales. ¿Somos capaces de encontrar tales pruebas en el océano profundo durante la glaciación? ¿Qué áreas sería importante tener en cuenta? ¿Qué trazadores serían clave para inferir el estado del ciclo del carbono, así como el inventario de carbono marino en el pasado? ¿Existen nuevas técnicas que nos podrían ayudar a explorar y entender mejor algún trazador?

Se piensa que el Océano Austral es un lugar clave para buscar dichas pruebas, ya que actualmente es la zona donde las masas de agua más envejecidas con un alto contenido en CO_2 hacen su primer contacto con la atmósfera, y donde además la mayor parte del océano interior intercambia gases con la atmósfera (Gebbie & Huybers 2011; Primeau 2005). Sin embargo, es importante monitorear otros lugares, como por ejemplo el Pacífico profundo que es relativamente homogéneo y representa la mayor parte del volumen del océano, o más específicamente el Pacífico Este Ecuatorial (EEP, por sus siglas en inglés) que está conectado directamente tanto con el Océano Austral como con el Pacífico Norte a través del transporte y el ascenso de aguas intermedias derivadas de estas altas latitudes.

Hay algunos trazadores específicos para reconstrucciones del ciclo del carbono que son extremadamente útiles cuando se combinan. Por ejemplo, la estimación de cambios en la tasa de ventilación del océano utilizando mediciones de radiocarbono en superficie y fondo y en comparación con la atmósfera, combinada con algunos parámetros del sistema del carbonato como [CO_3^{2-}] o pH, así como estimaciones de la cantidad de carbono producto de la respiración en las profundidades del océano a través de variaciones en el contenido de O_2 o de isótopos estables de carbono ($\delta^{13}C$), pueden indicar cambios en la acumulación de CO_2 a través de la bomba biológica de carbono, incluso llegando a obtener estimaciones cuantitativas.

Mediante el uso de estas técnicas y trazadores, algunos estudios previos han inferido una mayor acumulación de CO_2 en las aguas profundas del sector atlántico del Océano Austral durante la última glaciación, por ejemplo, en base a estimaciones de radiocarbono que indican una reducción en la ventilación a lo largo de la columna de agua (Skinner et al. 2010; Burke & Robinson 2012), así como niveles más bajos de O_2 y [CO_3^{2-}], que indican una mayor acumulación de CO_2 respirado en el fondo del océano (Gottschalk et al. 2015; Gottschalk et al. 2016). Pruebas similares se han llevado a cabo también en el Océano Pacífico, indicando una menor ventilación de radiocarbono en algunas áreas (e.j. Skinner et al. 2015; Galbraith et al. 2007), así como concentraciones más bajas de O_2 (e.j. Bradtmiller et al. 2010) y un contenido menor en $[CO_3^{2-}]$ (e.j. Yu & Elderfield 2007; Allen et al. 2015). Sin embargo, las reconstrucciones de alguno de estos trazadores en otras zonas del Pacífico no siempre concuerdan (e.j. Broecker et al. 2008; De Pol-Holz et al. 2010; Lund et al. 2011). Estas discrepancias se deben tratar con el fin de comprender adecuadamente el ciclo del carbono marino en la mayor de las cuencas de los océanos del mundo. Una explicación simple es que los desajustes aparentes podrían surgir de las diferentes técnicas que se aplican, y cómo se aplican en cada caso. Por ejemplo, para la estima de las edades de ventilación de radiocarbono durante el glacial, generalmente, no se tiene en cuenta la edad del reservorio superficial. Otro ejemplo es la técnica aplicada para la inferencia de $[CO_3^{2-}]$ en el pasado, cuya estimación se realiza cada vez más mediante el análisis de ratios de B/Ca en la concha de calcita de foraminíferos bentónicos, después de que Yu & Elderfield (2007) establecieran una relación empírica entre el estado de saturación de calcita $\Delta[CO_3^{2-}]$ y el ratio B/Ca. Estos análisis se realizan normalmente utilizando la técnica de solución-ICPMS. Sin embargo, este método no proporciona una visión de la incorporación de B en las conchas de foraminíferos, y por lo tanto puede pasar por alto información acerca de cómo el trazador podría o no funcionar en última instancia. Otras técnicas como LA-ICPMS permiten esta visión, pero su aplicación en análisis de B/Ca y otros elementos traza es aún relativamente novedosa. Con un mayor desarrollo, la técnica LA-ICPMS permitiría observar la distribución de B (y otros oligoelementos) en las conchas de foraminíferos, lo que sería muy útil para entender mejor los procesos que subyacen al trazador B/Ca y cómo los sesgos en las medidas podrían tener un impacto sobre la interpretación de los resultados.

2. Objetivos de la tesis

El objetivo principal de esta tesis es inferir la función del Pacífico Este Ecuatorial profundo en la evolución global del ciclo de carbono durante la última transición glacial-interglacial basado en la aplicación de algunos de los trazadores del ciclo del carbono descritos anteriormente, tales como radiocarbono (^{14}C), $[CO_3^{2-}]_{B/Ca\ based}$ y $\delta^{13}C$. Un aspecto innovador de esta tesis es la aplicación de la técnica LA-ICPMS para análisis de elementos trazas (en particular, B/Ca) en la concha de foraminíferos.

Más concretamente, los objetivos de esta tesis son:

- Estimar nuevos modelos de edad teniendo en cuenta los cambios en la edad del reservorio superficial durante la deglaciación.

- Inferir la evolución del ciclo del carbono marino en aguas superficiales y profundas del EEP en el pasado, utilizando radiocarbono, isótopos estables y reconstrucciones del sistema de carbonato.

- Configurar la técnica de ablación por láser (LA-ICPMS) para los estudios de B/Ca en foraminíferos.

- Comprobar la validez del ratio B/Ca como indicador de $\Delta[CO_3^{2-}]$ cuando se analiza utilizando la técnica LA-ICPMS.

- Interpretar nuevos resultados de radiocarbono, isótopos estables y reconstrucciones de iones de carbonato emergente en el contexto de otros paleo-datos disponibles procedentes de los océanos Pacífico y Austral, con el fin de conseguir una visión integrada de los cambios en el ciclo de carbono en la cuenca del océano más grande del mundo.

- Proporcionar nuevos conocimientos sobre la función del océano en el ciclo del carbono y en el cambio climático global del pasado mediante la evaluación de la magnitud y las causas de la variación en el inventario de carbono marino desde el último período glacial.

3. Material y métodos

ODP Site 1240: testigo de sedimento, área y oceanografía moderna

La secuencia sedimentaria ODP Site 1240 (Ocean Drilling Program, Leg 202, por sus siglas en inglés y de aquí en adelante nombrado como ODP1240 por simplicidad), se recogió utilizando un sacatestigos de pistón avanzado a bordo del buque de investigación JOIDES Resolution en 2002. Este zona está situada en el flanco norte de la Cordillera de Carnegie (0° 01.31’N, 86° 27.76’W) en el margen suroeste de la Cuenca de Panamá a 2.921 m de profundidad (Mix et al. 2003), en la región oriental del Pacífico Ecuatorial (EEP) (Fig. 3). Además, se encuentra bajo la surgencia ecuatorial del EEP causado por los vientos alisios, que es rica en nutrientes y se caracteriza por un presentar un alto contenido en fósiles y altas tasas de sedimentación (>10-15 cm/1000 años; Mix et al. 2003; Pena et al. 2008), permitiendo mediciones en alta resolución temporal minimizando posibles sesgos. Esta tesis se centra en los primeros ~400 cm del testigo de sedimento cubriendo el período comprendido entre 0 y 30.000 años.

El testigo de sedimento ODP1240 está bañado en una mezcla de Agua Profunda

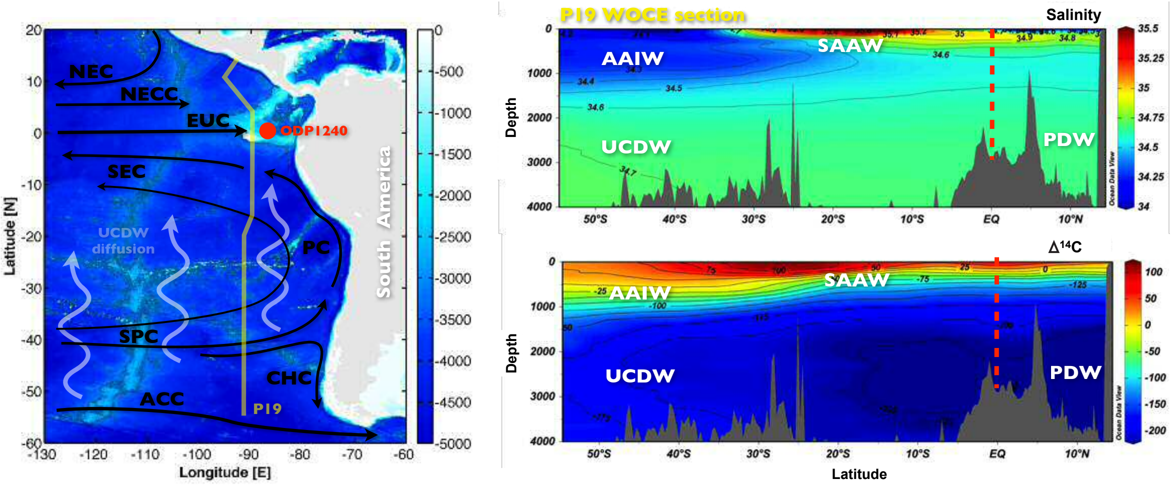

Figure 3. Hidrografía del EEP. En el panel izquierdo, se muestra un mapa de la zona en indicando la batimetría (escala de azules), la ubicación del testigo de sedimento ODP1240 (punto rojo), el transecto WOCE P19 (línea meridional amarilla), y un esquema de la circulación oceánica superficial (flechas negras) y profunda (flechas blancas): Corriente Norecuatorial (NEC), Contracorriente Norecuatorial (NECC), Contracorriente Ecuatorial (EUC), Corriente Surecuatorial (SEC), Corriente de Perú (PC), Corriente del Pacífico Sur (SPC), Corriente del Cabo de Hornos (CHC), Corriente Circumpolar Antártica (ACC) y la difusión hacia el norte de la masa de agua profunda Circumpolar Superior (UCDW). En el panel de la derecha, dos secciones verticales del transecto WOCE P19 mostrando salinidad y $\Delta^{14}C$. Las masas de agua indicadas son: Agua Intermedia Antártica (AIAA), UCDW, Agua Subantártica (SAAW) y Agua Profunda del Pacífico (PDW). La línea roja vertical discontinua indica la ubicación del testigo ODP1240.

de la Corriente Circumpolar Superior (UCDW, por sus siglas en inglés) y de Agua Profunda del Pacífico (PDW, por sus siglas en inglés), ya que ambos ocupan aproximadamente el mismo intervalo de densidad y profundidad en el Pacífico (Talley et al. 2011) (Fig. 3), y se caracterizan por contener bajos niveles de oxígeno, altos niveles de nutrientes y por ser masas de agua envejecidas. La circulación de la sub-superficie en esta ubicación está gobernada por la Contracorriente Ecuatorial (EUC, por sus siglas en inglés), cuyo centro está entre 50-300 m de profundidad fluyendo hacia el este a lo largo de los trópicos (Toggweiler et al. 1991; Lukas 1986; Tsuchiya et al. 1989), y que está alimentada en parte por masas de agua intermedias procedentes de la Antártida (Agua Intermedia Antártica (AAIW) y Agua Modal Subantártica (SAMW)) originadas a partir de la surgencia de Agua Profunda Circumpolar (CDW) en el Océano Austral (Kessler 2006).

Trazadores y metodologías

Todos los trazadores utilizados en el desarrollo de esta tesis han sido analizados en conchas de foraminíferos, cuya composición elemental refleja las condiciones hidrográficas, geoquímicas y climáticas del ambiente en el que se desarrollan, y que por tanto son ampliamente utilizadas para inferir condiciones ambientales marinas del pasado. Las dos especies de foraminíferos utilizadas son: *Cibicides wuellerstorfi* (Schwager 1866), que es una especie de foraminífero bentónico con concha calcárea sólida en forma de gancho con suturas visibles y forma trocospiral (Galloway 1933), cuyo hábitat, en la interfase agua-sedimento, refleja las propiedades del agua de fondo (Lütze y Thiel, 1989); y *Neogloboquadrina dutertrei* (d'Orbigny 1839), que es una especie planctónica que posee una concha con un número variable de cámaras globulares que crecen en forma de espiral (Parker 1962), cuyo hábitat está restringido principalmente a las zonas tropicales (Hilbrecht 1997) y es común en el máximo de clorofila (Fairbanks et al. 1982), así como en zonas de afloramiento superficial.

Radiocarbono. Radiocarbono (^{14}C) es un isótopo radiactivo natural, que se produce en la estratosfera por la interacción de rayos cósmicos con nitrógeno (^{14}N) (Lal & Peters 1967), incorporándose posteriormente a las moléculas de CO_2, las cuales son intercambiadas entre todos los reservorios de carbono, incluyendo el océano. El ^{14}C es una herramienta muy útil y ampliamente utilizada para la datación cronométrica y como trazador del ciclo del carbono. El ^{14}C entra en el océano cuando el CO_2 atmosférico se disuelve en la superficie del océano en función de la diferencia en la presión parcial de este gas entre la atmósfera y el océano, que a su vez depende de las propiedades físicas y químicas del agua de mar. Una vez en la superficie marina, es transportado por la circulación del océano y va decayendo con una vida media de 5.730 años (Godwin 1962), por lo que puede ser utilizado como un marcador de la "edad" de cualquier parcela de agua en el océano. La estimación de dicha edad es compleja ya que está influida, por ejemplo, por la mezcla de diferentes masas de agua cada una con un tiempo de transporte diferente y probablemente con actividades de ^{14}C atmosféricas diferentes en el momento de su formación. A pesar de la complejidad, las mediciones de radiocarbono proporcionan información muy útil acerca de la cantidad de tiempo, en promedio, que una parcela de agua ha estado sin entrar en contacto con la atmósfera, referido comúnmente como “ventilación oceánica de radiocarbono”. Una de las métricas más sencillas y disponibles para estimar la ventilación oceánica, que es la que se aplica en esta tesis, es la diferencia de ^{14}C entre foraminíferos planctónicos y bentónicos (B-P) (Fig. 4). Las diferencias B-P medidas a lo largo de un testigo de sedimento marino, proporcionan una estimación de los cambios en la tasa de ventilación del fondo marino frente a la superficie del océano a lo largo del tiempo. De la misma manera, la diferencia entre el ^{14}C de foraminíferos planctónicos y la atmósfera (a menudo referida como “edad del reservorio superficial”) ofrece información sobre el grado de equilibrio entre los reservorios marino y atmosférico (Fig. 4). Sin embargo, la edad del reservorio superficial no es siempre fácil de estimar, ya que necesita un control de edad independiente para ser estimada con precisión, lo cual a menudo no está disponible o es difícil de obtener. Esta es la razón por la que muchos de los estudios de ventilación oceánica del pasado normalmente aplican valores regionales actuales de reservorios superficiales. En cualquier caso, mediante la combinación de estos dos tipos de diferencias en ^{14}C, es posible inferir cambios en la ventilación del océano profundo con respecto a la atmósfera (B-Atm) (Fig. 4). Estos tres indicadores juntos pueden ayudar a clarificar cambios en el ciclo del carbono y en la circulación oceánica entre períodos glacial-interglacial, así como su papel en la dinámica climática del pasado.

Para poder medir el contenido en ^{14}C de la concha de foraminiferos, el carbono

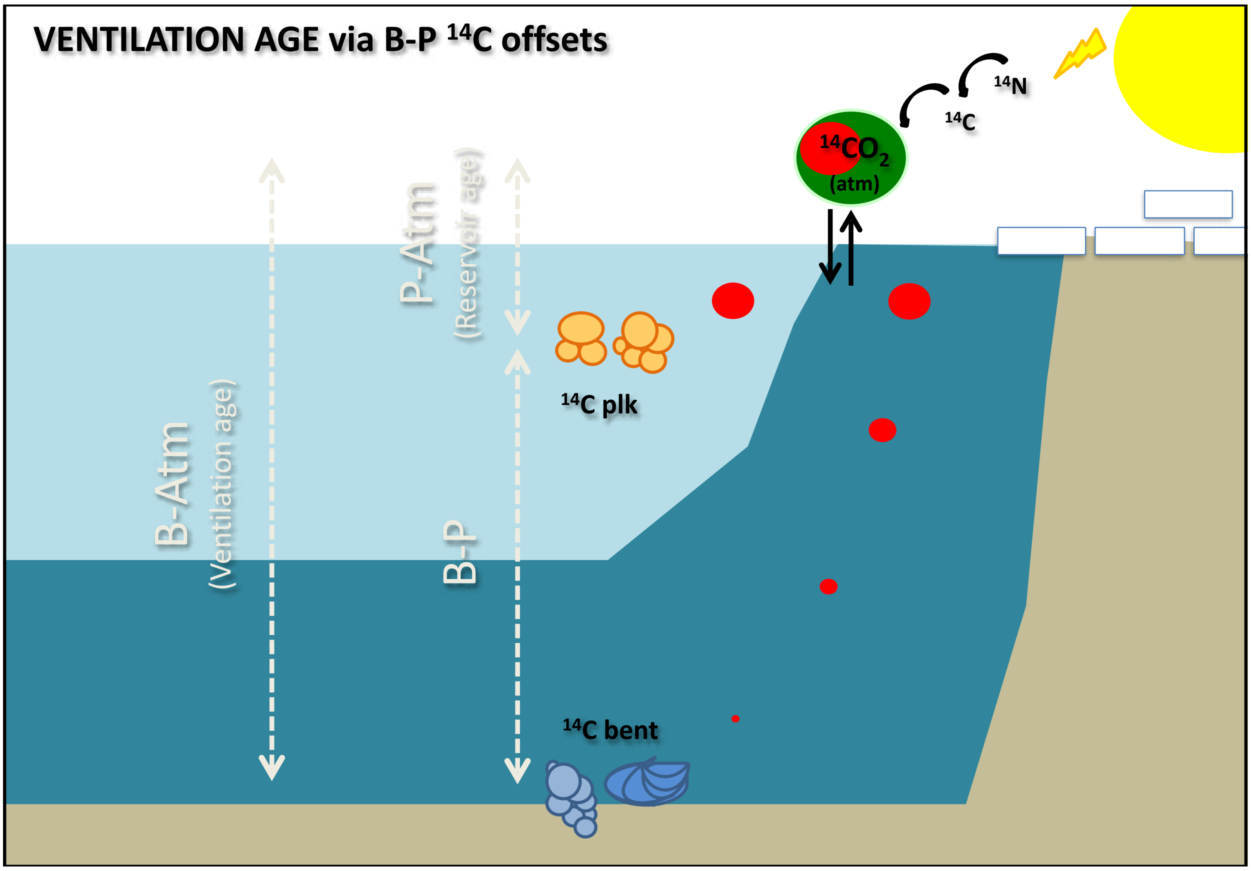

Figura 4. Representación esquemática del ciclo del radiocarbono (^{14}C) entre la atmósfera y el océano y la utilidad de radiocarbono como trazador de la edad de ventilación a través de la diferencia de (^{14}C) entre foraminíferos bentónicos y planctónicos (B-P) y entre foraminíferos bentónicos y la atmósfera (B-Atm). Los átomos de radiocarbono, que se producen en la atmósfera por impactos de rayos cósmicos en los átomos de ^{14}N, se incorporar en las moléculas de CO_2 (círculo verde) que son intercambiadas con la la superficie del océano. Una vez allí, poco a poco son advectadas hacia el interior del océano, lejos del intercambio con la atmósfera, y por tanto el (^{14}C) empieza a decaer de nuevo a átomos de N. El tamaño de los círculos de color rojo representa el nivel de actividad de radiocarbono (cuanto más pequeños, menos actividad, es decir, menos radiocarbono, y viceversa). Las flechas blancas verticales indican las métricas aplicadas en esta tesis para estimar la ventilación oceánica (B-Atm) que se basan, en una primera etapa, en la diferencia de ^{14}C entre foraminíferos bentónicos y planctónicos (B-P), y en segundo lugar, en la diferencia de ^{14}C entre foraminíferos planctónicos y la atmósfera, la llamada “edad de reservorio superficial”. Es importante tener en cuenta que la actividad de ^{14}C en la sub-superficie es inferior a la de la atmósfera (representada por círculos rojos de diferente tamaño), por lo que se requieren estimaciones de la edad del reservorio superficial para estimar de forma precisa tanto la ventilación oceánica como los modelos de edad.

tiene que concentrarse en forma de grafito, pudiendo así ser fácilmente ionizado en un espectrómetro de masas con acelerador (AMS, por sus siglas en inglés). El proceso de grafitación ha sido llevado a cabo en el Godwin Laboratory for Palaeoclimatic Research de la University of Cambridge (Reino Unido). Consiste, resumidamente, en liberar el contenido de carbono de las conchas de calcita en forma de CO_2 mediante disolución en ácido fosfórico, el cual es posteriormente introducido en una línea de vacío donde se reduce a grafito al reaccionar con hierro (que actúa como catalizador) en presencia de H puro al calentarse a 550-650 °C en un reactor (Santos et al. 2004). Las muestras grafitadas fueron analizadas por AMS en el Chrono Centre de la Queen's University Belfast (Reino Unido).

Ratios B/Ca. La incorporación de boro en relación al calcio (B/Ca) en la concha de calcita de foraminiferos ha sido teórica y experimentalmente propuesta como trazador del sistema del carbonato. La teoría del B/Ca tiene sus raíces en las especies disueltas de B en el agua de mar y cómo sus concentraciones relativas y composición isotópica varían en función del pH marino (Hemming & Hanson, 1992) (Fig. 5).

La relación teórica entre B/Ca y el sistema de carbonato puede resumirse de la forma siguiente:

1) El B se encuentra principalmente en el agua de mar en dos especies moleculares disueltas, el ácido bórico ($B(OH)_3$) y el ión borato ($B(OH)_4^-$), que dependen del pH marino y cuya constante de equilibrio estequiométrico (K_B) es cercana al pH marino

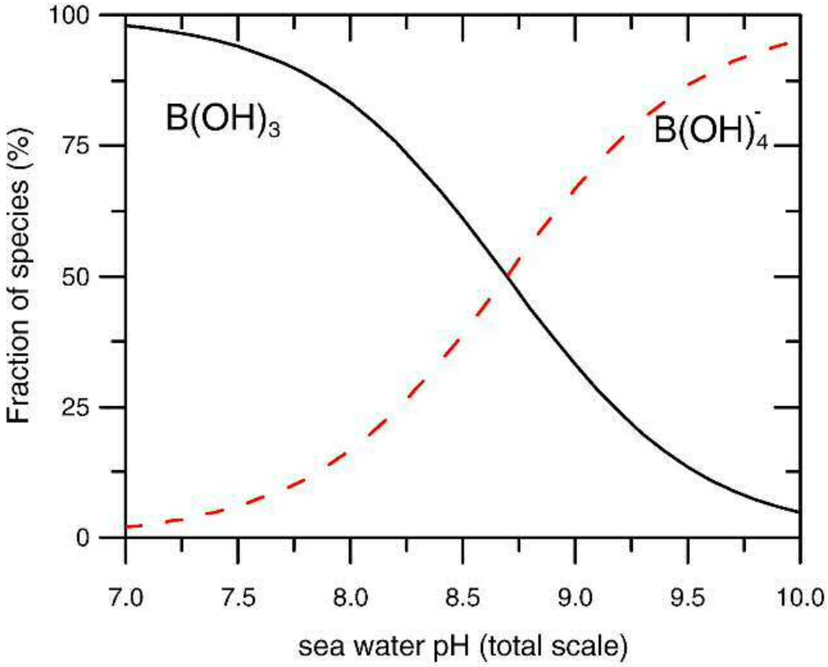

Figure 5. Proporciones de las especies de boro disueltas, $B(OH)_3$ and $B(OH)_4^-$, cambiando con el pH del agua de mar. Las curvas se calculan mediante condiciones típicas de agua de fondo: T = 2 ° C, S = 35, profundidad de la columna de agua = 3500 m utilizando $[B]_{total}$ = 416 µmol/kg, $\delta^{11}B_{agua\ marina}$ = 39,5 ‰, y α = 1,0272 (Figura de Yu et al. 2010).

(pK_B = 8,6) (Fig. 5).

2) Se especula que sólo la especie cargada $B(OH)_4^-$ se incorporan en la calcita biogénica debido a la consistencia encontrada entre los valores isotópicos de carbonato marino actuales y la composición isotópica de $B(OH)_4^-$ en agua de mar (Hemming & Hanson 1992), descrito mediante la siguiente ecuación:

$$CaCO_3 + B(OH)_4^- \leftrightarrow CaHBO_3 + HCO_3^- + H_2O \qquad (6)$$

3) De esta manera, si aumenta el pH del agua de mar, la cantidad de boro disponible para incorporarse en la calcita como $B(OH)_4^-$ aumenta, lo que aumenta los ratios B/Ca en carbonatos marinos.

4) Por lo tanto, como el pH del agua de mar está controlado por la presión parcial de CO_2 (pCO_2) en el agua de mar, que a su vez está determinado por la ALK y el DIC (ALK/DIC), los ratios B/Ca parecen ser una buena herramienta para reconstruir el sistema del carbonato del océano en el pasado.

Aunque la asunción teórica de que el $B(OH)_4^-$ es la principal especie que controla la incorporación de B en carbonato cálcico biogénico es convincente, es un asunto que aún no está completamente resuelto (e.j. Klochko et al. 2009). Sin embargo, se ha demostrado empíricamente que el ratio B/Ca en foraminíferos bentónicos correlaciona con el estado de saturación del carbonato respecto a la calcita en aguas profundas ($\Delta[CO_3^{2-}]$), permitiendo así inferir la concentración de iones carbonato $[CO_3^{2-}]$ cuando se conocen la temperatura y la salinidad a lo largo del tiempo, o bien cuando se asume que estos parámetros no han variado con el tiempo (Yu & Elderfield 2007; Raitzsch et al. 2011; Yu et al. 2013).

En esta tesis, las muestras para el análisis de elementos traza han sido analizadas utilizando la técnica micro-analítica de ablación por laser acoplado a espectrometría de masas con plasma de inducción (LA-ICPMS) disponible en la Royal Holloway University of London (RHUL), Reino Unido, que consiste en un sistema de ablación por láser RESOlution M-50 193 nm ArF acoplado a un ICPMS Agilent 7500ce (Müller et al. 2009). LA-ICPMS es una técnica que ofrece varias ventajas en comparación con otras técnicas, ya que permite, por ejemplo, el análisis de la composición elemental e isotópica en material sólido (visualizando perfiles en profundidad) de forma exacta, precisa y con alta resolución espacial, o el uso de poco material, o incluso evitar procedimientos de limpieza laboriosos ahorrando tiempo y pérdida de muestra. Todas estas características hacen que esta técnica sea muy adecuada para investigar la incorporación de elementos traza en las conchas de foraminíferos, que pueden utilizarse para inferir las condiciones climáticas pasadas (e.j. Eggins et al. 2004, Raitzsch et al. 2011; Sadekov et al. 2009; Creech et al. 2010; Evans et al. 2013).

Los foraminíferos se montan sobre una cinta adhesiva de doble cara que se coloca en la célula de ablación, donde la perforación se lleva a cabo bajo una atmósfera de helio (He) (Eggins et al. 1998), añadiendo un gas-diatómico adicional (nitrógeno o hidrógeno). El material extraído es conducido con gas argón (Ar) a la antorcha del ICPMS donde los iones generados son separados por su relación masa-carga. Los estándares con concentraciones de elementos conocidos se analizan regularmente entre las muestras de foraminíferos con el fin de convertir las cuentas por segundo medidas en el ICPMS en ppm o mmol/mol.

Isótopos estables del carbono ($\delta^{13}C$). La composición isotópica de carbono estable de conchas de foraminíferos se utiliza como trazador de variaciones en la fijación/oxidación de materia orgánica en el océano. Cuando los organismos fotosintéticos producen su materia orgánica, el isótopo más ligero del carbono (^{12}C) es preferentemente captado. De esta manera, cuanto mayor sea la productividad, el agua de mar estará más enriquecido en el isótopo de carbono más pesado (^{13}C), por lo que $^{13}C/^{12}C$ ($\delta^{13}C$) es generalmente más alto en aguas superficiales. Por el contrario, cuando los organismos mueren y la materia orgánica se oxida, el isótopo más ligero se libera al agua de mar circundante disminuyendo el $\delta^{13}C$ a lo largo de la columna de agua. Estos dos procesos suelen producirse en profundidades muy diferentes en la columna de agua del océano, lo que nos permite rastrear cambios en la productividad superficial y en la residencia de las masas de agua con el tiempo cuando se analiza el contenido de $\delta^{13}C$ en conchas de foraminíferos planctónicos y bentónicos a lo largo de un testigo de sedimento. El contenido de $\delta^{13}C$ en foraminíferos bentónicos de ODP1240 se analizó en la University of Cambridge mediante un dispositivo Thermo Kiel unido a un espectrómetro de masas Thermo MAT253. Los foraminíferos se transfirieron a viales, y sobre la muestra de carbonato de calcio se añadió ácido ortofosfórico al 100% que produce CO_2, el cual se criogenizó posteriormente para el análisis isotópico por comparación con un gas de referencia. Los resultados se presentan en referencia a la norma internacional VPDB y la precisión es ± 0,06 ‰ para $^{12}C/^{13}C$.

4. Resultados y discusión

Modelos de edades

En esta tesis se ha reconstruido el modelo de edad de los últimos 25.000 años para el testigo ODP1240 mediante la evaluación de la edad del reservorio superficial a lo largo del tiempo, ya que el modelo de edad previo se corrigió con una edad de reservorio superficial constante (Pena et al. 2008). La evaluación de la edad del reservorio superficial en la zona del ODP1240 se ha realizado mediante alineamiento cronoestratigráfico entre el $\delta^{18}O$ de tres testigos de hielo de Groenlandia (NGRIP,

GRIP y GISP2 (Rasmussen et al. 2008)), utilizando la escala de tiempo GICC05 (Svensson et al. 2006) (Fig. 6a,b), y dos registros del ODP1240: a) Temperatura de la superficie del mar (SST, por sus siglas en inglés), basado en el índice $U^{K'}_{37}$ (Calvo et al, no publicado; Fig. 6c), y b) $\delta^{18}O_{sw}$ obtenido a partir del foraminífero planctónico *Globigerinoides ruber* (Pena et al. 2008; Fig. 6d). Las alineaciones propuestas se basan en una serie de estudios previos, que concluyen que las anomalías en la temperatura superficial del mar registradas mediante el análisis de alquenonas, y en la salinidad superficial obtenida en reconstrucciones de $\delta^{18}O$ superficiales en el ODP1240, deben coincidir en el tiempo con las anomalías de la temperatura del Atlántico Norte/Groenlandia (Kienast et a. 2006; Leduc et al. 2007; Dubois et al. 2014).

Para esta alineación, se seleccionaron cuatro puntos estratigráficos en los registros de los testigos de hielo coincidiendo con cambios climáticos importantes: al final del estadío Heinrich 2 (SH2), al inicio del estadío Heinrich 1 (HS1), en la transición del HS1 al Bølling-Allerød (BA) y al final del Younger Dryas (YD) (Fig. 6).

En base a los alineamientos anteriores y mediante la datación con radiocarbono de 19 muestras de la especie plantónica *N. dutertrei* del ODP1240, se generaron dos estimaciones de la edad del reservorio superficial (es decir, uno por cada registro de ODP1240 utilizado en la alineación estratigráfica) (Fig. 6e). Las edades del reservorio superficial se calcularon mediante la diferencia entre el ^{14}C planctónico del ODP1240 interpolado para cada punto de alineamiento escogido (Skinner et al. 2010) y la edad de ^{14}C atmosférico correspondiente a la “edad de calendario” de

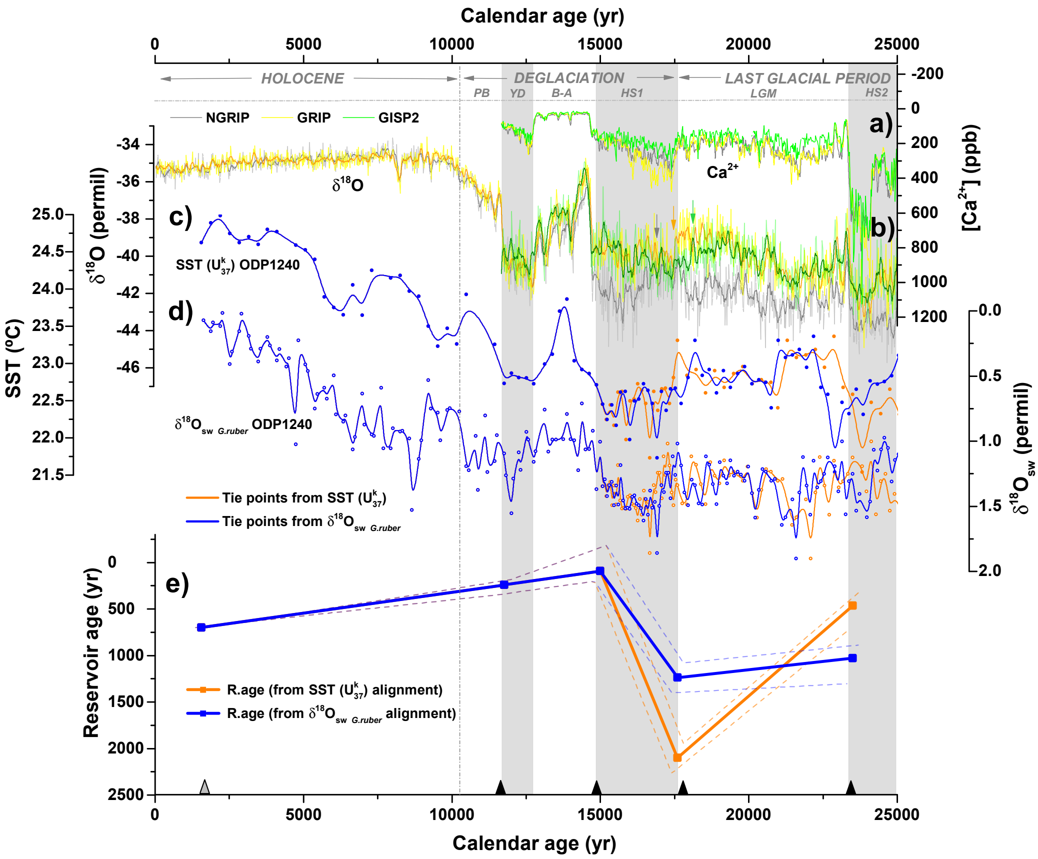

Figura 6. Estimación de la edad del reservorio superficial en el testigo de sedimento ODP1240 mediante la alineación entre dos registros independientes de ODP1240 y tres núcleos de hielo de Groenlandia durante los últimos 25.000 años. a) [Ca^{2+}] y b) registros de $\delta^{18}O$ de los testigos de hielo de Groenlandia (Rasmussen et al. 2008): NGRIP (gris), GRIP (amarillo) y GISP2 (verde). Las pequeñas flechas verticales por encima de los registros de $\delta^{18}O$ de Groenlandia indican el inicio del evento HS1 en cada testigo de hielo. c) Registros de SST basados en el índice y d) registro de $\delta^{18}O_{sw}$ (*G.ruber*) (Pena et al. 2008) del testigo ODP1240. La alineación basada en los puntos de alineamiento escogidos de SST se indica en azul, y la basada en los puntos de alineamiento escogidos de $\delta^{18}O_{sw\ (G.ruber)}$ en naranja. e) Estimación de los escenarios de la edad del reservorio superficial en ODP1240 usando las dos alineaciones: las líneas centrales gruesas representan la mejor estimación y las punteadas indican los límites superior e inferior (en naranja, basado en la correlación SST y en azul, basado en la correlación $\delta^{18}O_{sw\ (G.ruber)}$. Los puntos de alineamiento escogidos se indican en la parte inferior mediante triángulos negros. Se muestra también una datación adicional de la parte superior del testigo de sedimento (triángulo gris; Pena et al. 2008), corregido y calibrado. Las bandas grises destacan los estadíos fríos de los últimos 25.000 años como se definen en los registros de Groenlandia.

cada punto de alineamiento escogido (utilizando la curva de calibración IntCal09 (Reimer et al. 2009)).

Los resultados muestran que efectivamente la edad del reservorio superficial varío a lo largo de los últimos 25.000 años, viéndose unos ~405/540 años más envejecido durante el LGM respecto al Holoceno (Fig. 6e). En base a esta variación en la edad de los reservorios superficiales a lo largo del tiempo, se generaron nuevos modelos de edades utilizando el programa Bayesiano Bchron (Parnell et al. 2008) y la curva de calibración de radiocarbono IntCal09 (Reimer et al. 2009). Todos los modelos concuerdan bien, indicando un alto grado de consistencia entre las diversas restricciones cronoestratigráficas adoptadas para estas estimas y por tanto, en esta tesis, se aplican los nuevos modelos de edades generados para el testigo de sedimento ODP1240.

Ventilación oceánica

14 pares de dataciones de radiocarbono compuestas por *N. dutertrei* y mezcla de foraminíferos bentónicos (B-P) se realizaron en el testigo de sedimento ODP1240 con el fin de estimar cambios en las tasas de ventilación oceánica en el EEP que pudiesen estar relacionados con los cambios atmosféricos en ^{14}C observados durante el último glacial.

Las reconstrucciones de ventilación en el ODP1240 indican un cambio B-P glacial-interglacial de ~870 años que, teniendo en cuenta el cambio de ~405/540 años de los reservorios de edad descritos en los modelos de edades en el apartado anterior, implicaría un cambio en la edad de ventilación (B-Atm) entre el glacial y el interglacial de ~1.275/1.410 años. Estos resultados, en conjunto, indican que tanto la edad del reservorio superficial como la de las aguas profundas incrementó significativamente durante el LGM y que además evolucionaron de manera similar a lo largo de los últimos 25.000 años, con implicaciones en el inventario de radiocarbono global del océano glacial y su papel en el cambio de CO_2 glacial-interglacial (Broecker & Barker 2007).

En la Figura 7 se observa cómo la tasa de ventilación de radiocarbono, tanto en la termoclina como en el fondo del EEP, aumentó al inicio de la deglaciación al mismo tiempo que comenzaba a aumentar el CO_2 en la atmósfera (Monnin et al. 2001) y que el ^{14}C atmosférico disminuía (Hughen et al. 2004; Reimer et al. 2013). Estos resultados apoyarían la hipótesis de una reducción en las tasas de intercambio de CO_2 atmósfera-océano con implicaciones en el secuestro de carbono en el interior del océano glacial, así como en la liberación de este carbono a la atmósfera durante la última terminación. La demostración de la reducción de las tasas de ventilación de radiocarbono, tanto en la sub-superficie como en el fondo del Océano Pacífico es crucial en este sentido, ya que esta cuenca representa el ~50 % del volumen total del océano. Por lo tanto, pequeños efectos de ventilación o de secuestro de carbono en el Pacífico pueden tener un impacto particularmente grande en la química oceánica global, así como en la atmósfera.

Los resultados de la edad del reservorio superficial presentados en esta tesis

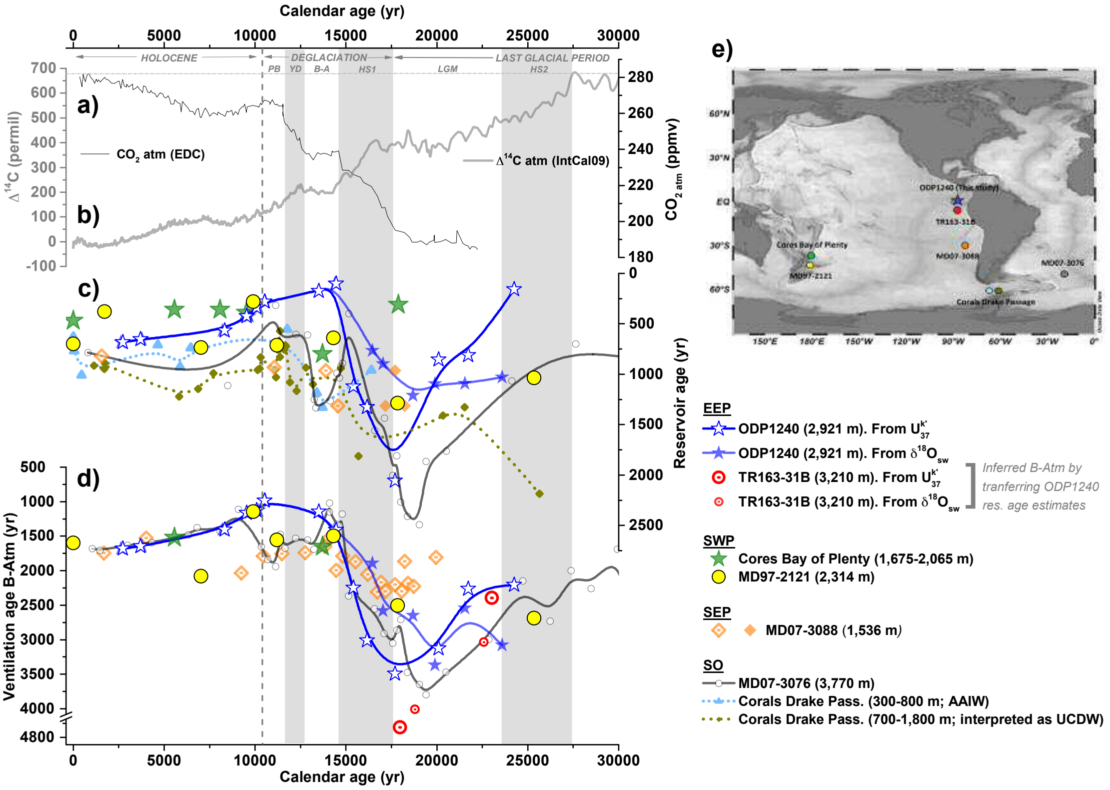

Figura 7. Comparación de las reconstrucciones de edad de reservorio superficial y de ventilación oceánica en el Pacífico Sur y el Océano Austral durante la última deglaciación agrupados según las masas de agua afiliadas. a) Concentración de CO_2 atmosférico procedente del testigo de hielo EPICA Domo C (EDC) (datos para deglaciación de Monnin et al. (2001) y para el Holoceno de Flückiger et al. (2002)), proyectado en la escala de edad de Lemieux-Dudon et al. (2010). b) Cambios en la actividad de ^{14}C atmosférico ($\Delta^{14}C$) (curva de calibración IntCal09; Reimer et al. 2009). c) registros de la edad de reservorio superficial/sub-superficial y d) reconstrucciones de ventilación de aguas profundas en varios lugares de los océanos Pacífico y Austral durante los últimos 25.000 años (suavizado B-spline): ODP1240 (2.921 m; *N. dutertrei*; estrellas azul oscuro sólidos/huecos de las alineaciones SST/$\delta^{18}O_{sw}$, respectivamente; este estudio); TR163-31B (3.210 m; *N. dutertrei*; círculos rojos grandes/pequeños de las alineaciones SST/$\delta^{18}O_{sw}$ en ODP1240, respectivamente; Shackleton et al. 1988); Bahía de Plenty (1,675-2,065 m; *Globorotalia inflata*; estrellas verdes; Sikes et al. 2000)); MD97-2121 (2.314 m; *G. Inflata*; puntos amarillos; Skinner et al. 2015); MD07-3088 (1.536 m; *Globigerina bulloides*; diamantes de color naranja claro de Haberle & Lumley (1998); Carel et al. (2011)); diamantes de color naranja oscuro de Siani et al. (2013)); MD07-3076 (3.770 m; *G. bulloides* y *G. inflata*, puntos grises oscuros; (Skinner et al. 2010); Corales del Pasaje de Drake (300-800 m "corales superficiales"; triángulos pequeños de color azul claro y 700-1,800 m "corales profundos" puntos pequeños de color verde oscuro; Burke & Robinson 2012). Fíjese que el eje "y" está interrumpido en d). e) Ubicación de los registros marinos mostraron en c) y d).

concuerdan también con otros registros similares del Pacífico, por ejemplo, en la Bahía de Plenty en el Pacífico Suroeste (SWP, por sus siglas en inglés; Sikes et al. 2000; Skinner et al. 2015), o en el Pacífico sureste (SEP, por sus siglas en inglés; Siani et al. 2013). La coherencia en las estimaciones de la edad del reservorio superficial entre diferentes regiones y profundidades de la columna de agua se puede explicar por las vías de transporte de la circulación que unen estas zonas actualmente, como algunos estudios han señalado anteriormente (Toggweiler et al. 1991; Tsuchiya et al. 1989; Kessler 2006). Bajo la premisa de que las vías de circulación glacial no eran muy diferentes de las actuales (es decir, un patrón similar en términos generales de flotabilidad y forzamiento del viento), se puede utilizar un modelo de simulación numérica para mostrar una conexión dinámica directa entre todas estas zonas y profundidades (Skinner et al. 2015). Esto ilustra que un aumento en la edad del reservorio sub-superficial del Océano Austral, debería comunicarse con la sub-superficie del EEP y del SWP a través de las vías dominantes de transporte del océano interior. De acuerdo con esta proposición, la edad del reservorio sub-superficial del ODP1240 presenta tendencias y valores coherentes con las reconstrucciones del Océano Austral, incluyendo los registros basados en dataciones de foraminíferos planctónicos del testigo MD07-3076 en el sector atlántico del Océano Austral (Skinner et al. 2010) y los corales del Pasaje de Drake a profundidades de 300-800 m y 700-1,800 m (Burke & Robinson 2012) (Fig. 7). Esta coherencia en las edades de reservorios sub-superficiales entre el EEP y los sectores Atlántico y Pacífico del Océano Austral apoyaría la idea de la conexión entre estas dos regiones a través de aguas intermedias transportadas por la EUC a la base de la termoclina del EEP;

una idea que se ha mostrado anteriormente en base a otros registros (Anderson et al. 2009; Lea & Spero 2002; Pena et al. 2008; Calvo et al. 2011). Por consiguiente, se propone aquí que la variabilidad observada en la termoclina del ODP1240 está relacionada principalmente con cambios en el Océano Austral que son transportados a la base de la termoclina del EEP. En conjunto, estas observaciones desafían la suposición común de que la edad de los reservorios superficiales no varía con el tiempo, y no sólo en altas latitudes, sino también en las zonas de afloramiento tropicales.

Además de la concordancia general en las reconstrucciones de la edad del reservorio superficial/sub-superficial, también se observa una gran similitud en la variabilidad de los registros de ventilación profunda del Pacífico Sur y Ecuatorial, así como del Océano Austral. De esta manera, las estimas de B-Atm del ODP1240 indican un cambio significativo en la ventilación de radiocarbono entre el período glacial y el interglacial, como también se observa en el testigo cercano TR163-31B (Shackleton et al. 1988), especialmente cuando se le aplican los reservorios de edad superficial estimados en esta tesis (Fig. 7d). Del mismo modo, se han observado cambios en la ventilación de las aguas profundas del SWP (Sikes et al. 2000; Skinner et al. 2015) y del SEP (Siani et al. 2013). Todos estos registros muestran tendencias muy similares en comparación con el EEP durante la deglaciación, así como valores de B-Atm comparables. Esta coherencia es muy significativa, ya que confirmaría que un gran volumen del océano interior estuvo, de hecho, peor ventilado durante el último período glacial; una proposición que hasta el momento no había sido bien esclarecida.

La aguas profundas del Pacífico sur y ecuatorial consisten actualmente en una mezcla de UCDW y PDW, que ocupan rangos de densidad y profundidad similares (Talley et al. 2011), por lo que una conexión hidrográfica/dinámica entre las distintas reconstrucciones de ventilación comparadas en la Fig. 7d es totalmente plausible. La ventilación de radiocarbono de las aguas profundas del ODP1240 y otros testigos del Pacífico concuerdan bien con las del testigo MD07-3076 del sector Atlántico del Océano Austral (Skinner et al. 2010) (Fig. 7d), lo que es consistente con una llegada de aguas profundas del Océano Austral al Pacífico.

Estimación de [CO_3^{2-}] basado en el análisis de ratios de B/Ca utilizando LA-ICPMS

Las estimaciones de [CO_3^{2-}] en el interior del océano son de gran utilidad en la inferencia del estado del ciclo del carbono en el pasado. Uno de los trazadores más recientes para dichas estimas es el ratio B/Ca medido en la concha de foraminíferos bentónicos, que comúnmente se realiza mediante la técnica de solución-ICPMS. Se ha demostrado que esta técnica es válida para estos análisis en la mayoría de los casos. Sin embargo, actualmente, aún existen conflictos entre los resultados de diferentes áreas, lo que podría estar relacionados con el tipo de técnica aplicada. Por esto, una técnica como LA-ICPMS que permite visualizar la incorporación de B a lo largo de la vida de los foraminíferos y por tanto entender mejor cómo este trazador podría realmente funcionar, parece muy adecuada.

Con el fin de realizar mediciones de B/Ca en la concha de foraminíferos utilizando la novedosa técnica de LA-ICPMS, se ha evaluado, primeramente, la precisión de la técnica analítica mediante el uso de diferentes estándares, tipos de tubos y gases.

La precisión y exactitud del sistema se evaluó durante varios meses calibrando análisis de cristales MPI-DING (GOR132 y GOR128 utilizados como incógnitas) con los estándares NIST610 y NIST612 (a través de todas las combinaciones posibles y utilizando los valores reportados en Jochum et al. (2011)). Se introdujeron dos variables adicionales con el fin de encontrar la mejor precisión para los elementos de interés, así como el estándar más adecuado para cada elemento: 1) el uso de dos gases diatómicos adicionales (N_2 y H_2), y 2) el uso de dos tipos de tubos (Nylon corriente y Nylon6 libre de azufre).

Los resultados de la puesta apunto del sistema de ablación por láser corroboran una vez más la idoneidad del láser con longitud de onda de 193 nm y de los estándares NIST en los análisis de B/Ca (Hathorne et al. 2008; Jochum et al. 2007; Jochum et al. 2012). La precisión de B mejora cuantiosamente cuando se utiliza el tubo Nylon6 libre de azufre, y la de Mn cuando se aplica H_2 como gas diatómico adicional. El resto de los elementos a penas experimentan cambios, con la excepción de Ba y U cuya precisión disminuye, lo que indica que no todos estos elementos pueden ser analizados con precisión al mismo tiempo. De hecho, una aplicación inicial en muestras reales de calcita indica que el uso de los tubos de Nylon corriente presenta resultados anómalos en los ratios B/Ca cuando se comparan con los resultados obtenidos utilizando tubos de Nylon6 libre de azufre, los cuales se apoyan en los resultados obtenidos del análisis en solución de los mismos especímenes. El uso de cinta adhesiva de doble cara no muestra ningún efecto en los análisis en solución, lo que resulta muy alentador ya que el uso de esta práctica permitiría medir varios trazadores utilizando los mismos individuos. De esta manera, se recomienda (y por tanto se aplica en esta tesis) el uso del tubo Nylon6-S libre de azufre y del gas H_2, así como la calibración con el estándar NIST612 en análisis de ratios B/Ca utilizando la técnica de LA-ICPMS.

Una vez el sistema estaba puesto apunto, se analizaron muestras de *C. Wuellerstorfi* del ODP1240 mediante ablación por láser, observando detenidamente la incorporación de B a lo largo de la concha foraminífero calcita (es decir, a través de la vida del foraminífero), las cuales se extrajeron posteriormente de la cinta adhesiva y se analizaron mediante la técnica de solución-ICPMS, para así poder comparar ambas técnicas cualitativa y cuantitativamente. Además, para dicha comparación, los resultados obtenidos mediante LA-ICPMS se procesaron utilizando dos estrategias distintas: 1) seleccionando la parte del perfil que presenta calcio plano (denominada estrategia de “calcita plana”) y, 2) seleccionando la parte de la ablación que presenta una disminución progresiva en la intensidad de los elemento (denominada estrategia de “ablación completa”). Esta disminución en la intensidad de los elemento a lo largo de la ablación es una característica típica del análisis con LA-ICPMS, ya que la extracción de material se vuelve más difícil a medida que aumenta la profundidad de ablación, y comúnmente se excluye de la integración (reteniendo sólo la parte de la ablación que presentan “calcita plana”), ya que podría producir fraccionamiento isotópico y/o alteración de las proporciones elemento/Ca. Sin embargo, como los análisis en solución-ICPMS utilizan especímenes enteros, los resultados de ablaciones completas podrían ser más comparables con los analizados en solución.

Además, también se han analizado muestras de *C. wuellerstorfi* de la parte superficial de testigos de sedimento de varias localizaciones en el Océano Atlántico utilizando LA-ICPMS, con el propósito de añadir nuevos datos a las calibraciones existentes. Por último, también se han analizado los ratios B/Ca en el foraminífero planctónico *N. dutertrei* para tener una visión preliminar de la su distribución de este elemento en esta especie.

Los resultados muestran que los análisis de B a través de las cámaras de *C. wuellerstorfi* presentan perfiles bastante regulares, sin enriquecimientos superficiales, y sin ninguna correlación con Al. Mg correlaciona con Mn, lo que señala la importancia de aplicar el protocolo de limpieza reductor si las muestras quieren emplearse para análisis de Mg/Ca en esta área (Pena et al. 2005; Pena et al. 2008). El espesor de la pared varía en función de las cámaras así como los ratios B/Ca, lo que parece estar relacionados con el crecimiento bilaminar de esta especie, yendo de valores más altos de B/Ca en la parte más gruesa y antigua a valores más bajos en la parte más fina y joven. Al comparar los promedios finales de B/Ca obtenidos de las dos estrategias aplicadas a los resultados de LA-ICPMS y de los análisis en solución-ICPMS realizados en las mismas muestras, se observa que las ablaciones más largas producen resultados más consistentes con los análisis en solución, presentando variaciones similares pero con una diferencia constante. Se especula que, además de la posible influencia del uso de estándares que no son de calcita, la diferencia tan constante que se observa entre la estrategia de “ablación completa” y los resultados en solución, podría ser debido a la eliminación de las cámaras finales que por lo general contienen valores de Al/Ca que superan el umbral de contaminación, así como valores altos de B/Ca. Curiosamente, los pocos valores derivados de la estrategia de “ablación completa” con LA-ICPMS que no coinciden con los valores obtenidos en solución, contienen valores de Al/Ca elevados, pero no lo suficiente como para ser excluidos basándose en umbrales típicos de contaminación. Esto podría sugerir una revisión del umbral de contaminación de Al/Ca en análisis en solución. Por otro lado, con el fin minimizar los errores y de que los resultados finales de B/Ca sean estadísticamente representativos del intervalo de tiempo que se analiza, se recomienda analizar un mínimo de 5-6 individuos por muestra, ya que, frecuentemente, 1 o 2 individuos causan sesgos importantes en la media final.

Los ratios B/Ca analizados con LA-ICPMS en muestras de *C. wuellerstorfi* provenientes de sedimentos superficiales de varias zonas del Océano Atlántico concuerdan bien con los valores actuales de $\Delta[CO_3^{2-}]$ del agua de mar específicos en cada localización. Por otra parte, a pesar de la diferencia constante entre los análisis realizados mediante LA-ICPMS y mediante solución, parece que las calibraciones hechas a través del análisis en sedimento superficial utilizando ambas técnicas, son indistinguibles, lo que sugiere que se pueden utilizar las dos técnicas en el análisis de B/Ca de foraminíferos bentónicos como trazador de $[CO_3^{2-}]$. Sin embargo, una calibración específica para datos de B/Ca medidos con LA-ICPMS podría ser necesaria en el futuro con el fin de poder hacer comparaciones precisas y cuantitativas entre los resultados obtenidos a través de ambas técnicas.

En cuanto al análisis de muestras de *N. dutertrei*, como en el caso de *C. wueller-*

storfi, no se observan enriquecimientos superficiales o correlación con Al, y la señal de B a través de las cámaras es típicamente bastante plana. El espesor de la pared también varía en función de las cámaras, así como los ratios B/Ca, pero curiosamente en sentido opuesto a *C. wuellerstorfi*, es decir, *N. dutertrei* muestra valores de B/Ca anómalamente bajos en las cámaras de paredes más finas. Cuando los mismos individuos se analizan en solución, la similitud entre técnicas no es tan sorprendente como en el caso de *C. wuellerstorfi*, lo que podría estar relacionado, por ejemplo, con la estructura de pared de esta especie planctónica, que no es tan "homogénea" como en foraminíferos bentónicos. Esta primera inspección en la distribución de B/Ca en *N. dutertrei* muestra valores típicos obtenidos anteriormente para esta especie mediante análisis en solución (Foster 2008; Dai et al. 2016), lo que podría sugerir que no es un buen trazador del sistema de carbonato (o, al menos, no de $\Delta[CO_3^{2-}]$; Dai et al. 2016). Sin embargo, sería necesario realizar cultivos de esta especie en el laboratorio cambiando diferentes parámetros del agua marina con el fin de entender qué variables oceanográficas/climáticas podrían estar relacionadas con los ratios de B/Ca en esta especie.

Como conclusión, este estudio demuestra la conveniencia y ventajas de la técnica de LA-ICPMS en el análisis de ratios de B/Ca en *C. wuellerstorfi*. Es importante destacar que esta técnica permite la eliminación de cámaras o incluso de individuos enteros que presenten valores anómalos, lo que permite evitar posibles sesgos en los promedios finales utilizados para la interpretación paleoceanográfica. Esto puede ser especialmente importante en los análisis de muestras muy pequeñas.

CO_2 *acumulado y eficiencia de la bomba biológica*

El registro de ventilación de radiocarbono del ODP1240 durante el último período glacial indicaba un tiempo de residencia mayor de las masas de agua en esta zona, lo que probablemente implicaría un aumento en la cantidad de materia orgánica oxidada en el interior del océano, y por tanto, más carbono respirado por microorganismos por unidad de volumen. Si esto hubiese ocurrido, las consecuencias más notables serían, por un lado, una disminución de $\delta^{13}C$ en el agua marina debido a una mayor liberación del isótopo ligero de carbono (^{12}C), y por el otro lado, una mayor acumulación de CO_2 en agua de mar como producto de un aumento en la oxidación de carbono. Tal aumento en la concentración de CO_2 en el agua de mar habría alterado el sistema de equilibrio del carbonato, lo que habría conllevado una disminución en $[CO_3^{2-}]$ con el fin de amortiguar un cambio de pH en el agua marina (Zeebe & Wolf-Gladrow 2001; Williams & Sigue a 2011; Sarmiento & Gruber 2004). Por tanto, para una búsqueda más directa de la potencial acumulación de CO_2 en el fondo oceánico durante el LGM, se ha analizado el contenido de $[CO_3^{2-}]$ (inferido de ratios B/Ca) y de $\delta^{13}C$ en muestras de *C. wuellerstorfi* cubriendo los últimos 30.000 años.

Los resultados muestran que los ratios B/Ca de *C. wuellerstorfi* en el ODP1240 son ~12 µmol/mol más bajos durante el último período glacial, con un promedio de ~172 ± 9 µmol/mol (± 2SE), que durante el Holoceno, que presenta valores de ~184 ± 21 µmol/mol (± 2SE). Cuando los ratios B/Ca se convierten a $[CO_3^{2-}]$, la diferencia entre el glacial (~71 µmol/kg) y el interglaciar (~81 µmol/kg) es de ~10 µmol/kg. $\delta^{13}C$ en ODP1240 también presenta una disminución durante el LGM en comparación con el Holoceno, de ~0,4 ‰.

Los resultados obtenidos de $[CO_3^{2-}]$ y $\delta^{13}C$ del ODP1240 concuerdan con la sugerencia de un mayor tiempo de residencia del agua profunda que "acciona" una bomba biológica de carbono más eficiente (Fig. 8d,e). Valores más negativos de $\delta^{13}C$ durante el final del glacial reflejaría niveles más altos de DIC respirado durante este período, lo que a su vez se indica por una disminución en los niveles de $[CO_3^{2-}]$. Por extensión, en respuesta a una mayor ventilación del océano profundo a lo largo de la última deglaciación, la cantidad de carbono orgánico oxidado habría disminuido (indicado por valores más positivos de $\delta^{13}C$) acompañada de una concentración inferior de CO_2 disuelto (indicado por valores más altos de $[CO_3^{2-}]$).

Otra consecuencia del aumento hipotético de carbono respirado en el fondo marino durante el LGM habría sido una disminución en el contenido en O_2, ya que los microorganismos consumen O_2 durante el proceso de la respiración con el fin de descomponer la materia orgánica. Las mediciones de uranio autigénico (aU) en el testigo ME0005-24JC (recuperado en la misma ubicación que el ODP1240; Kienast et al. 2007) apoyan esta idea, presentando valores mayores de aU (es decir, menor concentración de O_2) durante el glacial en comparación con el Holoceno (Bradtmiller et al. 2010). Este trazador de la oxigenación se basa en la química redox del U en agua de mar, y hace referencia al U precipitado en los sedimentos según se consume el O_2, pasando de la forma soluble U(VI) en las aguas oxigenadas

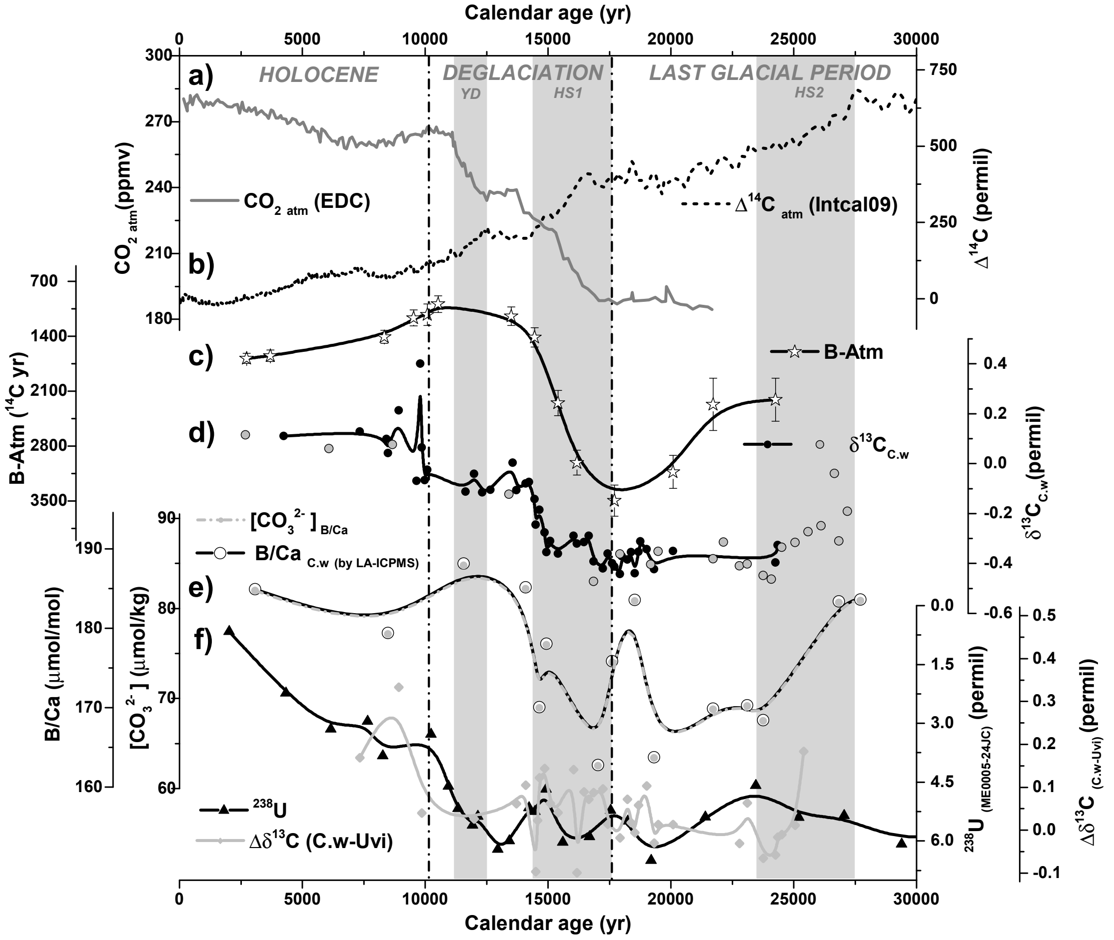

Figura 8. Comparación de los registros del océano profundo de ODP1240 con registros atmosféricos de CO_2 y de actividad de ^{14}C en los últimos 30.000 años. a) Concentración de CO_2 atmosférico procedente del testigo de hielo EPICA Domo C (EDC) (datos para deglaciación de Monnin et al. (2001) y para el Holoceno de Flückiger et al. (2002)), proyectado en la escala de edad de Lemieux-Dudon et al. (2010). b) Cambios en la actividad de ^{14}C atmosférico ($\Delta^{14}C$) (curva de calibración IntCal09; Reimer et al. 2009). c) Reconstrucciones de ventilación de las aguas profundas del ODP1240 (proveniente de la alineación SST en de la Fuente et al. (2015)). d) δ ^{13}C en *C. wuellerstorfi*. e) B/Ca y $[CO_3^{2-}]_{\text{(basado en B/ Ca)}}$ (solapado). f) Trazadores de oxigenación: ^{238}U del testifo ME0005-24JC (misma ubicación que el ODP1240; Bradtmiller et al. 2010; línea y triángulos negros), y $\Delta\delta^{13}C$ entre una especie de foraminífero epibentónico y otra infaunal (*C. wuellerstorfi* (esta tesis) y *Uvigerina sp.* (Povea et al. sin publicar), respectivamente; línea y puntos grises). Todas las líneas tienen un suavizado B-spline. Las líneas verticales discontinuas delimitan periodos climáticos importantes, y las bandas verticales grises resaltan los períodos más fríos de los últimos 30.000 años.

a las especies insolubles U(IV) según se agota el oxígeno en el medio (Cochran et al. 1986; Langmuir 1978; Morford & Emerson 1999). En apoyo a las mediciones de aU, estimaciones de $\Delta\delta^{13}C$ entre especies de foraminíferos epibentónicos e infaunal (McCorkle & Emerson 1988; Hoogakker et al. 2014), *C. wuellerstorfi* y *Uvigerina* en el testigo ODP1240, muestran tendencias similares (figura 8f, línea gris). El $\Delta\delta^{13}C$ entre la interfase sedimento/agua marina y el límite anóxico del sedimento debería variar con la concentración de oxígeno de las aguas del fondo. Por lo tanto, un $\Delta\delta^{13}C$ más pequeña durante el LGM indicaría una menor penetración de oxígeno en los sedimentos (donde vive *Uvigerina*), conllevando a una disminución en la respiración de carbono orgánico por debajo de la interfase sedimento/agua de mar.

Además de esto, estudios previos en trazadores de productividad en la zona del ODP1240 sugieren un aumento en la productividad superficial y exportada durante el LGM, lo que habría contribuido a aumentar la eficiencia de la bomba de carbono biológica y por tanto a la disminución de CO_2 atmosférico. Sin embargo, la contribución exacta de estos cambios de productividad sigue sin ser esclarecida.

Cabría esperar que la acción de cualquiera de estos mecanismos (solos o en conjunto) lograran una diferencia relativamente grande de $[CO_3^{2-}]$ entre el glacial y el Holoceno. Sin embargo, los resultados de esta tesis indican sólo un pequeño cambio de $[CO_3^{2-}]$ entre estos dos períodos (~12 µmol/kg), lo que sugiere la acción de un mecanismo “antagonista”, como podría ser la disolución de $CaCO_3$ en el fondo marino producto de una mayor respiración de materia orgánica. Cuando el carbonato cálcico se disuelve en el agua de mar, tanto el $[CO_3^{2-}]$ como la ALK aumentan (Broecker & Peng 1989; Zeebe & Wolf-Gladrow 2001).

Datos de la cantidad de $CaCO_3$ acumulado en el ODP1240 indican que no hubo cambios entre 25.000-15.000 años (Pichevin et al. 2009), lo que sugiere que la "huella" de flujos de $CaCO_3$ más altos durante el glacial en el ODP1240 podría haber sido diluido por un flujo mayor de sedimentos que no eran carbonatos. Por lo tanto, cualquier disolución de $CaCO_3$ que se produjo en las aguas profundas del EEP habría sido enmascarado por unas tasas de producción de carbonato más altas (por ejemplo, debido a una mayor productividad exportada). Por otra parte, la contribución de dicha disolución de $CaCO_3$ al aumento en promedio de $[CO_3^{2-}]$ en el océano profundo, habría sido enmascarado también en cierta medida por cambios en $[CO_3^{2-}]$ accionados por la respiración de carbono orgánico. Por lo tanto, un incremento en la disolución de $CaCO_3$ en el fondo del Pacífico, según consta en el testigo ODP1240, no sólo podría haber amortiguado cambios glaciales en $[CO_3^{2-}]$ sin afectar al $\delta^{13}C$ en el EEP, si no que también podría haber jugado un papel en la reducción del CO_2 atmosférico durante el LGM, contribuyendo al aumento de la alcalinidad media del océano a través del suministro de $[CO_3^{2-}]$ al océano (Keir 1995; Sigman & Boyle 2000). Esto habría reforzado aún más los efectos de una mayor eficiencia de la bomba biológica alcanzados mediante cambios en la circulación y en la productividad exportada propuestos anteriormente.

Todos los registros presentados aquí, es decir, $[CO_3^{2-}]$, $\delta^{13}C$ y trazadores de oxigenación, concuerdan con el registro de ventilación por radiocarbono de las aguas profundas del EEP, apoyando la hipótesis de una mayor eficiencia de la bomba biológica debido, principalmente, a cambios en la circulación, pero ayudados también por un posible aumento en la productividad exportada, y por un aumento en la ALK media del océano producto de una mayor disolución de carbonato cálcico. En conjunto, todos estos registros indican que las aguas profundas del EEP muy probablemente contribuyeron a la disminución de CO_2 atmosférico durante el LGM, mediante el almacenamiento de carbono respirado a expensas de los inventarios de carbono de la superficie oceánica y de la atmósfera.

5. Conclusiones

En esta tesis se ha abordado el papel del océano en el CO_2 atmosférico y el cambio climático glacial-interglacial mediante el uso de trazadores geoquímicos en el testigo de sedimento ODP1240 situado en el EEP, que ha derivado cuatro principales conclusiones:

- En primer lugar, las edades de ventilación de radiocarbono determinados mediante la combinación de las diferencias B-P con las estimaciones de la edad del reservorio superficial, demuestran que las aguas profundas del EEP estuvieron peor ventiladas en el LGM en comparación con el Holoceno, lo que habría contribuido directamente a una disminución en la "fuga" de CO_2, y por lo tanto a una mayor eficiencia de la bomba biológica durante el período glacial.

- En segundo lugar, la técnica LA-ICPMS es viable y particularmente informativa aplicada al análisis de ratios B/Ca en foraminíferos bentónicos, el cual es válido como trazador de $\Delta[CO_3^{2-}]$ de las aguas profundas y por lo tanto puede informar sobre cambios pasados en el inventario de carbono.

- En tercer lugar, las mediciones de ratios B/Ca mediante LA-ICPMS, conjuntamente con otros trazadores del ciclo del carbono ($\delta^{13}C$ y $\Delta\delta^{13}C$), sugieren que el $[CO_3^{2-}]$ de las aguas profundas y la oxigenación fueron más bajas en el LGM en comparación con el presente, lo que confirma un aumento de carbono respirado almacenado en el interior del EEP durante el último glacial.

- En cuarto lugar, las relaciones observadas entre $[CO_3^{2-}]$, $\delta^{13}C$ y radiocarbono en las aguas profundas del EEP, así como en registros similares de los Océanos Pacífico y Austral, se interpretan como resultado de la disolución del carbonato en el océano profundo (derivado de un aumento en la eficiencia de la bomba biológica y la acumulación de CO_2 respirado), lo que habría contribuido aún más a la absorción de CO_2 por parte del océano durante el último período glacial mediante un aumento de la alcalinidad media del océano.

En general, estos resultados contribuyen a nuestra comprensión de los cambios de CO_2 observados durante épocas G/IG mediante la demostración de la contribución de la circulación oceánica en el secuestro de carbono durante el LGM, tanto en forma de impactos directos en la bomba de tejido blando e indirectos a través de los efectos de la disolución de $CaCO_3$ (alcalinidad). Los resultados presentados aquí también plantean nuevas preguntas, y hacen hincapié en cómo el estudio de la “huella biogeoquímica” aplicada en esta tesis mediante la combinación de ^{14}C, $[CO_3^{2-}]$, $\delta^{13}C$ y trazadores de oxigenación, podría aportar gran información sobre cambios en la bomba biológica durante el LGM, proporcionando así un modelo para estudios futuros.

En el futuro, por tanto, una aplicación más amplia de este enfoque multi-trazador a mayor resolución temporal y en áreas clave del océano, probablemente en combinación con modelos numéricos biogeoquímicos, tendría el potencial de mejorar la cuantificación de la magnitud de los cambios en el inventario de carbono entre reservorios y, por tanto, su impacto en el CO_2 atmosférico durante el Pleistoceno tardío.

References

Abe-Ouchi, A., Saito, F., Kawamura, K., Raymo, M.E., Okuno, J., Takahashi, K., Blatter, H., 2013. Insolation-driven 100,000-year glacial cycles and hysteresis of ice-sheet volume. Nature 500, 190–193.

Adkins, J., 2013. The role of deep ocean circulation in setting glacial climates. Paleoceanography 28, 539–561.

Adkins, J., Boyle, E., 1997. Changing atmospheric $\Delta^{14}C$ and the record of deep water paleoventilation ages. Paleoceanography 12, 337–344.

Adkins, J., McIntyre, K., Schrag, D.P., 2002. The salinity, temperature, and delta^{18}O of the glacial deep ocean. Science 298, 1769–73.

Ahagon, N., Ohkushi, K., Uchida, M., Mishima, T., 2003. Mid-depth circulation in the northwest Pacific during the last deglaciation: Evidence from foraminiferal radiocarbon ages. Geophys. Res. Lett. 30, 2097.

Allen, K. a., Honisch, B., 2012. The planktic foraminiferal B/Ca proxy for seawater carbonate chemistry: A critical evaluation. Earth Planet. Sci. Lett. 345-348, 203–211.

Allen, K. a., Honisch, B., Eggins, S., Rosenthal, Y., 2012. Environmental controls on B/Ca in calcite tests of the tropical planktic foraminifer species Globigerinoides ruber and Globigerinoides sacculifer. Earth Planet. Sci. Lett. 351-352, 270–280.

Allen, K. a., Honisch, B., Eggins, S., Yu, J., Spero, H.J., Elderfield, H., 2011. Controls on boron incorporation in cultured tests of the planktic foraminifer Orbulina universa. Earth Planet. Sci. Lett. 1–11.

Allen, K. a., Sikes, E.L., Hönisch, B., Elmore, A.C., Guilderson, T.P., Rosenthal, Y., Anderson, R.F., 2015. Southwest Pacific deep water carbonate chemistry linked to high southern latitude climate and atmospheric CO_2 during the Last Glacial Termination. Quat. Sci. Rev. 122, 180–191.

Anand, P., Elderfield, H., 2005. Variability of Mg/Ca and Sr/Ca between and within the planktonic foraminifers Globigerina bulloides and Globorotalia truncatulinoides. Geochemistry Geophys. Geosystems 6, 1–15.

Anderson, L.A., 1995. On the hydrogen and oxygen content of marine phytoplankton. Deep Sea Res. Part I Oceanogr. Res. Pap. 42, 1675–1680.

Anderson, R.F., Ali, S., Bradtmiller, L., Nielsen, S.H.H., Fleisher, M.Q., Burk, C.,

2009. Wind-driven upwelling in the Southern Ocean and the deglacial rise in atmospheric CO_2. Science 323, 1443–1448.

Archer, D., 1996. A data-driven model of the global calcite lysocline. Global Biogeochem. Cycles 10, 511–526.

Archer, D., 1991. Equatorial Pacific calcite preservation cycles: production or dissolution? Paleoceanography 6, 561–571.

Archer, D., Maier-Reimer, E., 1994. Effect of deep-sea sedimentary calcite preservation on atmospheric CO_2 concentration. Nature 367, 260–263.

Bard, E., Mangerud, J., Paterne, M., Labeyrie, L., Duprat, J., Mi, M., 1994. The North Atlantic atmosphere-sea surface ^{14}C gradient during the Younger Dryas climatic event. Earth Planet. Sci. Lett. 126, 275–287.

Barker, S., Greaves, M., Elderfield, H., 2003. A study of cleaning procedures used for foraminiferal Mg/Ca paleothermometry. Geochemistry Geophys. Geosystems 4, 1–20.

Barnola, J., Raynaud, D., Korotkevich, Y., Lorius, C., 1987. Vostok ice core provides 160,000-year record of atmospheric CO_2. Nature 329, 408–414.

Berger, A., 1999. Parameters of the Earth's orbit for the last 5 Million years in 1 kyr resolution. PANGAEA.

Berger, A., Loutre, M.F., 1991. Insolation values for the climate of the last 10 million years. Quat. Sci. Rev. 10, 297–317.

Berger, W.H., 1982. Increase of carbon dioxide in the atmosphere during deglaciation: the coral reef hypothesis. Naturwissenschaften 69, 87–88.

Bolton, A., Baker, J. a., Dunbar, G.B., Carter, L., Smith, E.G.C., Neil, H.L., 2011. Environmental versus biological controls on Mg/Ca variability in Globigerinoides ruber (white) from core top and plankton tow samples in the southwest Pacific Ocean. Paleoceanography 26, 1–14.

Boyle, E., 1983. Manganese carbonate overgrowths on foraminifera tests. Geochim. Cosmochim. Acta 47, 1815–1819.

Bradtmiller, L., Anderson, R.F., Sachs, J.P., Fleisher, M.Q., 2010. A deeper respired carbon pool in the glacial equatorial Pacific Ocean. Earth Planet. Sci. Lett. 299, 417–425.

Broecker, W.S., 1982a. Glacial to interglacial changes in ocean chemistry. Prog. Oceanogr. 11, 151–197.

Broecker, W.S., 1982b. Ocean chemistry during glacial time. Geochim. Cosmochim. Acta 46, 1689–1705.

Broecker, W.S., Andree, M., Bonani, G., Wolfli, W., Oeschger, H., Klas, M., Mix, A., Curry, W., 1988. Preliminary estimates for the radiocarbon age of deep water in the glacial ocean. Paleoceanography 3, 659–669.

Broecker, W.S., Barker, S., 2007. A 190‰ drop in atmosphere's $\Delta^{14}C$ during the "Mystery Interval" (17.5 to 14.5 kyr). Earth Planet. Sci. Lett. 256, 90–99.

Broecker, W.S., Barker, S., Clark, E., Hajdas, I., Bonani, G., Stott, L., 2004a. Ventilation of the glacial deep Pacific Ocean. Science 306, 1169–72.

Broecker, W.S., Clark, E., Barker, S., 2008. Near constancy of the Pacific Ocean surface to mid-depth radiocarbon-age difference over the last 20 kyr. Earth Planet. Sci. Lett. 274, 322–326.

Broecker, W.S., Clark, E., Barker, S., Hajdas, I., Bonani, G., Moreno, E., 2007. Radiocarbon age of late glacial deep water from the equatorial Pacific. Paleoceanography 22, 1–6.

Broecker, W.S., Clark, E., Hajdas, I., Bonani, G., 2004b. Glacial ventilation rates for the deep Pacific Ocean. Paleoceanography 19, 1–12.

Broecker, W.S., Peng, T.-H., 1989. The cause of the glacial to interglacial atmospheric CO_2 change: A polar alkalinity hypothesis. Global Biogeochem. Cycles 3, 215–239.

Broecker, W.S., Peng, T.-H., Trumbore, S., Bonani, G., Wolflp, W., 1990. The distribution of radiocarbon in the glacial ocean. Global Biogeochem. Cycles 4, 103–117.

Brovkin, V., Ganopolski, A., Archer, D., Munhoven, G., 2012. Glacial CO_2 cycle as a succession of key physical and biogeochemical processes. Clim. Past 8, 251–264.

Brown, R.E., Anderson, L.D., Thomas, E., Zachos, J.C., 2011. A core-top calibration of B/Ca in the benthic foraminifers Nuttallides umbonifera and Oridorsalis umbonatus: A proxy for Cenozoic bottom water carbonate saturation. Earth Planet. Sci. Lett. 310, 360–368.

Brzezinski, M.A., Pride, C.J., Franck, V.M., Sigman, D.M., Sarmiento, J.L., Matsumoto, K., Gruber, N., Rau, G.H., Coale, K., 2002. A switch from $Si(OH)_4$ to NO_3^- depletion in the glacial Southern Ocean. Geophys. Res. Lett. 29, 3–6.

Burke, A., Robinson, L., 2012. The Southern Ocean's role in carbon exchange during the last deglaciation. Science 335.

Butzin, M., Prange, M., Lohmann, G., 2012. Readjustment of glacial radiocarbon chronologies by self-consistent three-dimensional ocean circulation modeling. Earth Planet. Sci. Lett. 317-318, 177–184.

Calvo, E., Pelejero, C., Logan, G. a, De Deckker, P., 2004. Dust-induced changes in phytoplankton composition in the Tasman Sea during the last four glacial cycles. Paleoceanography 19, 1–10.

Calvo, E., Pelejero, C., Pena, L.D., Cacho, I., Logan, G. a, 2011. Eastern equatorial pacific productivity and related-CO_2 changes since the last glacial period. Proc. Natl. Acad. Sci. U. S. A. 108, 5537–41.

Carel, M., Siani, G., Delpech, G., 2011. Tephrostratigraphy of a deep-sea sediment sequence off the south Chilean margin: New insight into the Hudson volcanic activity since the last glacial period. J. Volcanol. Geotherm. Res. 208, 99–111.

Cochran, J.K., Carey, A.E., Sholkovitz, E., Surprenant, L., 1986. The geochemistry of uranium and thorium in coastal marine sediments and sediment pore waters. Geochim. Cosmochim. Acta 50, 663–680.

Creech, J.B., Baker, J. a., Hollis, C.J., Morgans, H.E.G., Smith, E.G.C., 2010. Eocene sea temperatures for the mid-latitude southwest Pacific from Mg/Ca ratios in planktonic and benthic foraminifera. Earth Planet. Sci. Lett. 299, 483–495.

d'Orbigny, A., 1839. Foraminiferes de l'ile de Cuba.

Dai, Y., Yu, J., Johnstone, H., 2016. Distinct responses of planktonic foraminiferal B/Ca to dissolution on seafloor. Geochemistry Geophys. Geosystems 17, 1339–1348.

de la Fuente, M., Skinner, L., Calvo, E., Pelejero, C., Cacho, I., 2015. Increased reservoir ages and poorly ventilated deep waters inferred in the glacial Eastern Equatorial Pacific. Nat. Commun. 6, 7420.

De Pol-Holz, R., Keigwin, L., Southon, J., Hebbeln, D., Mohtadi, M., 2010. No signature of abyssal carbon in intermediate waters off Chile during deglaciation. Nat. Geosci. 3, 192–195.

Denton, G., Anderson, R.F., Toggweiler, J.R., Edwards, R.L., Schaefer, J.M., Putnam, A.E., 2010. The last glacial termination. Science 328, 1652–6.

DeVries, T., 2014. The oceanic anthropogenic CO_2 sink: Storage, air-sea fluxes and transports over the industrial era. Global Biogeochem. Cycles 28, 1–17.

Devries, T., Primeau, F., 2011. Dynamically and observationally constrained estimates of water-mass distributions and ages in the Global Ocean. J. Phys. Oceanogr. 41, 2381–2401.

Dickson, A.G., Millero, F.J., 1987. A comparison of the equilibrium constants for the dissociation of carbonic acid in seawater media. Deep Sea Res. Part A. Oceanogr. Res. Pap. 34, 1733–1743.

Doss, W., Marchitto, T.M., 2013. Glacial deep ocean sequestration of CO_2 driven by the eastern equatorial Pacific biologic pump. Earth Planet. Sci. Lett. 377-378, 43–54.

Dubois, N., Kienast, M., Kienast, S., Timmermann, A., 2014. Millennial-scale Atlantic/East Pacific sea surface temperature linkages during the last 100,000 years. Earth Planet. Sci. Lett. 396, 134–142.

Eggins, S., De Deckker, P., Marshall, J.F., 2003. Mg/Ca variation in planktonic foraminifera tests: implications for reconstructing palaeo-seawater temperature and habitat migration. Earth Planet. Sci. Lett. 212, 291–306.

Eggins, S., Kinsley, L.P.J., Shelley, J.M.G., 1998. Deposition and element fractionation processes during atmospheric pressure laser sampling for analysis by ICP-MS. Appl. Surf. Sci. 127-129, 278–286.

Eggins, S., Sadekov, A., De Deckker, P., 2004. Modulation and daily banding of Mg/Ca in tests by symbiont photosynthesis and respiration: a complication for seawater thermometry? Earth Planet. Sci. Lett. 225, 411–419.

Elmore, A.C., McClymont, E.L., Elderfield, H., Kender, S., Cook, M.R., Leng, M.J., Greaves, M., Misra, S., 2015. Antarctic Intermediate Water properties since 400 ka recorded in infaunal (*Uvigerina peregrina*) and epifaunal (*Planulina wuellerstorfi*) benthic foraminifera. Earth Planet. Sci. Lett. IN REVIEW, 193–203.

Evans, D., Erez, J., Oron, S., Müller, W., 2015. Mg/Ca-temperature and seawater-test chemistry relationships in the shallow-dwelling large benthic foraminifera *Operculina ammonoides*. Geochim. Cosmochim. Acta 148, 325–342.

Evans, D., Müller, W., 2013. LA-ICPMS elemental imaging of complex discontinuous carbonates: An example using large benthic foraminifera. J. Anal. At. Spectrom. 28, 1039.

Evans, D., Müller, W., Oron, S., Renema, W., 2013. Eocene seasonality and seawater alkaline earth reconstruction using shallow-dwelling large benthic foraminifera. Earth Planet. Sci. Lett. 381, 104–115.

Fairbanks, R., Sverdlove, M.S., Free, R., Wiebe, P., Be, A., 1982. Vertical distribution and isotopic fractionation of living planktonic foraminifera from the Panama Basin. Nature 298, 841–844.

Ferrari, R., Jansen, M.F., Adkins, J., Burke, A., Stewart, A.L., Thompson, A.F., 2014. Antarctic sea ice control on ocean circulation in present and glacial climates.

Proc. Natl. Acad. Sci. 111, 8754–8758.

Flückiger, J., Monnin, E., Stauffer, B., Schwander, J., Stocker, T.F., 2002. High-resolution Holocene N_2O ice core record and its relationship with CH_4 and CO_2. Global Biogeochem. Cycles 16.

Foster, G.L., 2008. Seawater pH, pCO_2 and $[CO_3^{2-}]$ variations in the Caribbean Sea over the last 130 kyr: A boron isotope and B/Ca study of planktic foraminifera. Earth Planet. Sci. Lett. 271, 254–266.

Freeman, E., Skinner, L., Reimer, R., Scrivner, A., Fallon, S., 2016. Graphitization of small carbonate samples for palaeoceanographic research at the Godwin Radiocarbon Laboratory, University of Cambridge. Radiocarbon.

Galbraith, E., Jaccard, S., Pedersen, T.F., Sigman, D.M., Haug, G.H., Cook, M., Southon, J., François, R., 2007. Carbon dioxide release from the North Pacific abyss during the last deglaciation. Nature 449, 890–3.

Galloway, J.J., 1933. A manual of Foraminifera. Principia press.

Ganopolski, A., Calov, R., 2011. The role of orbital forcing, carbon dioxide and regolith in 100 kyr glacial cycles. Clim. Past 7, 1415–1425.

Ganopolski, A., Winkelmann, R., Schellnhuber, H.J., 2016. Critical insolation-CO_2 relation for diagnosing past and future glacial inception. Nature 529, 200–203.

Gebbie, G., Huybers, P., 2011. How is the ocean filled? Geophys. Res. Lett. 38, n/a–n/a.

Godwin, H., 1962. Half-life of radiocarbon. Nature 195.

Gottschalk, J., Skinner, L., Lippold, J., Vogel, H., Frank, N., Jaccard, S.L., Waelbroeck, C., 2016. Biological and physical controls in the Southern Ocean on past millennial-scale atmospheric CO_2 changes. Nat Commun 7.

Gottschalk, J., Skinner, L., Misra, S., Waelbroeck, C., Menviel, L., Timmermann, A., 2015. Abrupt changes in the southern extent of North Atlantic Deep Water during Dansgaard–Oeschger events. Nat. Geosci. 1–6.

Gregoire, L.J., Payne, A.J., Valdes, P.J., 2012. Deglacial rapid sea level rises caused by ice-sheet saddle collapses. Nature 487, 219–22.

Haberle, S.G., Lumley, S.H., 1998. Age and origin of tephras recorded in postglacial lake sediments to the west of the southern Andes, 44°S to 47°S. J. Volcanol. Geotherm. Res. 84, 239–256.

Hain, M.P., Sigman, D.M., Haug, G.H., 2010. Carbon dioxide effects of Antarctic stratification, North Atlantic Intermediate Water formation, and subantarctic nutrient drawdown during the last ice age: Diagnosis and synthesis in a geochemical box model. Global Biogeochem. Cycles 24, 1–19.

Hathorne, E.C., Alard, O., James, R.H., Rogers, N.W., 2003. Determination of intratest variability of trace elements in foraminifera by laser ablation inductively coupled plasma-mass spectrometry. Geochemistry Geophys. Geosystems 4.

Hathorne, E.C., Gagnon, A., Felis, T., Adkins, J., Asami, R., Boer, W., Caillon, N., Case, D., Cobb, K.M., Douville, E., Demenocal, P., Eisenhauer, A., Garbe-Schönberg, D., Geibert, W., Goldstein, S., Hughen, K., Inoue, M., Kawahata, H., Kölling, M., Cornec, F.L., Linsley, B.K., McGregor, H. V., Montagna, P., Nurhati, I.S., Quinn, T.M., Raddatz, J., Rebaubier, H., Robinson, L., Sadekov, A., Sherrell, R., Sinclair, D., Tudhope, A.W., Wei, G., Wong, H., Wu, H.C., You, C.F., 2013. Interlaboratory study for coral Sr/Ca and other element/Ca ratio measurements. Geochemistry, Geophys. Geosystems 14, 3730–3750.

Hathorne, E.C., James, R.H., Lampitt, R.S., 2009. Environmental versus biomineralization controls on the intratest variation in the trace element composition of the planktonic foraminifera G. inflata and G. scitula. Paleoceanography 24, 1–14.

Hathorne, E.C., James, R.H., Savage, P., Alard, O., 2008. Physical and chemical characteristics of particles produced by laser ablation of biogenic calcium carbonate w. J. Anal. At. Spectrom. 23, 240–243.

Hays, J., Imbrie, J., Shackleton, N., 1976. Variations in the Earth’s orbit: Pacemaker of the Ice Ages. Science 194, 1121–1132.

Heinze, C., Maier-Reimer, E., Winn, K., 1991. Glacial *p*CO_2 reduction by the world ocean: Experiments with the Hamburg Carbon Cycle Model. Paleoceanography 6, 395–430.

Hemleben, C., Spindler, M., Anderson, O.R., 1989. Modern planktonic foraminifera. Springer Science & Business Media.

Hemming, N., Hanson, G., 1992. Boron isotopic composition and concentration in modern marine carbonates. Geochim. Cosmochim. Acta 56, 537–543.

Hey, R., Johnson, G.L., Lowrie, A., 1977. Recent plate motions in the Galapagos area. Geol. Soc. Am. Bull. 88, 1385–1403.

Hilbrecht, H., 1997. Morphologic gradation and ecology in *Neogloboquadrina pachyderma* and *N. dutertrei* (planktic foraminifera) from core top sediments. Mar. Micropaleontol. 31, 31–43.

Hoogakker, B. a. a., Elderfield, H., Schmiedl, G., McCave, N.I., Rickaby, R.E.M., 2014. Glacial–interglacial changes in bottom-water oxygen content on the Portuguese margin. Nat. Geosci. 8, 40–43.

Hughen, K., Lehman, S.J., Southon, J., Overpeck, J., Marchal, O., Herring, C., Turnbull, J., 2004. ^{14}C Activity and Global Carbon cycle changes over the past 50,000 years. Science 303, 202–207.

Hughen, K., Southon, J., Lehman, S.J., Bertrand, C.J.H., Turnbull, J., 2006. Marine-derived ^{14}C calibration and activity record for the past 50,000 years updated from the Cariaco Basin. Quat. Sci. Rev. 25, 3216–3227.

Huybers, P., 2006. Early Pleistocene glacial cycles and the integrated summer insolation forcing. Science 313, 508–511.

Ikehara, K., Danhara, T., Yamashita, T., Tanahashi, M., Morita, S., Ohkushi, K., 2011. Paleoceanographic control on a large marine reservoir effect offshore of Tokai, south of Japan, NW Pacific, during the last glacial maximum-deglaciation. Quat. Int. 246, 213–221.

Imbrie, J., Imbrie, J.Z., 1980. Modeling the climatic response to orbital variations. Science 207, 943–953.

Ito, T., Follows, M.J., 2013. Air-sea disequilibrium of carbon dioxide enhances the biological carbon sequestration in the Southern Ocean. Global Biogeochem. Cycles 27, 1129–1138.

Jaccard, S.L., Hayes, C.T., Martínez-Garcia, A., Hodell, D.A., Anderson, R.F., Sigman, D.M., Haug, G.H., 2013. Two modes of change in Southern Ocean productivity over the past million years. Science 339, 1419–23.

Jochum, K.P., Scholz, D., Stoll, B., Weis, U., Wilson, S. a., Yang, Q., Schwalb, A., Börner, N., Jacob, D.E., Andreae, M.O., 2012. Accurate trace element analysis of speleothems and biogenic calcium carbonates by LA-ICP-MS. Chem. Geol. 318-319, 31–44.

Jochum, K.P., Stoll, B., Herwig, K., Willbold, M., 2007. Validation of LA-ICP-MS trace element analysis of geological glasses using a new solid-state 193 nm Nd:YAG laser and matrix-matched calibration. J. Anal. At. Spectrom. 22, 112.

Jochum, K.P., Stoll, B., Herwig, K., Willbold, M., Hofmann, A.W., Amini, M., Aarburg, S., Abouchami, W., Hellebrand, E., Mocek, B., Raczek, I., Stracke, A., Alard, O., Bouman, C., Becker, S., Dücking, M., Brätz, H., Klemd, R., de Bruin, D., Canil, D., Cornell, D., de Hoog, C.-J., Dalpé, C., Danyushevsky, L., Eisenhauer, A., Gao, Y., Snow, J.E., Groschopf, N., Günther, D., Latkoczy, C., Guillong, M., Hauri, E.H., Höfer, H.E., Lahaye, Y., Horz, K., Jacob, D.E., Kasemann, S., Kent, A.J.R., Ludwig, T., Zack, T., Massolo, S., Meixner, A., Rosner, M., Misawa, K., Nash, B.P., Pfänder, J., Premo, W.R., Sun, W.D., Tiepolo, M., Vannucci, R., Vennemann, T., Wayne, D., Woodhead, J.D., 2006. MPI-DING reference glasses for in situ microanalysis: New reference values for element concentrations and isotope ratios. Geochemistry Geophys. Geosystems 7.

Jochum, K.P., Weis, U., Stoll, B., Kuzmin, D., Yang, Q., Raczek, I., Jacob, D.E., Stracke, A., Birbaum, K., Frick, D. a., Günther, D., Enzweiler, J., 2011. Determination of Reference Values for NIST SRM 610-617 Glasses Following ISO Guidelines. Geostand. Geoanalytical Res. 35, 397–429.

Jouzel, J., Masson-Delmotte, V., Cattani, O., Dreyfus, G., Falourd, S., Hoffmann, G., Minster, B., Nouet, J., Barnola, J., Chappellaz, J., Fischer, H., Gallet, J.C., Johnsen, S., Leuenberger, M., Loulergue, L., Luethi, D., Oerter, H., Parrenin, F., Raisbeck, G.M., Raynaud, D., Schilt, A., Schwander, J., Selmo, E., Souchez, R., Spahni, R., Stauffer, B., Steffensen, J.P., Stenni, B., Stocker, T.F., Tison, J.L., Werner, M., Wolff, E., 2007. Orbital and millennial Antarctic climate variability over the past 800,000 years. Science 317, 793–6.

Keir, R.S., 1995. Is there a component of Pleistocene CO_2 change associated with carbonate dissolution cycles? Paleoceanography 10.

Kessler, W., 2006. The circulation of the eastern tropical Pacific: A review ☆ . Prog. Oceanogr. 69, 181–217.

Key, R.M., Kozyr, A., Sabine, C.L., Lee, K., Wanninkhof, R., Bullister, J.L., Feely, R. a, Millero, F.J., Mordy, C., Peng, T.H., 2004. A global ocean carbon climatology: Results from Global Data Analysis Project (GLODAP). Global Biogeochem. Cycles 18, 1–23.

Kienast, M., Kienast, S., Calvert, S.E., Eglinton, T.I., Mollenhauer, G., François, R., Mix, A., 2006. Eastern Pacific cooling and Atlantic overturning circulation during the last deglaciation. Nature 443, 846–9.

Kienast, S., Kienast, M., Mix, A., Calvert, S.E., François, R., 2007. Thorium-230 normalized particle flux and sediment focusing in the Panama Basin region during the last 30,000 years. Paleoceanography 22, 1–19.

Klochko, K., Cody, G.D., Tossell, J., Dera, P., Kaufman, A.J., 2009. Re-evaluating boron speciation in biogenic calcite and aragonite using ^{11}B MAS NMR. Geochim. Cosmochim. Acta 73, 1890–1900.

Kohfeld, K.E., Ridgwell, A., 2009. Glacial-interglacial variability in atmospheric CO_2.

Surf. Ocean Low. Atmos. Process. 187, 251–286.

Köhler, P., Bintanja, R., Fischer, H., Joos, F., Knutti, R., Lohmann, G., Masson-Delmotte, V., 2010. What caused Earth's temperature variations during the last 800,000 years? Data-based evidence on radiative forcing and constraints on climate sensitivity. Quat. Sci. Rev. 29, 129–145.

Kovaltsov, G.A., Mishev, A., Usoskin, I.G., 2012. A new model of cosmogenic production of radiocarbon ^{14}C in the atmosphere. Earth Planet. Sci. Lett. 337-338, 114–120.

Kwon, E.Y., Primeau, F., 2008. Optimization and sensitivity of a global biogeochemistry ocean model using combined in situ DIC, alkalinity, and phosphate data. J. Geophys. Res. Ocean. 113, 1–23.

Kwon, E.Y., Primeau, F., Sarmiento, J.L., 2009. The impact of remineralization depth on the air–sea carbon balance. Nat. Geosci. 2, 630–635.

Laird, N.P., 1971. Panama Basin deep water- properties and circulation. J. Mar. Res. 29, 226–234.

Lal, D., Peters, B., 1967. Cosmic Ray produced radioactivity on the Earth, in: Sitte, K. (Ed.),. Springer Berlin Heidelberg, Berlin, Heidelberg, pp. 551–612.

Langmuir, D., 1978. Uranium solution-mineral equilibria at low temperatures with applications to sedimentary ore deposits. Geochim. Cosmochim. Acta 42, 547–569.

Leduc, G., Vidal, L., Tachikawa, K., Rostek, F., Sonzogni, C., Beaufort, L., Bard, E., 2007. Moisture transport across Central America as a positive feedback on abrupt climatic changes. Nature 445, 908–11.

Lemieux-Dudon, B., Blayo, E., Petit, J.-R., Waelbroeck, C., Svensson, A., Ritz, C., Barnola, J., Narcisi, B.M., Parrenin, F., 2010. Consistent dating for Antarctic and Greenland ice cores. Quat. Sci. Rev. 29, 8–20.

Lewis, E., Wallace, D., Allison, L.J., 1998. Program developed for CO_2 system calculations. Carbon Dioxide Information Analysis Center, managed by Lockheed Martin Energy Research Corporation for the US Department of Energy Tennessee.

Li, Y.H., Takahashi, T., Broecker, W.S., 1969. Degree of saturation of $CaCO_3$ in the oceans. J. Geophys. Res. 74, 5507 –5525.

Libby, W.F., 1955. Radiocarbon dating, second. ed, Univ. ChicagoPress.

Lisiecki, L.E., Lisiecki, P.A., 2002. Application of dynamic programming to the correlation of paleoclimate records. Paleoceanography 17, 1–12.

Lisiecki, L.E., Raymo, M.E., 2005. A Pliocene-Pleistocene stack of 57 globally distributed benthic δ^{18}O records. Paleoceanography 20, 1–17.

Llanillo, P.J., Karstensen, J., Pelegrí, J.L., Stramma, L., 2013. Physical and biogeochemical forcing of oxygen and nitrate changes during El Niño/El Viejo and La Niña/La Vieja upper-ocean phases in the tropical eastern South Pacific along 86° W. Biogeosciences 10, 6339–6355.

Lonsdale, P., Malfait, B., 1974. Abyssal dunes of foraminiferal sand on the Carnegie Ridge. Geol. Soc. Am. Bull.

Lukas, R., 1986. The termination of the Equatorial Undercurrent in the eastern Pacific. Prog. Oceanogr. 16, 63–90.

Lund, D.C., Mix, A., Southon, J., 2011. Increased ventilation age of the deep northeast Pacific Ocean during the last deglaciation. Nat. Geosci. 4, 771–774.

Lüthi, D., Le Floch, M., Bereiter, B., Blunier, T., Barnola, J., Siegenthaler, U., Raynaud, D., Jouzel, J., Fischer, H., Kawamura, K., Stocker, T.F., 2008. High-resolution carbon dioxide concentration record 650,000-800,000 years before present. Nature 453, 379–82.

Lutze, G.F., Thiel, H., 1989. Epibenthic foraminifera from elevated microhabitats; *Cibicidoides wuellerstorfi* and *Planulina ariminensis*. J. Foraminifer. Res. 19, 153–158.

Marchitto, T.M., Lehman, S.J., Ortiz, J.D., Flückiger, J., van Geen, A., 2007. Marine radiocarbon evidence for the mechanism of deglacial atmospheric CO_2 rise. Science 316, 1456–9.

Marr, J.P., Baker, J. a., Carter, L., Allan, A.S.R., Dunbar, G.B., Bostock, H.C., 2011. Ecological and temperature controls on Mg/Ca ratios of Globigerina bulloides from the southwest Pacific Ocean. Paleoceanography 26, 1–15.

Martínez-Garcia, A., Sigman, D.M., Ren, H., Anderson, R.F., Straub, M., Hodell, D. a, Jaccard, S., Eglinton, T.I., Haug, G.H., 2014. Iron fertilization of the Subantarctic ocean during the last ice age. Science 343, 1347–50.

Matsumoto, K., 2007. Biology-mediated temperature control on atmospheric $p\mathrm{CO}_2$ and ocean biogeochemistry. Geophys. Res. Lett. 34, 1–5.

Matsumoto, K., Sarmiento, J.L., Brzezinski, M.A., 2002. Silicic acid leakage from the Southern Ocean: A possible explanation for glacial atmospheric $p\mathrm{CO}_2$. Global Biogeochem. Cycles 16.

Max, L., Lembke-Jene, L., Riethdorf, J.-R., Tiedemann, R., Nürnberg, D., Kühn, H., Mackensen, a., 2014. Pulses of enhanced North Pacific Intermediate Water ventilation from the Okhotsk Sea and Bering Sea during the last deglaciation. Clim. Past 10, 591–605.

McCorkle, D.C., Emerson, S.R., 1988. The relationship between pore water carbon isotopic composition and bottom water oxygen concentration. Geochim. Cosmochim. Acta 52, 1169–1178.

McGee, D., Marcantonio, F., Lynch-Stieglitz, J., 2007. Deglacial changes in dust flux in the eastern equatorial Pacific. Earth Planet. Sci. Lett. 257, 215–230.

Mehrbach, C., Culberson, C.H., Hawley, J.E., Pytowicz, R.M., 1973. Measurements of the apparent dissociation constants of carbonic acid in seawater at atmospheric pressure. Limnol. Oceanogr. 18, 897–907.

Milankovitch, M., 1941. Kanon der Erdebestrahlung und seine Anwendung auf das Eiszeitenproblem. Königlich Serbische Akademie.

Misra, S., Greaves, M., Owen, R., Kerr, J., Elmore, A.C., Elderfield, H., 2014. Determination of B/Ca of natural carbonates by HR-ICP-MS. Geochemistry, Geophys. Geosystems 15, 1617–1628.

Mix, A., Tiedemann, R., Blum, P., 2003. Leg 202 summary, Proceedings of the Ocean Drilling Program, Initial Reports.

Monnin, E., Indermühle, A., Dällenbach, a, Flückiger, J., Stauffer, B., Stocker, T.F., Raynaud, D., Barnola, J., 2001. Atmospheric CO_2 concentrations over the last glacial termination. Science 291, 112–4.

Montgomery, R.B., 1958. Water characteristics of Atlantic Ocean and of world ocean*. Deep Sea Res. 5, 134–148.

Morford, J.L., Emerson, S., 1999. The geochemistry of redox sensitive trace metals in sediments. Geochim. Cosmochim. Acta 63, 1735–1750.

Müller, W., Shelley, J.M.G., Miller, P., Broude, S., 2009. Initial performance metrics of a new custom-designed ArF excimer LA-ICPMS system coupled to a two-volume laser-ablation cell. J. Anal. At. Spectrom. 24, 209.

Muscheler, R., Beer, J., Kubik, P.W., Synal, H.A., 2005. Geomagnetic field intensity during the last 60,000 years based on ^{10}Be and ^{36}Cl from the Summit ice cores and ^{14}C. Quat. Sci. Rev. 24, 1849–1860.

Muscheler, R., Beer, J., Wagner, G., Laj, C., Kissel, C., Raisbeck, G.M., Yiou, F., Kubik, P.W., 2004. Changes in the carbon cycle during the last deglaciation as indicated by the comparison of ^{10}Be and ^{14}C records. Earth Planet. Sci. Lett. 219, 325–340.

Okazaki, Y., Sagawa, T., Asahi, H., Horikawa, K., Onodera, J., 2012. Ventilation changes in the western North Pacific since the last glacial period. Clim. Past 8, 17–24.

Opdyke, B.N., Walker, J.C.G., 1992. Return of the coral reef hypothesis: Basin to shelf partitioning of $CaCO_3$ and its effect on atmospheric CO_2. Geology 20, 733–736.

Orsi, a. H., Johnson, G.C., Bullister, J.L., 1999. Circulation, mixing, and production of Antarctic Bottom Water. Prog. Oceanogr. 43, 55–109.

Paillard, D., 2001. Glacial cycles: Towards a new paradigm. Rev. Geophys. 39, 325–346.

Paillard, D., 1998. The timing of Pleistocene glaciations from a simple multiple-state climate model. Nature 391, 916–918.

Paillard, D., Parrenin, F., 2004. The Antarctic ice sheet and the triggering of deglaciations. Earth Planet. Sci. Lett. 227, 263–271.

Parker, F.L., 1962. Planktonic foraminiferal species in Pacific sediments. Micropaleontology 8, 219–254.

Parnell, A., Haslett, J., Allen, J.R.M., Buck, C.E., Huntley, B., 2008. A flexible approach to assessing synchroneity of past events using Bayesian reconstructions of sedimentation history. Quat. Sci. Rev. 27, 1872–1885.

Pedersen, T.F., 1983. Increased productivity in the eastern equatorial Pacific during the last glacial maximum (19,000 to 14,000 yr B.P). Geology 11, 16–19.

Pena, L.D., Cacho, I., Calvo, E., Pelejero, C., Eggins, S., Sadekov, A., 2008a. Characterization of contaminant phases in foraminifera carbonates by electron microprobe mapping. Geochemistry Geophys. Geosystems 9, 1–12.

Pena, L.D., Cacho, I., Ferretti, P., Hall, M.A., 2008b. El Niño–Southern Oscillation–like variability during glacial terminations and interlatitudinal teleconnections. Paleoceanography 23, 1–8.

Pena, L.D., Calvo, E., Cacho, I., Eggins, S., Pelejero, C., 2005. Identification and removal of Mn-Mg-rich contaminant phases on foraminiferal tests: Implications for Mg/Ca past temperature reconstructions. Geochemistry Geophys. Geosystems 6.

Pena, L.D., Goldstein, S., Hemming, S.R., Jones, K.M., Calvo, E., Pelejero, C., Cacho, I., 2013. Rapid changes in meridional advection of Southern Ocean intermediate waters to the tropical Pacific during the last 30 kyr. Earth Planet. Sci. Lett. 368, 20–32.

Petit, J.-R., Raynaud, D., Basile, I., Chappellaz, J., Davisk, M., Ritz, C., Delmotte, M., Legrand, M., Lorius, C., Pe, L., Saltzmank, E., 1999. Climate and atmospheric history of the past 420,000 years from the Vostok ice core, Antarctica. Nature 399.

Philander, S.G.H., Gu, D., Halpern, D., Lambert, G., Lau, N.C., Li, T., Pacanowski, R.C., 1996. Why the ITCZ is mostly north of the equator. J. Clim.

Pichevin, L., Reynolds, B.C., Ganeshram, R.S., Cacho, I., Pena, L.D., Keefe, K., Ellam, R.M., 2009. Enhanced carbon pump inferred from relaxation of nutrient limitation in the glacial ocean. Nature 459, 1114–7.

Pierrot, D., Lewis, E., Wallace, D.W.R., 2006. MS Excel program developed for CO_2 system calculations. ORNL/CDIAC-105a. Carbon Dioxide Inf. Anal. Center, Oak Ridge Natl. Lab. US Dep. Energy, Oak Ridge, Tennessee.

Primeau, F., 2005. Characterizing transport between the surface mixed layer and the ocean interior with a forward and adjoint global ocean transport model. J. Phys. Oceanogr. 35, 545–564.

Rae, J.W.B., Foster, G.L., Schmidt, D.N., Elliott, T., 2011. Boron isotopes and B/Ca in benthic foraminifera: Proxies for the deep ocean carbonate system. Earth Planet. Sci. Lett. 1–11.

Raitzsch, M., Hathorne, E.C., Kuhnert, H., Groeneveld, J., Bickert, T., 2011. Modern and late Pleistocene B/Ca ratios of the benthic foraminifer Planulina wuellerstorfi determined with laser ablation ICP-MS. Geology 39, 1039–1042.

Rasmussen, S.O., Seierstad, I.K., Andersen, K.K., Bigler, M., Dahl-Jensen, D., Johnsen, S.J., 2008. Synchronization of the NGRIP, GRIP, and GISP2 ice cores across MIS 2 and palaeoclimatic implications. Quat. Sci. Rev. 27, 18–28.

Redfield, A.C., 1963. The influence of organisms on the composition of sea-water. sea 26–77.

Reichart, G.-J., Jorissen, F., Anschutz, P., Mason, P.R.D., 2003. Single foraminiferal test chemistry records the marine environment. Geology 31, 355.

Reimer, P.J., Baillie, M.G.L., Bard, E., Bayliss, A., Berk, J., Blackwell, P.G., Bronk Ramsey, C., Burk, C., Burr, G.S., 2009. IntCal09 and marine09 radiocarbon age calibration curves, 0-50,000 years cal BP. Radiocarbon 51, 1111–1150.

Reimer, P.J., Bard, E., Bayliss, A., Beck, J.W., Blackwell, P.G., Bronk, C., Caitlin, R., Hai, E.B., Edwards, R.L., 2013. Intcal13 and marine13 radiocarbon age calibration curves 0 – 50,000 years cal BP. Radiocarbon 55, 1869–1887.

Reimer, P.J., Brown, T.A., Reimer, R.W., 2004. Discussion: Reporting and calibration of post-bomb ^{14}C data. Radiocarbon 46.

Roberts, J., Gottschalk, J., Skinner, L., Peck, V.L., Kender, S., Elderfield, H., Waelbroeck, C., Vázquez Riveiros, N., Hodell, D.A., 2016. Evolution of South Atlantic density and chemical stratification across the last deglaciation. Proc. Natl. Acad. Sci. U. S. A. 1511252113.

Robinson, R., Martinez, P., Pena, L.D., Cacho, I., 2009. Nitrogen isotopic evidence for deglacial changes in nutrient supply in the eastern equatorial Pacific. Paleoceanography 24, 1–12.

Sadekov, A., Eggins, S., De Deckker, P., 2005. Characterization of Mg/Ca distributions in planktonic foraminifera species by electron microprobe mapping. Geochemistry Geophys. Geosystems 6.

Sadekov, A., Eggins, S., De Deckker, P., Kroon, D., 2008. Uncertainties in seawater thermometry deriving from intratest and intertest Mg/Ca variability in Globigerinoides ruber. Paleoceanography 23, 1–12.

Sadekov, A., Eggins, S., De Deckker, P., Ninnemann, U., Kuhnt, W., Bassinot, F., 2009. Surface and subsurface seawater temperature reconstruction using Mg/Ca microanalysis of planktonic foraminifera *Globigerinoides ruber*, *Globigerinoides sacculifer*, and *Pulleniatina obliquiloculata*. Paleoceanography 24, 1–17.

Santos, G.M., Southon, J., Griffin, S., Beaupre, S.R., Druffel, E.R.M., 2007. Ultra small-mass AMS ^{14}C sample preparation and analyses at KCCAMS/UCI Facility. Nucl. Instruments Methods Phys. Res. Sect. B Beam Interact. with Mater. Atoms 259, 293–302.

Santos, G.M., Southon, J.R., Druffel-Rodriguez, K.C., Griffin, S., Mazon, M., 2004. Magnesium perchlorate as an alternative water trap in AMS graphite sample preparation: A report on sample preparation at KCCAMS at the University of California, Irvine. Radiocarbon 46, 165–173.

Saraswati, P.K., Srinivasan, M.S., 2015. Micropaleontology: Principles and Applications. Springer.

Sarmiento, J.L., Gruber, N., 2004. Ocean Biogeochemical Dynamics.

Sarnthein, M., Schneider, B., Grootes, P.M., 2013. Peak glacial ^{14}C ventilation ages suggest major draw-down of carbon into the abyssal ocean. Clim. Past 9, 2595–2614.

Schmitt, J., Schneider, R., Elsig, J., Leuenberger, D., Lourantou, A., Chappellaz, J., Köhler, P., Joos, F., Stocker, T.F., Leuenberger, M., Fischer, H., 2012. Carbon isotope constraints on the deglacial CO_2 rise from ice cores. Science 336, 711–4.

Schoof, C., 2007. Ice sheet grounding line dynamics: Steady states, stability, and hysteresis. J. Geophys. Res. Earth Surf. 112, 1–19.

Schwager, C., 1866. Fossile Foraminiferen von Kar Nikobar. In Reise der Österreichischen Fregatte Novara um die Erde in den Jahren 1857, 1858, 1859 unter den Befehlen des Commodore B von Wüllerstorf-Urbair. Zweite Abtheilung.

Shackleton, N., 2000. The 100,000-Year Ice-Age cycle identified and found to lag temperature, carbon dioxide, and orbital eccentricity. Science 289, 1897–1902.

Shackleton, N., Duplessy, J.-C., Arnold, M., Maurice, P., Hall, M.A., Cartlidge, J., 1988. Radiocarbon age of last glacial Pacific deep water. Nature 335, 708–711.

Shackleton, N., Hall, M.A., Vincent, E., 2000. Phase relationships between millennial-scale events 64,000-24,000 years ago. Paleoceanography 15, 565–569.

Siani, G., Michel, E., De Pol-Holz, R., Devries, T., Lamy, F., Carel, M., Isguder, G., Dewilde, F., Lourantou, A., 2013. Carbon isotope records reveal precise timing of enhanced Southern Ocean upwelling during the last deglaciation. Nat. Commun. 4, 2758.

Siani, G., Paterne, M., Michel, E., Sulpizio, R., Sbrana, A., Arnold, M., Haddad, G., 2001. Mediterranean Sea surface radiocarbon reservoir age changes since the last glacial maximum. Science 294, 1917–20.

Siegenthaler, U., Stocker, T.F., Monnin, E., Lüthi, D., Schwander, J., Stauffer, B., Raynaud, D., Barnola, J., Fischer, H., Masson-Delmotte, V., Jouzel, J., 2005. Stable carbon cycle-climate relationship during the Late Pleistocene. Science 310, 1313–7.

Sigman, D.M., Boyle, E.A., 2000. Glacial/interglacial variations in atmospheric carbon dioxide. Nature 407, 859–869.

Sigman, D.M., Hain, M.P., Haug, G.H., 2010. The polar ocean and glacial cycles in atmospheric CO_2 concentration. Nat. Rev. 466, 47–55.

Sikes, E.L., Samson, C.R., Guilderson, T.P., Howard, W.R., 2000. Old radiocarbon ages in the southwest Pacific Ocean during the last glacial period and deglaciation. Nature 303, 555–559.

Skinner, L., 2009. Glacial-interglacial atmospheric CO_2 change: a possible "standing volume" effect on deep-ocean carbon sequestration. Clim. Past 5, 537–550.

Skinner, L., Fallon, S.J., Waelbroeck, C., Michel, E., Barker, S., 2010. Ventilation of the deep Southern Ocean and deglacial CO_2 rise. Science 328, 1147–51.

Skinner, L., McCave, N.I., Carter, L., Fallon, S.J., Scrivner, A., Primeau, F., 2015.

Reduced ventilation and enhanced magnitude of the deep Pacific carbon pool during the last glacial period. Earth Planet. Sci. Lett. 411, 45–52.

Skinner, L., Scrivner, A., Vance, D., Barker, S., Fallon, S.J., Waelbroeck, C., 2013. North Atlantic versus Southern Ocean contributions to a deglacial surge in deep ocean ventilation. Geology 41, 667–670.

Skinner, L., Shackleton, N., 2004. Rapid transient changes in northeast Atlantic deep water ventilation age across Termination I. Paleoceanography 19, 1–12.

Skinner, L., Waelbroeck, C., Scrivner, A., Fallon, S.J., 2014. Radiocarbon evidence for alternating northern and southern sources of ventilation of the deep Atlantic carbon pool during the last deglaciation. Proc. Natl. Acad. Sci. 1–5.

Soulet, G., Skinner, L., Beaupre, S.R., Galy, V., 2016. A Note on reporting of reservoir ^{14}C disequilibria and age offsets. Radiocarbon.

Spero, H.J., Lea, D., 2002. The cause of carbon isotope minimum events on glacial terminations. Science 296, 522–5.

Spratt, R.M., Lisiecki, L.E., 2016. A Late Pleistocene sea level stack. Clim. Past 12, 1079.

Stephens, B.B., Keeling, R.F., 2000. The infuence of Antarctic sea ice on glacial-interglacial CO_2 variations. Nature 404, 171–174.

Stott, L., Southon, J., Timmermann, A., Koutavas, A., 2009. Radiocarbon age anomaly at intermediate water depth in the Pacific Ocean during the last deglaciation. Paleoceanography 24, PA2223.

Stuiver, M., Polach, H.A., 1977. Radiocarbon, discussion reporting of ^{14}C data. Radiocarbon 19, 355–363.

Svensson, A., Andersen, K.K., Bigler, M., Clausen, H.B., Dahl-Jensen, D., Davies, S.M., Johnsen, S.J., Muscheler, R., Rasmussen, S.O., Röthlisberger, R., 2006. The Greenland Ice Core Chronology 2005, 15–42ka. Part 2: comparison to other records. Quat. Sci. Rev. 25, 3258–3267.

Talley, L.D., Pickard, G.L., Emery, W.J., Swift, J.H., 2011. Descriptive Physical Oceanography: An introduction, 6th ed. Elsevier, Boston.

Toggweiler, J.R., 2009. Shifting Westerlies. Science 323, 1434–1435.

Toggweiler, J.R., 1999. Variation of atmospheric CO_2 by ventilation of the ocean's deepest water. Paleoceanography 14, 571–588.

Toggweiler, J.R., Dixon, K., Broecker, W.S., 1991. The Peru Upwelling and the ventilation of the South Pacific Thermocline. J. Geophys. Res. 96, 20467–20497.

Toggweiler, J.R., Russell, J., Carson, S.R., 2006. Midlatitude westerlies, atmospheric CO_2, and climate change during the ice ages. Paleoceanography 21, 1–15.

Tsuchiya, M., Lukas, R., Fine, R. a., 1989. Source Waters of the Pacific Equatorial Undercurrent. Prog. Oceanogr. 23, 101–147.

Tsuchiya, M., Talley, L.D., 1998. A Pacific hydrography section at 88°W: Water-property distribution. J. Geophys. Res. 103, 12,899–12,918.

Tzedakis, P.C., Channell, J.E.T., Hodell, D. a, Kleiven, H.F., Skinner, L., 2012. Determining the natural length of the current interglacial. Nat. Geosci. 5, 1–4.

Uchikawa, J., Penman, D.E., Zachos, J.C., Zeebe, R., 2015. Experimental evidence for kinetic effects on B/Ca in synthetic calcite: Implications for potential $B(OH)_4^-$ and $B(OH)_3$ incorporation. Geochim. Cosmochim. Acta 150, 171–191.

Vandergoes, M.J., Hogg, A.G., Lowe, D.J., Newnham, R.M., Denton, G., Southon, J., Barrell, D.J. a., Wilson, C.J.N., McGlone, M.S., Allan, A.S.R., Almond, P.C., Petchey, F., Dabell, K., Dieffenbacher-Krall, A.C., Blaauw, M., 2013. A revised age for the Kawakawa/Oruanui tephra, a key marker for the Last Glacial Maximum in New Zealand. Quat. Sci. Rev. 74, 195–201.

Vogel, J.S., Southon, J.R., Nelson, D.E., Brown, T.A., 1984. Performance of catalytically condensed carbon for use in accelerator mass spectrometry. Nucl. Instruments Methods Phys. Res. B5 289–293.

Volk, T., Hoffert, M.I., 1985. Ocean carbon pumps: analyisis of relative strengths and efficiencies in ocean-driven atmospheric CO_2 changes. Geophys. Monogr. Ser. 32.

Waelbroeck, C., Skinner, L., Labeyrie, L., Duplessy, J.-C., Michel, E., Vazquez Riveiros, N., Gherardi, J.-M., Dewilde, F., 2011. The timing of deglacial circulation changes in the Atlantic. Paleoceanography 26, PA3213.

Wallmann, K., 2010. Phosphorus imbalance in the global ocean? Global Biogeochem. Cycles 24, 1–12.

Wanninkhof, R., 1992. Relationship between wind speed and gas exchange over the ocean. J. Geophys. Res. 97, 7373–7382.

Watson, A., Naveira Garabato, A.C., 2006. The role of Southern Ocean mixing and upwelling in glacial-interglacial atmospheric CO_2 change. Tellus 58B, 73–87.

Williams, R.G., Follows, M.J., 2011. Ocean dynamics and the carbon cycle: Principles and mechanisms. Cambridge University Press.

Yu, J., Anderson, R.F., Jin, Z., Rae, J.W.B., Opdyke, B.N., Eggins, S., 2013. Responses of the deep ocean carbonate system to carbon reorganization during the Last Glacial–interglacial cycle. Quat. Sci. Rev. 76, 39–52.

Yu, J., Anderson, R.F., Rohling, E.J., 2014. Deep ocean carbonate chemistry and glacial-interglacial atmospheric CO_2 changes. Oceanography 27, 16–25.

Yu, J., Broecker, W.S., Elderfield, H., Jin, Z., McManus, J.F., Zhang, F., 2010a. Loss of carbon from the deep sea since the Last Glacial Maximum. Science 330, 1084–7.

Yu, J., Elderfield, H., 2007. Benthic foraminiferal B/Ca ratios reflect deep water carbonate saturation state. Earth Planet. Sci. Lett. 258, 73–86.

Yu, J., Elderfield, H., Greaves, M., Day, J., 2007a. Preferential dissolution of benthic foraminiferal calcite during laboratory reductive cleaning. Geochemistry Geophys. Geosystems 8.

Yu, J., Elderfield, H., Honisch, B., 2007b. B/Ca in planktonic foraminifera as a proxy for surface seawater pH. Paleoceanography 22.

Yu, J., Foster, G.L., Elderfield, H., Broecker, W.S., Clark, E., 2010b. An evaluation of benthic foraminiferal B/Ca and $\delta^{11}B$ for deep ocean carbonate ion and pH reconstructions. Earth Planet. Sci. Lett. 293, 114–120.

Zeebe, R., 2012. History of seawater carbonate chemistry, atmospheric CO_2, and ocean acidification. Annu. Rev. Earth Planet. Sci. 141–165.

Zeebe, R., Wolf-Gladrow, D.A., 2001. CO_2 in seawater: equilibrium, kinetics, isotopes. Gulf Professional Publishing.

By Eva Calvo

ACKNOWLEDGEMENTS/AGRADECIMIENTOS

Muchísimas gracias Eva e Isa, porque además de mis directoras de tesis, sois mis amigas, y sois dos excelentes científicas y de las mejores personas que me he encontrado por el mundo. Muchas gracias Eva por darme la oportunidad de empezar esta tesis, por confiar en mí y por ser siempre tan cercana. El camino ha sido largo, pero aquí estamos! Las muchas conversaciones que hemos tenido en tu despacho, de ciencia y de la vida, no tienen precio! Isa, gracias por estar al 100% en los pequeños ratos de charla y gracias por haber corrido como "Espiri" Gonzáles estos últimos meses! Y por supuesto, gracias por las reuniones en los cafés modernos del barrio. Gracias a las dos, porque me habéis hecho crecer mucho.

Gracias compañeros de grupo, Àngel que tanto me has ayudado con las macros y los scripts, siempre disponible, Elisa y nuestras charletas y risas en el despacho, Juancho por tu ayuda este último mes (aún te debo unas birritas!), Lucía, y Carles, muchas gracias por ser tan sereno, siempre con una sonrisa y ciencia para discutir.

Miles de gracias Patri, Judit y Albert por todas esas horas de picking infernal! Y por echarme una buena mano llena de risas cada vez que tenía que ir a la UB.

Gracias compañeros de despacho, Edgar, Elisa, Mireia y Encarna, porque ahí todos junticos cual teleoperadores hemos pasado momentos de todo tipo! Muy divertido.. Y todos vosotros compañeros del ICM, Francisquito y su maravillosa música, mi Maripi Anamari y su salero sevillano que tanta alegría me ha traído, Ramiro, Guillem, Fran (mi más alto amigo), Sergio y sus rastas, Pedro y su Océano Pacífico, Elena, Caterina, y más y más! Y gracias a Conchita, Eva López y Jordi Estaña por su eficiencia y por ayudarme siempre con una sonrisa.

Mil gracias mis bootcamperos/as y compañeros/as de carreras nocturnas montañeras, Fran, Anamari, Eli, Carlos y Antoñito, por tan buenos momentos llenos de energía! fue un verano genial. Y también por todos esos partidos de volley, jun-

to con vosotros/as compañeros/as de recursos, Dafni, Fede, John y el wuevoncito Claudio. Gracias por enseñarme a jugar!.

Gracias también a El Cometa, al Espai Capra y al Taranna que tanta inspiración me han traído en los fantásticos espacios que han creado. Y gracias a la buena música (y no tan buena) que me ha acompañado todo este tiempo, que me ha hecho bailar en la silla mientras hacia gráficas y disfrutar de todo esto mas que si lo hubiese hecho solita.

Many thanks Wolfgang and David for making my stay in RHUL so pleasant, for helping me with machines and all, and for trusting me at 1 am in the lab! Thanks for all the nice discussions. And thank you all Egham people, Oris, Giovanni, Damiano, Miguelito, Julia, Gerd, Seb and Eldert, for being able to do so many nice things in such a small village! It was great there.

Thanks Daniel for so much encoragment and for teaching me english!

Thanks very much to all Cambridge people, specially Aleksey (done!), Anna Lena (for absolutely everything!), Adam, Sambuddha, Julia, Jo, Mervyn, David (and his JC089 cruise!), Benoit and Natalia (gracias por introducirme en el mundo del licor café Natalia!). And Samba Band! And thank you so much Vas and Chronis for all the nice dinners and chats in your place. Cambridge is even more beautiful when you are there.

Muchas gracias a todas las personas que me han ayudado a crecer científicamente durante estos años, que son muchas muchas y de muchos lados!

Gracias amigas “Mandrileñas”, amigas de toda la vida, Carol, Alicia, Almu y Marina, porque aunque estamos repartidas por el mundo ahí seguimos en conexión total. Con vosotras he pasado muchos de los mejores momentos de mi vida.

Gracias Paula, porque ha sido muy divertido compartir nuestro estrés conjunto durante estos últimos meses de la tesis, vamos que ya lo tenemos!

Gracias Joselín, amigo mío, por tantos años compartidos, aquí y allí, en todos lados. Por tener un don para la escucha y por acordarte de todo! Es un placer tenerte como amigo.

Muchas gracias compañeros de piso, Alex, Marttita, Manelito, Mireia, Rubén y Julen. Por escucharme, por divertirnos juntos, por las pelis en el proyector, por sacarme de casa a pasear y por todas la cañas en el barrio! Que alegría haber caído en esa casa.

Merci beaucoup François por ayudarme a venir a Barcelona a empezar esta tesis, y más aún, por cambiar el rumbo de mi vida hace ya unos cuantos años y por haber crecido juntos.

Gracias amigo y hermano Suso, porque desde que te montaste en mi Kadett gitanesco hace ya más de 10 años, no hemos parado de seguirnos por el mundo. Gracias porque sin tu insistencia no estaría aquí, y gracias por tanta discusión (paleo?) oceanográfica (incrédulo el!), y por supuesto, por ser el mejor capitán de barco. Tú, y tus mil habilidades sois geniales!

Gracias a Barcelona, por todo lo que he vivido en ella, porque es mi casa.

Miles de gracias familia, mamá, papá, Carol, Moni, cuñados y mis albondiguillas, mis sobrinos Noel y Nora. Gracias por la confianza, por el interés, por la alegría, por el cariño, por la fuerza y por toda la ayuda constante. Sois lo más grande..

And thank you so much Luke, because you have given me a new way to look at science, at life. Thanks very much for all your help, disscusion, trust, patience, laugh, and love.. for being such a big part of my life and having a smile when i need it.. for being such a great scientist y por ayudarme a creer en mí misma cada día más.. gracias Luke.. :)

Platja Ses Covetes, Majorca, Abril de 2015